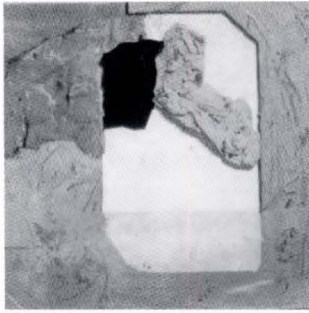



FUJITSU

**SCIENTIFIC & TECHNICAL
JOURNAL**

Autumn 1992 VOL.28, NO.3
Special Issue on Electronic Materials





The Issue's Cover :

ZONA CONFINARIA (Boundary Zone)
by Junroh MANABE

FUJITSU Scientific & Technical Journal is published quarterly by FUJITSU LIMITED of Japan to report the results of research conducted by FUJITSU LIMITED, FUJITSU LABORATORIES LTD., and their associated companies in communications, electronics, and related fields. It is the publisher's intent that FSTJ will promote the international exchange of such information, and we encourage the distribution of FSTJ on an exchange basis. All correspondence concerning the exchange of periodicals should be addressed to the editor.

FSTJ can be purchased through KINOKUNIYA COMPANY LTD., 38-1, Sakuragaoka 5-Chome, Setagaya-ku, Tokyo 156, Japan, (Telephone : +81-3-3439-0162, Facsimile : +81-3-3706-7479).

The price is US\$7.00 per copy, excluding postage.

FUJITSU LIMITED reserves all rights concerning the republication and publication after translation into other languages of articles appearing herein.

Permission to publish these articles may be obtained by contacting the editor.

FUJITSU LIMITED

Tadashi Sekizawa, *President*

FUJITSU LABORATORIES LTD.

Mikio Ohtsuki, *President*

Editorial Board

Editor Shigeru Sato

Associated Editors Hajime Ishikawa Hideo Takahashi

Editorial Representatives

Sadao Fujii	Tetsuya Isayama	Ken-ichi Itoh
Yoshihiko Kaiju	Masasuke Matsumoto	Yoshimasa Miura
Makoto Mukai	Yasushi Nakajima	Hiroshi Nishi
Koichi Niwa	Hajime Nonogaki	Juro Ohga
Shinji Ohkawa	Shinya Okuda	Hirofumi Okuyama
Teruo Sakurai	Yoshio Tago	Shozo Taguchi
Makoto Saito	Mitsuhiko Toda	Takao Uehara
Akira Yoshida		

Editorial Coordinator

Yukichi Iwasaki

FUJITSU LIMITED 1015 Kamikodanaka, Nakahara-ku,
Kawasaki 211, Japan

Cable Address : FUJITSULIMITED KAWASAKI

Telephone : +81-44-777-1111

Facsimile : +81-44-754-3562

Printed by MIZUNO PRITECH Co., Ltd. in Japan

© 1992 FUJITSU LIMITED (September 25, 1992)

CONTENTS

Featuring Papers

- 299 Preface
● Masao Hiyane
- 301 Flip-Chip Connection Materials for Packaging of VLSIs Operating in Liquid Nitrogen
● Kaoru Hashimoto ● Teru Nakanishi ● Masayuki Ochiai
- 310 Laser Welding of Copper and Copper Alloys
● Kozo Shimizu ● Kaoru Hashimoto
- 316 High-Efficiency Coolant for Direct-Immersion Cooling
● Mitsutaka Yamada ● Kishio Yokouchi ● Nobuo Kamehara
- 321 Multilayer Ceramic Substrate for HEMT Packaging (Liquid Nitrogen Packaging for GaAs Devices)
● Shigenori Aoki ● Yoshihiko Imanaka ● Kishio Yokouchi
- 329 High-Frequency Response in Bi-Based Superconducting Microstriplines
● Atsushi Tanaka ● Nobuo Kawahara ● Koichi Niwa
- 335 Flash Fusible Color Toner for Color Laser Printers
● Katsuji Ebisu ● Takahiro Kashikawa ● Norio Sawatari
- 347 High Sensitive Organic Photoconductor
● Tsuneo Watanuki ● Norio Sawatari
- 357 High Contrast SSFLC Display Utilizing Naphthalene Base Liquid Crystal Materials and Conductive Orientation Films
● Akihiro Mochizuki ● Katsusada Motoyoshi
- 369 Super High Information Content Projection Display Using an NCPT Liquid Crystal
● Akihiro Mochizuki ● Shigeo Kasahara ● Yoshikazu Yabe
- 377 Polysiloxane as a Bi-Level Resist for VLSI Lithographies
● Keiji Watanabe ● Takahisa Namiki ● Yasuhiro Yoneda
- 385 Polysiloxane as an Interlevel Dielectric for VLSI Fabrication
● Shun-ichi Fukuyama ● Michiko Kobayashi ● Yasuhiro Yoneda
- 393 Micromachined Clark Oxygen Electrodes and Biosensors
● Hiroaki Suzuki ● Akio Sugama ● Naomi Kojima
- 402 Development of a Molecular Orbital Package for Spectroscopy (MOS-F) and its Application to Nonlinear Optics
● Azuma Matsuura ● Tomoaki Hayano

Papers

413 **Interactive Extraction of Rules Concerning Variations in Speech**

● Shinta Kimura

422 **Automated MDF System for Switching System**

● Shun-ichi Tominaga

● Sadao Fujii

● Akira Fukuoka

UDC 621.3.049.771

FUJITSU Sci. Tech. J., **28**, 3, pp. 301-309(1992)**Flip-Chip Connection Materials for Packaging of VLSIs Operating in Liquid Nitrogen**

• Kaoru Hashimoto • Teru Nakanishi • Masayuki Ochiai

Solder and metallization materials used for flip-chip connections in liquid nitrogen were studied. Flip-chip connection models consisting of a GaAs model chip and an alumina substrate were made using indium (In), In alloys, and Sn-Pb solders. Indium solder exhibited the longest fatigue life in thermal shock tests between liquid nitrogen and room temperatures. Wettability and dissolution tests showed that Au film is well wetted with In solder and that Pt film is resistant to dissolution into In solder. A random number generator was assembled from HEMT LSIs using flip-chip connections with In solder and Au/Pt/Ti film. The generator operates correctly after several hundred cycles between liquid nitrogen and room temperatures, indicating that this combination is suitable for flip-chip connections in liquid nitrogen.

UDC 621.375.823:621.791:669.3

FUJITSU Sci. Tech. J., **28**, 3, pp. 310-315(1992)**Laser Welding of Copper and Copper Alloys**

• Kozo Shimizu • Kaoru Hashimoto

The laser welding of pure copper and copper alloy is difficult because of copper's high thermal conductivity and reflectivity. To solve this problem, this paper examines the nickel plating of copper. The paper also examines heat-treatment to obtain a nickel-copper solid solution to reduce the thermal conductivity. Because the thermal conductivity of the solid solution is lower than that of pure copper, the laser penetrates the nickel-plated copper more deeply. The experimental results indicate that nickel plating and heat-treatment make it possible to laser-weld copper and copper alloys.

UDC 621.5.047:621.564.3

FUJITSU Sci. Tech. J., **28**, 3, pp. 316-320(1992)**High-Efficiency Coolant for Direct-Immersion Cooling**

• Mitsutaka Yamada • Kishio Yokouchi • Nobuo Kamehara

Direct-Immersion cooling is considered to be one of the most effective cooling technologies for high-speed computers. However, there are many problems in practical applications, such as temperature overshoot. To eliminate this problem, using a mixture of various coolants has been found to provide several benefits. At room temperature, the temperature overshoot on the chip surface at the onset of boiling is decreased by using a mixture of coolants having different boiling points. At liquid nitrogen temperature (77 K), the maximum heat flux is increased by adding fluorocarbon to pure liquid nitrogen. This paper discusses the effects of using a mixture of coolants and adding fluorocarbons.

UDC 621.3.049.772:621.382.3:666.266.6

FUJITSU Sci. Tech. J., **28**, 3, pp. 321-328(1992)**Multilayer Ceramic Substrate for HEMT Packaging (Liquid Nitrogen Packaging for GaAs Devices)**

• Shigenori Aoki • Yoshihiko Imanaka • Kishio Yokouchi

For flip-chip bonding of HEMTs, the thermal expansion of zirconia/borosilicate glass composite substrate must match that of GaAs below room temperature. Normally, zirconium silicate reduces the expansion of the composite substrate. In this research, zirconia powder coated with alumina by freeze-drying was used to prevent the formation of zirconium silicate. By also controlling the ratio of glass to alumina-coated powder, the difference in thermal expansions of GaAs and the new composite was limited to 0.4×10^{-4} between 77 K and room temperature. This compares favorably with the figure for conventional alumina. A test module of the new composite verified that connection reliability in liquid nitrogen is greatly improved.

UDC 538.945:621.3.029.6

FUJITSU Sci. Tech. J., **28**, 3, pp. 329-334(1992)**High-Frequency Response in Bi-Based Superconducting Microstriplines**

• Atsushi Tanaka • Nobuo Kamehara • Koichi Niwa

The microwave transmission losses and phase velocities of Bi-Sr-Ca-Cu-O (BSCCO) micro-striplines were measured as a function of temperature and frequency. Microstrip meander lines 78 mm long and 200 μm wide were prepared using Bi-based superconducting film. The transmission properties of these lines were studied at frequencies up to 18 GHz using a vector network analyzer. The loss in these lines was less than that in a geometrically equipivalent gold line up to 18 GHz and was 1.5 dB and 10 GHz and 54.6 K. The phase velocity of the BSCCO lines was 1.18×10^{10} cm/s at 54 K and 1 GHz, which is slightly lower than the figure obtained for the gold line.

UDC 667.526:681.327.5

FUJITSU Sci. Tech. J., **28**, 3, pp. 335-346(1992)**Flash Fusible Color Toner for Color Laser Printers**

• Katsuji Ebisu • Takahiro Kashikawa • Norio Sawatari

A flash fusible color toner for color laser printers with flash fusing sub-systems has been developed. This paper describes the materials developed for the color toner.

Conventional color toners cannot be used for flash fusing because they do not absorb light energy in the near-infrared region, where the spectral intensity of flash lamps is high. Therefore a near-infrared absorbent that enables a color toner to absorb most of the flash lamp's light energy was developed. A polyester resin and an amine-modified styrene-acryl resin for the toner binders were developed to give the toner good fusibility. The final color toner has excellent fused fixing quality and brightness.

UDC 621.375.826:771.5

FUJITSU Sci. Tech. J., **28**, 3, pp. 347-356(1992)**High Sensitive Organic Photoconductor**

• Tsuneo Watanuki • Norio Sawatari

This paper reports on experiments performed to determine the optimal multi-layered organic photoconductor comprising a phthalocyanine pigment and a carrier transport material. Meta-stable form titanium oxide phthalocyanine, characterized by its unique X-ray diffraction pattern, is sensitive enough to near-infrared light to be used with a compact light source such as a laser diode (LD). The photoconductor device using this pigment in combination with a butadiene derivative exhibits half decay exposure of less than $0.2 \mu\text{J}/\text{cm}^2$, low residual potential, and excellent durability.

UDC 548-144

FUJITSU Sci. Tech. J., **28**, 3, pp. 357-368(1992)**High Contrast SSFLC Display Utilizing Naphthalene Base Liquid Crystal Materials and Conductive Orientation Films**

• Akihiro Mochizuki • Katsusada Motoyoshi

This paper describes the electrical properties of a surface stabilized ferroelectric liquid crystal (SSFLC) display provided by an almost ideal bookshelf layer structure. The bookshelf layer structure is produced by using ordinary rubbed polymer film cells together with a special liquid crystal containing a naphthalene ring. Both the layer structure of the naphthalene base FLCs and their electrooptic switching are discussed. Some polarization switching phenomena in conjunction with the conductivity of the orientation layer are also shown. A multiplexed FLC prototype was built with a 640 x 201 pixel display, and this gave a 40 : 1 contrast ratio and 40 percent transmittance.

UDC 548-144

FUJITSU Sci. Tech. J., **28**, 3, pp. 369-376(1992)**Super High Information Content Projection Display Using an NCPT Liquid Crystal**

● Akihiro Mochizuki ● Shigeo Kasahara ● Yoshikazu Yabe

A multiplexed high luminance liquid crystal projection display with 2240 x 2240 (5 million) pixels for use with a conventional overhead projector has been developed. It has been clarified theoretically and by experiment that the surface effect on the cholesteric-nematic phase transition results in stable bistability. Optimizing the helical pitch of chiralnematic liquid crystal in conjunction with the surface anchoring strength has made possible super-high information content. Moreover the fact that this display requires no polarizers enables very bright screen images. These characteristics match with high resolution (typically 300 dpi) printer output. The combined result of the theoretical investigation and the materials research is a practical high performance liquid crystal display.

UDC 621.3.049.76

FUJITSU Sci. Tech. J., **28**, 3, pp. 377-384(1992)**Polysiloxane as a Bi-Level Resist for VLSI Lithographies**

● Keiji Watanabe ● Takahisa Namiki ● Yasuhiro Yoneda

A newly designed organosilicon resist, three-dimensional polysilphenylenesiloxane (TSPS), has been developed for use as a high-resolution negative bi-level electron-beam resist or KrF-excimer laser resist. The TSPS molecule is a rigid three-dimensional mesh consisting of a silphenylenesiloxane core surrounded by functional groups. The advantages of such a structure are low swelling, a high oxygen-reactive ion etching resistance, and a high softening temperature. A 0.075 μm line-and-space pattern is well-defined after electron beam exposure. TSPS can also be used as a deep-UV resist. A 0.25 μm pattern can be delineated using a TSPS/novolac bi-level resist systems with a KrF-excimer laser stepper (NA = 0.37).

UDC 621.3.049.772

FUJITSU Sci. Tech. J., **28**, 3, pp. 385-392(1992)**Polysiloxane as an Interlevel Dielectric for VLSI Fabrication**

● Shun-ichi Fukuyama ● Michiko Kobayashi ● Yasuhiro Yoneda

A new silylated polymethylsilsequioxane (PMSS) resin has been developed and evaluated for use as an interlevel dielectric in VLSI multilevel interconnections. PMSS has good heat resistance. The dielectric constant is 3, which is lower than that of conventional inorganic dielectrics. Degassing from PMSS is very low. PMSS does not crack even when it is 4 μm thick on a 1 μm thick metal topographic substrate that is heated to 450 °C in nitrogen. PMSS has excellent planarity. Trilevel interconnections using PMSS as an interlevel dielectric can be fabricated. Well-planarized metal wiring patterns can be obtained, and no cracks have been found in PMSS layers.

UDC 621.3.035.2:661.937

FUJITSU Sci. Tech. J., **28**, 3, pp. 393-401(1992)**Micromachined Clark Oxygen Electrodes and Biosensors**

● Hiroaki Suzuki ● Akio Sugama ● Naomi Kojima

Miniature Clark oxygen electrodes were fabricated using micro-machining. The type I model has the following components: a cathode and anode formed in a V-groove made by anisotropic etching of silicon, a solid electrolyte, and a gas-permeable membrane. Improving the electrolyte and membrane materials produced excellent long-term storage stability and sterilization tolerance. The type I model was used to monitor fermentation and to make miniature biosensors. The type II model consists of a glass substrate with detecting electrodes bonded to a silicon container substrate with V-grooves. The gas-permeable membrane is thermally adhered fluorinated ethylene-propylene (FEP). Improving the membrane adhesion made the oxygen electrode tolerant to steam-sterilization.

UDC 539.193:547.12

FUJITSU Sci. Tech. J., **28**, 3, pp. 402-412(1992)**Development of a Molecular Orbital Package for Spectroscopy (MOS-F) and its Application to Nonlinear Optics**

● Azuma Matsuura ● Tomoaki Hayano

A molecular orbital package, MOS-F (semiempirical Molecular Orbital package for Spectroscopy-Fujitsu version), has been developed for high-speed computations for large organic optical molecules. MOS-F has been used to screen and design organic nonlinear optical materials. A novel electro-optic polymer which shows an optical nonlinearity almost as large as that of lithium niobate was found. Using MOS-F, optical nonlinearity of long azomethine conjugated systems was predicted. Frontier molecular orbital analysis revealed that donor/acceptor regions are induced in the main chain without a donor/acceptor substituent. It was also found that nonlinearity is improved by substituting donor groups at donor regions and acceptor groups at acceptor regions.

UDC 534.78

FUJITSU Sci. Tech. J., **28**, 3, pp. 413-421(1992)**Interactive Extraction of Rules Concerning Variations in Speech**

● Shinta Kimura

This paper describes the interactive extraction of rules that estimate acoustic-segment sequences from an orthography of Japanese language. The rules are in the format of context-sensitive rewriting rules and are arranged into four layers. Initial rules are given by traditional Japanese phonology. In the interactive rule extraction, top-down segmentation is used to automatically detect speech data that contains variations that are not described by the existing rules. In the extraction experiments, 163 rules were extracted from 1000 Japanese phrases spoken by one male and 255 rules were extracted from 10000 Japanese phrases spoken by ten males. The rules account for 21 kinds of variation phenomena.

UDC 621.395.72

FUJITSU Sci. Tech. J., **28**, 3, pp. 422-438(1992)**Automated MDF System for Switching System**

● Shun-ichi Tominaga ● Sadao Fujii ● Akira Fukuoka

This paper describes an automated main distributing frame (MDF) system designed to provide the MDF system of a switching system with remote control and automatic jumpering. The MDF system crossconnects between subscriber cables and office equipment cables by jumpering. Until now, jumpering has been done manually and automating this operation for telephone services has been an objective for a long time. In this system, a high-precision robot jumperers telephone lines by inserting miniature contact pins into cross-point holes in matrix boards. A single automated MDF system can handle up to 2100 office-equipment cable terminals, and a larger automated MDF system can be realized by operating multiple systems in parallel.



Preface

Special Issue on Electronic Materials

Masao Hiyane
Managing Director
FUJITSU LABORATORIES LTD.

This special issue is a collection of papers which illustrate the range of Fujitsu's research and development activities in the materials field. Included in this issue are papers on the development of packaging for main frame computers, a color toner for high-speed printers, and new types of displays and bio-sensors.

This issue shows that the material group's activities are not limited to the development of materials, but also include the refinement of treatment techniques in manufacturing processes. This issue also shows that materials research and development at Fujitsu is often undertaken so that device and systems engineers can meet our customers' needs. This collaboration between engineers and customers often generates novel solutions which surpass the basic goals of a project. Three examples of Fujitsu's research and development successes in this field are described below.

- 1) Fujitsu has developed a unique lubrication method that enables the head of a magnetic recording system to fly closer to the recording medium in order to increase the recording density. In this method, specially blended organic compounds and ferrite powder are heat-treated to form evenly distributed pores which can only be seen under a high-resolution scanning electron microscope. Tiny amounts of lubricant absorbed in these pores are released continuously into the head gap. The combination of this lubrication method and the use of media having superior magnetic properties have enhanced the performance of Fujitsu's magnetic disk storage systems.
- 2) The ceramic printed circuit boards used in supercomputers greatly reduce the signal propagation delay. However, it has been difficult to incorporate copper conductors into these boards because the firing processes that effectively decompose the binder compound also unintentionally oxidize the copper patterns. Now, after painstaking research we have found a unique firing method which decomposes the binder completely without oxidizing the copper.
- 3) In most xerographic printing methods, a dry powder ink is fixed onto paper by a heated roller. However, for high speed printing, it takes a large amount of energy to keep the roller at the required temperature. The flash fusing method eliminates the roller by using a brief, intense flash of light to heat the powder ink (called the toner) without over-heating the unprinted paper areas. A new flash fusible color toner has been developed for high-speed printers that print up to ten thousand lines per minute. This toner has a high light-absorptivity in the near-infrared region and does not reduce the triboelectric charging properties.

Fujitsu has had many other successes, some of which have stemmed from a researcher's personal interest in a particular phenomenon. The undertaking of a series of scrupulously careful experiments on the basis of a personal whim may be peculiar to materials research. A high degree of care and attention to detail is needed at all stages of manufacture, from the preparation of raw materials to the finishing treatments. Every variable must be controlled, including the ambient atmosphere and the presence of dust particles.

Formerly, materials processing and machining were done in different sections of the factory. Nowadays, however, modern techniques such as the formation of chemically functional surfaces and highly precise or fine structures involve a wide variety of chemical and mechanical processes.

Furthermore, the need to minimize waste and to ensure the eventual safe disposal of products have become important issues. Although materials research has traditionally been at the latter end of the development process, it will play a much bigger role in the future.

Computer-aided design (CAD) is not yet as popular among materials engineers as it is in other engineering fields. An article in a latter section reports on the recent remarkable progress in simulation techniques for molecular dynamics and electron behavior in organic compounds. These techniques allow researchers to predict the properties of new materials prior to their actual synthesis. Fujitsu will continue to provide simulation tools based on products developed for in-house use.

In addition to its many successful innovations, Fujitsu is also developing new materials that have no current application, which often raises the question of "Seeds or needs?". We hope that this issue will encourage people to tell us about their own special needs.

UDC 621.3.049.771

Flip-Chip Connection Materials for Packaging of VLSIs Operating in Liquid Nitrogen

• Kaoru Hashimoto • Teru Nakanishi • Masayuki Ochiai

(Manuscript received February 3, 1992)

Solder and metallization materials used for flip-chip connections in liquid nitrogen were studied. Flip-chip connection models consisting of a GaAs model chip and an alumina substrate were made using indium (In), In alloys, and Sn-Pb solders. Indium solder exhibited the longest fatigue life in thermal shock tests between liquid nitrogen and room temperatures. Wettability and dissolution tests showed that Au film is well wetted with In solder and that Pt film is resistant to dissolution into In solder. A random number generator was assembled from HEMT LSIs using flip-chip connections with In solder and Au/Pt/Ti film. The generator operates correctly after several hundred cycles between liquid nitrogen and room temperatures, indicating that this combination is suitable for flip-chip connections in liquid nitrogen.

1. Introduction

High-speed, large-scale computers require LSIs with many gates per chip and a fast switching speed. These computers also require packaging technologies which minimize the signal path length between LSIs. According to Rent's rule¹⁾, the number of input and output (I/O) terminals required for logic integrated circuits increases with the number of gates. For future VLSIs, the number of I/O terminals may increase well above one thousand in a limited chip area. Compared to wire bonding and tape automated bonding (TAB), flip-chip connection enables a smaller bonding area, shorter interconnection length, and lower inductance. Therefore, flip-chip connection is favoured for VLSIs having many I/O terminals.

Also, to obtain higher switching speeds, GaAs devices will be used, and Si and GaAs

A part of this study was presented at the 1988 IEEE VLSI and GaAs Chip Packaging Workshop, Santa Clara, CA, September 12-14, 1988, and also was published in *IEICE Trans.*, **E74**, 8, pp. 2362-2368 (1991).

VLSIs will be operated in liquid nitrogen, at which temperature the carrier mobility in COMS²⁾ and HEMT^{3),4)} devices is higher than that at room temperature.

In anticipation of the above developments, a study was made to find suitable materials for flip-chip connections of Si and GaAs chips operating in liquid nitrogen.

When VLSI chips are operated in liquid nitrogen, a high stress is induced in the solder bumps due to the following: the thermal expansion mismatch between the chip and substrate at the very low temperature, the large distance between the solder bumps and the neutral point, and the narrow spacing between the chip and substrate. Therefore, a new solder with a longer fatigue life is required. Moreover, the reliability of flip-chip connections is affected by the metallization of the bonding pads. Metallization materials must have good compatibility with solders (i.e., good wettability and minimum dissolution).

This paper reports on studies made to find

a suitable solder for a liquid nitrogen environment. Thermal shock tests were performed on Si and GaAs chips that were connected using indium (In) alloy solders and Sn-Pb eutectic solder on alumina substrates in liquid nitrogen. The elongation and tensile strength of these solders were measured, and the effects of these properties on fatigue life were examined. Also, the metallization materials and the multilayer structure were examined with respect to wettability and dissolution using the solder that was found to be suitable for use in flip-chip connection in liquid nitrogen.

2. Experimental procedure

2.1 Solders and solder bump formation

On the basis of a preliminary study, four kinds of solder alloys were examined: In, In-50%Pb, In-48%Sn, and Sn-37%Pb (the percent symbol stands for mass percent). Solder bumps with these compositions were formed by vapor deposition on chips and substrates using a metal mask. Si and GaAs chips and alumina substrates were used. Because of the considerable differences in the vapor pressures of the elemental metals of the solder bumps, the alloy composition of the solder bumps was controlled by correcting the composition of the mother alloy melted in the crucible during deposition. The deposition thickness of the solder bumps was about 100 μm .

2.2 Thermal shock tests

Flip-chip connection models were made using Si and GaAs model chips and alumina substrates. The bump diameter was 200 μm , and the pitch was 400 μm . When the solder bumps were formed on both the chip and the substrate, the bump height after flip-chip connection was about 130 μm . The metallization film of bonding pads was gold over platinum with a titanium underlayer (Au/Pt/Ti).

The thermal shock tests were performed by immersing the models in liquid nitrogen for 30 s, exposing them to nitrogen gas at room temperature for 30 s, and then re-immersing them in liquid nitrogen. The changes in electrical resistance at the solder bumps were measured as

a function of the number of test cycles. Resistance was measured using the four-point probe method.

To examine the effects of mechanical properties on fatigue life, the elongation and tensile strengths of solders were measured in liquid nitrogen using an Instron Universal Tester with a crosshead speed of 0.5 mm/min. The test samples were prepared by punching pieces from the cast and rolled sheets of solder, followed by annealing for 24 hours at room temperature before testing.

2.3 Wettability and dissolution

Wettability and dissolution were examined using In solder because this solder exhibited the longest fatigue life in the thermal shock tests. The wettability of various metallization materials with In solder was measured using a meniscograph (Multicore Universal Solderability Tester, Multicore Solders Ltd.). The metallization materials used in this experiment were Au, Cu, Pd, Ni, and Pt. The thin films were deposited to a thickness of 1000 Å on rectangular Si plates (5 × 30 × 0.3^t mm) by electron-beam vacuum evaporation. The films were treated with a mildly activated rosin flux, and then immersed in an In solder bath at 20 mm/s to a depth of 5 mm. Wettability was evaluated from the wetting time defined in Fig. 1. The shorter the wetting time, the better the wettability.

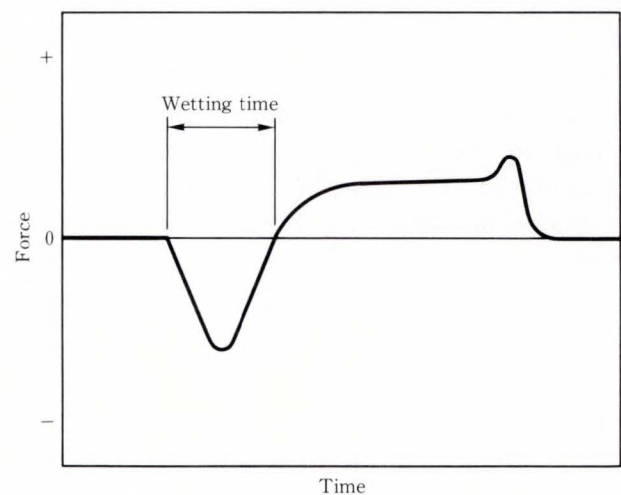


Fig. 1—Time-to-wetting curve according to meniscograph test. Wetting time is defined as shown in the figure.

Dissolution of metallization materials into the In solder was examined by reflowing the solder on each type of thin film. Four types of two-layer metallization films: gold over nickel (Au/Ni), gold over palladium (Au/Pd), gold over copper (Au/Cu), and gold over platinum (Au/Pt) were studied as well as Au, Cu, Pd, Ni, and Pt films. Metallization patterns (3 × 3 mm) were vapor-deposited on glass substrates (10 × 20 × 1^t mm) using the lift-off technique. An In solder sheet (3 × 3 × 2^t mm) was placed on each pattern, then the In solder was melted with a mildly activated rosin flux by heating it to 220 °C. As soon as the solder had begun to wet the metallized film the substrate was tilted and a timer was started. When the solder lost its adhesion and ran down the substrate (i.e., because the metallized film had completely dissolved into the solder) the timer was stopped. The measured time was then recorded as a measure of dissolution⁵). If the solder sample did not

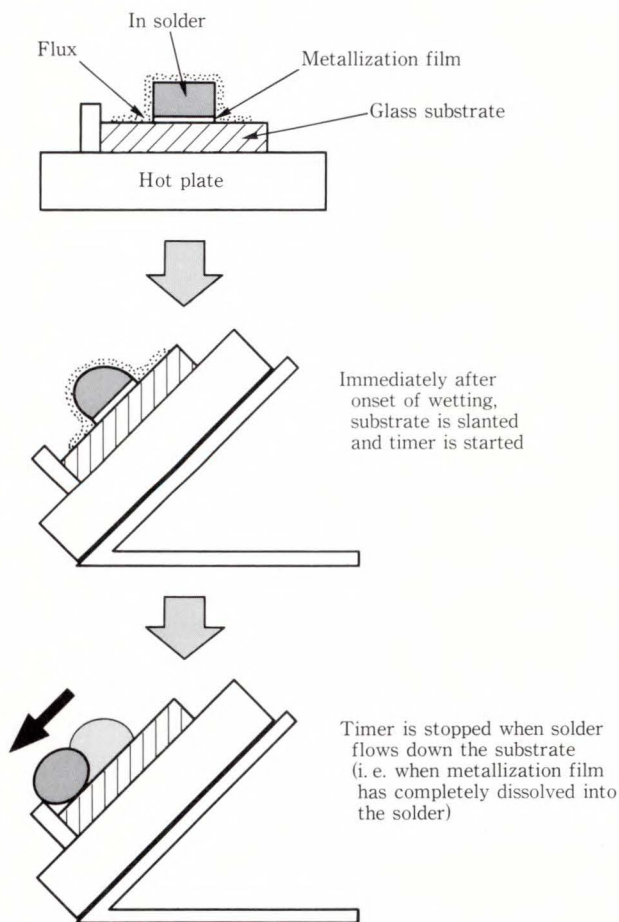


Fig. 2—Method for measuring dissolution time.

run after 720 s, the test was discontinued. The test method is shown in Fig. 2.

3. Results and discussion

3.1 Thermal shock tests

Figure 3 shows an example of an as-deposited solder bump. Figure 4 shows a close-up of a typical flip-chip connection model formed using a GaAs chip and an alumina substrate.

Figure 5 shows the results of thermal shock tests of a Si chip on an alumina substrate. The resistance of Sn-37%Pb solder increases after 80 cycles. The resistance of In-48%Sn and In-50%Pb solders increases after 150 cycles. The resistance of In remains at its initial value even after 300 cycles. This indicates that In and In alloys have a longer fatigue life than Sn-Pb solder, and that they are suitable for Si flip-chip connections in liquid nitrogen.

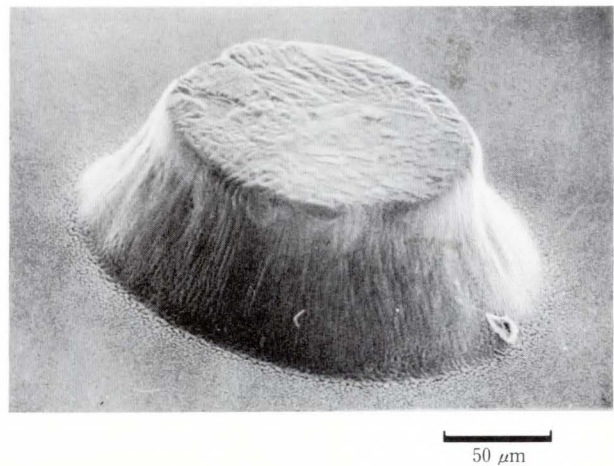


Fig. 3—As-deposited solder bump.

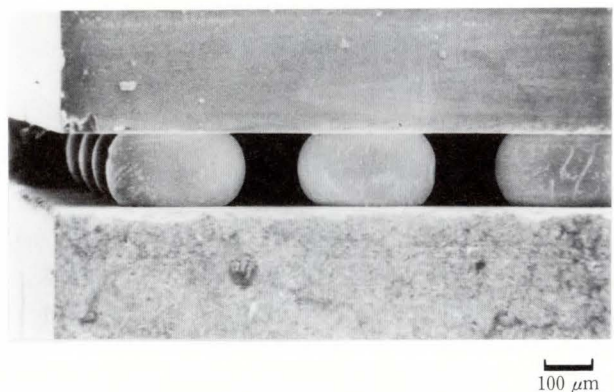


Fig. 4—Close-up of flip-chip connection model consisting of a GaAs chip and an alumina substrate.

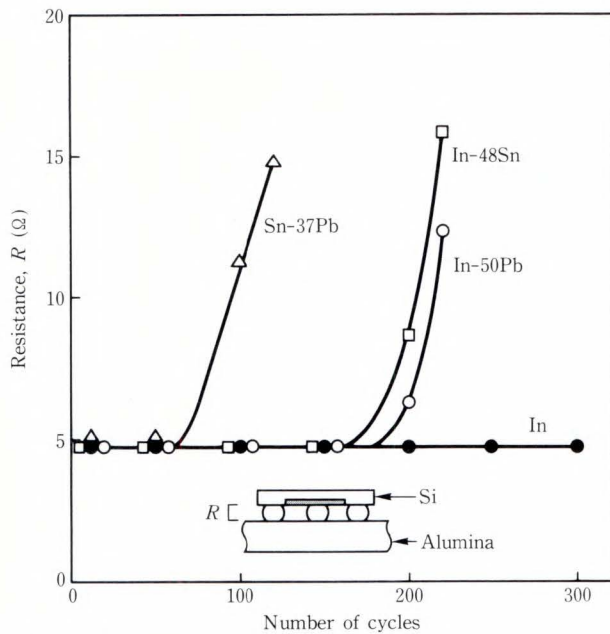


Fig. 5—Changes in resistance during thermal shock tests between liquid nitrogen and room temperatures of a Si chip/alumina substrate flip-chip connection model.

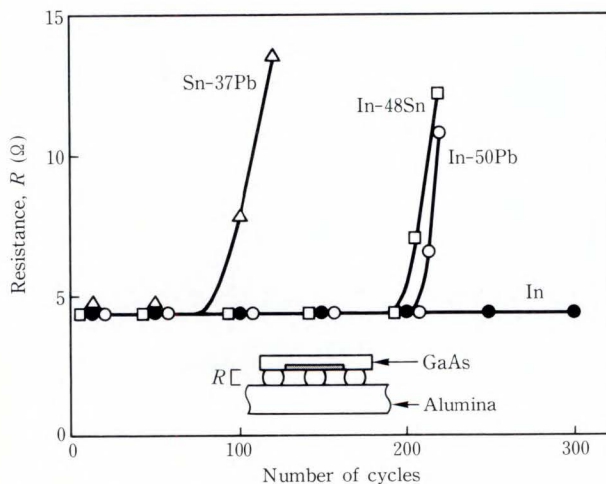


Fig. 6—Changes in resistance during thermal shock tests between liquid nitrogen and room temperatures of a GaAs chip/alumina substrate flip-chip connection model.

Figure 6 shows the results of thermal shock tests of a GaAs chip on an alumina substrate. The resistance of Sn-37%Pb solder increases after 100 cycles. The resistance of In-48%Sn and In-50%Pb solders increases after 200 cycles. The resistance of In remains at its initial value even after 300 cycles. Therefore, as with Si chips, In and In alloys are suitable for GaAs flip-chip connections in liquid nitrogen.

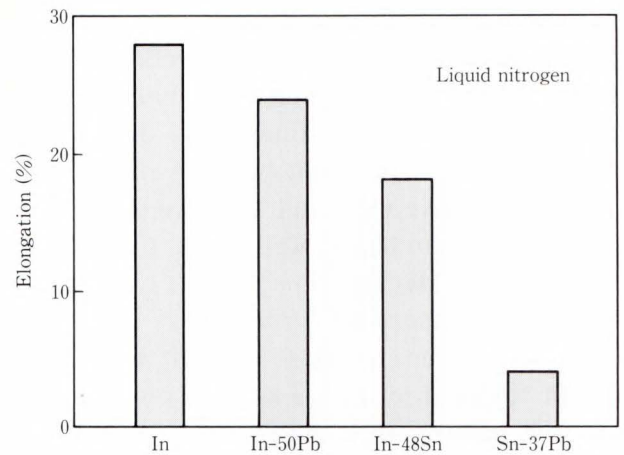


Fig. 7—Elongation of In, In-50%Pb, In-48%Sn, and Sn-37%Pb solders in liquid nitrogen.

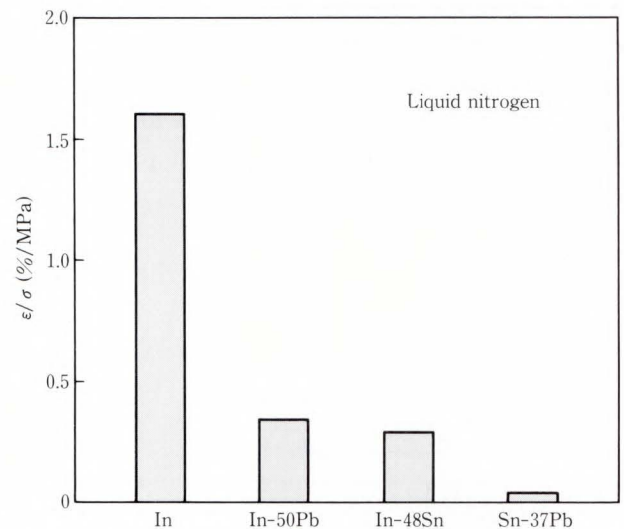


Fig. 8—Elongation to tensile strength ratios (ϵ/σ) of In, In-50%Pb, In-48%Sn, and Sn-37%Pb solders in liquid nitrogen.

The differences in the fatigue lives of the solders are related to their mechanical properties. Figure 7 shows the elongation of each solder in liquid nitrogen. The elongations of In and In alloy (In-50%Pb and In-48%Sn) are almost the same and are much higher than the elongation of Sn-37%Pb solder. Therefore, the large difference in the fatigue lives of In and In alloys is not due to differences in elongation.

To explain this difference in fatigue life, a new factor, the elongation to tensile strength ratio, ϵ/σ^6 , was introduced. As shown in Fig. 8, In solder exhibits a higher ϵ/σ value than In-50%Pb, In-48%Sn, and Sn-37%Pb. This agrees

well with the results of the thermal shock tests. Thus, the ϵ/σ value is considered to be useful for estimating the fatigue life of solder bumps applied to flip-chip connections.

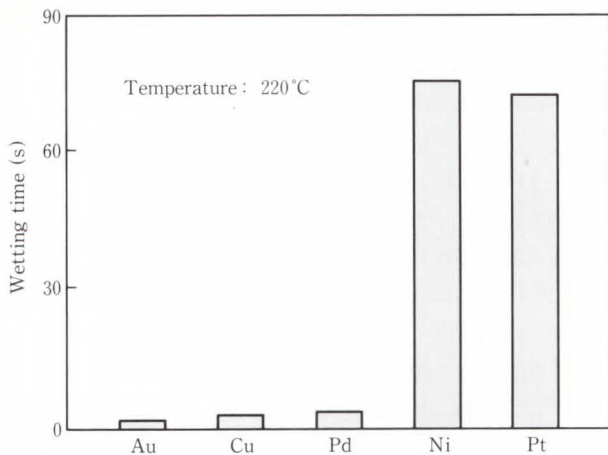


Fig. 9—Wetting time for In solder with various metallization materials.

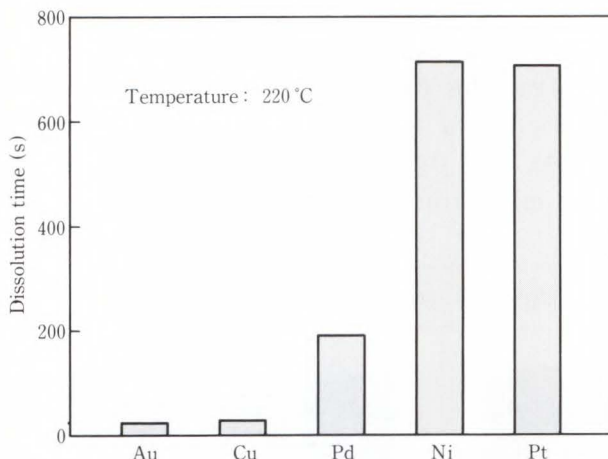


Fig. 10—Dissolution times of Au, Cu, Pd, Ni, and Pt films into In solder.

3.2 Wettability and dissolution

Figure 9 shows the wetting time for different films. The wetting time for Au, Cu, and Pb films is below 1.5 s, which is extremely short compared with that for Ni and Pt films. The short wetting time for Au film (0.7 s) makes it especially suitable for the top layer in multilayer metallization films.

Au and Cu films tend to dissolve into In solder as shown in Fig. 10, disappearing in less than 20 s after the onset of wetting. Pd film dissolves in 200 s, which is 10 times longer than the times for Au and Cu films, but is much shorter than the times for Ni and Pt films. No diffusion was observed for Ni and Pt films even after 720 s, the longest measuring time in the experiment. These results correspond to those shown in Fig. 9. Au and Cu films exhibit good

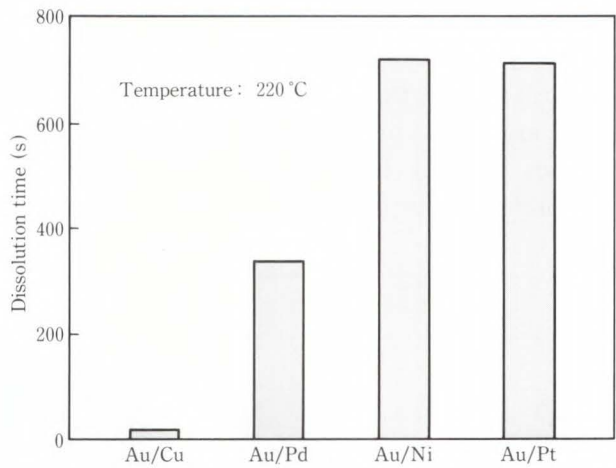
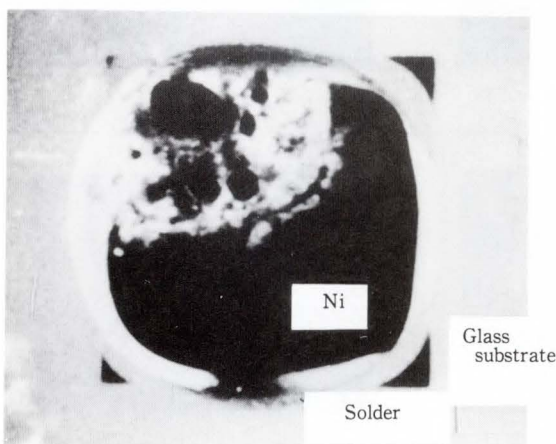
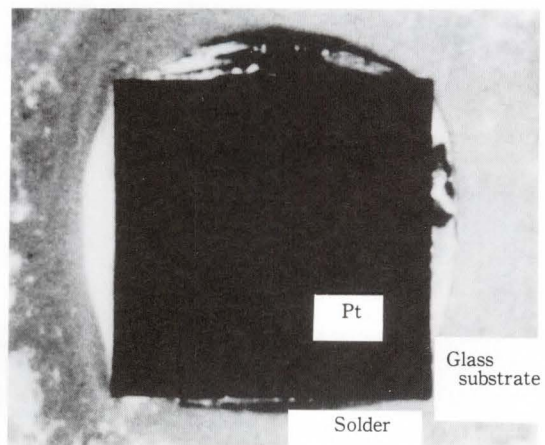


Fig. 11—Dissolution times of Au/Cu, Au/Pd, Au/Ni, and Au/Pt films into In solder.



a) Au/Ni



b) Au/Pt

Fig. 12—Comparison of Au/Ni and Au/Pt films on glass substrates after reflowing In solder for 720 s at 220 °C.

wettability with In solder and readily dissolve into it. Ni and Pt films have poor wettability and are extremely resistant to dissolution.

The same dissolution phenomena is observed with Au/Cu, Au/Pd, Au/Ni, and Au/Pt films, as shown in Fig. 11. Au/Cu film rapidly dissolves into In solder, while Au/Pd film dissolves at a moderate rate. Au/Ni and Au/Pt films, as mentioned above, do not dissolve, even after 720 s. These results indicate that Ni and Pt films are suitable for the barrier layer in multilayer metallization films.

To clarify the difference between Ni and Pt films, glass substrates were used so that the undersides of the films could be inspected. Figure 12 shows the undersides of the films on these glass substrates after the In solder was reflowed for 720 s. The Ni film in Fig. 12 appears partly leached at the edge, whereas the Pt film shows no dissolution at all. Figure 13 shows the results of EDAX analysis on the cross sections of connections. When the chip and substrate are connected by heating, most of the Ni diffuses into the In solder from the initial contact areas of the chip and substrate. The Ni is

therefore widely distributed in the In solder. The Pt, however, diffuses only slightly into the In solder, and most of it remains at the initial contact areas. This suggests that Pt film is superior to Ni film as a metallization material for use as a barrier layer.

Based on the above observations, Cr and Ti film were evaluated for use as the underlayer for adhesion to chips and substrates using Au/Pt/Cr and Au/Pt/Ti metallization patterns. These patterns (3 × 3 mm) were vapor-deposited on Si chips and alumina substrates. The Si chips and alumina substrates were then connected using In solder. Tensile tests were then performed on these models using an Instron Universal Tester.

The tests showed that fractures occur at In solder junctions with Au/Pt/Cr and Au/Pt/Ti films, indicating that both Cr and Ti play a role in the adhesion layer. The average fracture strength of the ten Au/Pt/Cr films and ten Au/Pt/Ti films that were sampled was about 5.6 MPa. This figure is slightly higher than that obtained in a tensile test on a bulk In solder sample. This difference is probably due to the finer microstructure of the solder used in this

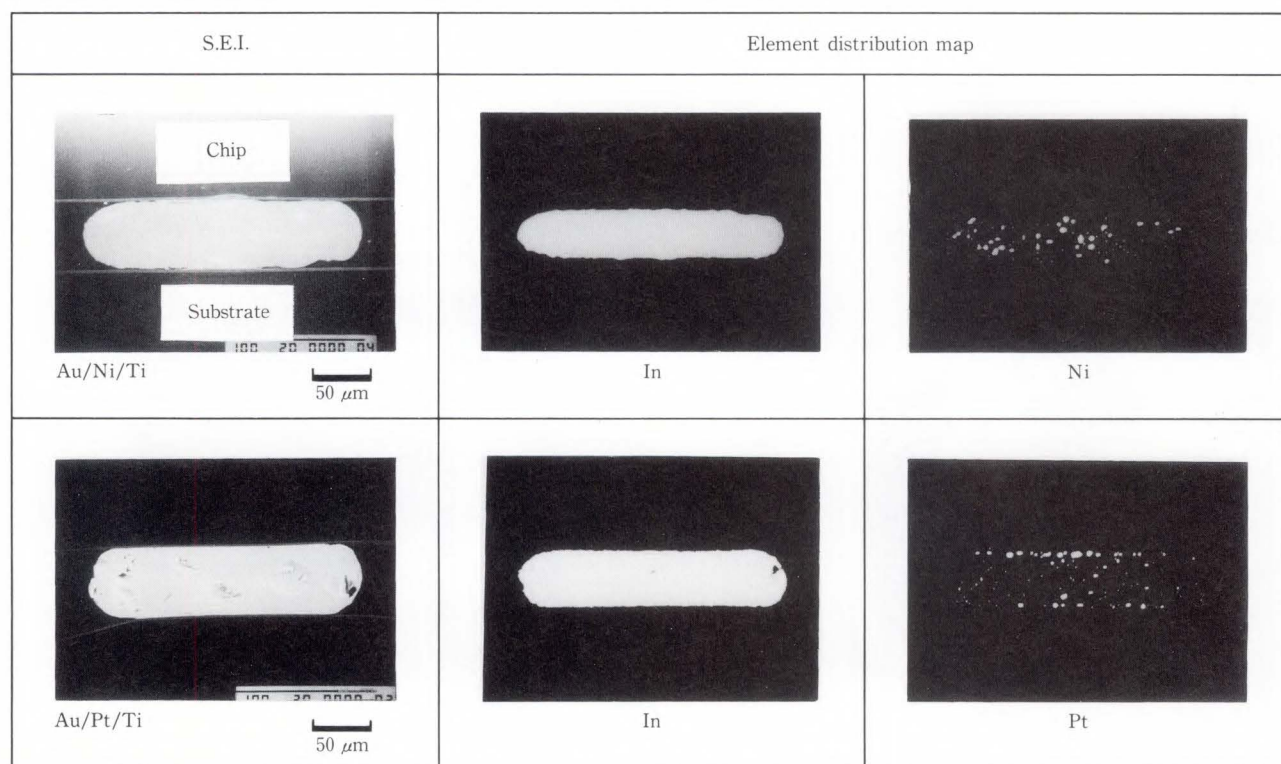


Fig. 13—Results of EDAX analysis on cross sections of connections on Au/Ni/Ti and Au/Pt/Ti films.

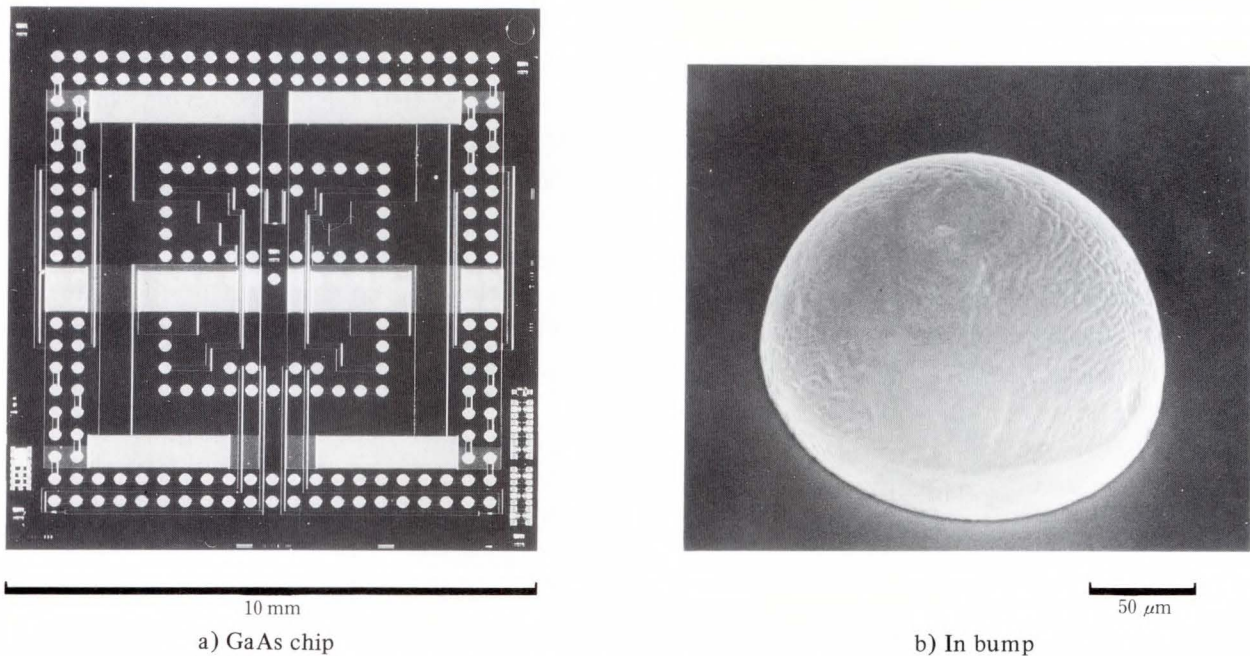


Fig. 14—GaAs model chip with In solder bumps on Au/Pt/Ti metallization pads.

experiment and to rapid cooling after reflowing.

The tensile test results indicate that Au/Pt/Cr and Au/Pt/Ti metallization films have almost the same characteristics, and that they are suitable for use with In solder.

3.3 Power cycle tests

The good results obtained from the combination of In solder and Au/Pt/Ti metallization film lead to their use in GaAs flip-chip connections in liquid nitrogen. Therefore, flip-chip connection models combining In solder and Au/Pt/Ti metallization film were made. The Au/Pt/Ti films of these models were formed as bonding pads on GaAs model chips. Then, In solder was vapor-deposited on these pads to a thickness of 100 μm and a diameter of 200 μm. The model chips and alumina substrates were then connected to each other. A GaAs model chip with In solder bumps is shown in Fig. 14. Figure 14 shows the GaAs chip and a close-up of an In bump after the wet-back treatment.

Power cycle tests were performed on these GaAs flip-chip connection models in liquid nitrogen by applying power to heat sources formed on the chip. Two power levels, 15 W and 30 W, were used to examine the effects of different cooling conditions. Nucleate boiling

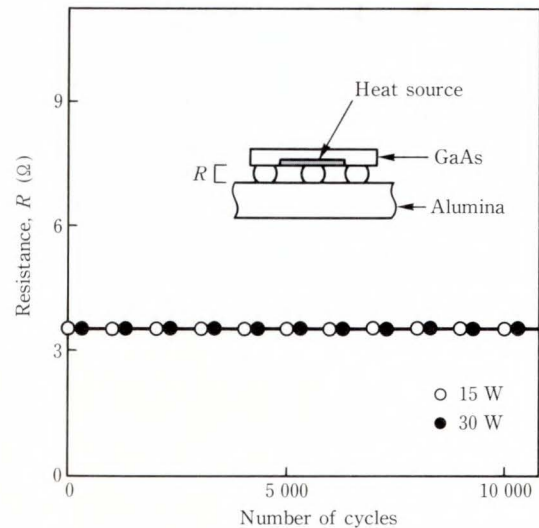


Fig. 15—Change in resistance during power cycle tests in liquid nitrogen of a GaAs chip/alumina substrate flip-chip connection model.

occurred at 15 W, and film boiling occurred at 30 W.

Figure 15 shows the results of the power cycle tests. After ten thousand cycles, the resistance of the In solder bump was the same as the initial value. Once again, In solder proved to be the most suitable solder for use in liquid nitrogen.

4. Random number generator

Indium solder and Au/Pt/Ti metallization film were used for flip-chip connections of HEMT LSI chips to produce a random number generator. Figure 16 shows a close-up of the In solder bumps on one of the HEMT LSIs. Twenty HEMT LSI chips were interconnected on a multilayer ceramic circuit board⁷⁾ using flip-chip connection. Associated resistors and capacitors were also mounted on the circuit board. Figure 17 shows the random number generator fixed to its I/O frame.

The random number generator was cooled to -196°C (77 K) using a closed loop cooling system⁸⁾, and was then powered on. The genera-

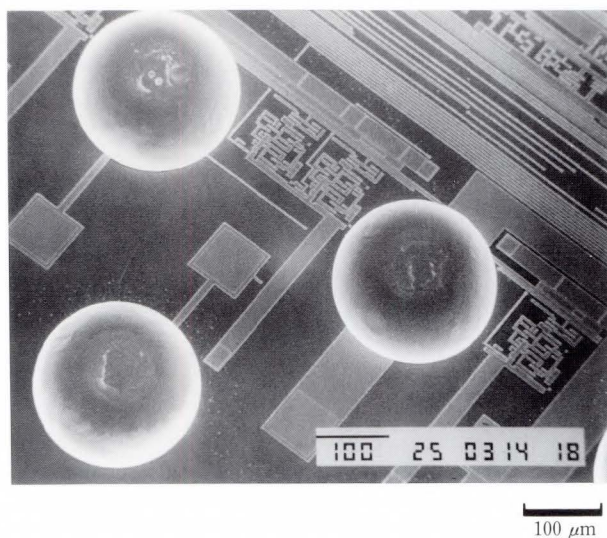


Fig. 16—Close-up of In solder bumps formed on a HEMT LSI.

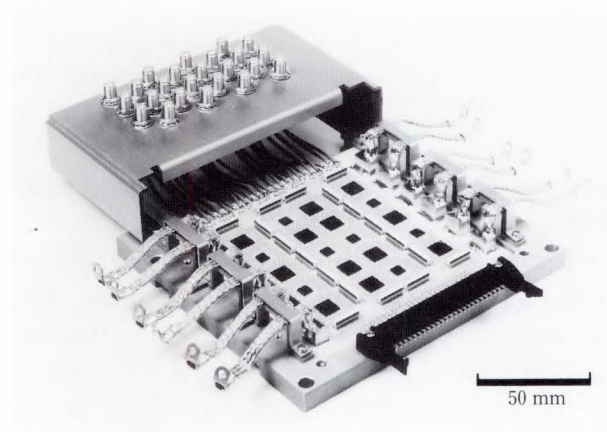


Fig. 17—Random number generator made using flip-chip-connected HEMT LSIs.

tor operated correctly and generated random numbers at a clock cycle of 1.49 ns, which demonstrates the higher switching speed of HEMTs and the effectiveness of the flip-chip connections. The generator operated correctly after several hundred cycles between liquid nitrogen and room temperatures. These results indicate that the combination of In solder and Au/Pt/Ti film is suitable for use in flip-chip connections in liquid nitrogen.

5. Conclusion

A study was made to find materials suitable for flip-chip connections of VLSIs operated in liquid nitrogen. Tests on fatigue life during thermal shock tests, and tests on wettability and dissolution between various solders and metallization films indicate the following:

- 1) Indium (In) and In alloy solders are suitable for GaAs flip-chip connections in liquid nitrogen.
- 2) In alloy solders have a long fatigue life when used with GaAs and Si chips. In solder has the longest fatigue life of the solders investigated.
- 3) Fatigue life is closely related to the mechanical properties of the solder. In and In alloy solder have high ratios of elongation to tensile strength. This high ratio means that these solders have a long fatigue life.
- 4) Au/Pt/Ti and Au/Pt/Cr metallization films are suitable for use with In solder in flip-chip connections in liquid nitrogen.
- 5) An Au top layer has good wettability with In solder, providing good solderability.
- 6) Pt film is extremely resistant to dissolution into In solder, suggesting good barrier layer characteristics.

A random number generator was made by mounting HEMT LSI chips on a multilayer ceramic circuit board using flip-chip connections with In solder and Au/Pt/Ti metallization film. The generator operated correctly after several hundred cycles between liquid nitrogen and room temperatures, indicating that the combination of In solder and Au/Pt/Ti film is suitable for flip-chip connections in liquid nitrogen.

References

- 1) Landman, B.S., and Russo, R.L.: On a Pin Versus Block Relationship for Partition of Logic Graphs. *IEEE Trans Comput.*, **C-20**, pp. 1469-1479 (1971).
- 2) Gaensslen, F.H.: MOS Devices and Integrated Circuits at Liquid Nitrogen Temperature. Proc. IEEE 1980 Int. Conf. Circuits and Computers, **I**, pp. 450-452.
- 3) Mimura, T., Hiyamizu, S., Fujii, T., and Nanbu, K.: A New Field-Effect Transistor with Selectively Doped GaAs/n-Al_xGa_{1-x}As Heterojunctions. *Jpn. J. Appl. Phys.*, **19**, 5, pp. L225-227 (1980).
- 4) Mimura, T., Joshin, K., Hiyamizu, S., Hikosaka, K., and Abe, M.: High Electron Mobility Transistor Logic. *Jpn. J. Appl. Phys.*, **20**, 8, pp. L598-L600 (1981).
- 5) Ochiai, M., Nakanishi, T., Karasawa, K., Hashimoto, K., and Niwa, K.: Metallization of Pure Indium Solder Used in Flip-Chip Bonding in Liquid Nitrogen. Proc. 1990 Int. Microelectronics Conf., pp. 115-119.
- 6) Yamada, T., Horikoshi, E., Hashimoto, K., Sato, T., Sakai, T., and Henmi, Z.: Thermal Fatigue Failure of Flip-Chip Solder Joints Using Pb-Sn and Pb-In Solder Alloys. (in Japanese), Proc. 1986 Fall Meet. Jpn. Inst. Metals, p. 410.
- 7) Aoki, S., Mada, G., Imanaka, Y., Yokouchi, K., Kamehara, N., Niwa, K.: Multilayer Ceramic Circuit Board for HEMT Packaging. (in Japanese), Proc. IEICE 1990 Autumn Natl. Convention, **5**, p. 123.
- 8) Fujisaki, A., Udagawa, Y., Yamamoto, H., and Yokouchi, K.: Cryogenic Cooling System for HEMT LSI. (in Japanese), Proc. IEICE 1990 Autumn Natl. Convention, **5**, p. 124.



Kaoru Hashimoto

Advanced Materials Laboratory
FUJITSU LABORATORIES, ATSUGI
Bachelor of Applied Physics
Nagoya University 1971
Specializing in Interconnection
Materials for Computers



Masayuki Ochiai

Advanced Materials Laboratory
FUJITSU LABORATORIES, ATSUGI
Bachelor of Precision Eng.
Hiroshima University 1983
Specializing in Interconnection
Materials for Computers



Teru Nakanishi

Advanced Materials Laboratory
FUJITSU LABORATORIES, ATSUGI
Hiratsuka Technical High School 1986
Specializing in Interconnection
Materials for Computers

Laser Welding of Copper and Copper Alloys

• Kozo Shimizu • Kaoru Hashimoto

(Manuscript received February 3, 1992)

The laser welding of pure copper and copper alloy is difficult because of copper's high thermal conductivity and reflectivity. To solve this problem, this paper examines the nickel plating of copper. The paper also examines heat-treatment to obtain a nickel-copper solid solution to reduce the thermal conductivity. Because the thermal conductivity of the solid solution is lower than that of pure copper, the laser penetrates the nickel-plated copper more deeply. The experimental results indicate that nickel plating and heat-treatment make it possible to laser-weld copper and copper alloys.

1. Introduction

Recently laser welding has become widely used in material processing, such as for hermetic sealing and for mounting electronic parts. The advantage of laser welding over electron beam welding, is that the former does not need vacuum equipment.

One example of laser welding is that of bellows. Bellows are used for pressure capsules, temperature sensors, pressure switches and cooling devices for electric and electronic equipment. They are generally made of phosphor bronze, beryllium-copper or stainless steel to meet the particular requirements, such as a high degree of elasticity and resistance to corrosion.

The heat generated by electronic devices is steadily increasing. Therefore future cooling devices must be highly effective. Such a cooling device consists of bellows and a cooling plate called a header. Each part is made of beryllium-copper having high elasticity, and is laser welded with high accuracy.

The application of pure copper to the header is effective because of its high thermal conductivity. In this case, the cooling device consists of beryllium-copper bellows and a pure copper header. Although beryllium-copper is relatively easy to laser weld, the laser welding of

pure copper is extremely difficult because of its high thermal conductivity and reflectivity. To solve this problem, the authors studied the nickel plating and heat-treating of pure copper before laser welding it.

2. Background

2.1 Bellows

Bellows are mainly used for either a thermal sensor as shown in Fig. 1a) or a cooling device as shown in Fig. 1b). In the cooling devices examined in this study, bellows are used in combination with a cooling plate called a header. Phosphor bronze and beryllium-copper alloys are commonly used for the bellows and header.

2.2 Beryllium-copper

Beryllium-copper alloys have excellent fatigue characteristics and greater flexibility than pure copper. In addition, if the alloys are subjected to aging treatment¹⁾, they have excellent resistance to corrosion.

The thermal conductivity of beryllium-copper (90 W/m·K at 295 K) is less than a quarter that of pure copper (418 W/m·K at 295 K). This suggests that a greater cooling capacity is achieved using pure copper.

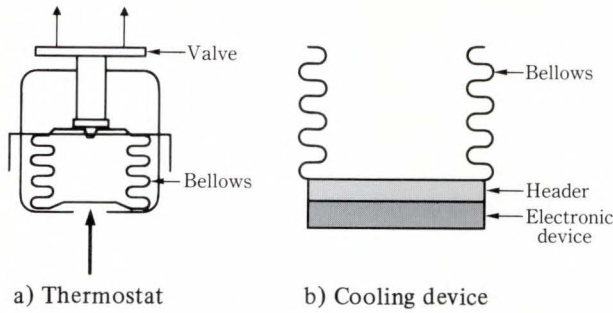


Fig. 1—Examples of bellows.

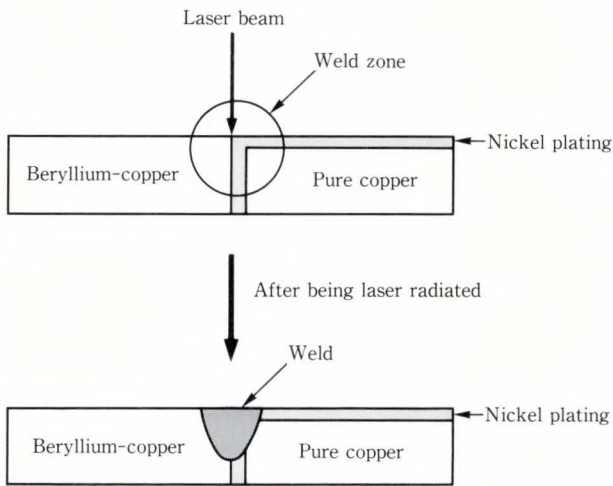


Fig. 2—Cross-section of the weld zone and weld.

2.3 Laser welding of pure copper and beryllium-copper

The laser welding of pure copper and beryllium-copper is difficult because their thermal conductivity differ greatly and the laser energy absorption of pure copper is low. When laser is radiated to melt the pure copper, the beryllium-copper evaporates because of excessive heating.

There are some techniques to reduce the thermal conductivity of pure copper and to increase its laser energy absorption. One technique is to add silicone or nickel to the weld zone, and is used in the laser welding of aluminum alloys for IC packages^{2),3)}. These additives form solid solution with aluminum, which reduces thermal conductivity of the weld zone and makes laser welding possible.

In the light of these techniques, the authors tried adding nickel to the weld zone. Nickel makes a solid solution with copper in all compositions⁴⁾. Nickel plating is used to form a nickel-

Material	Elements			
	Cu	Be	Fe	Ni + Co
Beryllium-Copper	97.76	1.85	0.03	0.26
Copper	>99.96	—	—	—

Plating bath temperature (°C)	65
Plating thickness (μm)	0 - 27
pH	6.9

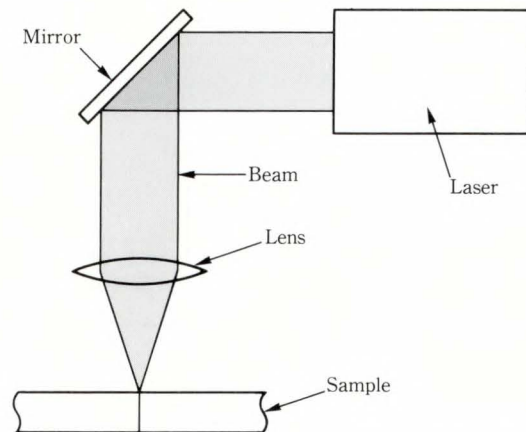


Fig. 3—Schematic illustration of laser welding.

copper solid solution phase³⁾. When nickel-plated pure copper is laser welded, the thermal conductivity of the weld zone decreases due to the formation of the nickel-copper solid solution. To obtain a uniform solid solution phase, it is effective to heat-treat the nickel-plated copper before welding. The cross-section of the weld zone and weld are shown Fig. 2.

3. Experimental procedure

Table 1 shows the chemical composition of copper and beryllium-copper used in this study. The nickel layer was plated onto the pure copper in a Ni-B electroless bath at 60 °C. Electroless plating makes it possible to obtain uniform thickness⁵⁾. Table 2 shows the plating conditions.

The nickel-plated copper was heat-treated in a vacuum (1×10^{-5} Torr) at a temperature range of between 800 °C and 1 000 °C. The heating time was varied from 1 h to 10 h.

Laser welding was done using a pulsed Nd-YAG laser (a Raytheon MPA-Y550) as shown in Fig. 3. Table 3 shows the welding conditions.

To examine laser weldability, the joint strength of the weld was measured with an Instron Material Tester at a cross-head speed of a 0.5 mm/min using the sample in Fig. 4. The metal hardness of the weld was measured with a micro-Vickers hardness tester at a load of 50 g.

Table 3. Laser-welding conditions

Pulse rate (pps)	30
Output power (W)	120
Pulse duration (ms)	2
Spot size* (mm)	0.3
Defocus (mm)	0
Focal length (mm)	100
Welding speed (mm/s)	150
Shield gas	Ar
Shield gas flow rate (l/min)	30

*: Spot size of the weld

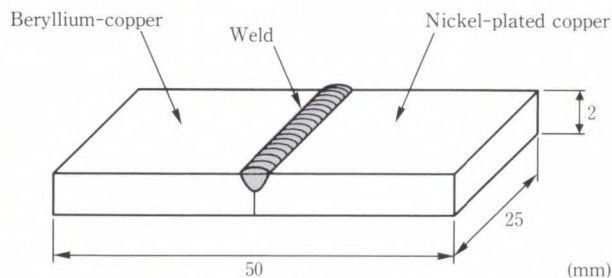


Fig. 4—Sample for joint strength test.

The micro-structure of the weld was examined with a microscope, and the nickel content of the weld was measured with an electron probe micro analyzer.

4. Results and discussion

4.1 Effect of nickel plating thickness on laser weldability

As the thickness of nickel plating and the laser power increase, the joint strength increases as shown in Fig. 5. In samples welded with a laser power 60 W, the joint strength is extremely low. In samples welded with 120 W, the joint strength increases rapidly with thicknesses above

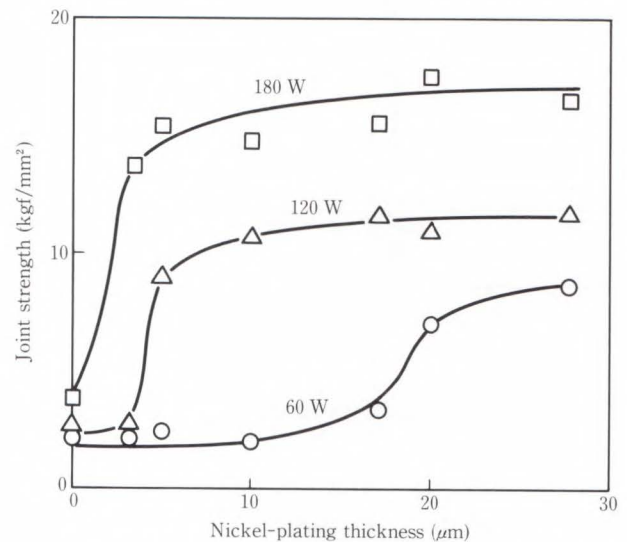


Fig. 5—Relationship between joint strength and nickel-plating thickness.

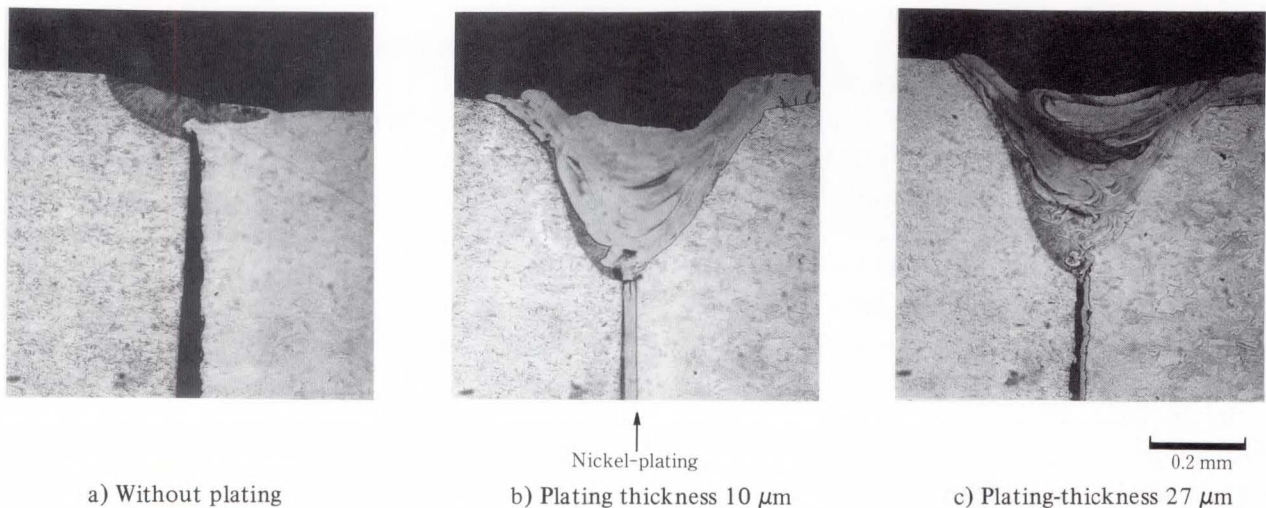


Fig. 6—Weld cross-sections.

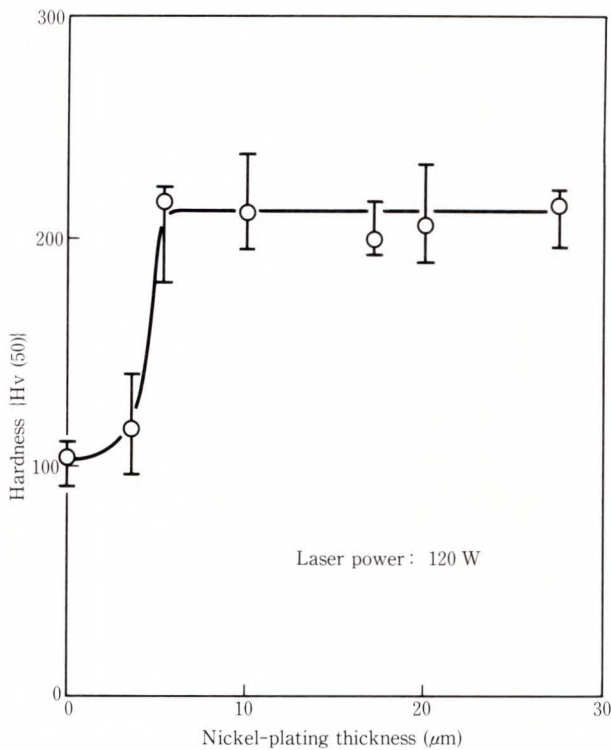


Fig. 7—Relationship between weld metal hardness and nickel-plating thickness.

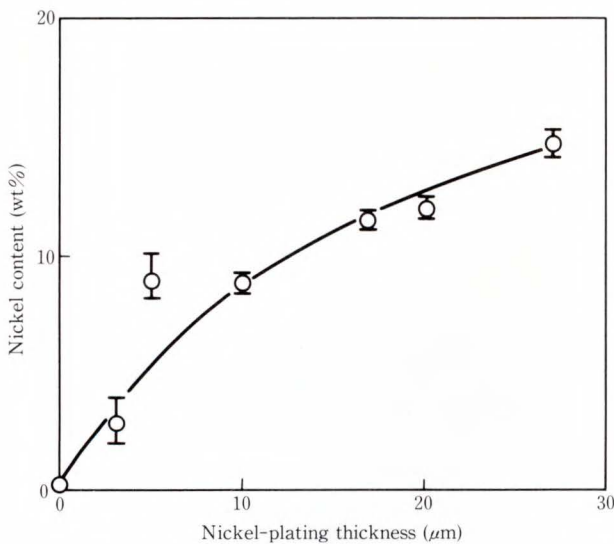


Fig. 8—Relationship between nickel content and nickel-plating thickness.

5 μm . However, the surface of the weld is rough at thicknesses exceeding 17 μm , due to the evaporation of the weld. The joints are strong in samples welded at 180 W, but the surface of the weld is rough.

Figure 6 shows the cross-sectional micro-structure of three typical welds. The weld does

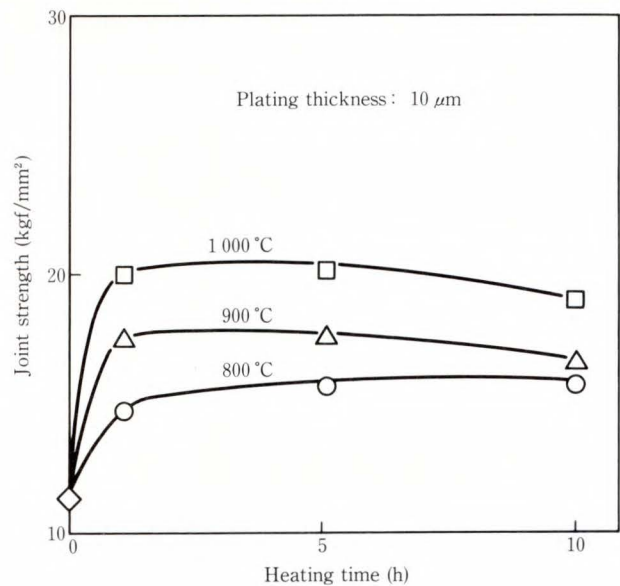


Fig. 9—Relationship between joint strength and heating time.

not penetrate much when the plating thicknesses is 0 μm , but penetrates a great deal for plating thicknesses of 10 μm and 27 μm . Based on the appearance of the weld surface, the optimum thickness of nickel plating is 10 μm , and the optimum laser power is about 120 W.

As shown in Fig. 7, the hardness of the weld metal increases with the nickel plating thickness. This suggests that solid solution hardening occurs in the weld due to a structure caused by a complete solid solution between copper and nickel⁴⁾.

The nickel content in the weld is above 10 wt% when the nickel plating is more than 10 μm as shown in Fig. 8. The thermal conductivity of Cu-10 wt% Ni is 61.5 W/m·K at 293 K and that of pure copper is 418 W/m·K at 295.2 K⁶⁾. The deep penetration of the weld at plating thicknesses above 10 μm is due to the decrease in thermal conductivity in the weld. This result indicates that nickel plating is effective.

4.2 Effect of heat-treatment on joint strength

Figure 9 shows the relationship between the joint strength and heat-treating time for the samples heat-treated before laser welding. Here, the thickness of the nickel plating is 10 μm and laser power is 120 W. The joint strength increases

as the heating time and temperature increase. For samples heated to 1000 °C, the joint strength is almost equal to the tensile strength of the parent metal and the tensile strength is approximately 20 kg/mm²⁷⁾. Figure 10 shows the cross-section of the weld.

In this way, heat-treatment increases the joint strength. Figure 11 shows the cross-sections of two typical samples with and without heat-treatment. In the sample without heat-treatment, the pure copper fails at the area affected by heat. In the sample with heat-treat-

ment, however, the failure occurs in the weld. This difference is related to the uniformity of nickel distribution in the weld.

When copper with nickel plating is heat-treated, a nickel-copper solid solution is formed. If laser is radiated on the area of the sample which consists of this solid solution, the distribution of the solute (i.e. nickel) in the weld becomes more homogeneous than that in the sample without heat-treatment (i.e. no solid solution before laser welding). This is the reason why the joint strength in the sample with heat-treatment is much higher.

5. Conclusion

In the development of a laser welding technique for pure copper, this paper examines the laser weldability of pure copper with nickel plating. The results are summarized as follows.

- 1) Nickel-plating the pure copper makes it possible to laser weld pure copper and copper alloys. This is due to the decrease in thermal conductivity of the weld by the formation of a nickel-copper solid solution.
- 2) The joint strength in the laser-welded samples increases rapidly with nickel content above 5 wt%. This is due to the solid solution hardening in the weld.
- 3) Heat-treatment of the nickel-plated copper

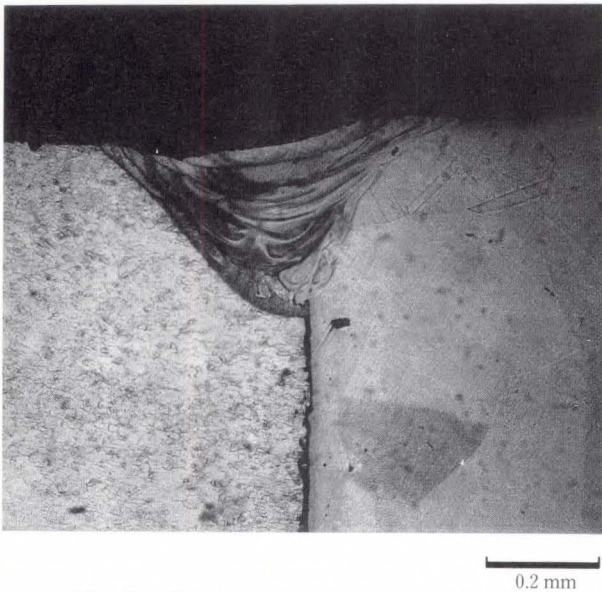
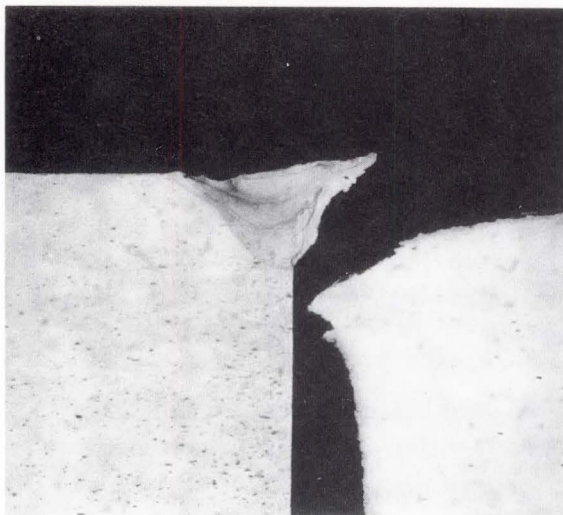


Fig. 10—Cross-section of heat-treated weld.



a) Not heat-treated



b) Heat-treated

Fig. 11—Effects of heat-treatment.

before laser welding enhances the joint strength because of the more homogeneous distribution of nickel in the weld. In this case, the joint strength is almost equal to the tensile strength of the parent metal.

References

- 1) Beryllium-Copper Alloy Special Committee: "Report of the Society of Electrical Engineers". (in Japanese), 1971, 98p.
- 2) Iikawa, T., Sakai T., Okamoto, S., Natori. K., and Nagai, T.: Aluminum Alloy Package for Microwave Amplifier. Proc. 1985 ISHM Conf., pp. 141-145.
- 3) Sakai, T., Okamoto, S., Iikawa, T., Sato, T., and Henmi, Z.: A New Laser Hermetic Sealing Technique for Aluminum Package. *IEEE Trans. Components Hybrids and Manuf. Technol.*, **CHMT-10**, 3, pp. 433-436 (1987).
- 4) Hansen, M.: "Constitution of Binary Alloys". McGraw-Hill, New York, 1985, pp. 601-604.
- 5) Bull. Jpn. Inst. Metals: "13.7 Surface Modification Methods". (in Japanese), Metal Handbook, 5th ed., Tokyo, Maruzen, 1990, pp. 915-917.
- 6) Touloukian, Y. S.: "Thermo-physical Properties of Matter". Vol. 1, IFI/Plenum, New York, 1970, pp. 68-81 and pp. 561-567.
- 7) Bull. Jpn. Inst. Metals: "2.2 Copper Alloy". (in Japanese), Metal Data Book, 2nd ed. Tokyo, Maruzen, 1984, pp. 164-165.



Kozo Shimizu

Advanced Materials Laboratory
FUJITSU LABORATORIES, ATUSGI
Bachelor of Inorganic Material
Nagoya Institute of Technology 1987
Specializing in Computer Packaging
Materials



Kaoru Hashimoto

Advanced Materials Laboratory
FUJITSU LABORATORIES, ATUSGI
Bachelor of Applied Physics
Nagoya University 1971
Specializing in Computer Packaging
Materials

High-Efficiency Coolant for Direct-Immersion Cooling

• Mitsutaka Yamada • Kishio Yokouchi • Nobuo Kamehara

(Manuscript received February 13, 1992)

Direct-immersion cooling is considered to be one of the most effective cooling technologies for high-speed computers. However, there are many problems in practical applications, such as temperature overshoot. To eliminate this problem, using a mixture of various coolants has been found to provide several benefits. At room temperature, the temperature overshoot on the chip surface at the onset of boiling is decreased by using a mixture of coolants having different boiling points. At liquid nitrogen temperature (77 K), the maximum heat flux is increased by adding fluorocarbon to pure liquid nitrogen. This paper discusses the effects of using a mixture of coolants and adding fluorocarbons.

1. Introduction

LSI chips mounted on circuit boards in high-speed computers generate large amounts of heat. The problem of heat dissipation makes cooling technology increasingly important in high-density packaging. Recently, the activities in cryogenic electronics have greatly increased because operating devices at liquid-nitrogen temperature (77 K) yield a direct improvement in performance^{1),2)}. Therefore, power dissipation at 77 K also increases with faster switching and shorter gate lengths of devices.

A number of cooling technologies have been proposed and developed, such as direct or indirect forced liquid cooling³⁾⁻⁵⁾. Direct-immersion cooling is the one of the most effective techniques for cooling high-density LSI devices on circuit boards. This technique transfers the heat at boiling and has a large heat-transfer capacity. Direct-immersion cooling with fluorocarbon or liquid nitrogen has about ten times the cooling capability of forced-air cooling. However, there are some problems in the practical applications of direct-immersion cooling in high-speed computers. One is the temperature overshoot on the chip surface at the onset of boiling. The overshoot produces unstable

cooling, and is an obstacle to practical application⁶⁾. Another is that there are few low-temperature coolants and their cooling capacity is too low for cryogenic devices.

To solve these problems, the authors investigated the coolant composition and found suitable combinations of coolants having different boiling points which prevent temperature overshoot. Furthermore, it was found that adding fluorocarbons to liquid nitrogen improved the cooling capability on a 77 K GaAs chip to 60 W/cm², three times that of liquid nitrogen. This study discusses the effects of using a mixture of coolants on cooling at the boiling point.

2. Experiment

Two kinds of immersion-cooling models were used to evaluate the effects of using a mixture of coolants. One model uses fluorocarbons at room temperature, and the other is the 77 K cooling model using a nitrogen liquefier.

To evaluate the effects on the prevention of temperature overshoot, the authors used a sealed 1 000 cm³ cooling module with a water-cooled heat-exchanger in the head. Si LSI models (10 × 10 mm) mounted on the glass-

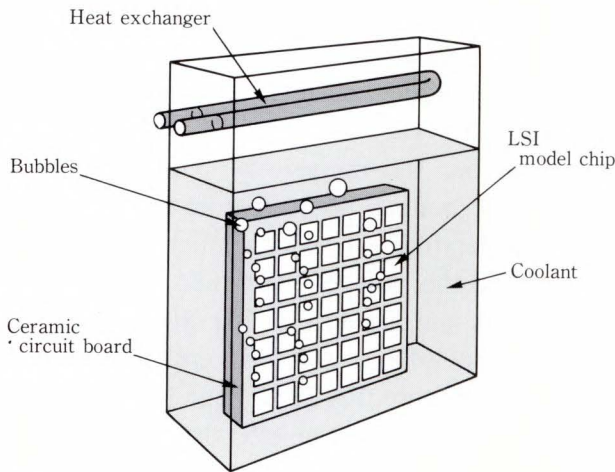


Fig. 1—Immersion-cooling module for room-temperature cooling.

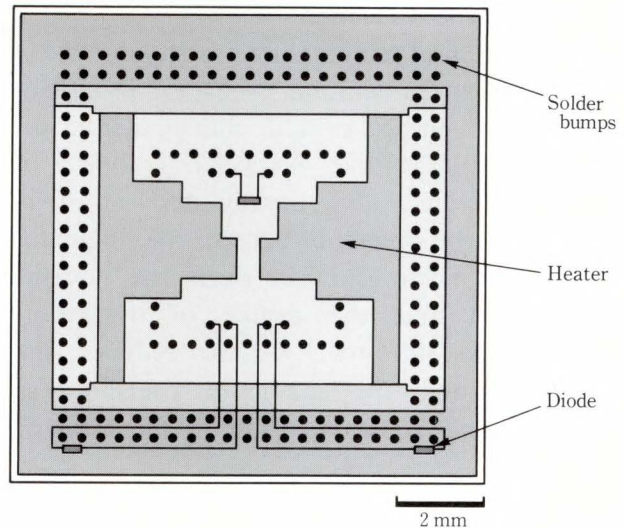


Fig. 3—GaAs LSI chip model.

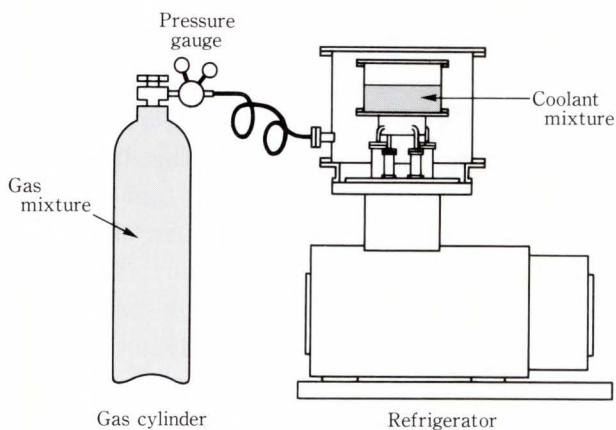


Fig. 2—Liquefier for cryogenic cooling.

ceramic circuit board ($100 \times 100 \times 6$ mm)⁷⁾ by flip-chip bonding are immersed vertically in the module, as shown in Fig. 1. The gap between the chip and circuit board is $120 \mu\text{m}$. The module is filled with coolant except for a small space for the vapor. The coolants are mixtures of two fluorocarbons, FX-3250 (boiling point: 56°C) and FX-3300 (boiling point: 102°C). Coolant FX-3300 was mixed with FX-3250 at volume ratio from 0 percent to 100 percent. The boiling point of the mixture of coolants was also measured in the module.

The liquefier consisted of a stirling cycle refrigerator and a high-pressure cylinder containing mixed gas as shown in Fig. 2. An insulated

thermostat in the cold head of the refrigerator was used to evaluate the coolants, pure nitrogen, and several concentrations of the fluorocarbons CF_4 and C_2F_6 with nitrogen added. The volume of the thermostat is $\phi 180 \times 150$ mm³. A circuit board with GaAs chips (10×10 mm) is immersed vertically in the coolant in this thermostat. The pressure in the thermostat was held at 0.1 MPa. The cooling capability is defined as the heat flux at the transition point from nucleate boiling to film boiling. The transition point is determined by measuring the relationship between the chip temperature and the power dissipation. The chip temperature was measured by the diodes embedded in the chip.

The authors evaluated the cooling capability using GaAs chip as the model of a high electron mobility transistor (HEMT) device. The chip layout is given in Fig. 3. The chips have 215 indium solder bumps 0.2 mm in diameter for flip-chip bonding, a heater occupying an 8×8 mm area, and three diodes, one at center of chip, and two at the corners. The thermal expansion of the multilayer ceramic circuit board ($100 \times 100 \times 5$ mm) conformed to GaAs⁸⁾. The distance between the chip and circuit board is $120 \mu\text{m}$, the same height as the bumps.

3. Results and discussion

3.1 Prevention of temperature overshoot

A typical temperature overshoot phenomenon on the surface of LSI chip immersed directly in fluorocarbon FX-3250 is shown in Fig. 4. Nucleate boiling usually starts at about 65 °C, but the overshoot exceeds 5 K. Figure 5 shows the relationship between the coolant composition and the degree of overshoot. Adding FX-3300 to FX-3250 reduces the overshoot, and the minimum overshoot is reached using coolants mixed in the ratio of

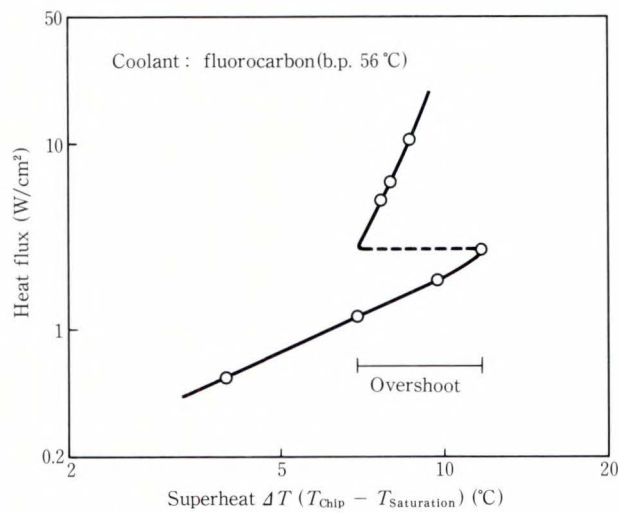


Fig. 4—Typical temperature overshoot phenomena on chip surface.

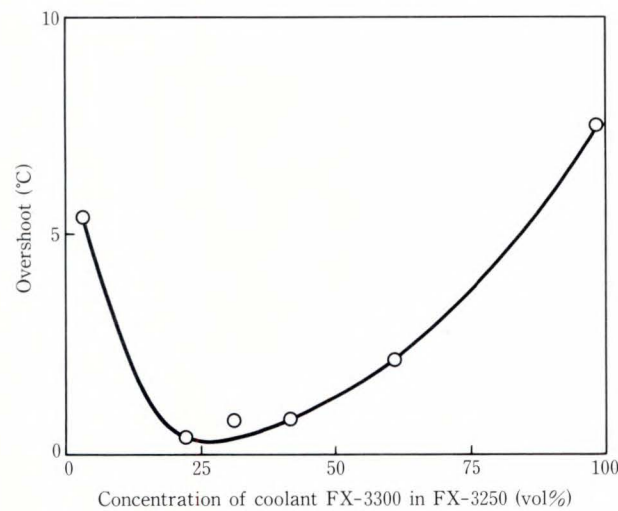


Fig. 5—Prevention of overshoot.

80:20. This may be due to the onset temperature of nucleate boiling being reduced as azeotropic boiling occurs. Alternatively, the material with the lower boiling point starts boiling before the mixture of coolants having the typical boiling point. Figure 6 shows the chip temperature at which nucleate boiling starts when the pure coolants and the mixture of coolants are used. For the 80:20 coolant mixture, the boiling point is only 5 K higher than that of pure FX-3250, but it creates no problems concerning the effectiveness of cooling.

3.2 High-capability cryogenic coolant

Figure 7 shows the boiling characteristics of fluorocarbon containing nitrogen. As low-temperature coolants are used at boiling point, the heat is transferred in the nucleate boiling region. The cooling capability, equal to the maximum boiling heat that can be transferred, is the maximum heat flux at the transition point from nucleate boiling to film boiling. The maximum heat flux of GaAs chips immersed in pure nitrogen is 20 W/cm². The cooling capability of nitrogen can barely handle the maximum power density of 4.1 kgates HEMT, 20 W/cm²⁹⁾.

CF₄ mixed with nitrogen increases the cooling capability to three times that of liquid

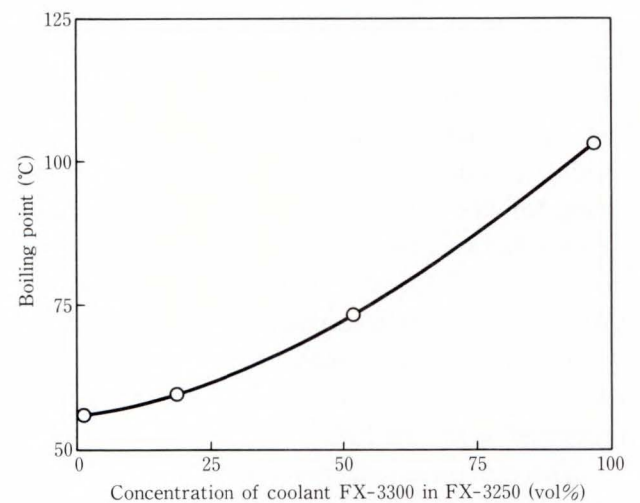


Fig. 6—Starting point of nucleate on chip surface.

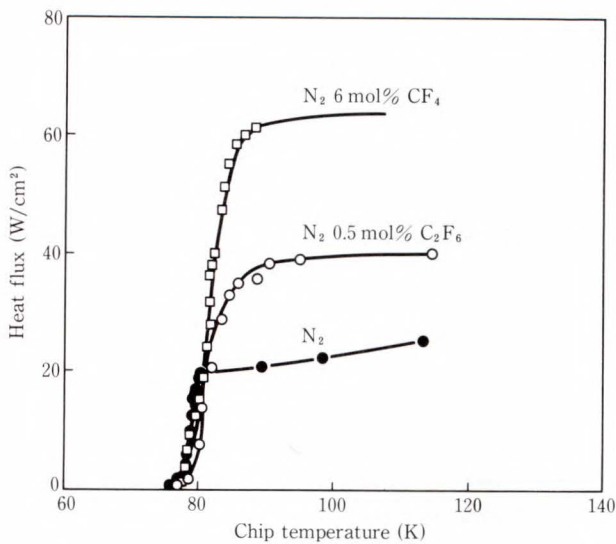


Fig. 7—Improvement of cooling capacity.

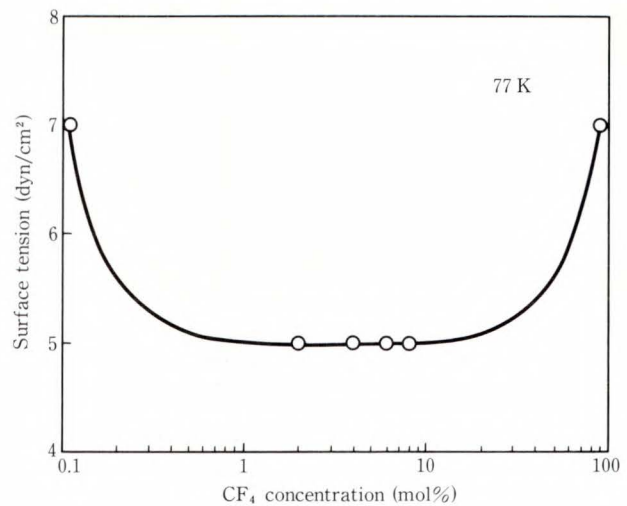


Fig. 9—Relationship between surface tension of liquid nitrogen and CF_4 concentration.

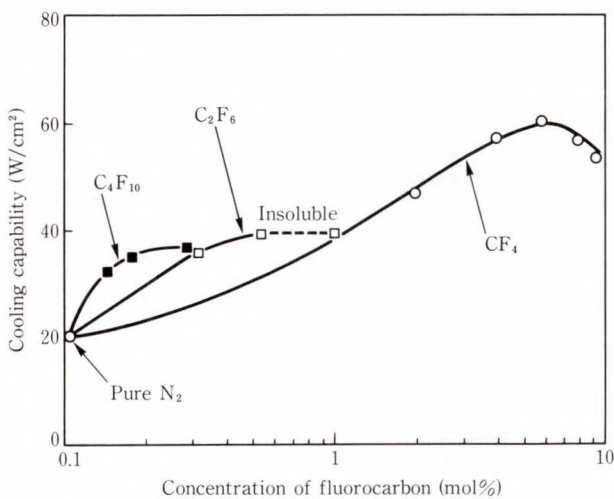


Fig. 8—Influence of fluorocarbon concentration added to N_2 on cooling capacity.

nitrogen. CF_4 is able to be dissolved in the liquid nitrogen irrespective of the concentration. The superheat of GaAs chips at the transition point when the film boils is less than 12 K, which is three times that of pure nitrogen. In addition, the boiling point is the same as pure nitrogen, since the only a small amount of CF_4 is added. Figure 8 shows the influence of the fluorocarbon concentration. The maximum cooling capacity, 60 W/cm^2 , is attained at 6 mol%. Fluorocarbon containing liquid nitrogen is a little thicker, and the bubbles generated

at boiling are smaller and more uniform in size than those of nitrogen alone. The C_2F_6 solubility in liquid nitrogen is only 0.5 mol%, because it easily freezes at the boiling point of nitrogen. Nevertheless, adding C_2F_6 increases the capability to 40 W/cm^2 . The superheat and boiling point are the same as CF_4 containing liquid nitrogen.

Some of the factors that improve the cooling capability are as follows. One is the volume decrease due to mixing, like that in mixing water and alcohol. When the mean free path diameters of molecules differ greatly, the volume of the mixture is decreased by close packing. Therefore, the heat of vaporization per volume increases and this increases the cooling capability. As the dependency of the CF_4 concentration is a maximum, the effect of the volume appears to be the cause of the increased cooling capability. However, the mean free path diameters of molecules calculated from the density are very similar to each other.

Another reason for the increase is the reduced surface tension. The mixed coolant has smaller, more uniform bubbles than pure nitrogen. The following equation shows the diameter d_B and the bubble generation speed $f^{(10)}$.

$$d_B^{1/2} f = 0.56 \text{ g}^{1/2} = 17.5 \text{ cm}^{1/2} \text{ s}^{-1}$$

Because the bubbles destroy the boundary layer of the coolant, the cooling capability increases as the bubbles are generated faster. The surface tension of the coolant mixture is shown in Fig. 9. The surface tension of the coolant mixture is lower than those of pure nitrogen and CF_4 .

4. Conclusion

A new cooling technique for high-density packaging and heat dissipation in LSI devices is the use of a coolant mixture. The mixture contains two fluorocarbons having different boiling points and prevents temperature overshoot on the chip surface. Furthermore, adding fluorocarbon to liquid nitrogen increases the maximum heat flux of liquid nitrogen. By adding 6 mol% CF_4 to nitrogen, the cooling capability on 77 K GaAs chips increases to $60 W/cm^2$, three times that of nitrogen alone. The increased cooling capability is thought to be caused by the decrease in surface tension when adding CF_4 .

The cooling capacity is sufficient to disperse the heat generated by HEMT or CMOS LSIs, and will contribute to the future development of cryogenic devices with greater power dissipation and computers using these devices.

References

1) Masuhara, T., Aoki, M., and Yano, K.: Liquid nitrogen cooled CMOS in low temperature electronics. Ext. Abs. 1987 Electrochem. Soc. Fall Mtg.,

pp. 462-463.
2) Jaeger, R.C., and Gaensslen, F.H.: Low temperature semiconductor electronics. Proc. 1988 Int. Soc. Conf. Thermal Phenomena in the Fabrication and Operating of Electronic Components., pp. 106-111, 1988.
3) Simons, R.E., Moran, K.P., Antonetti, V.W., and Chu, R.C.: Thermal design of the IBM 3081 computer. Proc. 1982 Natl. Electron. Packaging and Production Conf., pp. 124-142.
4) Danielson, R.D.: Cooling a super-fast computer. Proc. 1986 Natl. Electron. Packaging and Production Conf., pp. 44-45.
5) Kamehara, N., Yokouchi, K., Niwa, K., and Murakawa, K.: Direct immersion cooling for high density packaging. Ext. Abs. 1980 Electrochem. Soc. Spring Mtg., pp. 218-220.
6) Chu, R.C., Hwang, U.P., and Simons, R.E.: Conduction cooling for an LSI package: A one-dimensional approach. *IBM J. Res. Develop.*, **26**, 1, pp. 45-54 (1982).
7) Niwa, K., Kamehara, N., Yokoyama, H., Yokouchi, K., and Kurihara, K.: Multilayer ceramic circuit board with copper conductor, *Advanced Ceramics. Multilayer Ceramic Devices*, **19**, pp. 41-47 (1987).
8) Yokouchi, K., Aoki, S., Kamehara, N., and Niwa, K.: Thermal expansion characteristics of ZrO_2 glass-ceramics hybrid material. Proc. 1988 Fall Symp. Jpn. Ceramics Soc. Mtg., pp. 525-526.
9) Abe, M., Mimura, T., and Kobayashi, M.: Ultra-High-Speed HEMT LSI Technology. *FUJITSU Sci. Tech. J.*, **24**, 4, pp. 271-283 (1988).
10) McFadden, P.S., and Grassmann, P.: *Int. J. Heat Mass Transfer*, **5**, pp. 169-174 (1962).



Mitsutaka Yamada
Computer Packaging Materials
Laboratory
FUJITSU LABORATORIES, ATSUGI
Bachelor of Chemistry
Kanazawa University 1986
Specializing in Computer Cooling
Materials



Nobuo Kamehara
Advanced Materials Laboratory
FUJITSU LABORATORIES, ATSUGI
Bachelor of Chemistry
Niigata University 1970
Specializing in Advanced Ceramic
Materials



Kishio Yokouchi
Manufacturing Engineering Dept.
Printed Wiring Board Div.
FUJITSU LIMITED
Bachelor of Chemical Eng.
Yokohama National University 1977
Master of Chemical Eng.
Yokohama National University 1979
Specializing in Packaging and Cooling
Technology for High Speed
Computers

Multilayer Ceramic Substrate for HEMT Packaging (Liquid Nitrogen Packaging for GaAs Devices)

• Shigenori Aoki • Yoshihiko Imanaka • Kishio Yokouchi

(Manuscript received February 13, 1992)

For flip-chip bonding of HEMTs, the thermal expansion of zirconia/borosilicate glass composite substrate must match that of GaAs below room temperature. Normally, zirconium silicate reduces the expansion of the composite substrate. In this research, zirconia powder coated with alumina by freeze-drying was used to prevent the formation of zirconium silicate. By also controlling the ratio of glass to alumina-coated powder, the difference in thermal expansions of GaAs and the new composite was limited to 0.4×10^{-4} between 77 K and room temperature. This compares favorably with the figure for conventional alumina. A test module of the new composite verified that connection reliability in liquid nitrogen is greatly improved.

1. Introduction

To take full advantage of the superior switching speed of the high electron mobility transistor (HEMT) in applications such as large scale computers, packaging technologies that minimize the signal paths between HEMT LSI devices are needed. This requirement makes flip-chip connection a better choice than wire bonding and tape automated bonding (TAB).

Operation in liquid nitrogen makes the HEMT computer more attractive because HEMTs switch faster at lower temperatures¹⁾. However, because of the large difference in packaging and operating temperatures, stable operation down to 77 K cannot be achieved unless the substrate and chip have closely matched thermal expansions.

The thermal expansion of GaAs is greater than that of silicon and other conventional

packaging materials; therefore, a new material is needed. As far as we know, such a material has not been reported, except one of our previously proposed composite materials^{2),3)}.

This paper describes the fabrication and performance of the new multilayer substrate material. This paper also describes a module that generates random numbers at 77 K. The module consists of twenty HEMT chips flip-chip-bonded to a multilayer substrate having copper conductors.

2. Experiment

Figure 1 shows the thermal expansions of GaAs, zirconia (ZrO_2), and four conventional packaging materials below room temperature. As can be seen, the thermal expansion of GaAs is greater than that of the conventional ceramics and less than that of zirconia. (Zirconia is one of the few ceramics that has a greater thermal expansion than GaAs.) We therefore developed glass/ceramic composites based on zirconia and borosilicate glass to obtain a new material

This paper was presented at the 1991 International Electronics Packaging Conference (IEPC), September 17, 1991, at San Diego, CA, USA.

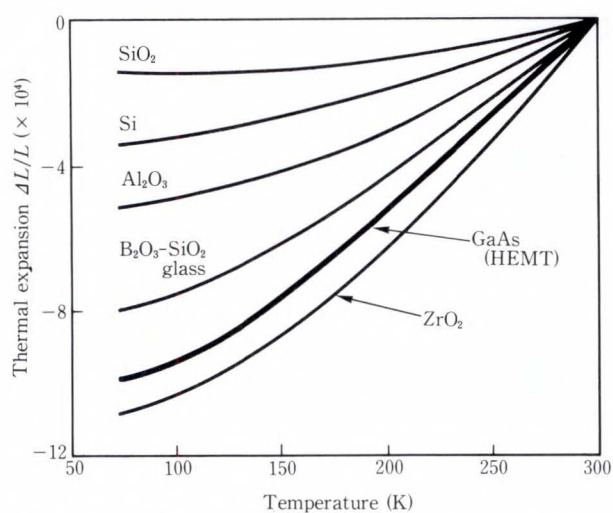


Fig. 1—Thermal expansions of GaAs, ZrO₂, and conventional ceramics below room temperature.

whose thermal expansion is close to that of GaAs.

2.1 Glass/ceramic composite

2.1.1 Powder processing

The thermal expansion of composites can be controlled by adjusting the ratio of glass to zirconia. However, when doing this it is necessary to prevent the formation of a new crystalline phase having a thermal expansion other than the designed value. Therefore, the zirconia powder was processed with alumina by freeze-drying prior to mixing with borosilicate glass.

The zirconia powder was partially stabilized with a 3-mol% Y₂O₃ additive. The average particle size was 0.8 μm. The zirconia powder was mixed with Al₂(SO₄)₃ solution to obtain a zirconia content of 10 wt%. The suspension was injected into liquid nitrogen through a nozzle with a 0.5 mm inside diameter and frozen into 1-mm-diameter particles. The particles were then freeze-dried, with the atmospheric pressure in the dryer kept at 0.1 Torr and the temperature increased gradually over a 50 h period. Finally, the dried particles were heated at 1400 °C in air to decompose the Al₂(SO₄)₃ into Al₂O₃.

2.1.2 Mixing powders and firing

Borosilicate glass, zirconia (as-received), alumina, and alumina-treated zirconia powders were used in this experiment. The ratios of the glass and ceramics used are listed in Table 1.

Table 1. Compositions of glass/ceramic composites

Composite	(wt%)			
	Borosilicate glass	ZrO ₂	Al ₂ O ₃	Al ₂ O ₃ -treated ZrO ₂
GZ	50	50	0	0
GZ + A	50	40	10	0
GAZ	40-60	0	0	40-60

GZ: Glass and zirconia

GZ + A: Glass, zirconia, and alumina additive

GAZ: Glass and alumina-treated zirconia

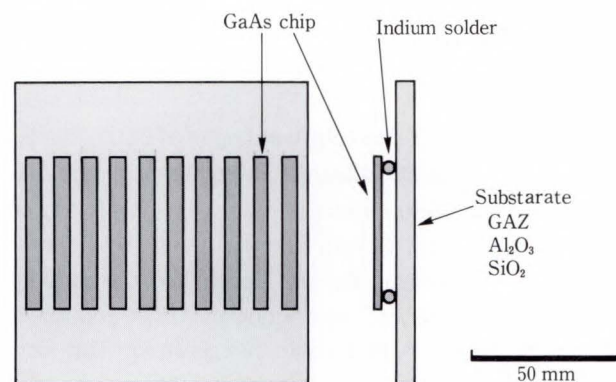


Fig. 2—Construction of thermal shock test samples.

The powders were milled in a plastic mill pot with a binder and solvent for 20 h. The slurry was cast using a doctor blade. The cast green sheets were laminated and fired in nitrogen at 900 °C at the rate of 200 °C/h.

2.2 Evaluation

2.2.1 X-ray diffraction analysis and thermal expansion measurement

We identified the crystals in the glass/ceramic composites by X-ray diffraction analysis (Cu target, 40 kV, 20 mA). The thermal expansion was measured using a push-rod dilatometer between 300 K and 77 K. Fused silica was used as the standard specimen.

2.2.2 Thermal shock test

A thermal shock test was performed using a composite of alumina-treated zirconia and borosilicate glass having an alumina-treated zirconia content of 50 wt%. Figure 2 shows the construction of the test samples. The GaAs chips were flip-chip-bonded to three types of substrate: the composite substrate, a 99 percent alumina substrate, and a fused silica substrate. The GaAs chips were 50 × 5 × 0.6 mm (about

ten times larger than LSI chips), and the substrates were 100 × 100 × 3 mm. A thin Au/Pt/Ti metallization film was formed by sputtering the polished surfaces of the substrates. The GaAs chips were mounted on the substrates and bonded at both ends with indium solder. Indium was used because of its good fatigue-resistance in liquid nitrogen.

We conducted a thermal shock test by immersing the models in liquid nitrogen for 30 s, then exposing them to nitrogen gas at room temperature for 30 s. The bonding failure rate was determined from the number of chips that had detached from the substrates on one or more sides.

3. Results

3.1 Thermal expansion of the composites

Figure 3 shows the X-ray diffraction analyses of the three glass/ceramic composites listed in Table 1. The figure shows that zirconium silicate formed in the GZ and GZ + A composites but not in the GAZ composite.

Figure 4 shows the thermal expansions of GaAs and the three composites between 300 K and 77 K. The thermal expansion of the GAZ composite was closest to that of GaAs. The thermal expansions of the GZ and GZ + A composites were the lowest.

Figures 3 and 4 suggest that the alumina

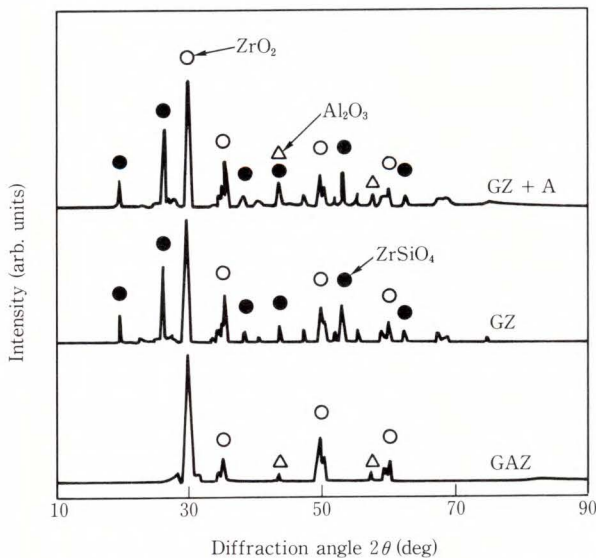


Fig. 3—X-ray diffraction analyses of glass/ceramic composites.

treatment of zirconia powder prevents zirconium silicate formation in glass/ceramic composites, and, therefore, provides thermal expansion matching.

Figure 5 shows how the content of alumina-treated zirconia powder in the glass affects the difference in the thermal expansions (ΔTE) of GaAs and the GAZ composite between 77 K and 300 K. The figure shows that the increase in thermal expansion varies with the content of alumina-treated zirconia powder. When the alumina-treated zirconia content was 50 wt%, ΔTE remained within 1×10^{-4} between 77 K and 300 K.

3.2 Thermal shock test

Figure 6 shows the bonding failure rates of the SiO₂, Al₂O₃, and GAZ composite after

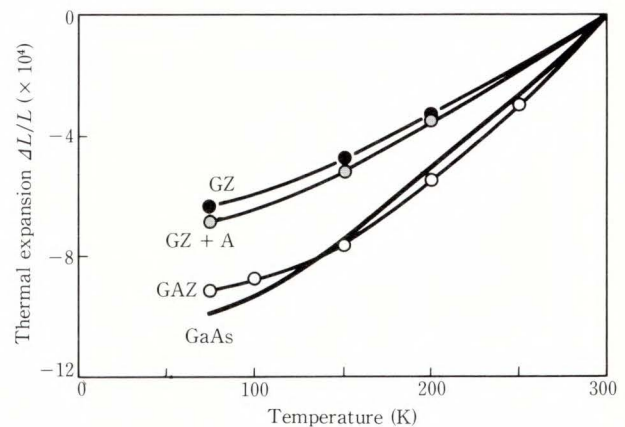


Fig. 4—Thermal expansions of GaAs and glass/ceramic composites between 77 K and 300 K.

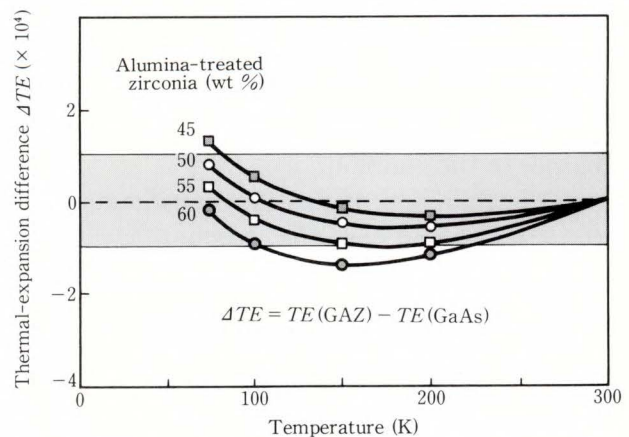


Fig. 5—Effect of alumina-treated zirconia on the difference in thermal expansions (ΔTE) of GaAs and GAZ composite between 77 K and 300 K.

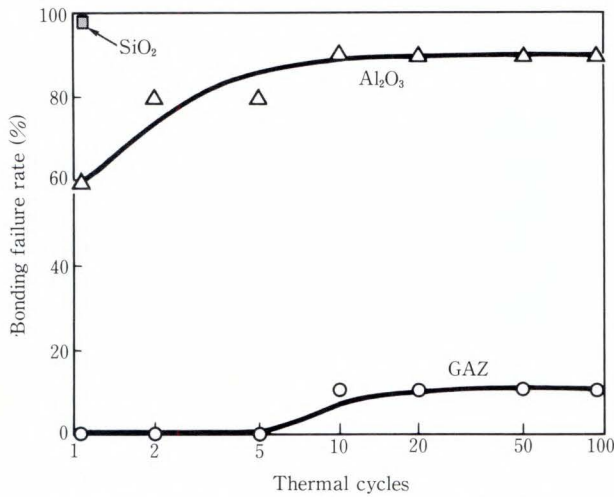


Fig. 6—Bonding failure rates after thermal shock testing.

thermal shock testing. All of the chips on the fused silica substrates detached after one thermal shock cycle. Sixty percent of all the chips on the alumina substrates detached after one cycle, and the failure rate increased with each cycle. However, only ten percent of the chips on the GAZ composite substrates detached after 100 cycles.

4. Discussion

4.1 Thermal expansion matching

Figure 7 shows our model of how zirconium silicate formation is prevented in the GAZ composite. In the GZ composite, zirconia readily combines with the silica in the glass to form zirconium silicate. In Fig. 7, the diagram for the GZ + A composite shows that simply adding alumina powder does not prevent the formation of zirconium silicate. However, we think that the alumina treatment of zirconia powder creates a thin film of alumina on the surface of the zirconia powder which acts as a barrier to the reaction.

The thickness of this film is estimated to be 0.01 μm, based on the composition of the suspension. This can be checked using a method such as transmission electron microscopy.

The thermal expansion coefficient of composite materials is generally described by

$$\alpha = \frac{\sum(\alpha_i V_i E_i)}{\sum(V_i E_i)}, \dots \dots (1)$$

Where α is the thermal expansion coefficient, V is the volume ratio, and E is Young's modulus⁴⁾. The differences in thermal expansions shown in

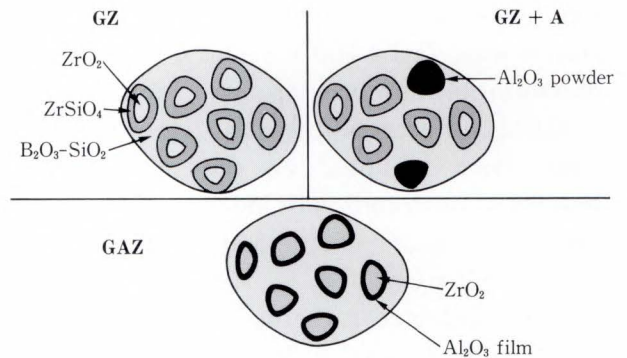


Fig. 7—Model of how zirconium silicate formation is prevented.

Table 2. Differences in thermal expansions (ΔTE) between 77 K and 300 K, and bonding failure rates after 100 thermal cycles

Substrate	ΔTE (77-300 K)	Bonding failure rate after 100 cycles (%)
GAZ	0.4 × 10 ⁻⁴	10
Al ₂ O ₃	3.7 × 10 ⁻⁴	90
SiO ₂	9.6 × 10 ⁻⁴	100

Fig. 5 closely match those obtained using Equation (1).

4.2 Thermal shock resistance

Table 2 shows the differences in thermal expansions (ΔTE) between 77 K and 300 K and the bonding failure rates after 100 thermal shock cycles for GaAs bonded to the SiO₂, Al₂O₃, and GAZ composite substrates. The ΔTE values were calculated from Figs. 1 and 5. The table shows that the bonding failure rate increases with the difference in thermal expansions. Ninety percent of the GAZ composite samples survived 100 thermal shock cycles.

In the thermal shock test, the temperature was changed from 77 K to 300 K in 30 s, and the test chips were about ten times larger than LSI chips. These results suggest that reducing the rate of temperature change and the size of LSI chips will limit the bonding failure rate to under ten percent.

The high bonding reliability of the GAZ composite observed in these experiments suggests that it is the best choice for HEMT packaging.

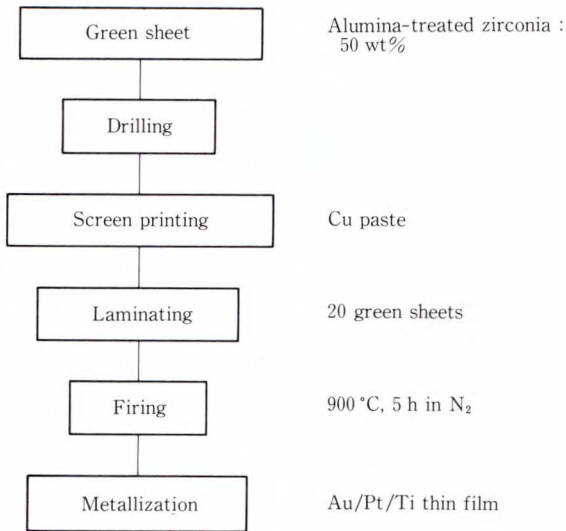


Fig. 8—Fabrication of multilayer substrate.

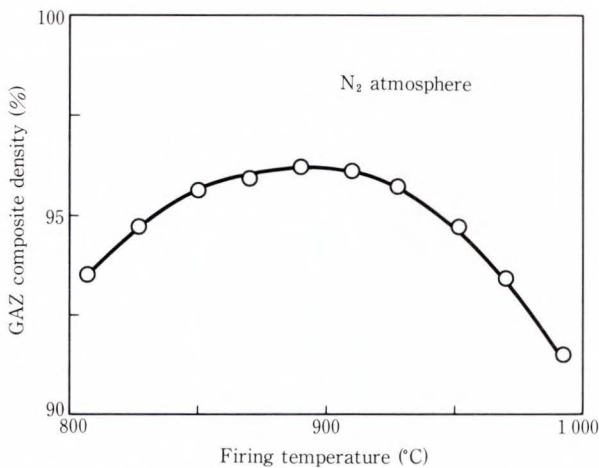


Fig. 9—Relationship between GAZ composite density and firing temperature.

5. Application

We developed a multilayer substrate using the GAZ composite and copper conductors, and used it to fabricate a HEMT random number generator. The electrical specifications of this module in liquid nitrogen were then obtained.

5.1 Multilayer ceramic substrate

Figure 8 shows the fabrication process of the multilayer substrate. Green sheets of borosilicate glass and the alumina-treated zirconia powder (GAZ) composite (alumina-treated zirconia content: 50 wt%) were cast, cut into 180 mm squares, and then drilled. Copper paste was screen-printed onto the sheets to form the wiring patterns and to fill the holes. Twenty

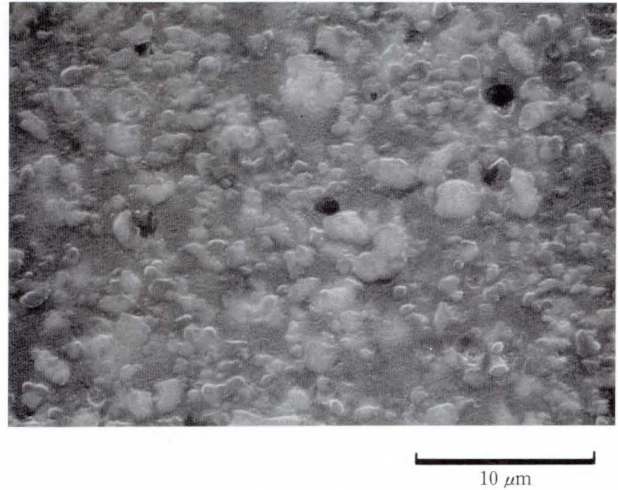


Fig. 10—SEM of polished surface of composite.

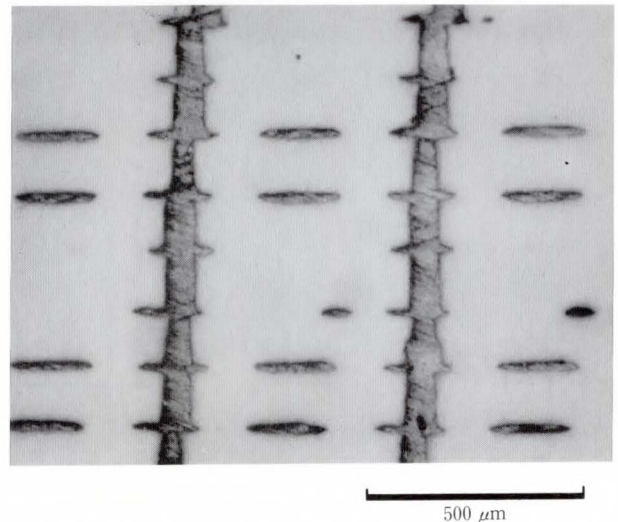


Fig. 11—Cross section of multilayer substrate.

sheets were aligned and laminated to form a 5-mm thick sheet. Then the lamination was fired in nitrogen at 900 °C for 5 h.

Figure 9 shows the relationship between the GAZ composite density and the firing temperature. The density exceeded 96 percent at the optimum firing temperature of 900 °C. Figure 10 shows the microstructure of the GAZ composite after firing at 900 °C in nitrogen. The figure shows that the resulting composite is dense and homogeneous. Firing under these conditions enables the composite to co-fire with the copper conductors. Copper is the most suitable material for wiring because it is inexpensive, has the lowest conductivity of all metals at liquid nitrogen temperature⁵⁾, and

Table 3. Design values of vias and wiring patterns

Conductor	Cu
Via diameter (μm)	100
Line width (μm)	100
Line spacing (μm)	300
Multilayer design	
Signal	8 layers
Power	8 layers

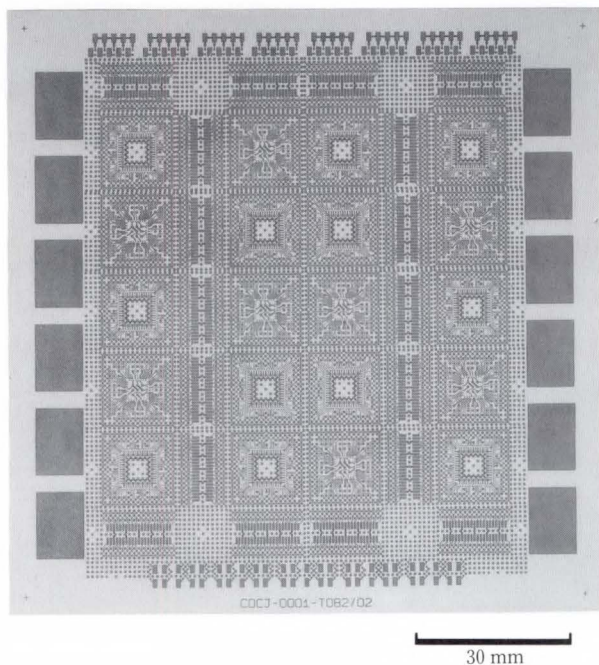


Fig. 12—Multilayer substrate prior to assembly.

has a strong resistance to migration.

Figure 11 shows a cross section of the multilayer substrate. The substrate has 16 thick-film layers connected by copper conductors. Table 3 lists the design values of the vias and wiring patterns.

The substrate is 120 mm square and 4 mm thick. Figure 12 shows the substrate prior to assembly. A metallization film for bonding pads was formed by sputtering both substrate surfaces after polishing them so that their roughness was less than $0.05 \mu\text{m Ra}^{\text{note}}$. The metallization film is gold over platinum with a titanium underlayer formed by the lift-off process. The metallization film is $2.5 \mu\text{m}$ thick.

Note) Ra: Average surface roughness

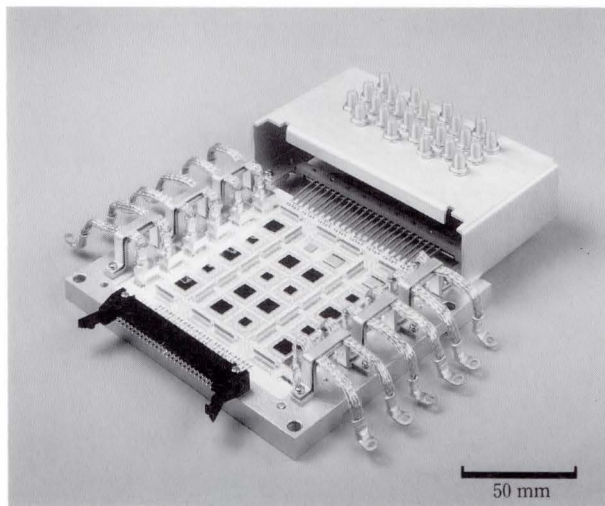


Fig. 13—Random number generator module consisting of 20 HEMT chips. The chips are flip-chip-bonded to the multilayer substrate⁶⁾.

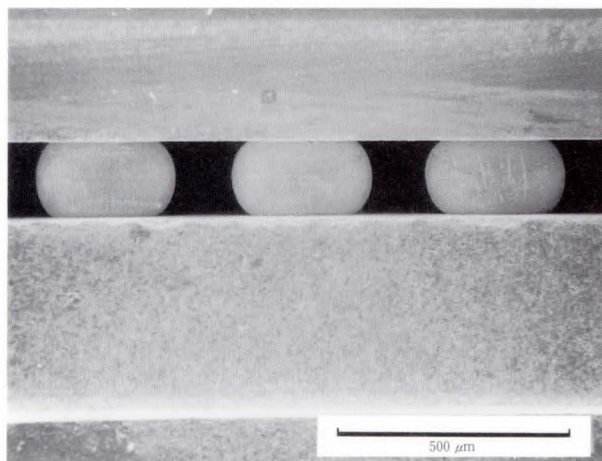


Fig. 14—Close-up of the flip-chip bond. GaAs chips are flip-chip-bonded to the substrate with indium solder.

5.2 Random number generator

The random number generator module consists of 20 HEMT chips flip-chip-bonded to the multilayer substrate⁶⁾ (see Fig. 13). The module generates 32-bit random numbers using a 47-step shift register loop, and is fixed to a frame for mechanical support and I/O connection. Twelve of these chips are 8.2-mm-square logic chips having 124 terminals, and the other eight are 5-mm-square RAM chips having 72 terminals. Indium was used for the solder bumps because of its resistance to fatigue in liquid nitrogen⁷⁾. Figure 14 shows a close-up of the flip-chip bond.

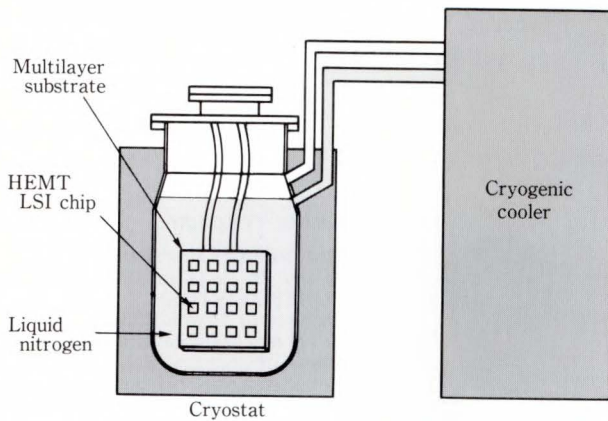


Fig. 15—Closed-loop cooling system for random number generator module.

Table 4. Electrical specifications of random number generator

Resistivity ($m\Omega/cm$)	200
Impedance (Ω)	50
Dielectric constant	8.9
T_{pd} (ns/m)	10
Clock cycle (ns)	1.49

The module was cooled to 77 K over an interval of one hour using a closed-loop cryogenic cooling system (see Fig. 15), and then powered up⁸⁾. The module operated stably in liquid nitrogen for 500 thermal cycles between 300 K and 77 K. Table 4 lists the electrical specifications of the module and substrate. The shortest clock cycle was 1.49 ns. The resistivity of the wiring between chips was less than 200 $m\Omega/cm$, and the signal propagation delay was 10 ns/m.

This module confirms that the new substrate enables flip-chip connection of HEMTs for operation at 77 K. However, due to routing limitations, the HEMT chips in this module occupy only 16 percent of the available substrate area. Although we can soon achieve higher packaging densities (either by increasing the number of wiring layers or by reducing the wiring line pitch), to approach full utilization using GaAs⁹⁾, further refinements in multilayer ceramic wiring techniques will be required.

6. Conclusion

We developed a new ceramic material

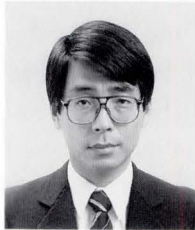
composed of glass and alumina-treated zirconia powders. The thermal expansion of the material was closely adjusted to that of GaAs by controlling the ratio of glass to alumina-treated zirconia powder. The reliability of flip-chip bonds between GaAs chips and substrates made from the new ceramic was high. We built a random number generator consisting of twenty HEMT chips flip-chip-bonded to a multilayer substrate made from the new ceramic. The module stably generated random numbers at a 1.49-ns clock cycle at 77 K, indicating that this packaging technique does not degrade the switching speed of HEMTs at 77 K.

References

- 1) Mimura, T., Hiyamizu, S., Fujii, T., and Nanbu, K.: A New Field-Effect Transistor with Selectively Doped GaAs/n-Al_xGa_{1-x}As Heterojunctions. *J. Appl. Phys.*, **25**, pp. L225-L227 (1980).
- 2) Yokouchi, K., Kamehara, N., and Niwa, K.: Multilayer Ceramic Substrate for HEMT Packaging. (in Japanese), *Denshi-Zairyo*, **28**, 4, pp. 111-115 (1989).
- 3) Aoki, S., Imanaka, Y., Yokouchi, K., and Kamehara, N.: Multilayer Ceramic Substrate for HEMT packaging. Proc. 1991 Int. Elect. Pack. Conf., 1991, pp. 329-341.
- 4) Imanaka, Y., Aoki, S., Kamehara, N., and Niwa, K.: Crystallization of Low Temperature Fired Glass/Ceramic Composite. *Yogyo-Kyokai-Shi*, **95**, pp. 1066-1068 (1987).
- 5) National Astronomical Observatory ed.: 1990 Chronological Scientific Tables. Tokyo, Maruzen, 1989, 527p.
- 6) Aoki, S., Imanaka, Y., Yokouchi, K., and Kamehara, N.: Special Issue on Advanced Packaging Technology for Microelectronics Manufacturing: Packaging Technology for HEMT LSI Devices Operated in Liquid Nitrogen. *Trans. IEICE*, **E74**, 8, pp. 2317-2322 (1990).
- 7) Ochiai, M., Nakanishi, T., Karasawa, K., Hashimoto, K., and Niwa, K.: Metallization of Pure Indium Solder Used in Flip-chip Bonding in Liquid Nitrogen. Proc. 1990 Int. Microelec. Conf., 1990, pp. 115-119.
- 8) Fujisaki, A., Udagawa, Y., Yamamoto, H., and Yokouchi, K.: Cryogenic Cooling System for HEMT LSI. (in Japanese), Proc. 1990 Autumn Natl. Conv. Rec., IEICE, 5, 1990, p. 124.

9) Kaneko, A., Kuwabara, K., Kikuchi, S., and Kano, T.: Hardware Technology for FUJITSU VP2000 Series. *FUJITSU Sci. Tech. J.*, 27, 2

(Special Issue on Supercomputer VP2000 Series), pp. 158-168 (1991).



Shigenori Aoki

Computer Packaging Materials
Laboratory
FUJITSU LABORATORIES, ATSUGI
Bachelor of Science
Kyoto University 1985
Specializing in Ceramic Substrates



Kishio Yokouchi

Manufacturing Engineering Dept.
Printed Wiring Board Div.
FUJITSU LIMITED
Bachelor of Chemical Eng.
Yokohama National University 1977
Master of Chemical Eng.
Yokohama National University 1979
Specializing in Packaging and Cooling
Technology for High Speed
Computers



Yoshihiko Imanaka

Computer Packaging Materials
Laboratory
FUJITSU LABORATORIES, ATSUGI
Bachelor of Metallurgical Eng.
Kyushu University 1983
Specializing in Ceramic Substrates

High-Frequency Response in Bi-Based Superconducting Microstriplines

• Atsushi Tanaka • Nobuo Kamehara • Koichi Niwa

(Manuscript received February 3, 1992)

The microwave transmission losses and phase velocities of Bi-Sr-Ca-Cu-O (BSCCO) microstriplines were measured as a function of temperature and frequency. Microstrip meander lines 78 mm long and 200 μm wide were prepared using Bi-based superconducting films. The transmission properties of these lines were studied at frequencies up to 18 GHz using a vector network analyzer. The loss in these lines was less than that in a geometrically equivalent gold line up to 18 GHz and was 1.5 dB at 10 GHz and 54.6 K. The phase velocity of the BSCCO lines was 1.18×10^{10} cm/s at 54 K and 1 GHz, which is slightly lower than the figure obtained for the gold line.

1. Introduction

A thorough characterization of the microwave response of oxide superconductors has far-reaching implications, both as a tool for investigating the superconducting mechanism and also as a means of assessing the suitability of these materials in high-frequency applications. To date, most studies on the microwave properties of oxide superconductors have been done using cavity perturbation methods, focusing mainly on Y-Ba-Cu-O (YBCO)¹⁾⁻⁵⁾. Results have also been reported for Tl-Ba-Ca-Cu-O^{6),7)}. The perturbation method is excellent for surface impedance measurements because the materials couple to the electromagnetic field without ohmic contact. However, direct investigation of practical microwave devices such as microstrip transmission lines, stripline resonators, and delay lines is more relevant.

The propagation properties of superconducting transmission lines have been studied by several researchers⁸⁾⁻¹⁰⁾. These studies have shown that superconducting transmission lines act as low attenuation and frequency dispersionless transmission lines up to well-below their gap frequency, ω_g . The ω_g figures for high- T_C materials are expected to be more than 10 THz.

High- T_C superconducting transmission lines will enhance the performance of high-speed digital communication systems.

Although Bi-Sr-Ca-Cu-O (BSCCO) is generally more difficult to synthesize¹¹⁾, its high- T_C phase ($\text{Bi}_2\text{Sr}_2\text{Ca}_2\text{Cu}_3\text{O}_x$) has several potential advantages because its higher T_C implies less loss due to thermally excited quasiparticles. We have studied BSCCO microwave properties and have reported on microwave transmission through polycrystalline BSCCO double-sided microstriplines^{12),13)}.

This paper discusses the results of microwave measurements on meander microstriplines that were made using as-deposited superconducting BSCCO films. The transmission losses and phase delays versus temperature of samples produced on a 0.25 mm thick MgO substrate were obtained for frequencies up to 18 GHz. These results were then compared with those obtained for a geometrically identical gold microstripline.

2. Sample preparation and characterization

2.1 Sputtering

Since high-frequency properties in superconductors are extremely sensitive to the presence of intergrowths and impurity phases, the

Table 1. Sputtering conditions

Item	Conditions
Target	Bi: Sr:Ca:Cu = 3:1.9:2:3.5
Heater temperature (°C)	760
Sputtering gas	Ar:O ₂ = 1:1
Gas pressure (Torr)	10
rf power (W)	25 (0.3 W/cm ²)

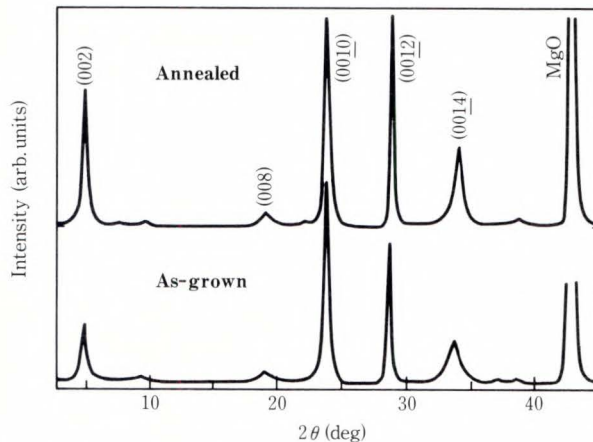


Fig. 1—X-ray diffraction patterns for as-deposited and post-deposition annealed films. Each peak is assigned to the (00*n*) plane of high-*T_C* phase materials, where *n* is an even number. Annealing increases the intensity of the peaks, but does not significantly change their positions.

synthesis conditions must be carefully monitored and controlled in order to minimize their formation.

Superconducting films were grown on MgO substrates by radio frequency (rf) magnetron sputtering from a composite BSCCO target (Bi: Sr:Ca:Cu = 3:1.9:2:3.5). The deposited film was slightly Cu-rich but almost stoichiometric. The sputtering conditions are shown in Table 1. The substrates were secured to a stainless steel block that was heated to 760 °C during deposition. In order to grow a high-*T_C* phase film, the deposition was done at the very slow rate of 0.3 nm/min to 1 nm/min. The total film thickness was about 200 nm after ten hours of deposition.

2.2 Film characterization

Post-deposition annealing at 850 °C was done to improve the superconducting properties. X-ray diffraction patterns showed that the films

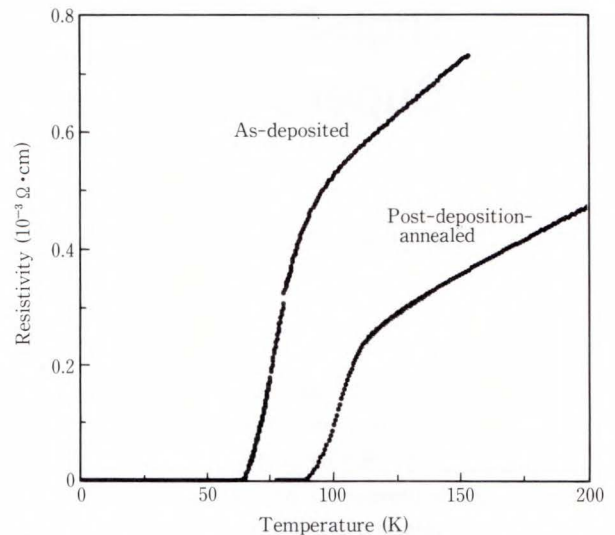


Fig. 2—Resistivity versus temperature for as-deposited film and annealed film. Onset temperatures are 97 K and 119 K. *T_C* values (*R* = 0) are 64 K and 89 K.

were nearly single-phase high-*T_C* materials (see Fig. 1). Figure 2 shows the temperature dependence of the film's resistivity. Before annealing, *T_C* (*R* = 0) was 64 K. This figure improved to 89 K after annealing.

2.3 Fabrication of microstripline

Annealed films were wet etched to produce a meander line 78 mm long and 200 μm wide. Before making the microwave measurements, the temperature dependence of the stripline's resistance was measured using a simple two-point probe method.

The onset temperature was 94 K, and *T_C* (*R* = 0) was about 60 K. After patterning, a gold ground plane was deposited on the reverse side of the MgO substrate by conventional e-gun evaporation.

3. Microwave measurements

3.1 Measurement system

The loss and phase delay between 50 MHz and 18 GHz were measured using a Hewlett-Packard HP-8510 vector network analyzer.

Figure 3 shows the schematic diagram of the measurement system. The sample is placed on a cold stage in a high-vacuum chamber and cooled from room temperature to 40 K using a refrigerator with a closed helium gas cycle.

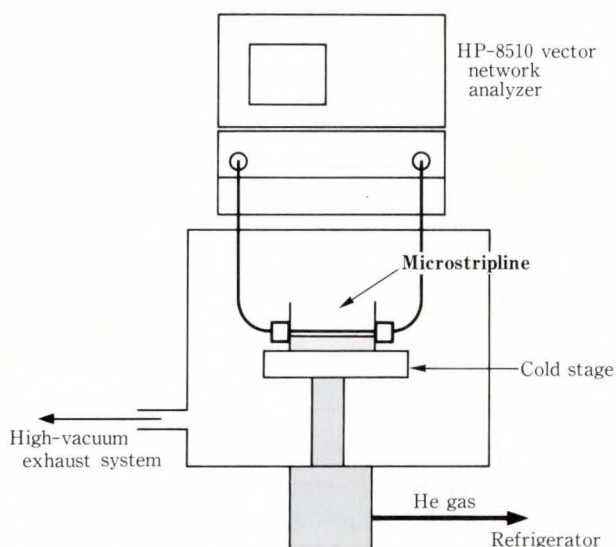


Fig. 3—Schematic diagram of the measurement system.

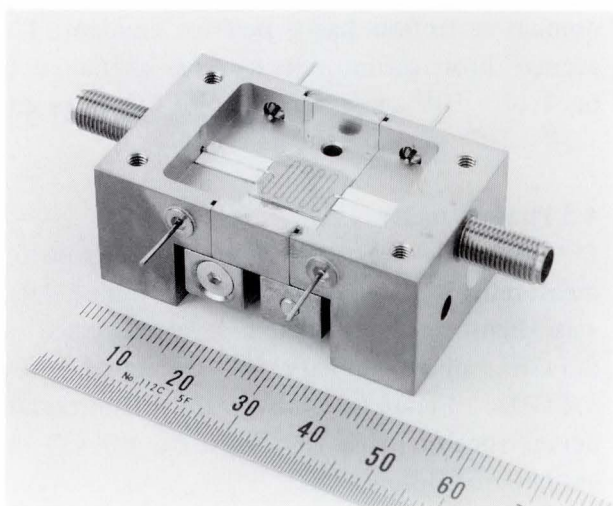


Fig. 4—BSCCO microstripline mounted on the measurement stage. Midsection is made of invar alloys. BSCCO meander line is connected to gold microstriplines of launcher blocks by gold ribbons.

3.2 Measurement module and calibration

The microstripline was mounted on a gold-plated stage consisting of a mid-section and two launcher blocks (see Fig. 4). The launcher blocks are Hewlett-Packard microcircuit modular packages. The superconducting line was connected to the launcher block stripline using silver paint and gold ribbons. The midsection is made of invar alloys to accommodate the thermal expansion mismatch between the stage and substrate. Microwave calibration was done using a through-

reflect-line (TRL) technique at room temperature. TRL calibration has the advantage that the measurement's reference planes are exactly at the ends of the superconducting microstripline. In other words, the magnitude and phase delay at the input end of the superconducting line are unity and zero, respectively, and the magnitude and phase of the output signal are measured at the output end of the line. This allows the transmission loss and phase delay to be measured without the introduction of errors from the launcher block striplines and connectors.

3.3 Reference sample

The transmission properties were compared with those of a geometrically identical 360-nm-thick gold reference sample on a MgO substrate. The reference sample was deposited by e-gun evaporation using a metal mask. The resistivity of the gold line was $3.0 \mu\Omega \cdot \text{cm}$ at 300 K and $1.0 \mu\Omega \cdot \text{cm}$ at 95 K.

4. Results

4.1 Transmission loss

Frequency dependent transmission loss rapidly decreased below the onset temperature (see Fig. 5). The losses at 10 GHz were as follows: 3.1 dB at 63.8 K, 1.9 dB at 59.2 K, and 1.5 dB at 54.6 K. The low points in transmission power around 6.5 GHz and 13 GHz were attributed to resonances in the meander line due to the high impedance parts at its curves.

The transmission losses of the BSCCO lines were compared with the loss of the geometrically identical gold line. Up to 18 GHz, the losses of the BSCCO lines were less than the loss of the gold line (see Fig. 6).

4.2 Time domain response

The time domain reflection for a step input was calculated from the frequency domain response using Fourier transformation (see Fig. 7). The plots that were obtained exhibit similar jumps at 0.3 ns and 1.6 ns caused by an impedance mismatch at the ends of the meander line. The reflection peaks seen in Fig. 7 correspond to the curves in the meander line. The gold

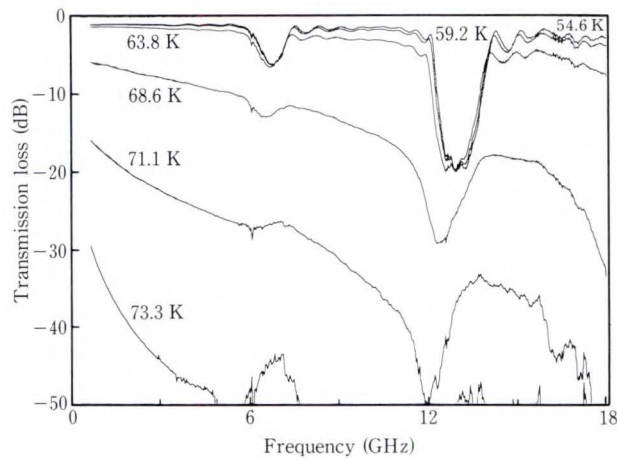


Fig. 5—Transmission loss versus frequency for BSCCO meander line below onset temperature. Low points around 6.5 GHz and 13 GHz and due to geometrical resonance.

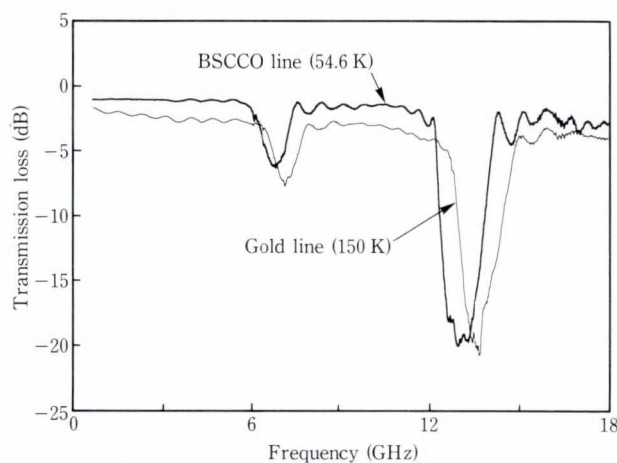


Fig. 6—Transmission loss of BSCCO and gold meander microstriplines.

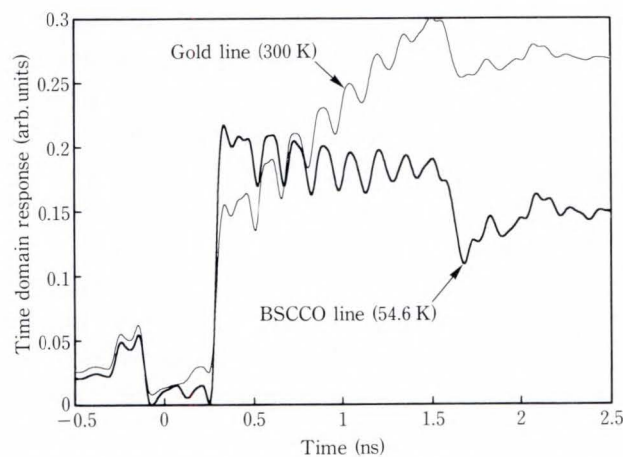


Fig. 7—Time domain reflection of BSCCO and gold meander lines for a step input. The reflection peaks correspond to the meander line curves.

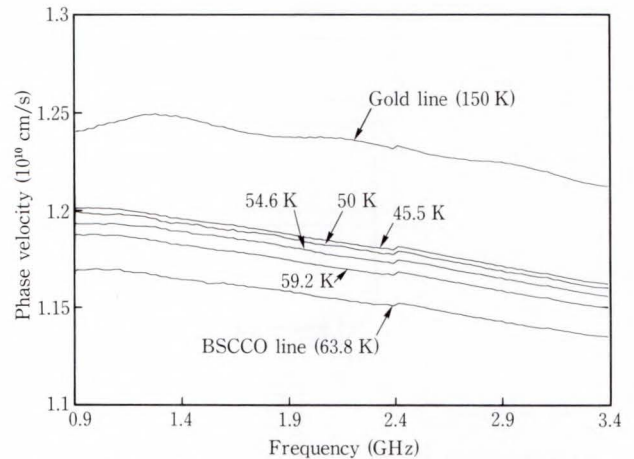


Fig. 8—Phase velocity versus temperature for BSCCO and gold microstriplines.

line has a DC resistance of $4.2 \Omega/\text{cm}$ at 300 K, and unlike the superconducting line, its time domain reflection has a positive gradient. The average propagation velocity was estimated to be $1.17 \times 10^{10} \text{ cm/s}$ for the BSCCO lines and $1.18 \times 10^{10} \text{ cm/s}$ for the gold line.

4.3 Phase velocity

The phase velocity was estimated from the measured phase delay. Because the phase delay was significantly affected by resonance at 6.5 GHz, phase velocity was estimated below 3.4 GHz. Figure 8 shows the temperature dependence of phase velocity in the BSCCO and gold microstriplines.

5. Discussion

When the stripline width, W , is much larger than the thickness of the dielectric, h , the transmission properties can be roughly estimated using conventional microwave theory⁹⁾. The attenuation constant, a , and phase velocity, v_p , for a normal metal stripline are given by Equations 1 and 2 below.

$$\alpha = \frac{1}{h} \sqrt{\frac{\omega \epsilon_r \epsilon_0}{2\sigma}} \left(1 + \frac{2}{WL_1} \sqrt{\frac{\mu_0}{2\sigma\omega}} \right)^{-1/2}, \quad (1)$$

$$\begin{aligned} v_p &= \frac{c}{\sqrt{\epsilon_r}} \left(1 + \frac{2}{WL_1} \sqrt{\frac{\mu_0}{2\sigma\omega}} \right)^{-1/2} \\ &= \frac{c}{\sqrt{\epsilon_r}} \left(1 + \frac{\delta_s}{h} \right)^{-1/2} \dots \dots (2) \end{aligned}$$

The phase velocity in normal metal is frequency dependent because the skin depth, δ_s , is frequency dependent. In this study, α and v_p were expected to be only slightly frequency dependent because the conductor thickness was less than the skin depth. A simple calculation of conductor loss showed that the attenuation constant of the reference sample was about 0.4 dB/cm, which agrees with the attenuation observed in the low frequency region.

The propagation constant of a superconducting stripline can be described using a two-fluid model⁹⁾ as shown below.

$$\alpha \approx \frac{\sigma_n \omega^2 \mu_0^{3/2} \epsilon^{1/2} \lambda^3}{h}, \quad \dots \dots (3)$$

$$v_p = \frac{c}{\sqrt{\epsilon_r}} \left(1 + \frac{2\mu_0 \lambda}{WL_1} \right)^{-1/2}$$

$$= \frac{c}{\sqrt{\epsilon_r}} \left(1 + \frac{2\lambda}{h} \right)^{-1/2}, \quad \dots \dots (4)$$

where λ is the penetration depth and σ_n is the real part of complex conductivity in the superconducting material and said normal current.

This two-fluid model states that attenuation is proportional to ω^2 . Measurements showed that the transmission loss of the microstripline increases above 9 GHz. However, below 6 GHz, the loss is only slightly frequency dependent and does not significantly decrease when the temperature decreases below 59.2 K. The loss in the low frequency region as extrapolated from the loss at 10 GHz using the ω^2 rule is much less than the loss that was actually observed. At present, other crucial factors, for example, the contact resistance between the superconductor and the normal metal, are believed to dominate transmission loss in the low frequency region.

The phase velocity of a superconducting transmission line is expected to depend on λ and not on frequency. In other words, a superconducting line has kinetic inductance due to the superconducting current flowing in the surface layer. Below the onset temperature, the observed phase velocity increased rapidly and almost saturated below 50 K. This is partially

explained by the temperature dependence of the penetration depth. Below 2 GHz, the phase velocity versus frequency of the superconducting line was more linear than that of the gold line, but was frequency dependent. As mentioned above, the measured line exhibited geometrical resonance at about 6.5 GHz, an effect not eliminated even at this frequency. Further study using a different BSCCO meander line pattern is required.

6. Conclusion

We fabricated nearly single-phase high- T_c Bi-Sr-Ca-Cu-O (BSCCO) meander microstriplines on MgO substrates by rf magnetron sputtering. The transmission losses and phase velocities of these lines were measured up to 18 GHz. The BSCCO lines showed a lower loss than a geometrically identical gold line. Phase velocity in the BSCCO lines is highly temperature dependent and slightly frequency dependent. These dependencies can be explained by changes in kinetic inductance or penetration depth in the lines. Further study using a sample that is free from geometrical resonance is required.

References

- 1) Sridhar, S., Shiffman, C.A., and Hamdeh, H.: Electrodynamical response of $Y_1Ba_2Cu_3O_7$ and $La_{1.85}Sr_{0.15}CuO_{4.8}$ in superconducting state. *Phys. Rev.*, **B36**, 4, pp. 2301-2303 (1987).
- 2) Awasthi, A.M., Carini, J.P., Alavi, B., and Gr uner G.: Millimeter-wave Surface Impedance Measurements of $YBa_2Cu_3O_{7.8}$ Ceramic Superconductors. *Sol. State Commun.*, **67**, 4, pp. 373-377 (1988).
- 3) Martens, J.S., and Beyer, J.B.: Microwave Surface Resistance of $YBa_2Cu_3O_{7.8}$. *Appl. Phys. Lett.*, **52**, 21, pp. 1822-1824 (1988).
- 4) Kobayashi, M., Okabe, K., Tanuma, S., Sankawa, I., Sato, M., Konaka, T., and Ishihara, K.: Microwave Surface Resistance of $YBa_2Cu_3O_{7.8}$. *IEEE Trans. Magnetics*, **25**, 2, pp. 997-1000 (1989).
- 5) Cooke, D.W., Gray, E.R., Arendt, P.N., Elliott, N.E., Rollett, A.D., Schofield, T.G., Mogro-Campero, A., and Turner, L.G.: Microwave surface resistance of $YBa_2Cu_3O_7$ thin films on $LaAlO_3$ Substrates. *J. Appl. Phys.*, **68**, 5, pp. 2514-2516 (1990).
- 6) Newman, H.S., Singh, A.K., Sadananda, K., and Imam M.A.: Microwave Surface Resistance of Bulk

- Tl-Ba-Ca-Cu-O Superconductors. *Appl. Phys. Lett.*, **54**, 4, pp. 389-390 (1989).
- 7) Chang, L.D., Moskowitz, M.J., Hammond, R.B., Eddy, M.M., Olson, W.L., Casavant, D.D., Smith, E.J., and Robinson, M.: Microwave Surface Resistance in Tl-based Superconducting Thin Films. *Appl. Phys. Lett.*, **55**, 13, pp. 1357-1359 (1989).
 - 8) Kautz, R.L.: Picosecond Pulses on Superconducting Striplines. *J. Appl. Phys.*, **49**, 1, pp. 308-314 (1987).
 - 9) Hornak, L.A., Tewksbury, S.K., and Hatamian, M.: The Impact of High- T_c Superconductivity on System Communications. Proc. 1988 Electron. Comp. Conf., Los Angeles, 1988, IEEE, 1988, pp. 152-158.
 - 10) Nuss, M.C., and Goossen, K.W.: Investigation of High-Temperature Superconductors with Terahertz Bandwidth Electrical Pulses. *IEEE J. Quantum Electron.*, **25**, 12, pp. 2596-2607 (1989).
 - 11) Tanaka, A., Kamehara, N. and Niwa, K.: Composition Dependence of high T_c Phase Formation in Pb-doped Bi-Sr-Ca-Cu-O Thin Films. *Appl. Phys. Lett.*, **55**, 12, pp. 1252-1254 (1989).
 - 12) Tanaka, A., Crain, J., and Niwa, K.: High-Frequency Transmission through Bi-Sr-Ca-Cu-O Double-Sided Microstripline on an MgO Substrate. *Jpn. J. Appl. Phys.*, **30**, 4B, pp. L700-L702 (1991).
 - 13) Tanaka, A., Crain, J., and Niwa, K.: Microstripline of Bi-Sr-Ca-Cu-O and their Microwave Properties. Proc. 3rd Int. Symp. Superconductivity, Tokyo, Springer, 1991, pp. 1179-1182.



Atsushi Tanaka

Advanced Materials Laboratory
FUJITSU LABORATORIES, ATSUGI
Bachelor of Applied Physics
The University of Tokyo 1979
Master of Applied Physics
The University of Tokyo 1981
Specializing in Superconducting
Materials



Koichi Niwa

Materials Laboratory
FUJITSU LABORATORIES, ATSUGI
Bachelor of Physics
Chiba University 1964
Dr. of Eng. in Electronic Ceramics
Tokyo Institute of Technology 1988
Specializing in Electronic Ceramics



Nobuo Kamehara

Advanced Materials Laboratory
FUJITSU LABORATORIES, ATSUGI
Bachelor of Chemistry
Niigata University 1970
Specializing in Advanced Ceramic
Materials

Flash Fusible Color Toner for Color Laser Printers

• Katsuji Ebisu • Takahiro Kashikawa • Norio Sawatari

(Manuscript received February 3, 1992)

A flash fusible color toner for color laser printers with flash fusing sub-systems has been developed. This paper describes the materials developed for the color toner.

Conventional color toners cannot be used for flash fusing because they do not absorb light energy in the near-infrared region, where the spectral intensity of flash lamps is high. Therefore a near-infrared absorbent that enables a color toner to absorb most of the flash lamp's light energy was developed. A polyester resin and an amine-modified styrene-acryl resin for the toner binders were developed to give the toner good fusibility. The final color toner has excellent fused fixing quality and brightness.

1. Introduction

Among the many fusing techniques used in laser printers, flash fusing has become well known, especially in high speed printer systems, for its good maintainability. Flash fusing systems are easy to maintain because they do not suffer from many of the problems found in other systems, for example, toner off set during heat-roll fusing. Fujitsu's F6715E and F6700 series of printers employ flash fusing using xenon lamps. Recently, there has been a demand for color laser printers that print in different colors without the need for pre-printed paper. If color laser printers could employ flash fusing, they would have a great advantage in the color printing field. However, conventional color toners cannot be used for flash fusing. This is because these toners do not absorb light energy in the near-infrared region, where the spectral intensity of xenon flash lamps is high.

This paper describes a color toner technology for color laser printers with xenon flash fusing subsystems. Spectrum analyses were carried out for several near-infrared absorbents to make a color toner having a significant absorption band in the near-infrared region. Other research was done on the melting behavior of

the toner binder polymer to achieve better fusing qualities, for example, good adhesion and minimal porosity in the fused image.

2. Material for absorbing flash light energy

Fusing is a process of melting a toner image and then fixing it to paper. The fusing methods used in printers, facsimile machines, and copying machines include heat-pressure, oven, pressure, solvent, and flash fusing. Of these methods, the flash fusing process is preferred because it has the following advantages.

- 1) Flash fusing is a non-contact method, so the resolution of the developed image is not degraded.
- 2) Quick starting is possible because there is no need to preheat the heater.
- 3) Even if a paper jam occurs in the fusing zone, there is no danger of fire.

The spectral intensity of xenon flash lamps is strong only in the near-infrared region from 800 nm to 1100 nm (see Fig. 1). The intensity is relatively weak in other regions, including the visible region from 400 nm to 800 nm. Black toners absorb light throughout the spectrum, but conventional color toners only absorb light in specific visible regions. For instance, the ab-

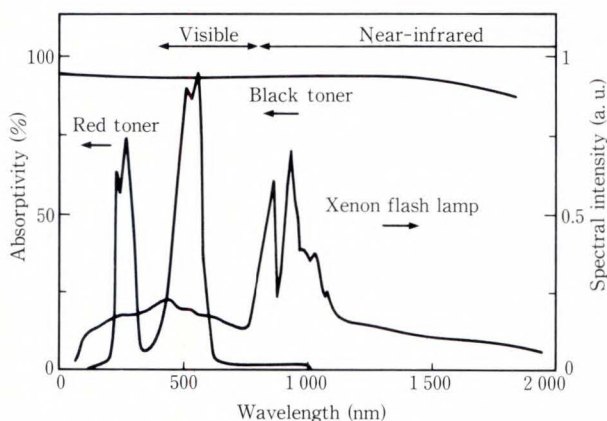


Fig. 1—Absorptivities of toners and spectral intensity of xenon lamp.

sorption band of red toner in the visible region is only from 400 nm to 600 nm. To be fused by flash lamps, the light absorption of the color toner must be high in the near-infrared region.

We added a near-infrared absorbent to a toner to produce a high absorption in the near-infrared region.

3. Near-infrared absorbent

A near-infrared absorbent should have the following characteristics:

- 1) Strong absorption in the near-infrared region.
- 2) No change in absorptivity due to light exposure.
- 3) Weak absorption in the visible region to avoid changes in the original color of the toner.
- 4) No degradation of the triboelectric charging characteristics of the toner.

Three near-infrared absorbents, ammonium salt, aminium salt, and a nickel complex were selected for study on the basis of these requirements.

3.1 Molecular structure and absorption spectra

The molecular structures of the near-infrared absorbents and their absorption spectra are shown in Figs. 2 and 3, respectively. Ammonium salt and aminium salts have wider absorption bands than the Ni complex. Ammonium salt has absorption peaks at 950 nm and 1600 nm,

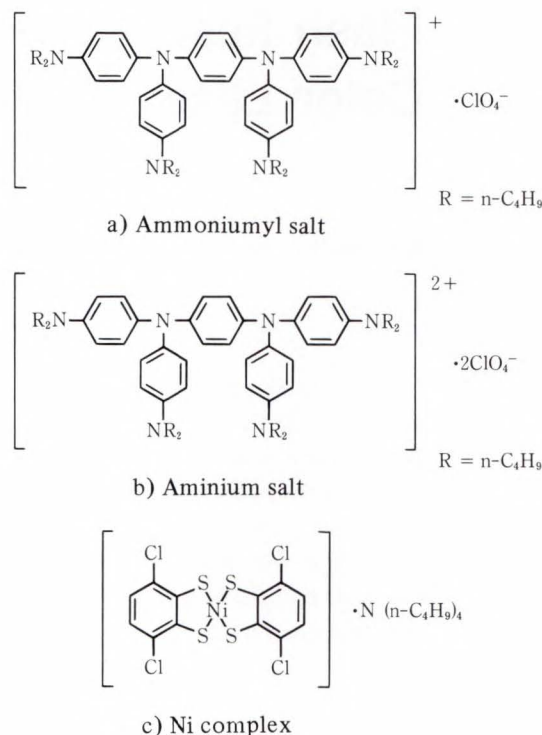


Fig. 2—Molecular structures of near-infrared absorbents.

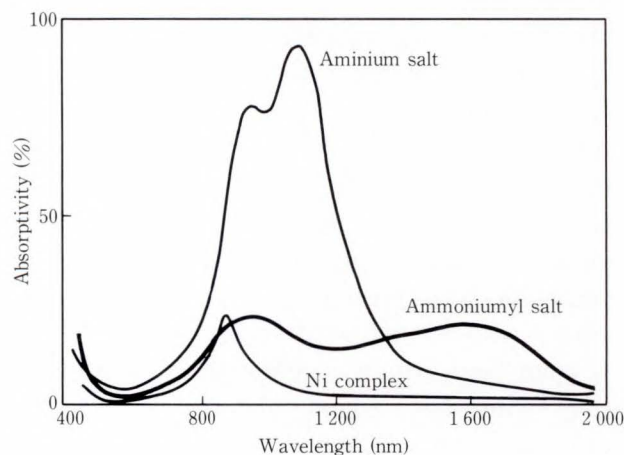


Fig. 3—Spectra of near-infrared absorbents.

while aminium salt has peaks at 975 nm and 1110 nm. The absorption band of the ammonium salt is especially wide and is from 800 nm to 1800 nm. (The absorption peak of a tautomeric compound is usually wide.) The wide absorption peak of ammonium salt is believed to be due to the presence of multi-isomer

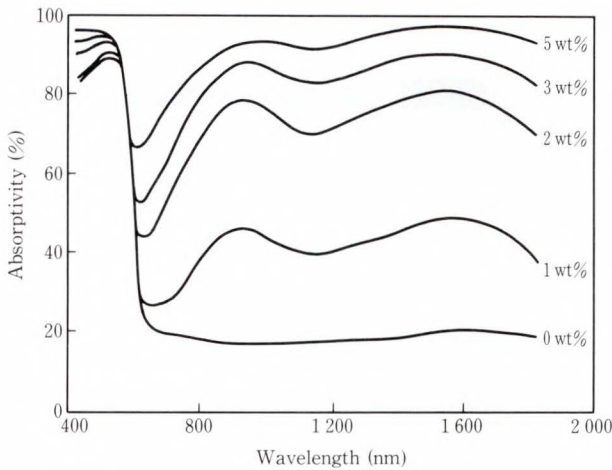


Fig. 4—Spectrum of red toner containing ammonium salt.

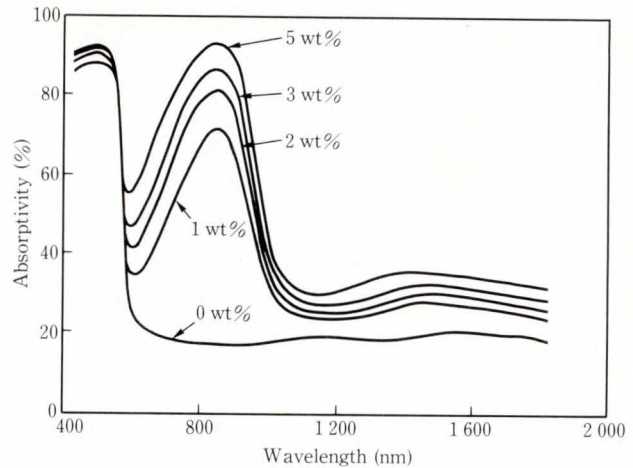


Fig. 6—Spectrum of red toner containing Ni complex.

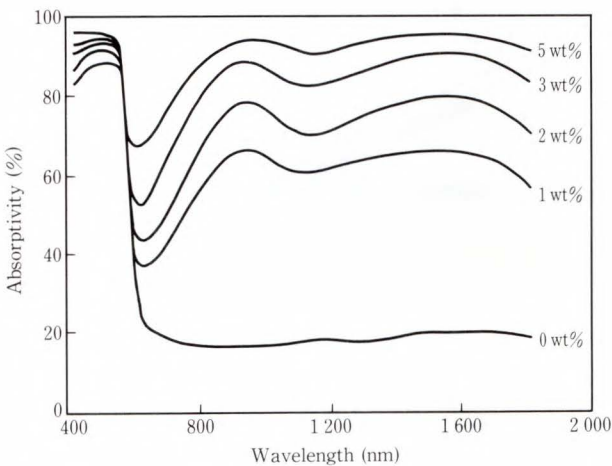


Fig. 5—Spectrum of red toner containing aminium salt.

compositions having ammonium ions that shift their molecular positions. Aminium salt has a very large coefficient of absorptivity at the maximum absorption peak (designated as λ_{\max}). This coefficient is assumed to be large because the divalent ammonium ion of aminium salt has a strong absorptivity in the wavelength region shown in Fig. 3.

3.2 Flash fusibility

Figures 4 to 6 show the spectra of red toners containing various quantities of the three near-infrared absorbents. These figures indicate that their λ_{\max} have a tendency to saturate at an

absorbent content of 2-3 wt%. The spectrum of the toner containing aminium salt is different from the spectrum of ammonium salt and closely resembles the spectrum of the toner containing ammonium salt. It is believed that most of the aminium ions change to more stable ammonium ions (see Fig. 2) during the kneading process. We conducted a fusing test on these red toners using a Fujitsu laser printer with a flash fuser that prints 2 000 lines per minute. The structure of the flash fuser is shown in Fig. 7 and the flash drive circuit is shown in Fig. 8. The fuser basically consists of two flash lamps and a reflector that focuses the flash light onto the paper. The most important factor affecting the fixing quality, especially the quality of adhesion to the paper, is the flash energy. Therefore the flash fusibility was assessed by measuring the adhesion of toners that contained various amounts of absorbent that were fused using various amounts of flash energy. The flash energy was varied by varying the voltage applied to the flash lamps. Adhesion of the fused image to the paper was measured using the tape adhesion test¹⁾ shown in Fig. 9. In this test, an adhesive tape is applied to the fused image and then pressed to the paper by two passes of an iron roller. The tape is then peeled off at right angles to the paper surface. The fusibility was calculated from the optical density values (O.D.) of the original and remaining images as follows:

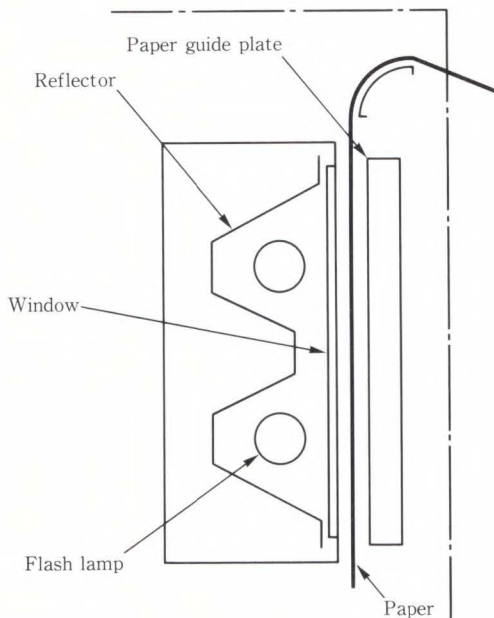


Fig. 7—Flash fuser.

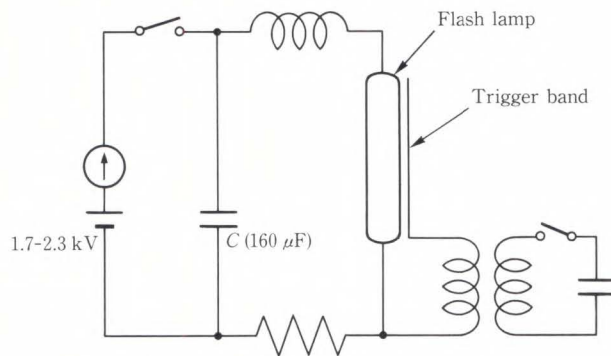


Fig. 8—Flash drive circuit.

$$\text{Fusibility (\%)} = \left(\frac{\text{original O.D.}}{\text{remaining O.D.}} \right) \times 100.$$

The results are shown in Figs. 10 to 12. The fusibility of the three types of toners increases as the amount of absorbent increases. When the flash energy is more than 1.2 J/cm^2 , red toner containing only 2 wt% of ammoniumyl or aminium salt has a fusibility above 90 percent. Toner containing the Ni complex cannot match this figure even when the Ni complex content is 5 wt%.

The integrated absorptivity of the toners in the region where the spectral intensity of xenon flash lamps is high (800 nm to 1100 nm) were

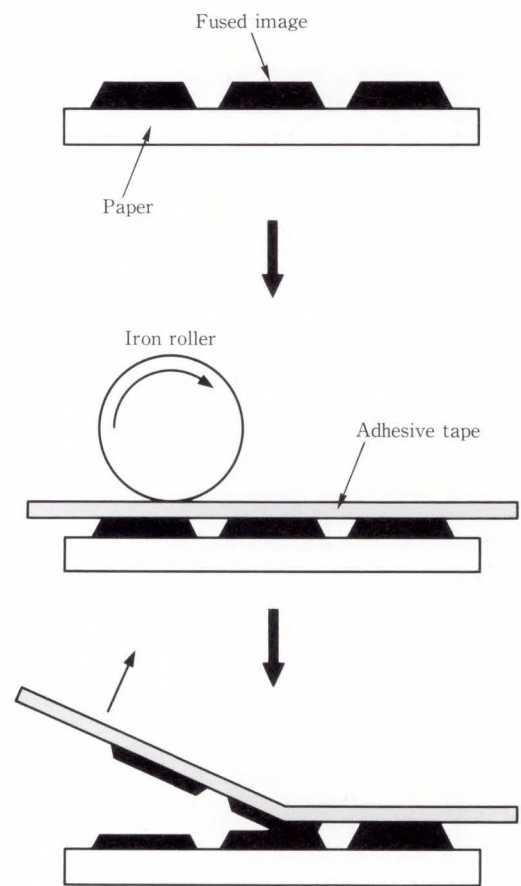


Fig. 9—Tape adhesion test.

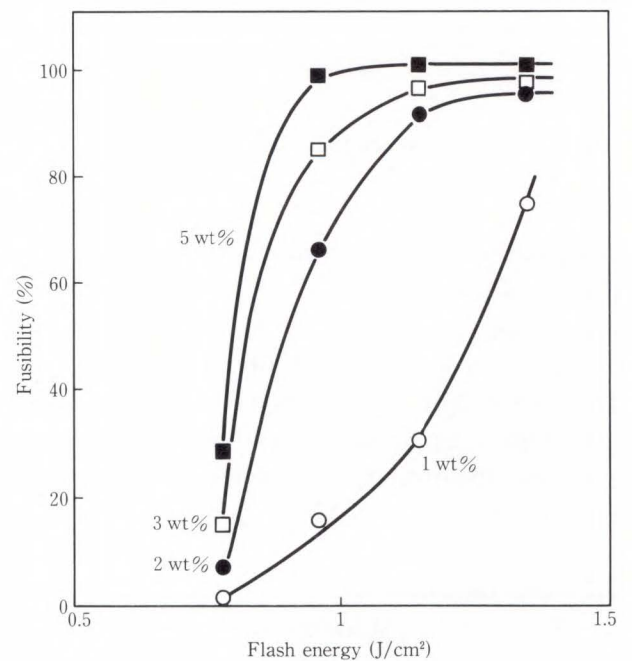


Fig. 10—Fusibilities of images made using red toner containing ammoniumyl salt.

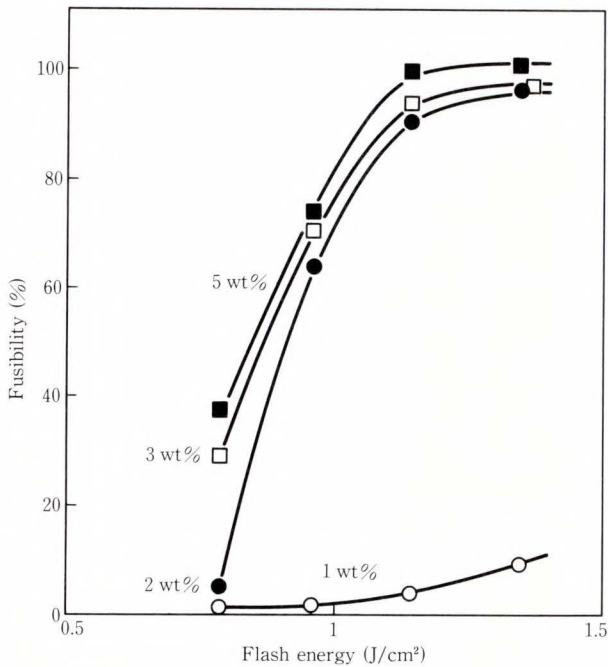


Fig. 11—Fusibilities of images made using red toner containing aminium salt.

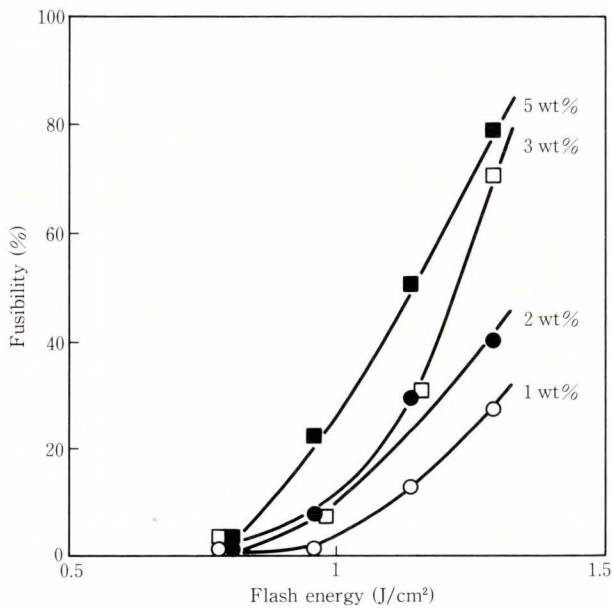


Fig. 12—Fusibilities of images made using red toner containing Ni complex.

calculated. Figure 13 shows the relationship between the fusibility and the integrated absorptivity. The fusibility increases as integrated ab-

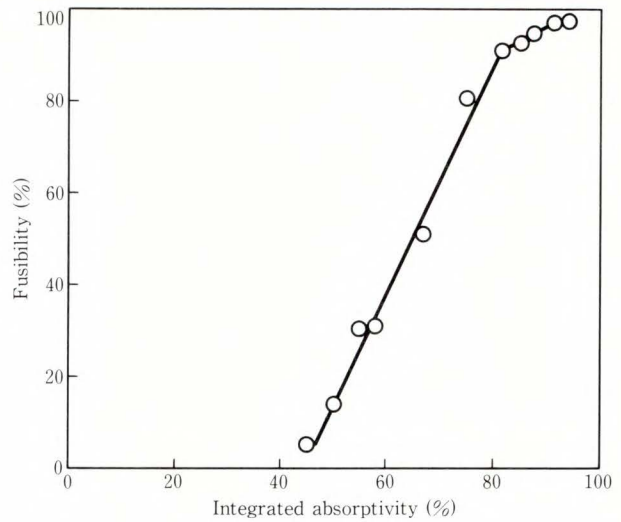


Fig. 13—Relationship between integrated absorptivity and fusibility.

sorptivity increases over the range of 40-80 percent. The fusibility saturates at integrated absorptivities above 80 percent. The fusibility at saturation is over 90 percent.

The above shows that a high absorption from 800 nm to 1 100 nm is required for good fixing quality.

3.3 Light resistivity

The light resistivity of the absorbent is an important property. A toner that has a high light resistivity does not lose absorptivity during toner manufacture and storage. The light resistivities of the three types of absorbent were evaluated spectrally using a fading-meter during exposure to ultraviolet light. Figures 14 to 16 show the changes in the spectra of the absorbents under ultraviolet light. The absorption peak of ammonium salt at 1 600 nm decreases rapidly, while the peak at 950 nm decreases more slowly. The absorption peak of aminium salt has a similar tendency to decrease. After 25 h the peak of aminium salt at 975 nm almost disappears. We measured the absorptivity of ammonium salt at 950 nm, aminium salt at 1 100 nm, and the Ni complex at 860 nm. Figures 17 and 18 show the absorptivities and remaining absorptivities (percentage change in absorptivity due to irradiation) of the three

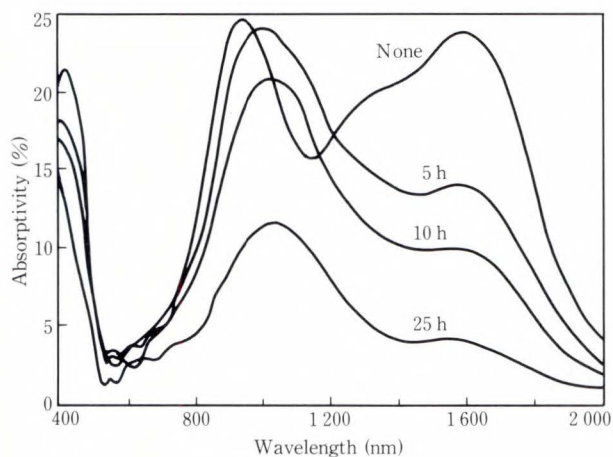


Fig. 14—Light resistivity of ammoniumyl salt.

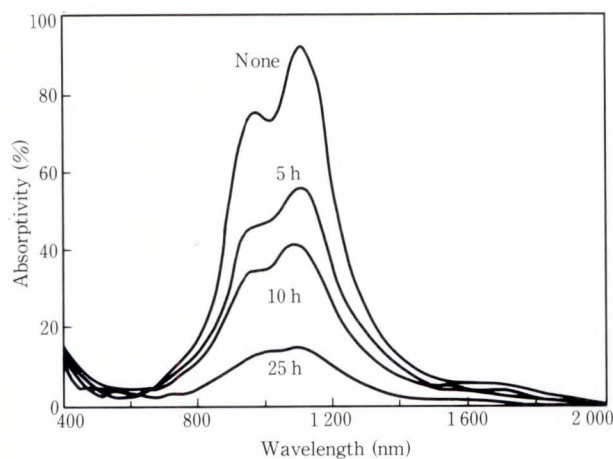


Fig. 15—Light resistivity of aminium salt.

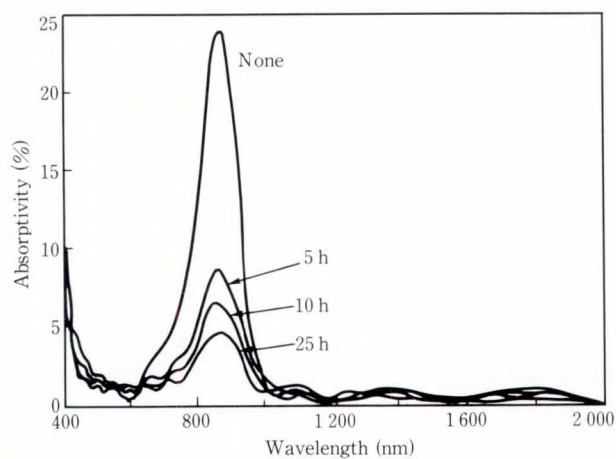


Fig. 16—Light resistivity of Ni complex.

absorbents as a function of exposure time. The relatively high remaining absorptivity of aminium salt is due to its high molecular extinction coefficient. However, the remaining absorptivity of aminium salt after 25 h is only 20 percent. The Ni complex shows the same behavior as aminium salt regarding changes in remaining absorptivity. The decrease in remaining absorptivity of the Ni complex is especially remarkable immediately after irradiation. The remaining absorptivity of ammoniumyl salt remains relatively stable and is still 50 percent after 25 h of irradiation.

IR analyses of ammoniumyl and aminium salt during light exposure indicate that the

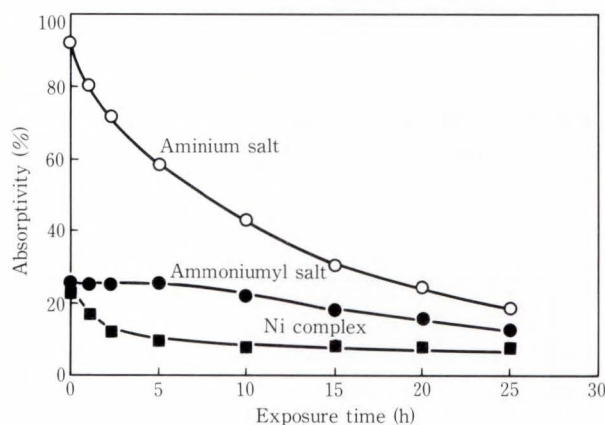


Fig. 17—Relationship between exposure time and absorptivity.

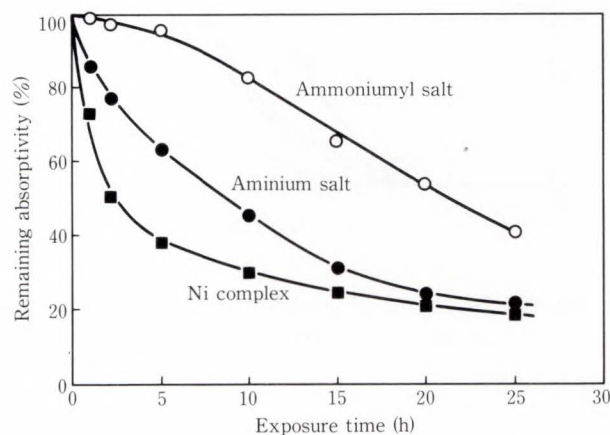


Fig. 18—Relationship between exposure time and remaining absorptivity.

decrease in absorptivity is caused by the loss of divalent ammonium ions. The difference in the absorptivities of ammoniumyl and aminium salt is due to the difference in the number of ions in the two molecules. Aminium salt is unstable because its molecule contains many ions. An accelerated test showed that the absorptivity of ammoniumyl salt drops soon after exposure but remains stable for at least two years under normal storage conditions. The above results show that ammoniumyl salt has a good light resistivity.

3.4 Affect on color

The low absorption of the absorbents in the visible region between 400 nm and 800 nm (see Fig. 3) significantly affects the color of the finished toner. Therefore, the affect of absorbent content on a color toner containing anthraquinone pigment was examined.

A color can be represented by its location in a three-dimensional color space, the axes of which are brightness, chroma, and hue (see Fig. 19). The color difference (ΔE) of a color is its distance in the color space from a standard color. We used the CIE $L^*a^*b^*$ system²⁾, which is one of the most popular systems for color estimation.

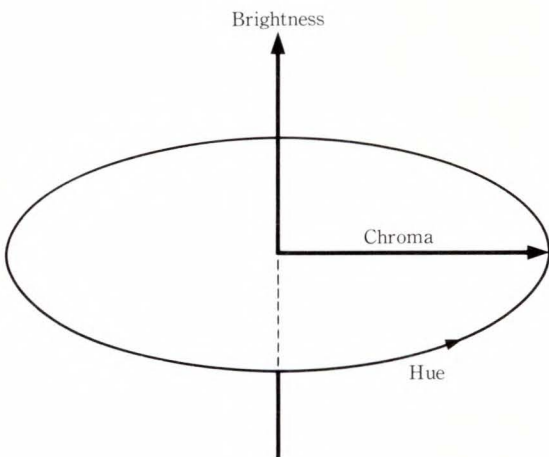


Fig. 19—Three-dimensional color space.

The ΔE is calculated as follows:

$$E = \{(\Delta L^*)^2 + (\Delta a^*)^2 + (\Delta b^*)^2\}^{1/2},$$

$$L^* = 116 (Y/Y_0)^{1/3} - 16,$$

$$a^* = 500 \{(X/X_0)^{1/3} - (Y/Y_0)^{1/3}\},$$

$$b^* = 200 \{(Y/Y_0)^{1/3} - (Z/Z_0)^{1/3}\},$$

where X_0 , Y_0 , and Z_0 are the excitation values for the complete scattering white board under the standard light ($X_0 = 98$, $Y_0 = 100$, and $Z_0 = 118$).

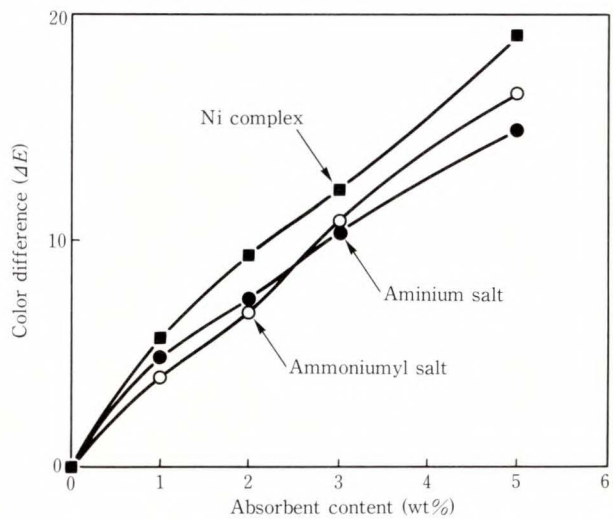


Fig. 20—Affect of near-infrared absorbents on the color of fused red toner.

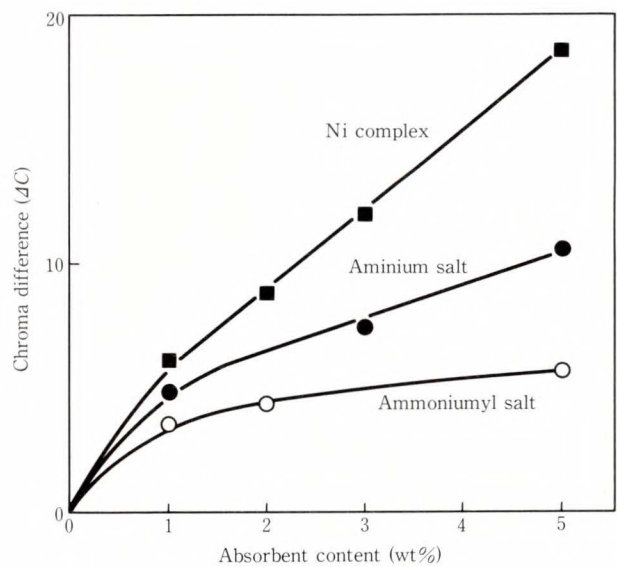


Fig. 21—Affect of near-infrared absorbents on the chroma of fused red toner.

Red toner without an absorbent was fused in an oven and used as the standard color. Then the L^* , a^* , and b^* values of images formed by flash fusing toners with various amounts of one of the three absorbents were measured and the ΔE values were calculated. The results are shown in Fig. 20. For the three absorbents, ΔE increases linearly with the absorbent content. However, the ΔE s of the toner containing ammonium salt and the toner containing aminium salt were low.

The affect of the absorbent content on ΔC , the difference between the toner chroma and the chroma of the standard color, are shown in Fig. 21. For the three absorbents, ΔC increases with the absorbent content. The ammonium salt causes the least increase in ΔC of the three absorbents. Because the absorbent affects the toner color, the absorbent content must be minimized. Using ammonium salt, we can produce not only bright red but also bright blue and green.

3.5 Affect on triboelectric charge

Adding an absorbent affects the triboelectric charging properties. The affect of ammonium salt content and Ni complex content on triboelectric charge is shown in Fig. 22. In the case of the Ni complex, the triboelectric charge is significantly reduced by the addition of only 0.5 wt%. This is probably due to the high conductivity of the Ni complex, which contains metallic components. Triboelectric charge increases with the addition of ammonium salt, which indicates that ammonium salt can also be used as a charge control agent. We therefore compared ammonium salt with polyamine, a common charge control agent. Figure 23 shows the affect of ammonium salt content and polyamine content on triboelectric charge. Although slightly inferior to poly-amine, ammonium salt provides a sufficiently high charge. The high charge provided by ammonium salt is due to the presence of amino groups. We therefore concluded that ammonium salt is the most suitable absorbent for color toners in terms of absorptivity, light resistivity, color characteristics, and triboelectric charge.

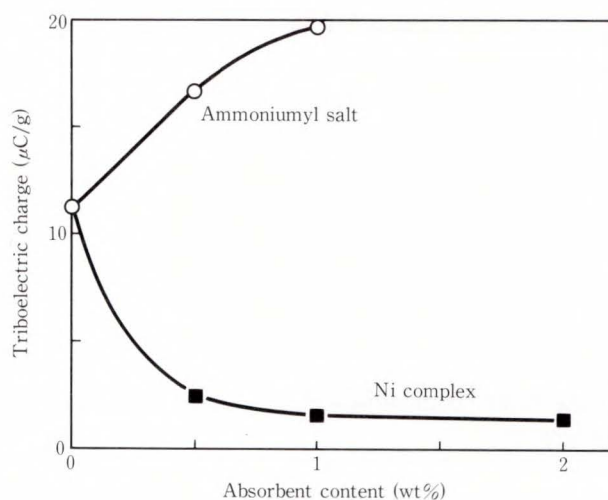


Fig. 22—Affect of ammonium salt content and Ni complex content on triboelectric charge.

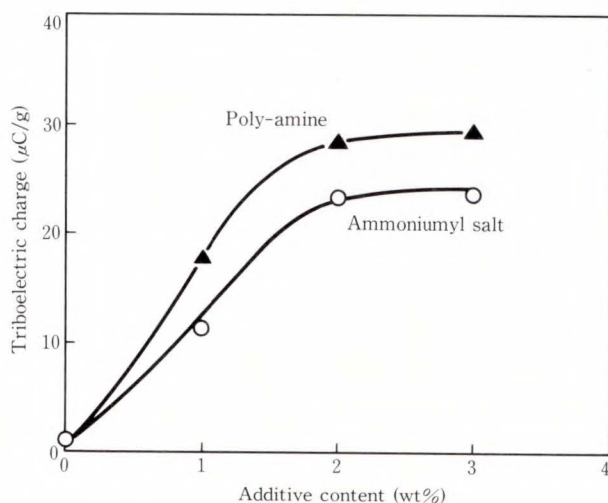


Fig. 23—Affect of ammonium salt content and poly-amine content on triboelectric charge.

4. Toner binder polymer

4.1 Main binder

Most toner binders contain epoxy, polyester, or styrene-acryl resin. Epoxy and polyester resins are suitable for flash fusible toners because they are stable under irradiation by flash light and have a high melt viscosity. We evaluated the fusibility of epoxy and polyester resins. (These resins have a melting point of 100 °C.) Figure 24 shows enlargements of fused images formed using an epoxy-based toner and a

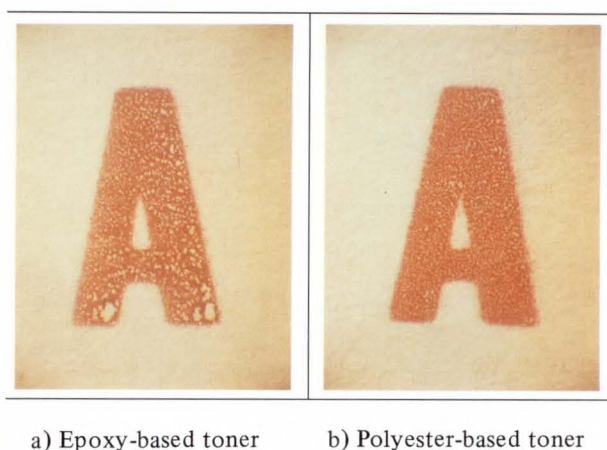


Fig. 24—Enlargements of fused images.

polyester-based toner. Table 1 shows the fusibilities of these toners. The polyester-based toner has a lower porosity and better fusibility than the epoxy-based toner. This is because polyester resin contains many radicals of the ester, carboxyl, and hydroxyl groups and therefore has a chemical affinity with paper. Another reason for the lower porosity is that the hydroxyl group in polyester resin forms a hydrogen bond with the cellulose in the paper. Figure 25 shows the relationship between the temperature and melt viscosity for each toner. A fused image of the polyester-based toner is less porous because polyester has a higher melt viscosity than epoxy resin, even though it has the same melting point.

Therefore, polyester resin is a suitable binder polymer for flash fusible color toners because it has a good fusibility and produces a low-porosity fused image.

4.2 Polymer additive

Polyester-based toner has a good fusibility but does not provide a good triboelectric charge. We therefore examined a polymer additive for the purpose of increasing the triboelectric charge. Styrene-acryl resin is polymerized with a styrene monomer and an acrylic acid ester monomer. A styrene-acryl resin whose acrylic acid ester group is a monomer containing an amino group with a strong electron donative provides a strong positive triboelectric charge. However, because its melt viscosity is high, the

Table 1. Fusibilities of toners

Epoxy-based toner	Polyester-based toner
88 %	94 %

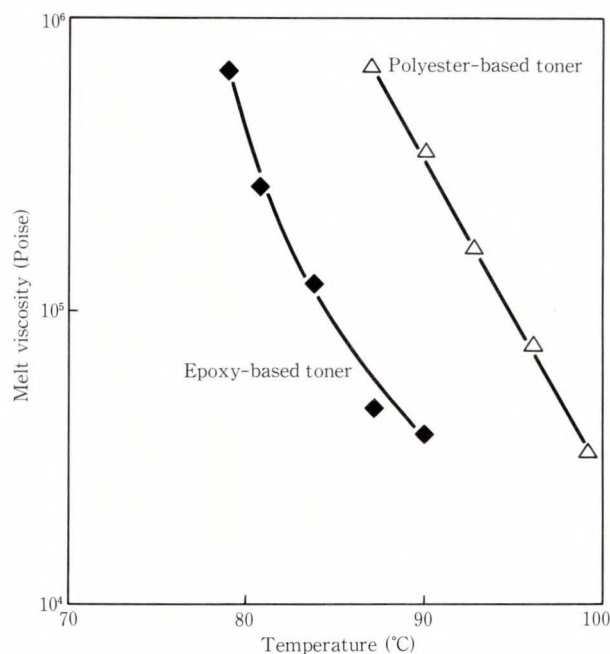


Fig. 25—Relationships between temperature and melt viscosities.

addition of styrene-acryl resin causes a reduction in toner fusibility. Styrene-acryl resin with an amino group (amine-modified styrene-acryl resin) was therefore evaluated for its affect on fusibility and triboelectric charge. Figure 26 shows how the amine-modified styrene-acryl resin content affects the toner fusibility. When the resin content is increased above 20 wt%, the fusibility falls to below 90 percent. The affect of the amine-modified styrene-acryl resin content on the triboelectric charge is shown in Fig. 27. The higher the resin content, the higher the triboelectric charge. The triboelectric charge must be above 15 $\mu\text{C/g}$ to allow for the reduction caused by humidity. The triboelectric charge increases with the styrene-acryl resin content. Figure 27 shows that a resin content of above 17 wt% is required to obtain a triboelectric charge of 15 $\mu\text{C/g}$. Thus, the optimum amino-modified styrene-acryl resin content is

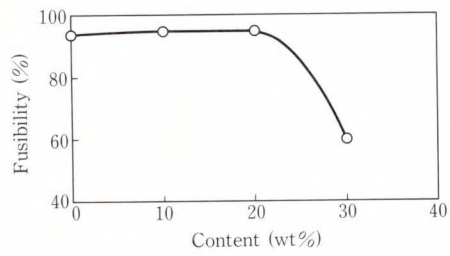


Fig. 26—Affect of amine-modified styrene-acryl resin content on fusibility.

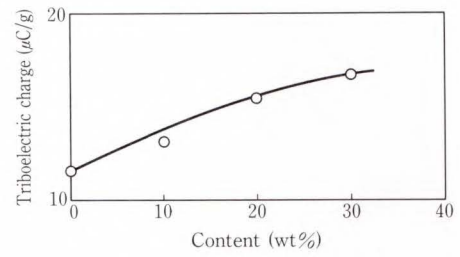
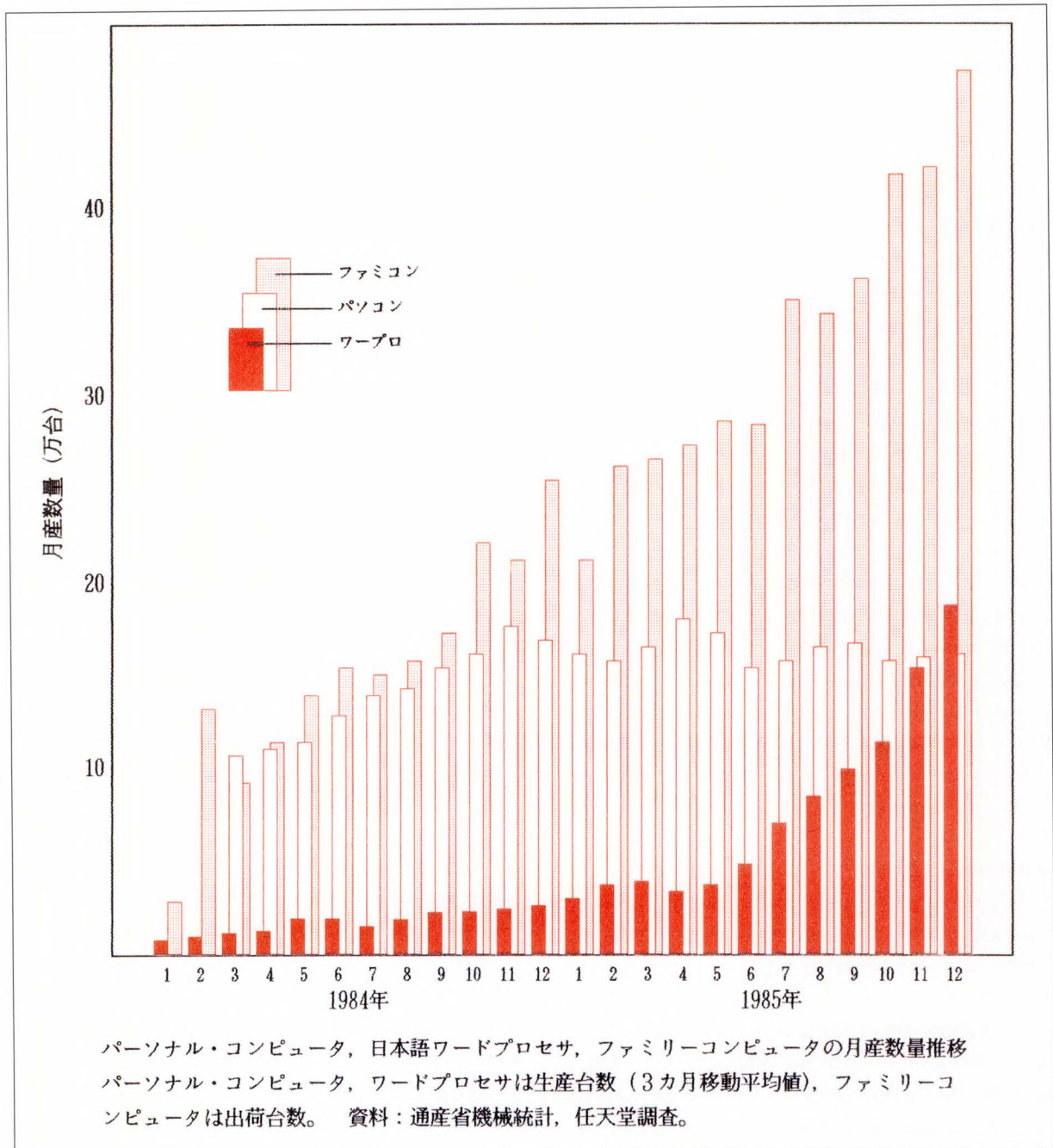


Fig. 27—Affect of amine-modified styrene-acryl resin content on triboelectric charge.



a) Red and black (full size)

Fig. 28—Print sample-1.

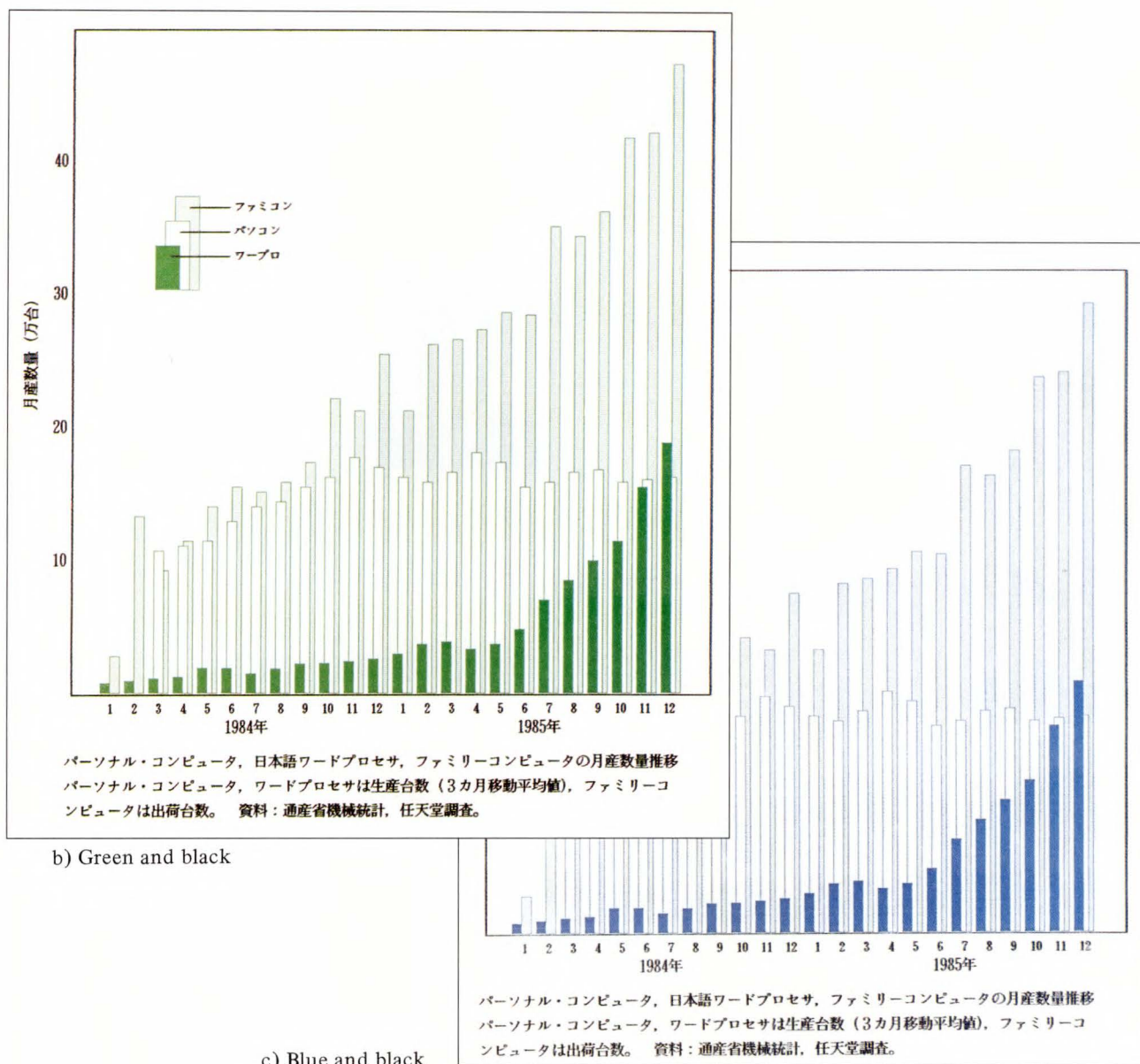


Fig. 28—Print sample-2.

20 wt%. Figure 28 shows two-colored images that were produced using the new color toners.

5. Conclusion

We developed a flash fusible color toner for color laser printers with flash fusing subsystems. The toner contains a near-infrared absorbent which allows the toner to absorb a flash lamp's light energy. The absorbent has good light resistivity and minimal influence on the color characteristics of the toner.

The main toner binder is a polyester resin

that provides good fusibility and low-porosity fused images. The toner also contains an amine-modified styrene-acryl resin additive that improves the triboelectric charging properties. The toner has excellent fixing qualities and color brightness.

This toner makes it possible to produce a high-speed flash-fusing color laser printer.

References

- 1) Narusawa, T., Sawatari, N., and Kuroda, H.: Flash Fusing Technology for Laser Printers – Toner and Fuser —. *FUJITSU Sci. Tech. J.*, **22**, 5, pp. 461-467 (1986).
- 2) Suzuki, S., Tsuda, M., and Mori, M.: A Filter-Alternating Color Scanner. *FUJITSU Sci. Tech. J.*, **25**, 4, pp. 279-286 (1989).



Katsuji Ebisu

Imaging Materials Laboratory
FUJITSU LABORATORIES, ATSUGI
Bachelor of Applied Chemical Eng.
Keio University 1981
Specializing in Imaging Materials



Norio Sawatari

Imaging Materials Laboratory
FUJITSU LABORATORIES, ATSUGI
Bachelor of Science
Hokkaido University 1974
Specializing in Imaging Materials



Takahiro Kashikawa

Imaging Materials Laboratory
FUJITSU LABORATORIES, ATSUGI
Sagamihara Technical High School
1985
Specializing in Imaging Materials

High Sensitive Organic Photoconductor

• Tsuneo Watanuki • Norio Sawatari

(Manuscript received February 3, 1992)

This paper reports on experiments performed to determine the optimal multi-layered organic photoconductor comprising a phthalocyanine pigment and a carrier transport material. Metastable form titanium oxide phthalocyanine, characterized by its unique X-ray diffraction pattern, is sensitive enough to near-infrared light to be used with a compact light source such as a laser diode (LD). The photoconductor device using this pigment in combination with a butadiene derivative exhibits half decay exposure of less than $0.2 \mu\text{J}/\text{cm}^2$, low residual potential, and excellent durability.

1. Introduction

In recent years, low cost, small, easily maintainable xerographic printers have been a great demand for office applications. Accordingly the photoconductor devices using organic materials that are used in such printers have attracted much attention because of their ease of mass production, low cost, and worker/user safety.

Most organic photoconductor (OPC) devices feature a multi-layered structure that consists of a blocking layer, a thin carrier generation layer (CGL) and a much thicker carrier transport layer (CTL) on an aluminum substrate. In this structure, photoconductivity operates as follows^{1),2)}: When a charged OPC is exposed to a light source, the CGL absorbs photons and generates electron-hole pairs. Then, these charge carriers (electrons or holes) travel into the CTL from the CGL, and then to the surface of the OPC. This neutralizes the OPC surface charges. The blocking layer does not contribute to the photoconductivity, but it prevents unnecessary charge injection from the ground substrate. Although xerographic characteristics depend on both the CGL and CTL, spectral properties of the OPC depend only on the CGL.

Commonly, an LD, emitting close to the 800 nm wavelength light, is used as a compact light source in desktop laser printers. Therefore,

carrier generation materials (CGMs) should be highly active at near-infrared wavelengths. We investigated τ -form metal free phthalocyanine ($\tau\text{-H}_2\text{Pc}$)^{3),4)} and some types of titanium oxide phthalocyanine (TiOPc)⁵⁾⁻⁷⁾, both of which are well-known near-infrared sensitive CGMs. We also studied combinations of CGMs and carrier transport materials (CTMs) to obtain an optimized OPC device. Finally, the optimized OPC device was tested on a desktop xerographic printer.

2. Experimental

2.1 Materials

1) Carrier generation materials

We used commercially available $\tau\text{-H}_2\text{Pc}$ pigment obtained from Toyo Ink Mfg. Co. Ltd., and prepared three types of TiOPc pigment from the crude product purchased from Orient Chem. Inc. The chemical structure of TiOPc and the preparation procedure of the three pigment polymorphs are shown in Fig. 1. To produce the TiOPc pigment polymorphs, a mixture of arbitrary amounts of the crude TiOPc and 10-times amount of sulfuric acid was stirred for one hour at a temperature below 5 °C. This was then gradually poured into 200-times amount of water and stirred for one hour at a temperature below 5 °C. After decantation and filtration, the

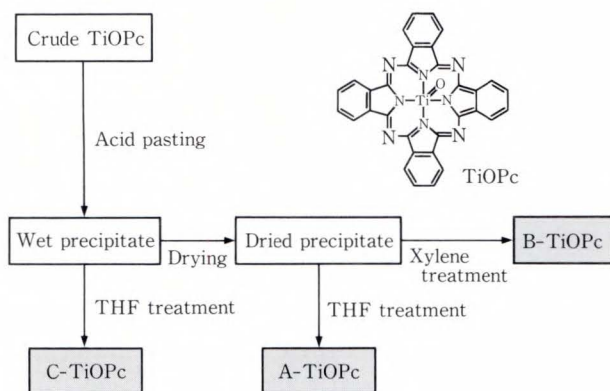


Fig. 1—TiOPc chemical structure and polymorph preparation procedure.

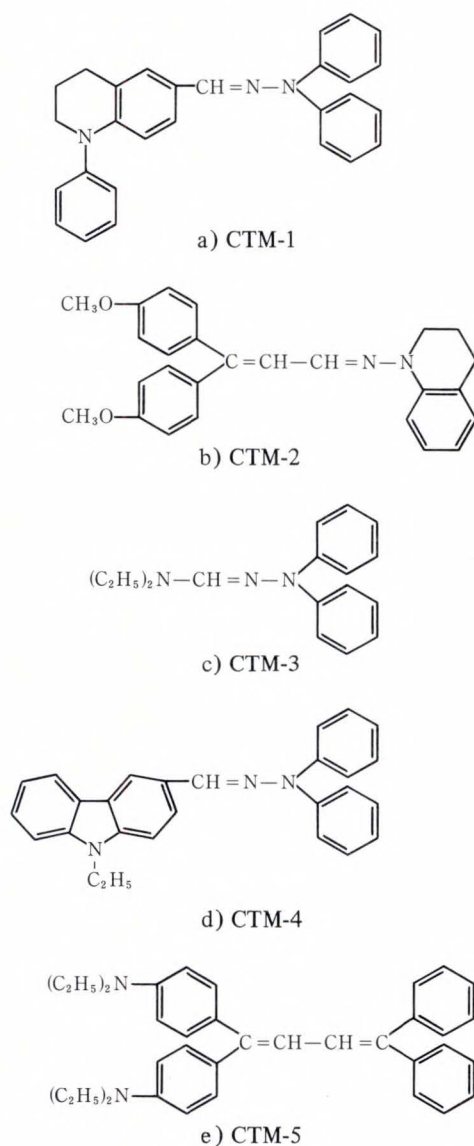


Fig. 2—Chemical structure of carrier transport materials (CTMs).

residue was washed with water until a filtrate of pH 6 was produced. Part of this wet precipitate was dried. The other part was added to 200-fold amount of solvent tetrahydrofuran (THF) and dispersed for about three hours. After filtration, the residue was washed with THF and dried at 110 °C for one hour, producing C-TiOPc. On the other hand, A- and B-TiOPc were obtained by treating the dried precipitate with solvents THF and xylene, respectively. A THF treatment of the dried precipitate produced A-TiOPc, while a xylene treatment produced B-TiOPc. These polymorphs were confirmed by X-ray diffraction testing.

2) Carrier transport materials

The chemical structure of the CTMs used is shown in Fig. 2. Three types of CTMs, 1-phenyl-1,2,3,4-tetrahydroquinoline-6-carboxaldehyde-1'1'-diphenylhydrazone (CTM-1), 3,3-bis(*p*-methoxyphenyl)acrolein-1'-amino-1'2'3'4'-tetrahydroquinolinehydrazone (CTM-2) and *p*-diethylaminophenyl (diphenyl) butadiene (CTM-5) were obtained commercially from ANAN Co., Ltd. and used without further purification. Two types of hydrazone derivatives, *p*-diethylaminobenzaldehyde-diphenylhydrazone (CTM-3) and 9-ethyl-3-carbazolecarbaldehyde-diphenylhydrazone (CTM-4) were synthesized⁸⁾. These CTMs were yellow crystals, nearly transparent to near-infrared light. (All CTMs transported holes, making our OPC devices negatively charged.)

2.2 Preparation of samples

Three types of OPC were prepared. The first type was a sandwich cell, for measuring CTM drift-mobility. OPC was coated on a transparent indium tin oxide (ITO)-deposited glass plate and a gold electrode was vacuum-evaporated on top. The second type was a convenient film-type device, for measuring ordinal xerographic properties. OPC was coated on an aluminum-electrode-evaporated polyester film. For the last type that is suitable for printer applications, OPC was coated on an aluminum cylinder with a diameter of 40 mm.

These OPCs all had the same structure, consisting of a blocking layer, a CGL and a

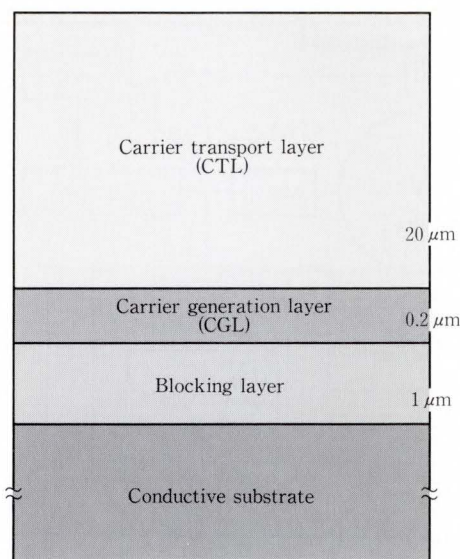


Fig. 3—Organic photoconductor (OPC) structure.

CTL in the order shown in Fig. 3. The blocking layer was prepared from an acetone solution of cyanoethylated pullulan resin (Shin-Etsu Chemical Co., Ltd.: CR-S) and 1 wt% polyisocyanate (Daicel-Huls Ltd.: B1370). The solution was coated on the substrate by dipping to obtain a film 1 μm thick. The CGL consisted of 50 wt% CGM dispersed in polyvinylbutyral resin (Denki Kagaku Kogyo K.K.: #5000A). The pigment dispersion was carried out in a sand grinder with organic solvent, polymer and 1 mm-diameter glass shots. The CGL was coated on the blocking layer by dipping and the dry CGL was about 0.2 μm thick. THF was the solvent for $\tau\text{-H}_2\text{Pc}$ and 1, 1, 2-trichloroethane was the solvent for TiOPcs. Other organic solvents gave less stable dispersion. The CTM and polycarbonate resin (Mitsubishi Gas Chemical Co., Inc.: Z200) were dissolved in a mixture of dichloromethane and 1, 2-dichloroethane (1:1 by volume), and the solution was coated on the CGL using a doctor blade or dipping. The ratio of the CTM to the binder resin was 50 wt%, except for that of the CTM-5 to the binder resin, which was from 10 wt% to 50 wt%. The dry CTL was approximately 20 μm thick.

2.3 Measurement technique

X-ray powder diffraction patterns were

measured using an X-ray powder diffractometer (Mac Science Ltd.: MXP03VA) that produces $\text{CuK}\alpha$ radiation.

Shapes of individual phthalocyanine particles were observed using a scanning electron microscope (JEOL Ltd.: JSM-6400).

Visible absorption spectra measurements ranging from 1 000 nm to 500 nm of cast films, $\tau\text{-H}_2\text{Pc}$ and TiOPc particles dispersed in the resin were performed using a spectrophotometer (Hitachi, Ltd.: 330).

The ionization potential of the CGMs and the CTMs were estimated conventionally using a surface analyzer (Riken Keiki Co., Ltd.: AC-1)⁹⁾.

The hole drift-mobility of the CTLs and its field dependence were measured using the well-known time-of-flight (TOF) technique¹⁰⁾⁻¹²⁾. A schematic diagram of the TOF measurement setup is shown in Fig. 4. The strength of the LD light (wavelength: 780 nm) which excited the CGM was kept low enough that the transient photocurrent would not be affected by space charges.

Xerographic properties were measured using both a photoconductor analysis setup (Gentec Co., Ltd.: Cynthia-30), the schematic diagram of which is shown in Fig. 4, and a prototype printer. *Statis* properties, which are conventional xerographic characteristics, were measured by the first system as follows: A corona-charged OPC was placed in the dark for one second, and then continuously exposed to weak light from a xenon lamp with monochromator, while its surface potential was recorded. The exposing light, except for the spectral measurement light, had a wavelength of 780 nm, and an intensity of 2 $\mu\text{W}/\text{cm}^2$. Sensitivity (half decay exposure $E_{1/2}$), residual potential V_r , and dark decay were calculated from the dark decay curve and the successive photo-induced discharge curve.

Cylinder-type OPC drums were tested using a printer (Fujitsu: prototype machine of RX7100). A light emitting diode (LED) array emitting 660 nm wavelength light was used as the writing light source. Its light energy could be discontinuously altered from 0 $\mu\text{J}/\text{cm}^2$ to 4 $\mu\text{J}/\text{cm}^2$ to measure *dynamic* photo-induced

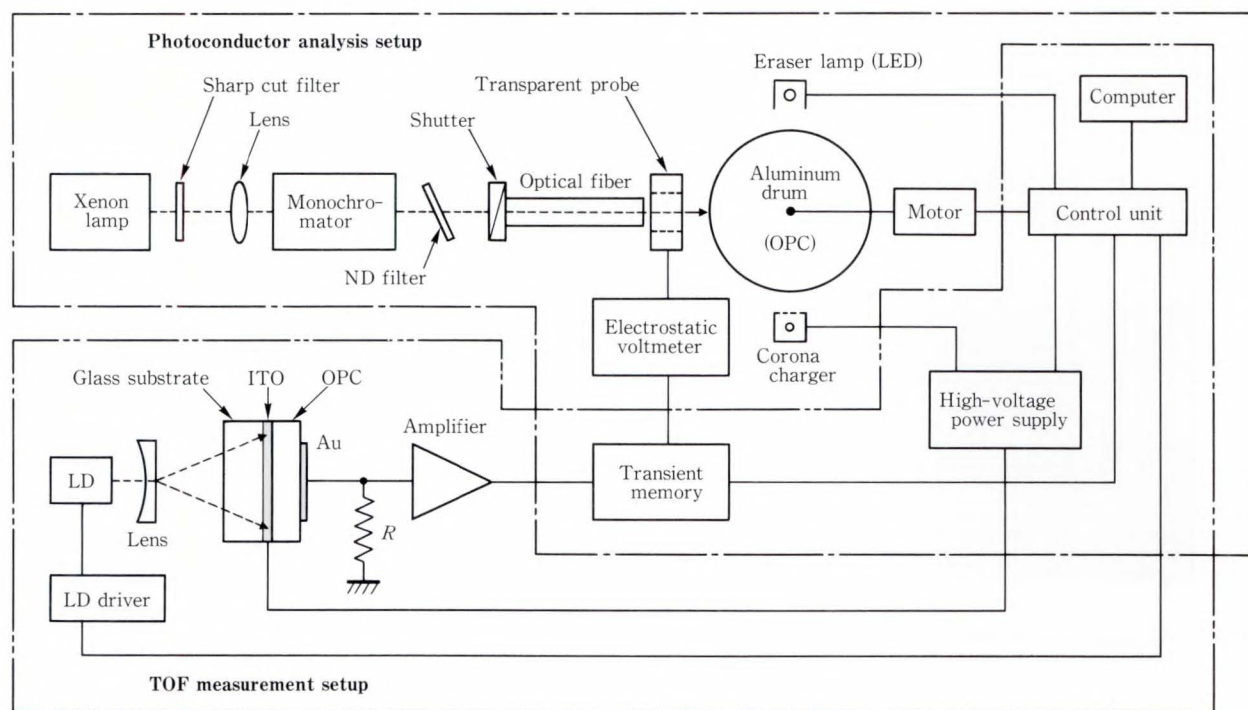


Fig. 4—Photoreceptor analysis and TOF measurement setups.

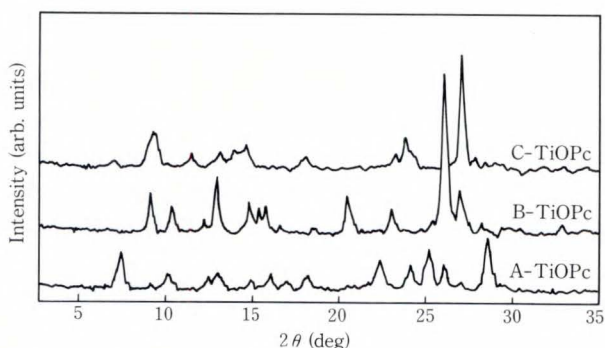


Fig. 5—TiOPc X-ray diffraction patterns.

discharge properties, which is the relationship between light energy and surface potential. Print tests were carried out using mono-component magnetic toner with $1.25 \mu\text{J}/\text{cm}^2$ light energy, and then the optimized OPC drum was tested in continuous printing. Image quality was based on the optical density of solid images and ΔY given by subtracting the optical reflection of the printed background from that of nonprinted paper.

3. Results and discussion

3.1 Material properties

The X-ray diffraction patterns for TiOPcs are shown in Fig. 5. The differences in diffraction patterns for the polymorphs indicate that the different solvent treatments promote different co-orientation of TiOPc molecules. The angles of diffraction (2θ) characteristic for A-TiOPc are 7.5° , 22.4° , 25.2° , 26.1° , and 28.6° . For B-TiOPc, they are 9.3° , 13.2° , 20.7° , 26.3° , and 27.1° , and for C-TiOPc, they are 9.4° , 9.7° , 14.9° , 24.0° , and 27.2° . The polymorphs of TiOPcs have been well investigated by Hiller et al⁵⁾. They found two main polymorphs of TiOPcs. One, called Phase I, is crystallized as a monoclinic. The other called Phase II is crystallized as a triclinic. The A-TiOPc corresponds to Phase II and the B-TiOPc corresponds to Phase I. The C-TiOPc is a metastable polymorph which could change to that of B-TiOPc after being heated above 260°C . The exact nature of this metastable polymorph has not been clarified yet.

Scanning electron microscope (SEM) images are shown in Fig. 6. A- and C-TiOPc particles are

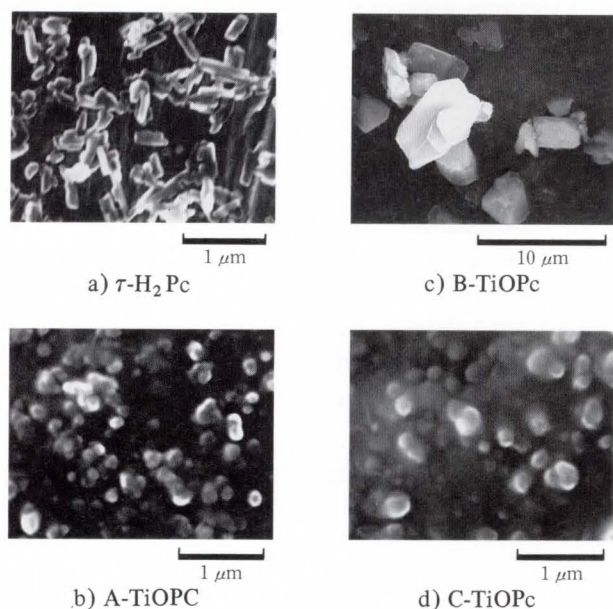


Fig. 6—CGM SEM images.

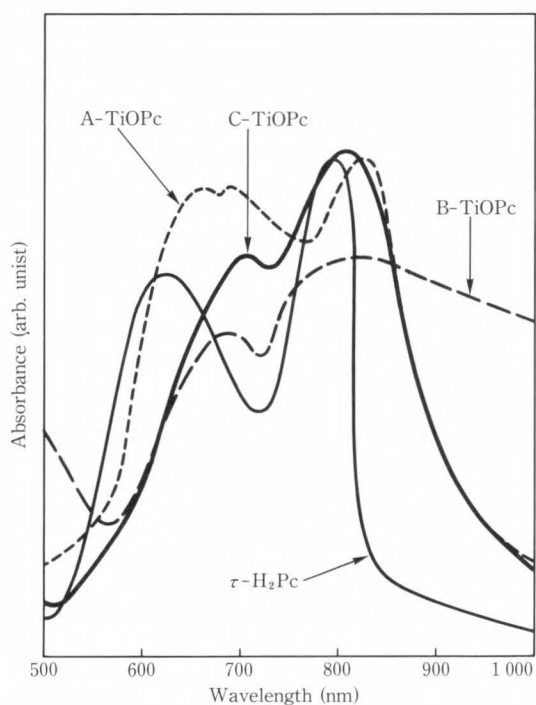


Fig. 7—CGM visible absorption spectra.

almost spherical with a diameter of about $0.2 \mu\text{m}$. In contrast, B-TiOPc particles are well crystallized, tetragonal-rod crystals with a diameter of above $5 \mu\text{m}$. This indicates that THF

Table 1. Ionization potential

CTM	I_p (eV)	CGM	I_p (eV)
CTM-1	5.02	$\tau\text{-H}_2\text{Pc}$	4.69
CTM-2	5.28	A-TiOPc	5.21
CTM-3	5.03	B-TiOPc	5.32
CTM-4	5.22	C-TiOPc	4.95
CTM-5	4.90		

treatments of A- and C-TiOPc accelerate dispersion of aggregated particles as well as individual co-orientation. A xylene treatment, in contrast, promotes the growth of the crystal as well as the co-orientation. Since a CGL is extremely thin and an increased surface area enhances the rate of photogeneration, A- and C-TiOPc are better suited to our needs. $\tau\text{-H}_2\text{Pc}$ particles were rod-line crystallized, but much smaller than B-TiOPc particles, with a long axis of about $0.5 \mu\text{m}$ and a short axis of about $0.2 \mu\text{m}$. They are also suitable for use as a CGM.

Visible absorption spectra of cast films are shown in Fig. 7. The absorption spectra of TiOPcs have a maximum at 810 nm which is red-shifted from the maximum absorption wavelength of $\tau\text{-H}_2\text{Pc}$. In our intended application, a CGM needs to exhibit high absorbance in the near-infrared region. In this respect, TiOPcs offer improved performance over $\tau\text{-H}_2\text{Pc}$.

The ionization potential (I_p) of the CGMs and these of the CTMs are shown in Table 1. CGM I_p increases from $\tau\text{-H}_2\text{Pc}$ to B-TiOPc and C-TiOPc has the smallest I_p among the TiOPcs. Of the CTMs, the butadiene derivative has the smallest I_p , even smaller than that of the TiOPcs. Hydrazone derivatives, CTM-1, CTM-3, CTM-4, and CTM-2, in that order, exhibit increasing I_p . We will discuss the effects of these differing I_p s later.

One of the most important CTM specifications is drift mobility μ . It should be as large as possible to provide the OPC with a quick response required in high-speed printing systems. Figure 8 shows the field dependence of μ . Only $\tau\text{-H}_2\text{Pc}$ was used in this measurement because CGMs have only a small affect the hole

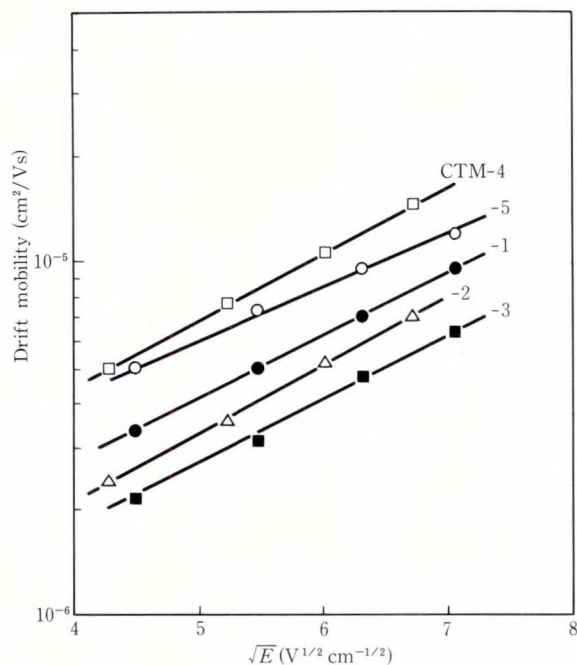


Fig. 8—Field dependence on drift mobility.

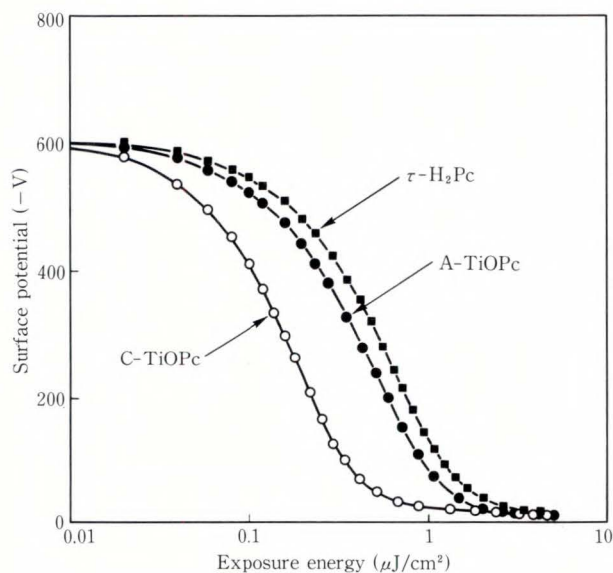


Fig. 9—Photo-induced discharge curve.

transport of the OPC, and generally produce the same results. All the CTMs conventionally exhibit the Poole-Frenkel field dependence of μ , i.e. $\log \mu$ is directly proportional to the square root of electric field $E^{1/2}$, and exhibit equally

Table 2. Xerographic characteristics (static)

Property CGM	$E_{1/2}$ ($\mu\text{J}/\text{cm}^2$)	V_r (V)	Dark decay* (V)
$\tau\text{-H}_2\text{Pc}$	0.52	-11	41
A-TiOPc	0.4	-10	17
C-TiOPc	0.16	-18	11

*: After one second

good hole mobility, although CTM-5 and CTM-4 have a slightly larger μ .

3.2 Xerographic characteristics

The *static* properties of OPCs that incorporate the three types of CGMs, and CTM-5 are shown in Fig. 9 and Table 2, where initial surface potential was approximately -600 V. C-TiOPc exhibits excellent photo-induced discharge properties, indicating high quantum efficiency (the multiplied result of carrier generation and carrier injection efficiency). This superior OPC device has a half decay exposure of less than $0.2 \mu\text{J}/\text{cm}^2$, low V_r , and low dark decay. A-TiOPc and $\tau\text{-H}_2\text{Pc}$ are fairly sensitive, although $\tau\text{-H}_2\text{Pc}$ exhibits fairly large dark decay. B-TiOPc poorly photoconductive and thus little studied, because its polymorph seemed too large for it to be applied as a CGM (see Fig. 6). Results for other combinations are shown in Figs. 10 and 11. The combination of C-TiOPc and CTM-5 gave the best results for our needs. Sensitivity and dark decay depend little on CTM I_p for the same CGM. In contrast, V_r becomes larger in proportion to CTM I_p , particularly notable for $\tau\text{-H}_2\text{Pc}$. Carrier generation efficiency is clearly equivalent for the same CGL and all the CTLs exhibit about the same drift mobility, suggesting that the I_p dependence of V_r is due to differences in CGL-to-CTL hole injection efficiency. Figure 12 shows the energy diagram of a CGM and a CTM¹⁾. When the CGM absorbs a photon, an electron is excited from the highest occupied molecular orbital (HOMO) to the lowest unoccupied molecular orbital (LUMO) and the remaining hole is injected into the CTM. The lower the CTM I_p is, the more easily holes are injected. A barrier occurs be-

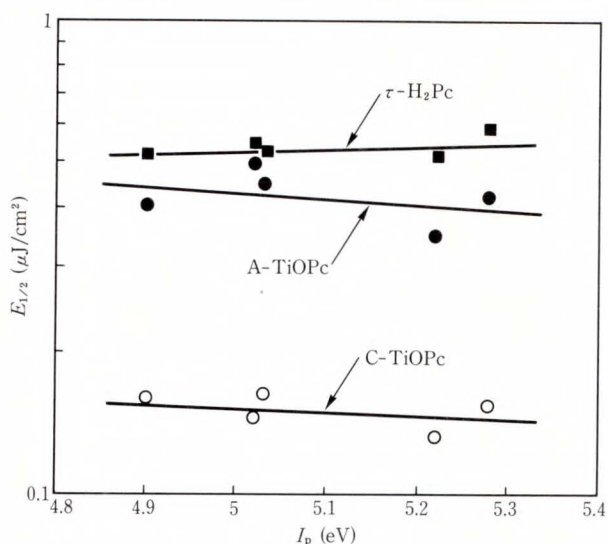


Fig. 10— I_p dependence on half-decay exposure.

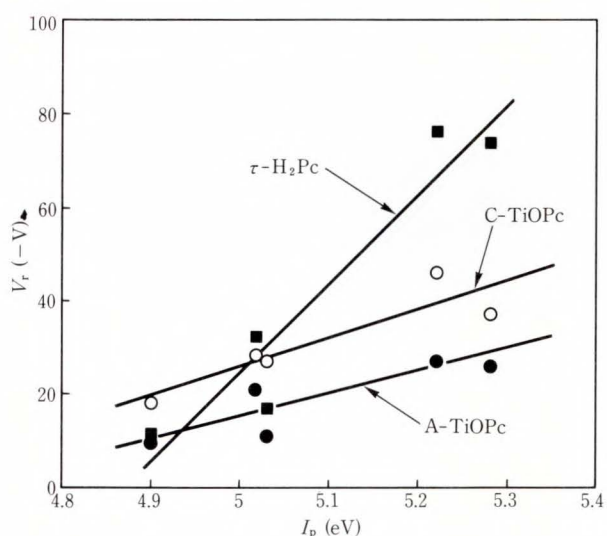


Fig. 11— I_p dependence on residual potential.

tween a CGM and a CTM if the CGM has a lower I_p than that of the CTM. Under a weak electric field, the barrier may prevent a hole from crossing easily, in cases of extreme I_p gap, such as the combination of $\tau\text{-H}_2\text{Pc}$ and CTM-2. On the other hand, under a much higher electric field, the intrinsic barrier seems less rigid because of the monotonous behavior of $E_{1/2}$. This suggests that under a weak electric field, photo-induced

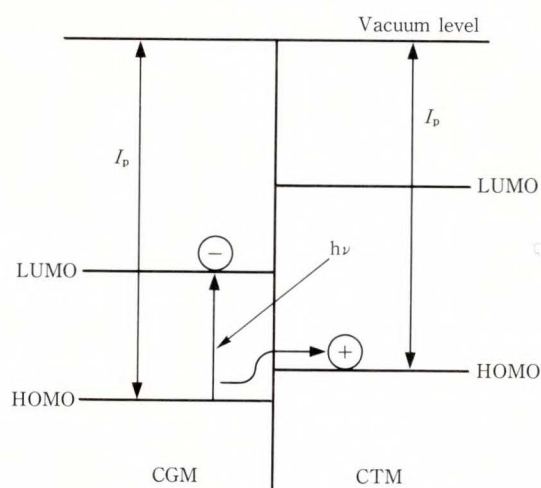


Fig. 12—Energy diagram of a CGM and a CTM.

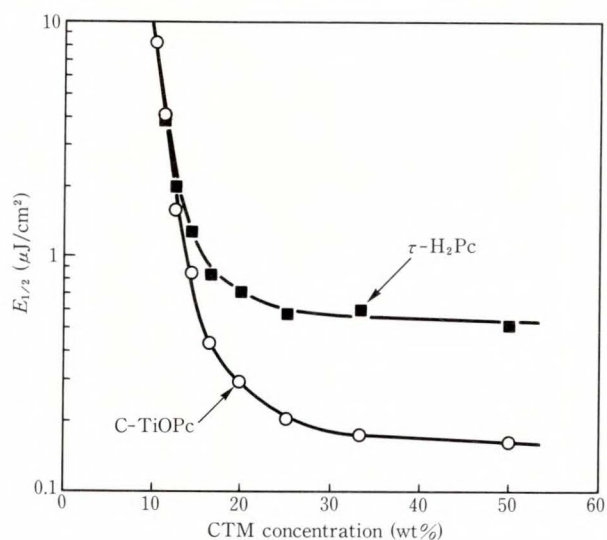


Fig. 13—CTM concentration and half-decay exposure.

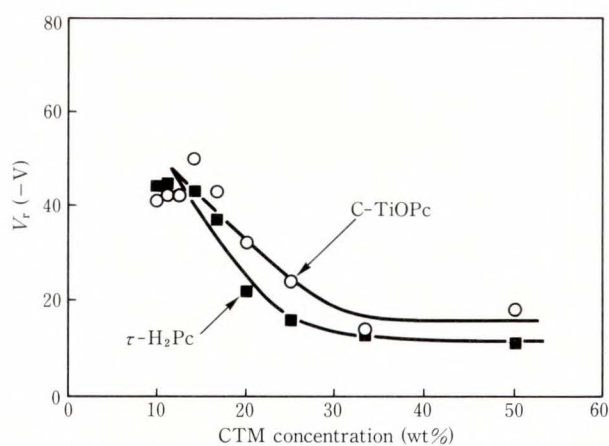


Fig. 14—CTM concentration and residual potential.

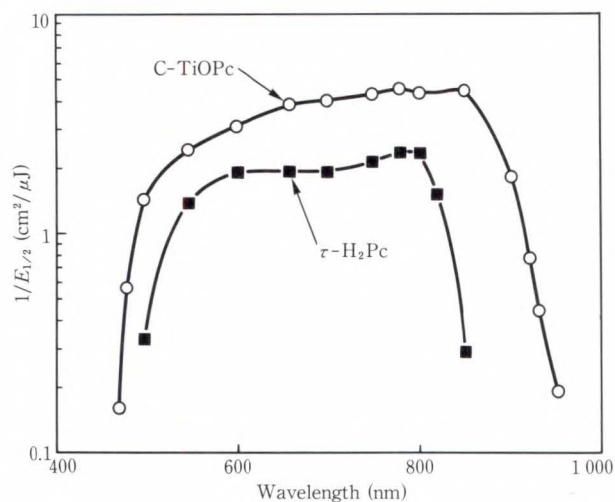


Fig. 15—Spectral sensitivity of OPCs.

discharge characteristics are determined mainly by hole injection, although, under a high electric field, carrier generation efficiency is the controlling factor.

We also studied that optimized CTM-5 has excellent drift mobility and low I_p . The concentration of the CTM makes a direct contribution toward improved xerographic properties as shown in Figs. 13 and 14. The concentration does not drastically change $E_{1/2}$ or V_r from 25 wt% to 50 wt% but, at concentrations below 20 wt%, the lower the concentration, the worse the photoconductivity. This is due to decreased drift mobility and hole injection at the contact between the CGM and the CTM. For improved mechanical durability, the concentration of small molecules should be low. The optimal ratio of CTM-5 to the binder resin was determined to be 25 wt% in later measurements of spectral sensitivity, dynamic properties and durability.

Figure 15 shows the spectral sensitivity of OPC using C-TiOPc and τ -H₂Pc. The spectral sensitivity curve is almost flat from 600 nm to 850 nm. Thus LDs, LEDs, He-Ne lasers, and electroluminescence (EL) light sources are suitable for use with our highly sensitive OPC device.

Figure 16 shows the dynamic xerographic properties of cylindrical OPC drums made from

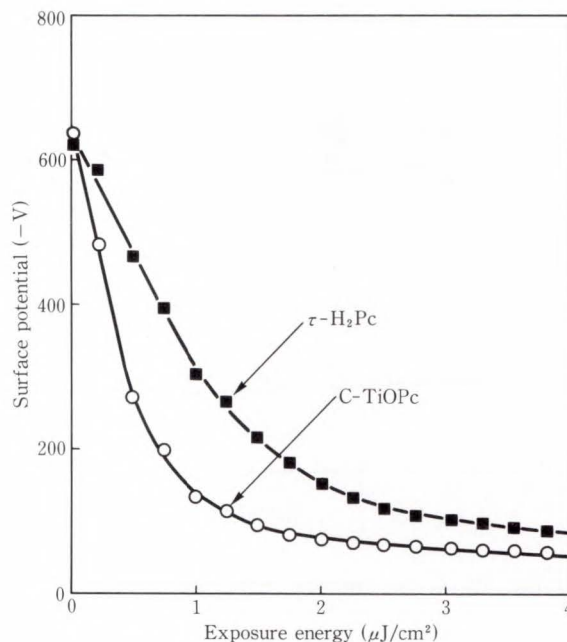


Fig. 16—Dynamic properties of OPCs.

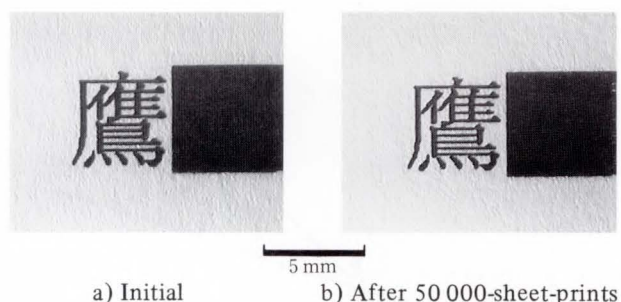


Fig. 17—Print samples.

CTM-5 and one of two types of CGM. *Static* and *dynamic* properties differ little, although the static residual potential is slightly lower than the dynamic potential when the OPC is exposed to high energy light. Such a small difference may be due to reciprocity law failure. The OPC device made from C-TiOPc and CTM-5 is highly sensitive and should be able to produce a high contrast electrostatic latent image. This was proved in an application to an LED printer.

3.3 Printer applications

The print sample in Fig. 17 shows good quality, high optical density and low fog.

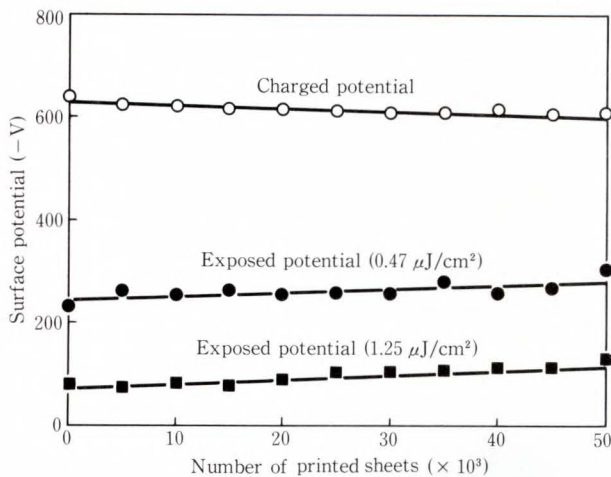
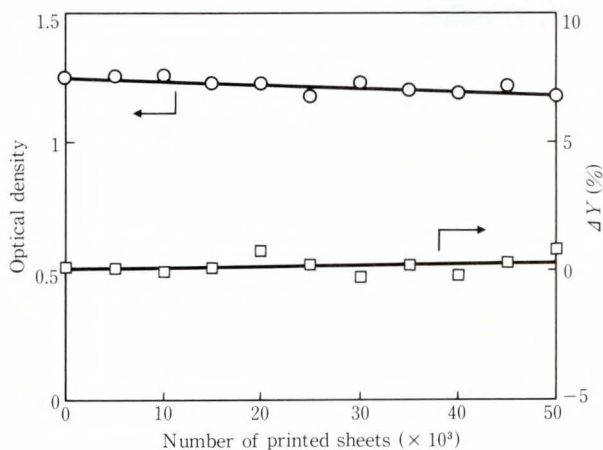


Fig. 18—Surface potential in the durability test.

Fig. 19—Optical density and ΔY in the durability test.

Figures 18 and 19 show the results of a durability test involving up to 50 000 prints. Little residual potential accumulated, and neither sensitivity nor charge acceptance was greatly reduced. Moreover, image quality remained stable as shown in Figs. 17 and 19. These demonstrate the OPC's durability against light-induced fatigue, ozone caused by the corona charger, and mechanical damage.

4. Conclusion

We studied phthalocyanine pigments and hole transport materials to obtain a highly sensitive organic photoconductor. Testing the optimized OPC device using an LED printer, the

following was determined:

- 1) The metastable TiOPc pigment characterized by its unique X-ray diffraction pattern can be used to fabricate a highly sensitive OPC device whose half decay exposure is almost $0.2 \mu\text{J}/\text{cm}^2$ for light in the 600-850 nm wavelength region.
- 2) CTM ionization potential I_p makes little difference to half decay exposure, although residual potential becomes proportionally larger.
- 3) The butadiene derivative is the best material for a CTM because of its high drift-mobility and low I_p , and is effective even in a low concentration.
- 4) An OPC device comprising the metastable TiOPc pigment and the butadiene derivative provides optimum image quality and durability.

References

- 1) Otsuka, S.: Organic Photoconductor — Its Electrophotographic Properties and Basic Physical Processes. (in Japanese), *Electrophoto.*, **27**, 4, pp. 588-594 (1988).
- 2) Ohta, K.: Organic Photoreceptor for Electrophotography. (in Japanese), *Jitsumu Hyomen Gijutsu*, **34**, 1, pp. 11-16 (1987).
- 3) Kakuta, A., Takano, S., Enokida, T., Shibuya, I., and Mori, Y.: New Organic Photoconductor for Diode Laser Use. (in Japanese), *Electrophoto.*, **24**, 2, pp. 102-107 (1985).
- 4) Enokida, T., and Ehashi, S.: Direct Synthesis of τ -Form Metal-Free Phthalocyanine from Phthalodinitrile by Seeding Procedure. *Chem. Lett.*, pp. 179-182 (1988).
- 5) Hiller, W., Strähle, J., Kobel, W., and Hanack, M.: Polymorphie, Leitfähigkeit und Kristallstrukturen von Oxophthalocyaninato-titan (4). *Z. Krist.*, **159**, pp. 173-183 (1982).
- 6) Enokida, T., Kurata, R., Seta, T., and Katsura, H.: Organic Photoreceptors Incorporating a New Polymorph of Oxotitanium Phthalocyanine Compounds. (in Japanese), *Electrophoto.*, **27**, 4, pp. 533-538 (1988).
- 7) Ohaku, K., Nakano, H., Kawara, T., Yokota, S., Takenouchi, O., and Aizawa, M.: Titanylphthalocyanine Photoreceptor Devices for Solid-State Diode Laser Beam Printers. (in Japanese), *Electrophoto.*, **25**, 3, pp. 258-263 (1986).

- 8) Sandler, R.S., and Karo, W.: "14-3. Hydrazones". Organic Functional Group Preparations, 2nd ed., New York, Academic Press, 1983, pp. 455-457.
- 9) Miyamoto, E., Yamaguchi, Y., and Yokoyama, M.: Ionization Potential of Organic Pigment Film by Atmospheric Photoelectron Emission Analysis. (in Japanese), *Electrophoto.*, **28**, 4, pp. 364-370 (1989).
- 10) Pinsler, H.: Time-of-Flight Transient Signals of Two-Layer Electrophotographic Photoreceptors. *J. Imaging Sci.*, **32**, 1, pp. 5-11 (1988).
- 11) Gill, D.W.: Drift Mobilities in Amorphous Charge-transfer Complexes of Trinitrofluorenone and Poly-n-vinylcarbazole. *J. Appl. Phys.*, **43**, 12, pp. 5033-5040 (1972).
- 12) Sher, H., and Montroll, W.E.: Anomalous Transit-time Dispersion in Amorphous Solids. *Phys. Rev.*, **B12**, 6, pp. 2455-2477 (1975).



Tsuneo Watanuki

Imaging Materials Laboratory
FUJITSU LABORATORIES, ATSUGI
Bachelor of Science
Tohoku University 1981
Master of Science
Tohoku University 1983
Specializing in Imaging Materials



Norio Sawatari

Imaging Materials Laboratory
FUJITSU LABORATORIES, ATSUGI
Bachelor of Science
Hokkaido University 1974
Specializing in Imaging Materials

High Contrast SSFLC Display Utilizing Naphthalene Base Liquid Crystal Materials and Conductive Orientation Films

• Akihiro Mochizuki • Katsusada Motoyoshi

(Manuscript received February 3, 1992)

This paper describes the electrical properties of a surface stabilized ferroelectric liquid crystal (SSFLC) display provided by an almost ideal bookshelf layer structure. The bookshelf layer structure is produced by using ordinary rubbed polymer film cells together with a special liquid crystal containing a naphthalene ring. Both the layer structure of the naphthalene base FLCs and their electrooptic switching are discussed. Some polarization switching phenomena in conjunction with the conductivity of the orientation layer are also shown. A multiplexed FLC prototype was built with a 640×201 pixel display, and this gave a 40 : 1 contrast ratio and 40 percent transmittance.

1. Introduction

A surface stabilized ferroelectric liquid crystal (SSFLC) display has great potential for high performance information displays, offering high information content, high resolution, a wide viewing angle, high contrast ratio, and a fast response time¹⁾. Although the SSFLC display has many attractive characteristics, a practical SSFLC display has yet to be built, and there are still several difficult problems to overcome before a commercial SSFLC display is possible. We have attempted to solve two of the major problems; firstly, the uniform molecular alignment of a bookshelf layer structure, and secondly, elimination of the depolarization field.

A quasi-bookshelf layer structure has been produced before in a rubbed SSFLC cell after the application of a low-frequency electric field²⁾. Oblique evaporation can prevent the formation of a chevron structure, and this leaves a uniformly tilted layer structure³⁾ without zigzag defects. The quasi-bookshelf structure reported by Rieger et al.⁴⁾ and Escher et al.⁵⁾ was created by using a special liquid crystal and

alignment material. However, we have created a bookshelf structure that forms spontaneously when the ambient temperature is decreased using naphthalene base liquid crystals.

The phase sequence of ferroelectric liquid crystals (FLCs) is known to govern the molecular alignment of an SSFLC display. Rubbed polymer orientation films are the most likely material for mass production, and an FLC with the most common phase sequence: isotropic (I)-chiralnematic (N*)-smectic A (S_A)-chiralsmectic C (S_C^*) is generally believed to provide a clean molecular alignment. We previously reported, however, that an FLC with a phase sequence: I- S_A - S_C^* and with a wide S_A phase temperature range can provide a better molecular alignment^{6),7)}. Here we describe the uniform molecular alignment of a rubbed polymer film panel which uses a special FLC material. This FLC contains a naphthalene ring in its molecular structure, has a phase sequence I- S_A - S_C , and has a wide temperature range of the S_A phase. In this paper, we analyze the layer structure by X-ray diffraction experiments and from the

molecular structure, verify the bookshelf structure. The relationship between the electrooptical properties such as the response time, memory capability and the layer structure is also discussed.

The second difficult problem of eliminating the depolarization field was solved by using an electrically conductive liquid crystal molecular alignment film⁸⁾ This film discharges the charges which accumulate in the interfacial regions and form the depolarization fields, which degrade the memory capability. The SSFLC display also has good anti-stress properties; the uniform molecular alignment of the display provides a high contrast ratio of 40 : 1 and a high transmittance of 40 percent including two polarizers under a multiplexing drive mode.

2. Smectic layer structure

2.1 X-ray diffraction profiles

The X-ray diffraction profiles of the naphthalene base FLC mixture cells indicate that the naphthalene base mixture provides both a quasi-bookshelf structure (see Fig. 1) and a bookshelf structure (see Fig. 2). The mixture for Fig. 1 contains 80 wt% naphthalene liquid crystals. The main component of this mixture is shown in Fig. 3. The mixture for Fig. 2 contains phenylpyrimidine liquid crystals and naphthalene liquid crystals which have a chiralnematic phase. The layer structure of Fig. 1 is somewhat different from that of the usual FLCs previously reported⁹⁾. As shown in Fig. 4, the layer tilt angle increases near the S_A to S_C^* transition temperature, then decreases with decreasing temperature. This temperature dependence of the layer tilt angle does not correspond with the temperature dependence of the molecular tilt angle shown in Fig. 5. This non-correspondence is to be expected when the layer spacing change is not caused only by molecular tilt from the layer normal.

As shown in Fig. 2, the naphthalene base mixture cell has a bookshelf structure. The smectic layer is almost perpendicular to the substrates. The bookshelf layer structure is maintained just below 40 °C during cooling. During heating, however, the bookshelf layer

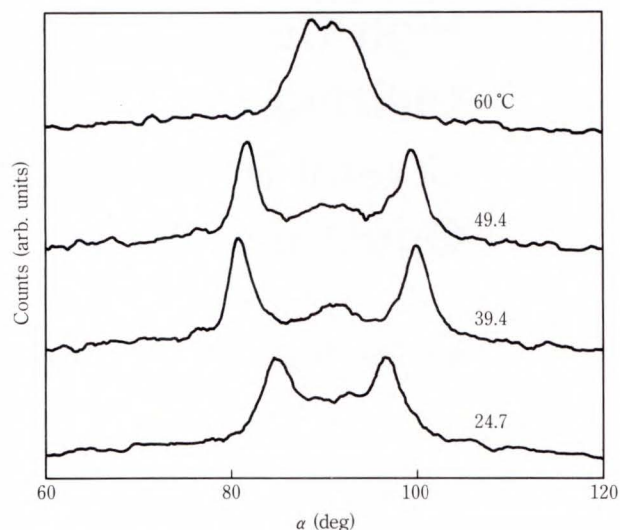


Fig. 1—X-ray diffraction profile of the Naphthalene base mixture 1. α is the layer leaning angle.

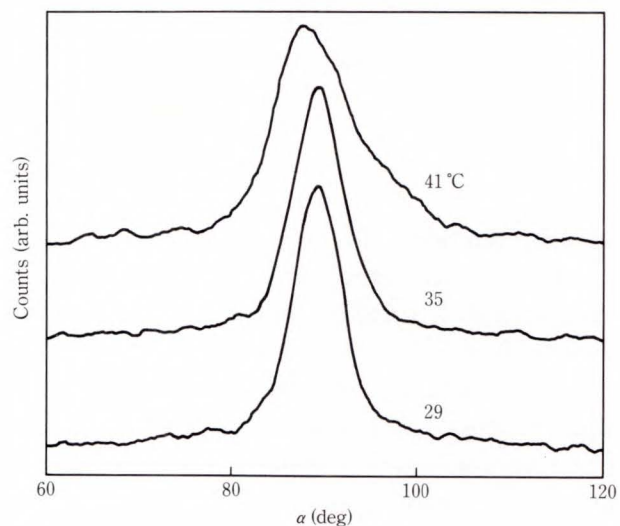


Fig. 2—X-ray diffraction profile of the Naphthalene base mixture 2. α is the layer leaning angle.



Fig. 3—Molecular structure of naphthalene base material.

structure readily undergoes a change to a chevron structure when heating starts, although the layer tilt angle remains rather small. Contrary to Fig. 2, the layer tilt angle shown in Fig. 1 shows exactly the same temperature dependence in

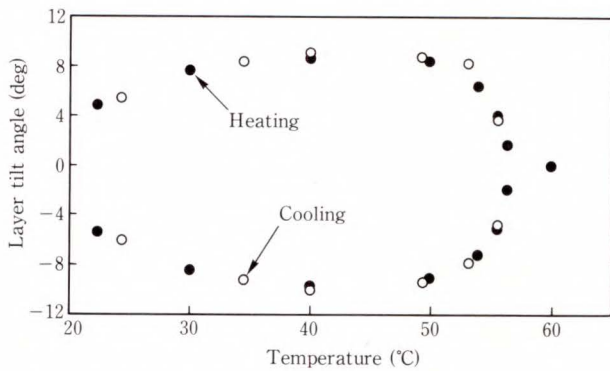


Fig. 4—Temperature dependence of layer tilt angle of the naphthalene base mixture.

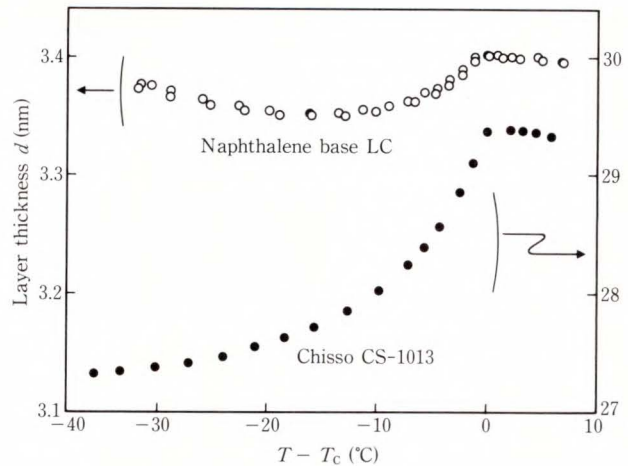


Fig. 6—Temperature dependences of the layer spacings of the naphthalene base mixture and Chisso mixture¹⁰.

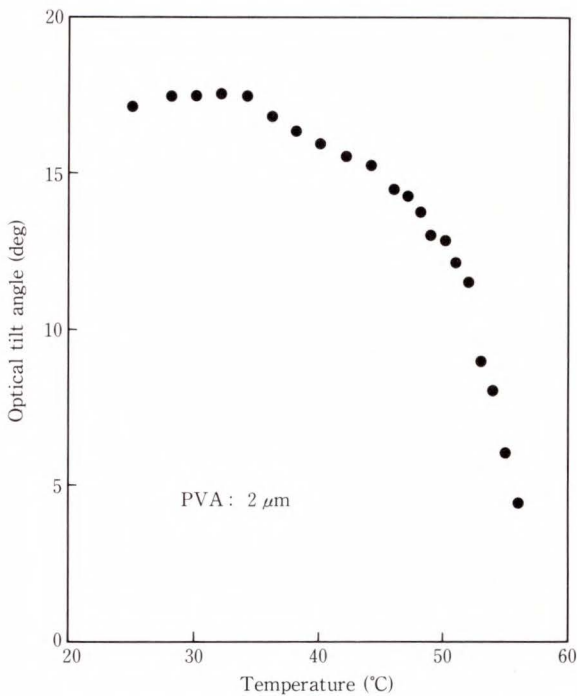


Fig. 5—Temperature dependence of optical tilt angle of the naphthalene base mixture.

both the heating and cooling processes. Thus, these two naphthalene base mixtures have both a different thermal hysteresis and a different structure.

2.2 Layer spacings

Takanishi et al. showed the temperature dependence of the layer tilt angle of both the naphthalene base mixture of Fig. 3 and the

Chisso mixture (see Fig. 6)¹⁰. Figure 6 indicates that the layer spacing reduction of the naphthalene base mixture is very small from the S_A phase to the S_C^* phase compared to the conventional FLC mixture. Moreover, in the lower temperature range below 15 °C for instance, the layer spacing of the naphthalene base mixture increases, as shown in Fig. 6. This demonstrates that the quasi-bookshelf or the bookshelf layer structure of the naphthalene base mixture is a spontaneous structure caused by decreasing temperature, unlike conventional FLC materials.

2.3 Phase sequences

It is widely believed that for a rubbed polymer alignment film cell, a chiralnematic phase is necessary to obtain a clean molecular alignment. In the chiralnematic phase, a parallel molecular alignment is possible, and this parallel molecular alignment may lead to the formation of smectic layers. However, we have observed that several types of FLC materials, such as naphthalene ring FLCs which have an $I-S_A-S_C^*$ phase sequence and show a wide temperature range of the S_A phase, also provide a clean molecular alignment. The bookshelf or quasi-bookshelf smectic layer structures are also possible in these materials. In contrast, it is almost impossible to obtain the spontaneous bookshelf

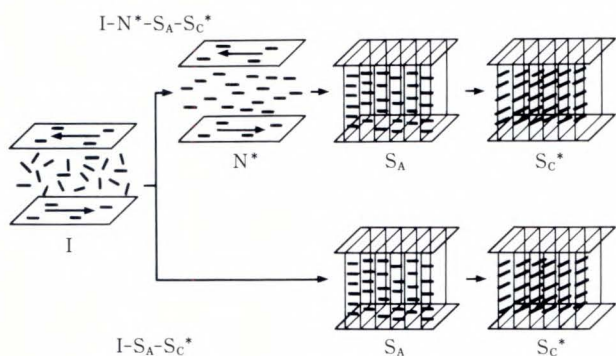


Fig. 7—Surface anchored liquid crystals in the isotropic phase.

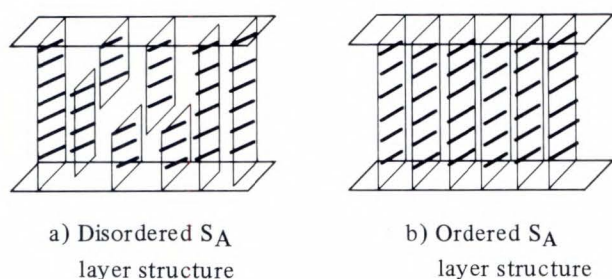


Fig. 8—Formation of the smectic layer structure in the SA phase.

structure using FLC materials with the I-N*-SA-SC* without an external treatment such as a high-frequency electric field²⁾. We assume that the phase sequence affects the smectic layer structure by surface anchoring caused by rubbing. Some liquid crystal molecules are anchored on the rubbed polymer surface even in the isotropic phase, as shown in Fig. 7. When the rubbed polymer film cell is filled with the most common FLC material of phase sequence I-N*-SA-SC*, a layer structure misfit tends to happen while cooling from the N* phase to the SA phase. This misfit may cause the disordered SA phase layer structure shown in Fig. 8a). If an FLC material of phase sequence I-SA-SC* and with a wide temperature SA phase range is filled in the rubbed polymer film cell, even though a layer structure misfit occurs, the wide temperature range of the SA phase may relax the layer misfit, resulting in an ordered smectic layer structure as shown in Fig. 8b).

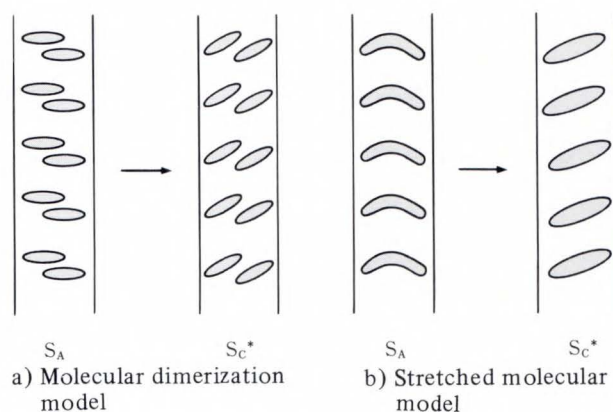


Fig. 9—Two possible liquid crystal molecule configurations in the SA and SC* phases.

During the cooling process into the SC* phase, the liquid crystal molecules tilt within the layers and the molecular length projected into the layer normal reduces. This transition induces a large amplitude of the density function distribution. To compensate for the density function distribution, the smectic layers bend and form a chevron structure^{11),12)}. When the smectic layer structure is disordered as shown in Fig. 8a), this density function distribution is so large that the smectic layer tends to turn into the chevron structure. If the smectic layer structure is ordered as shown in Fig. 8b), the amplitude of the density function distribution is relatively small, and the bookshelf layer structure which is formed in the SA phase can remain in the SC* phase.

Recently several papers have reported the formation of a quasi-bookshelf layer structure using rubbed polymer film cells^{4),5),13)}. The process described above may explain the formation of this quasi-bookshelf layer structure.

The mechanism of creating a bookshelf or quasi-bookshelf layer structure using a naphthalene base FLC mixture is now being investigated. The constant interlayer spacing of the naphthalene base material shown in Fig. 6 is thought to maintain the bookshelf layer structure in the SC* phase. The constant interlayer spacing may be provided by the constant effective molecular length projected into the layer normal. To keep the molecular length constant, the two liquid crystal molecule configurations shown in Fig. 9

may be possible. One configuration is molecular dimerization {see Fig. 9a)}. Liquid crystal molecules form dimers in the S_A phase, and the pair of FLC molecules slide over each other in the S_C^* phase. This maintains the same inter-layer spacing in the FLC, and we should be able to confirm this model by X-ray diffraction. If the pair of FLC molecules slide over each other, the liquid crystals will form a sub-layer in the original layer structure. This should produce a second order X-ray detected peak. However, we have not discovered this kind of second peak in this particular FLC cell.

The other configuration is a molecular stretch {see Fig. 9b)}. Liquid crystal molecules have a bend structure in the S_A phase. In the S_C^* phase, the liquid crystal molecule stretches. Thus the same molecular length is projected into the layer normal as in the S_A phase, even though the liquid crystal molecule tilts. In this case, it is difficult to obtain direct proof experimentally. It is necessary to know both the inter- and intro-molecular rotational behaviors in order to know the molecular length change between the S_A and S_C^* phases. We are now investigating this model by solid-state nuclear magnetic resonance (NMR) and time resolved infra-red (IR) research, and will report the results in due course.

3. Electrical properties

3.1 Response times

When an electric field E is applied to an SSFLC cell, the electrooptical response is governed by the FLC layer structure. The first order approximation of the electrooptical response time can be expressed as¹⁾,

$$\tau = \frac{\eta}{P_S E}, \quad \dots \dots \dots (1)$$

where P_S , η is the spontaneous polarization and is the viscosity coefficient of the FLC material. Equation (1) shows that the electrooptical response speed of the SSFLC cell is proportional to the electric field strength. In the past, however, SSFLC cells have not agreed with Equation (1). In many cases, the response time is known to be proportional to

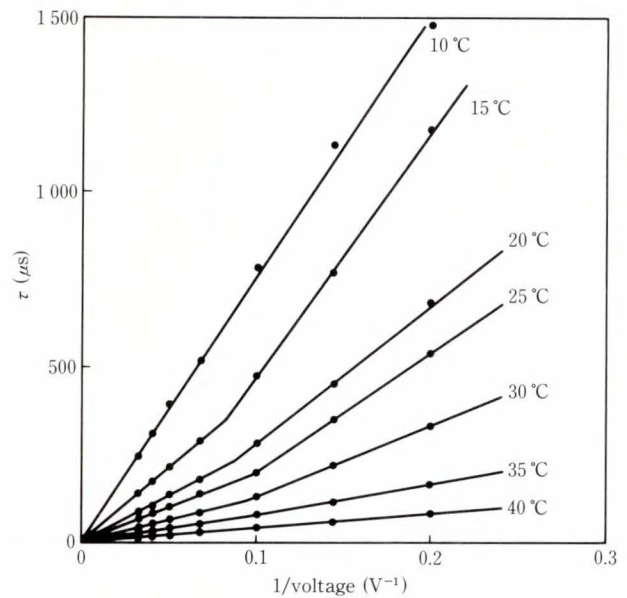


Fig. 10—Electrical response time of the naphthalene base mixture.

E^2 ¹⁴⁾. Thus, Equation (1) may be better expressed as,

$$\tau = \frac{\eta}{P_S E^n}, \quad \dots \dots \dots (2)$$

where n is the power of E ($n > 0$). The existence of domain walls may be the reason why the electrooptical response is not proportional to E ¹⁴⁾. Domain walls may form in the layer structure, particularly the chevron structure, and thus impede polarization switching. The bookshelf layer structure might therefore provide a smoother polarization switching. The electrooptical response of the naphthalene base mixture is shown in Fig. 10. This shows that the naphthalene base mixture undergoes some polarization structure change between 35 °C and 15 °C. Figures 10 and 4 suggest that the electric field strength dependence of the response time changes with the layer tilt angle.

Figure 11 shows, for the naphthalene base mixture, how the electric field strength required to induce optical switching depends on the layer tilt angle¹⁵⁾. This figure suggests that for small tilts, the optical switching of the naphthalene base mixture satisfies Equation (1), which was proposed for uniform molecular orientation.

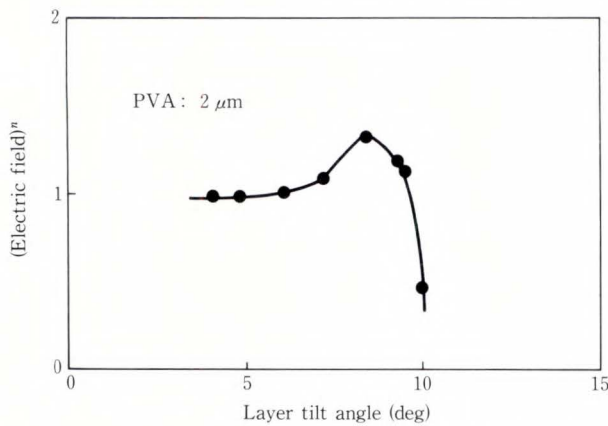


Fig. 11—Layer tilt angle dependence of optical switchings for the naphthalene base mixture. n is the power of applied electric field strength to produce optical switchings.

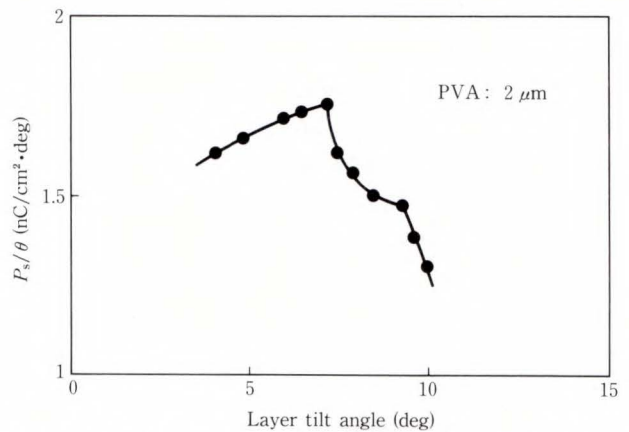


Fig. 13—Effective polarization dependence on the layer tilt angle. θ is the optical tilt angle.

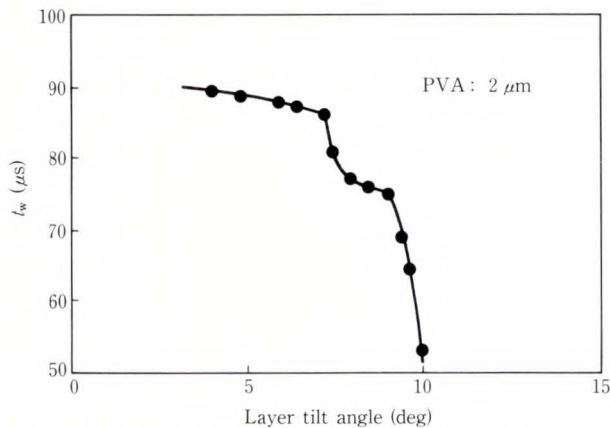


Fig. 12—Layer tilt angle dependence of polarization switching current peak. t_w is the full width at the half maximum of spontaneous polarization current peak.

However, we found that the power increased for a larger layer tilt angle, then decreased drastically. The decrease in power with layer tilt angle may be due to the existence of domain walls, probably caused by the chevron structure. The drastic decrease with larger layer tilt angle is curious. To investigate polarization switching in this layer tilt region, we measured the full width at half the maximum polarization current peak, t_w (see Fig. 12)¹⁵⁾. Comparing Figs. 11 and 12, we found that in the E^1 ($n = 1$) region, t_w decreases quite slowly as the layer tilt angle increases. In the $n > 1$ region, t_w decreases somewhat, then remains almost constant. In the

$n < 1$ region, t_w is thought to be much smaller than in the $n = 1$ region. Thus, Fig. 12 suggests that in the $n < 1$ region, sufficient polarization switching does not occur. When the layer tilt is large, the field cannot nucleate or unpin the domain walls.

This argument is supported by the behavior of P_S . Figure 13 shows the layer tilt angle dependence on P_S ¹⁵⁾. Here, θ is the optical tilt angle. The ratio P_S/θ starts to increase as the layer tilt angle is increased, and reaches a maximum at the same tilt angle which makes $n > 1$ in Fig. 11. Thus, at around 7-8°, there should be some structural change. Although P_S/θ decreases as the layer tilt angle exceeds 7-8°, P_S/θ is still relatively higher than for a small layer tilt angle. Therefore even if the angle is relatively large, P_S is still quite large; due to pinned domain walls, some P_S domains cannot switch, resulting in insufficient electro-optical switching. The optical switching thus occurs quickly.

3.2 Memory capability

To create a high contrast ratio in the SSFLC cell, it is necessary to have a good memory capability. We investigated the dependence of memory on the layer tilt angle. Memory stability of the material, which is the ratio of light transmittance 0.5 s after removing the drive voltage, to the transmittance when the drive voltage is applied, is shown in Fig. 14¹⁵⁾. This figure clearly shows that a small tilt angle produces a

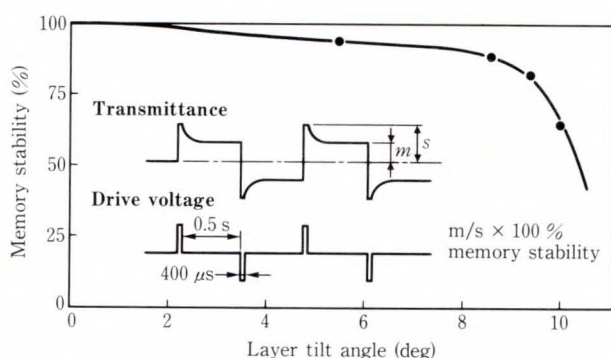


Fig. 14—Relationship between layer tilt angle and memory stability.

more stable memory. Several degrees of layer tilt indicate a quasi-bookshelf layer structure, providing more than 90 percent memory stability.

This correlation of memory stability with the layer tilt angle can be explained as follows. The director in the unperturbed memory state tends to be parallel to the boundary surfaces. In a perfect bookshelf structure, the direction orientation under an electric field is the same as in the memory state, resulting in full memory stability. In a chevron structure, however, the apparent tilt angle, which is the projection angle between the direction and the layer normal, in the memory state is smaller than when a field is applied. The associated change in transmittance by effectively terminating the field reduces the memory stability. Even though the layer structure is not a perfect bookshelf, the memory stability can reach 90 percent provided the layer tilt angle is kept within several degrees.

4. Charge transporting orientation polymers

Several papers have reported that the depolarization field which is induced by the polarization switching of FLCs destabilizes the polarization alignment, resulting in a poor contrast ratio¹⁶⁾⁻¹⁸⁾. This instability is probably caused by the depolarization field. Conventional orientation films such as polyimide films are insulators, and the depolarization field tends to stay in the liquid crystal cell for a while, causing

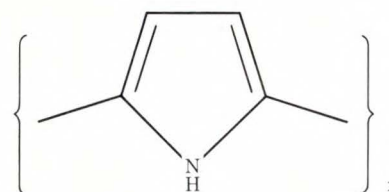


Fig. 15—Molecular structure of polypyrrole.

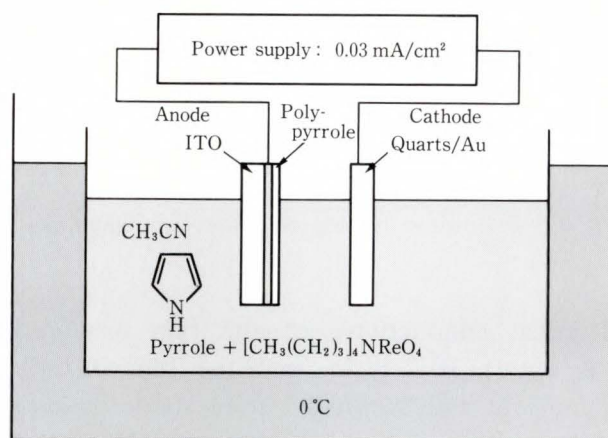


Fig. 16—Setup for the electrochemical synthesis of the polypyrrole film.

polarization alignment instability.

We tried to eliminate the depolarization field by using electrically conducting films, and used the conductive polymer film, polypyrrole, for the molecular orientation film.

4.1 Preparation of polypyrrole film

We synthesized polypyrrole (see Fig. 15) film by electrochemical polymerization deposition on a glass plate covered with an indium tin oxide (ITO) transparent electrode. The polymerization apparatus is shown in Fig. 16. The ITO coated glass plate was placed at the anode, and a fine gold wire coiled quartz plate was used as the cathode. We used tetrabutylammonium perrhenate as the electrolyte and acetonitrile as the solvent and controlled the temperature to 0 °C. The current density for the electrochemical polymerization was typically 0.03 mA/cm², and passing this current for twenty to thirty seconds was sufficient to obtain a 300 Å (30 nm) thick polypyrrole film. The

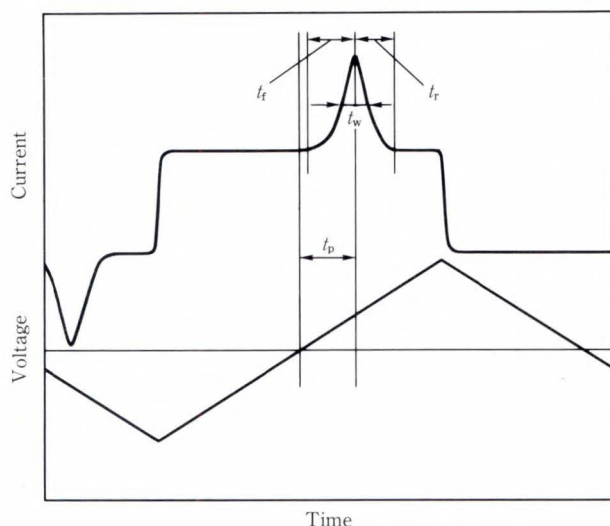


Fig. 17—Definitions of the polarization switching times.

electrical conductivity of the film produced was about 10^{-6} S/cm, and the film is both chemically and thermally quite stable because of its anode oxidation polymerization. Moreover, the electrochemically polymerized pyrrole film is not soluble in any of the usual solvents including liquid crystals. The film surface was rubbed the same with usual polyimide orientation films. One of the important characteristics of the electrochemical polymerized pyrrole film is that the film thickness and the precise surface flatness can be accurately controlled by adjusting the synthesis temperature and the current density.

4.2 Polarization switching properties

The polarization switching properties were investigated using a triangular voltage waveform. We thought to clarify the relationship between the electrical conductivity of the orientation film and the polarization switching times as defined in Fig. 17.

Each polarization switching time was defined as follows:

- t_f : The first half of the polarization switching time
- t_r : The last half of the polarization switching time
- t_w : Full-width at half the maximum of the polarization switching current peak.

Table 1. Polarization switching times of the ferroelectric liquid crystal (FLC) cell with different types of alignment films (μs)

Orientation film	t_f	t_r	t_w	t_p
Polyproole	109.4	94.5	90.7	242
PVA	126.3	161	120	244
PI	135.8	165.8	124.2	272
PVA/SiO ₂	159	188.4	161	435

PVA: Polyvinylalcohol PI: Polyimide

t_p : Switching time from when the applied triangular voltage changes polarity until the polarization switching current reaches its peak value.

Each half of the polarization switching time for four types of orientation film cell is summarized in Table 1. The polarization switching time, t_f in Fig. 17, is almost the same for the four types of cell. However, the last half of the polarization switching time, t_r in Fig. 17 has variations. The value of t_r for polypyrrole film which has a higher electrical conductivity than conventional polymer films⁸⁾, is almost half the value of t_r for polyvinylalcohol (PVA) with SiO₂ film. Polypyrrole film cells also have a shorter t_w or polarization switching time, than any other orientation film cell. The difference of t_p , which is related to the phase shift of the polarization switching current peak, suggests that an insulation layer exists which contributes to depolarization.

The difference of the polarization switching times may be due to the difference in formation of the depolarization field. The more electrically conductive polypyrrole film effectively suppresses the formation of the depolarization field, and this allows faster polarization switching, as shown in Table 1. The difference of t_r suggests that the time taken to form a depolarization field is equal to the polarization switching time. It is thus reasonable to assume that the polarization switching process is affected by the depolarization field. As the polarization is rotated, depolarization will be induced as shown in Fig. 18. When ϕ , which is the rotational angle of polarization in the smectic layer as shown in Fig. 19¹⁹⁾, is larger

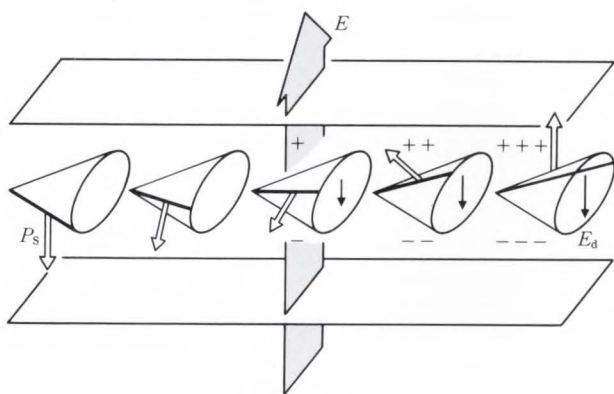


Fig. 18—Induction of the depolarization field by the polarization switching.

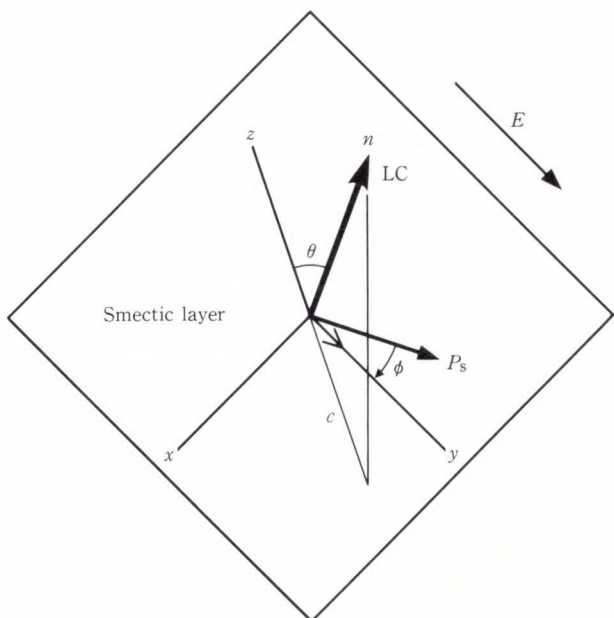


Fig. 19—Polarization switching geometry.

than $\pi/2$, the induced depolarization field E_d will suppress depolarization switching as indicated in Equation (3). In contrast, when ϕ is smaller than $\pi/2$, polarization switching may occur as expressed in Equation (4).

$$\eta \frac{\delta\phi}{\delta t} = P_s E \sin\phi + \frac{\Delta\xi}{4\pi} E^2 \sin^2\theta \sin\phi \cos\phi, \dots\dots\dots (3)$$

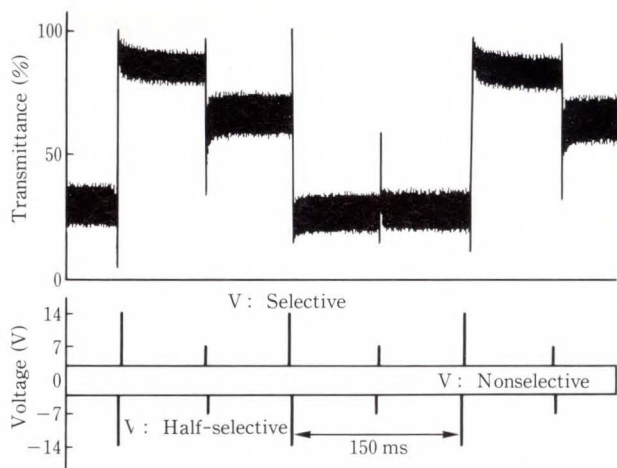


Fig. 20—Transmittance change of the polyimide films cell driven by 2-field multiplexing with 1/200 duty ratio.

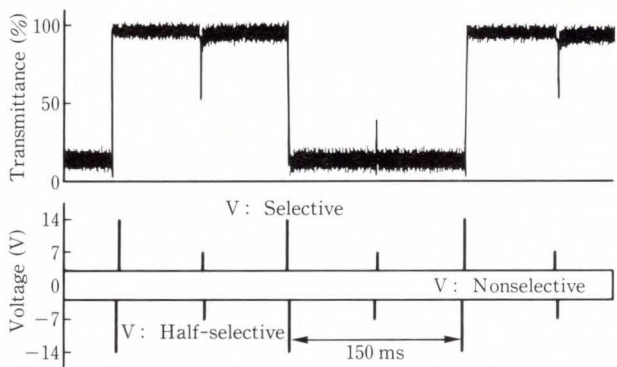


Fig. 21—Transmittance change of the polypyrrole films cell driven by 2-field multiplexing with 1/200 duty ratio.

$$\eta \frac{\delta\phi}{\delta t} = P_s E \sin\phi + \frac{\Delta\xi}{4\pi} E^2 \sin^2\theta \sin\phi \cos\phi - E_d \sin\left(\phi - \frac{\pi}{2}\right). \dots\dots\dots (4)$$

This kind of suppression not only destabilizes the memory, but also disturbs polarization switching.

4.3 Dynamic properties

The memory characteristics of the multiplexed FLC cell are different to the conventional polyimide film cell and the polypyrrole film cell. Figure 20 shows the change of transmittance of the polyimide film cell with the

naphthalene base FLC mixture driven by 2-field multiplexing²⁰⁾ with a 1/200 duty ratio. This panel shows a large transmittance change when a nonselective voltage is applied. The transmittance drops drastically when a half-selective voltage is applied, so the contrast ratio of this panel is low at 5 : 1. However, the polypyrrole film panel shows only a small transmittance change when a nonselective voltage is applied, as shown in Fig. 21. Furthermore, the transmittance behavior when a half-selective voltage is applied is significant. When the half-selective voltage is removed, the transmittance reduces. However, this reduction is temporary. When a half-selective voltage is applied again, the transmittance recovers to its previous level, as shown in Fig. 21. This cell therefore has a high contrast ratio, reaching 40 : 1. The temporary transmittance change may well be due to the elimination of the depolarization field.

5. Prototype

We constructed an SSFLC display utilizing a naphthalene base mixture as shown in Fig. 22. To avoid an electrical short between the upper and lower electrodes, a high dielectric constant insulation layer Ta₂O₅^{4),5)} was placed over the electrodes, which also suppresses the depolarization problem.

A naphthalene base mixture was used for the FLC. The spontaneous polarization was 17 nC/cm² at 25 °C. This display uses four-slot multiplexing driving with a 1/201 duty ratio. This configuration produced a contrast ratio of 40 : 1 and a transmittance of 40 percent including two polarizers. This display also showed almost no image retention when the screen image was refreshed. The detailed characteristics of the display are summarized in Table 2.

6. Stability of molecular alignment

The FLC display has a molecular alignment that is quite stable against mechanical shock. However, it is still vulnerable to bending stress. The anti-stress characteristics were measured using weights as shown in Fig. 23 and the molecular alignment changed as weights were added. The change of molecular alignment was

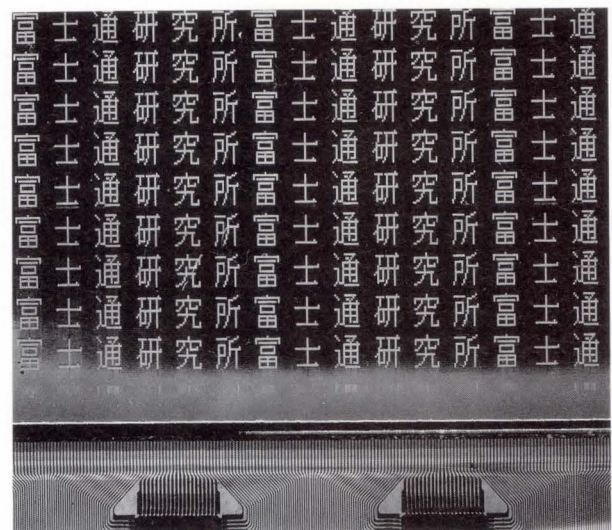


Fig. 22—FLC prototype using the naphthalen liquid crystal.

Table 2. Characteristics of the fabricated FLC display

Number of pixels (dot)	640 × 201
Effective display area (mm ²)	181 × 77
Contrast ratio	40 : 1
Viewing angle (± degree)	70
Transmittance (%)	40
Duty ratio	1/201
Addressing time (μs/line)	160
Drive voltage (V)	18

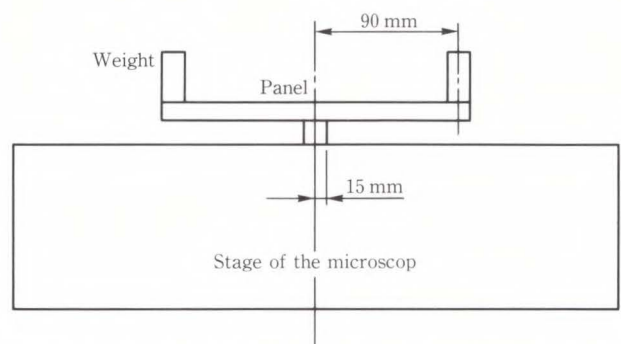


Fig. 23—Setup for measuring the anti-bend stress properties.

detected by the change of transmittance in cross-nicols geometry as shown in Fig. 24. The

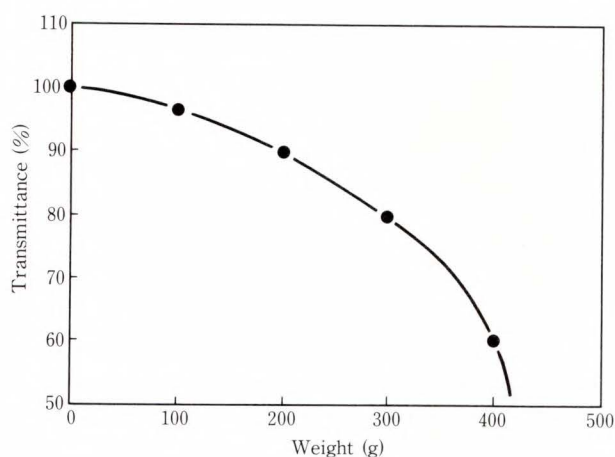


Fig. 24—Molecular alignment change of the fabricated FLC display by the bending stress.

thickness of the glass substrate of the FLC display was 0.7 mm. For weights up to 200 g on each side as shown in Fig. 23, the molecular alignment recovered after removing the weights. However, once 400 g was applied, the molecular alignment did not recover after removing the weight.

7. Conclusion

We investigated the relationship between the phase sequence and the smectic layer structure, and obtained both a bookshelf and a quasi-bookshelf layer structure using a naphthalene base FLC mixture. An electrically conductive polypyrrole alignment film was used to clarify the influence of the depolarization field on polarization switching. The FLC display fabricated using a naphthalene material gives a contrast ratio as high as 40 : 1 and a high transmittance of 40 percent. Although the display is still vulnerable to bending stress, it is tough enough to withstand mechanical shock. This display also proves that it is possible to create an ideal bookshelf structure in a practical SSFLC display with rubbed polymer alignment films.

8. Acknowledgement

The authors thank Professors A. Fukuda, H. Takezoe, Dr. Ouchi and Mr. Takanishi of

Tokyo Institute of Technology, Professor S. Kobayashi of Tokyo University of Agriculture and Technology, and Dr. M. Nakatsuka of Mitsui Toatsu Chemicals Inc. for their courteous discussions.

References

- 1) Clark, N.A., and Lagerwall, S.T.: Submicrosecond bistable electro-optic switching in liquid crystals. *Appl. Phys. Lett.*, **36**, 11, pp. 899-901 (1980).
- 2) Sato, Y., Tanaka, T., Kobayashi, H., Aoki, K., Watanabe, H., Takeshita, H., Ouchi, Y., Takezoe, H., and Fukuda, A.: High Quality Ferroelectric Liquid Crystal Display with Quasi-Bookshelf Layer Structure. *Jpn. J. Appl. Phys.*, **28**, 3, L483-L486 (1989).
- 3) Ouchi, Y., Lee, J., Takezoe, H., Fukuda, A., Kondo, K., Kitamura, T., and Mukoh, A.: Smectic Layer Structure of Thin Ferroelectric Liquid Crystal Cells Aligned by SiO Oblique Evaporation Technique. *Jpn. J. Appl. Phys.*, **27**, 11, pp. L1993-L1995 (1988).
- 4) Rieger, H., Escher, C., Illian, G., Jahn, H., Kaltbeitzel, A., Ohlendorf, D., and Rosch, N.: FLC Display Showing High Contrast and High Luminance. Conf. Rec. SID, Anaheim, Calif., 1991, pp. 396-399.
- 5) Escher, C., Illian, G., Jahn, H., Kaltbeitzel, A., Ohlendorf, D., Rosch, N., Harada, T., Yudasaka, M., Weippert, A., and Luder, E.: Fast FLC-Displays With High Contrast and High Brightness. Conf. Rec. 3rd Int. Conf. Ferroelectric Liquid Crystals, 1991, Q-27.
- 6) Mochizuki, A., Hirose, M., and Nakatsuka, M.: Zigzag Defect Free Alignment and Good Bistability of Surface Stabilized S_c^* Cells. *Ferroelectrics*, **113**, 14, pp. 353-359 (1991).
- 7) Mochizuki, A., Motoyoshi, K., and Nakatsuka, M.: A High Contrast and High Transmittance Multiplexing SSFLC Display Utilizing Naphthalene Base Liquid Crystals. *Ferroelectrics*, **122**, pp. 37-51 (1991).
- 8) Mochizuki, A., Motoyoshi, K., Yoneda, Y., Nakatsuka, M., Yoshida, M., and Kobayashi, S.: A High-Contrast Multiplexed Dot-Matrix FLC Display Using Naphthalene-Base FLC and Conductive Polymer Films for Orientations. Proc. SID, 1992, in print.
- 9) Miyasato, K., Abe, S., Takezoe, H., Fukuda, A., and Kuze, E.: Direct Method with Triangular Waves for Measuring Spontaneous Polarization in Ferroelectric Liquid Crystals. *Jpn. J. Appl. Phys.*, **22**,

- 10, pp. L661-L663 (1983).
- 10) Takanishi, Y., Ouchi, Y., Takezoe, H., Fukuda, A., Mochizuki, A., and Nakatsuka, M.: Spontaneous Formation of Quasi-Bookshelf Layer Structure in New Ferroelectric Liquid Crystals Derived from a Naphthalene-Ring. *Jpn. J. Appl. Phys.*, **29**, 6, pp. L984-L986 (1990).
 - 11) Clark, N.A., and Rieker, T.P.: Smectic-C "chevron," a planar liquid-crystal defect: Implications for the surface-stabilized ferroelectric liquid-crystal geometry. *Phys. Rev.* **A37**, 3, pp. 1053-1056 (1988).
 - 12) Rieker, T.P., Clark, N.A., Smith, G.S., Palmer, D.S., Sirota, E.B., and Safinya, C.R.: "Chevron" Local Layer Structure in Surface-Stabilized Ferroelectric Smectic-C Cells. *Phys. Rev. Lett.*, **59**, 23, pp. 2658-2661 (1987).
 - 13) Konuma, T., Mase, A., Yamazaki, S., Yagi, M., Kondo, H., and Hagiwara, T.: Ferroelectric Liquid-Crystal Display with Multi-Micro-Domains Driven by a Video Rate. Conf. Rec. SID, Anaheim, Calif., 1991, pp. 400-403.
 - 14) Clark, N.A., Handschy, M.A., and Lagerwell, S.T.: Ferroelectric Liquid Crystal Electro-Optic Using the Surface Stabilized Structure. *Mol. Cryst. Liq. Cryst.*, **94**, pp. 213-234 (1983).
 - 15) Mochizuki, A., Yoshihara, T., Iwasaki, M., Nakatsuka, M., Takanishi, Y., Ouchi, Y., Takezoe, H., and Fukuda, A.: Electro-Optical Switching of Book-shelf Layer Structure S_C^* Cells aligned with a Rubbed Polymer Film. *Proc. SID*, **31**, 2, pp. 123-133 (1990).
 - 16) Inaba, Y., Katagiri, K., Inoue, H., Kanbe, J., Yoshihara S., and Iijima, S.: Essential Factor in High-duty FLC Matrix Display. *Ferroelectrics*. **85**, pp. 255-264 (1988).
 - 17) Nakaya, K., Zhang, B.Y., Yoshida, M., Isa, I., Shindoh, S., and Kobayashi, S.: Electrooptic Bistability of a Ferroelectric Liquid Crystal Device Prepared Using Charge-Transfer Complex-Doped Polyimide-Orientation Films. *Jpn. J. Appl. Phys.*, **28**, 1, pp. L116-L118 (1989).
 - 18) Ikeno, H., Maeda, H., Yoshida, M., Zhang, B.Y., Kimura, M., and Kobayashi, S.: A Ferroelectric LCD with Gray-Scale Capability Using Conventional CTC-Doped Polyimide and/or Undoped LB Polyimide Alignment Layers. *Proc. SID*, **30**, 4, pp. 329-332 (1989).
 - 19) Jin-Zhi, X, Handschy, M., and Clark, N.: Electro-optical Response During Switching of a Ferroelectric Liquid Crystal Cell with Uniform Director Orientation. *Ferroelectrics*, **73**, pp. 305-314 (1987).
 - 20) Harada, T., Taguchi, M., Iwasa, K., and Kai, M.: An Application of Chiral Smectic-C Liquid Crystal to a Multiplexed Large-Area Display. Conf. Rec. SID, Orland, Fla., 1985, pp. 131-134.



Akihiro Mochizuki

Imaging Materials Laboratory
FUJITSU LABORATORIES, ATSUGI
Bachelor of Natural Science
The University of Tokyo 1980
Dr. of Electronics
Tokyo University of Agriculture and
Technology 1991
Specializing in Liquid Crystal
Materials and Organic Conducting
Materials



Katsusada Motoyoshi

Imaging Materials Laboratory
FUJITSU LABORATORIES, ATSUGI
Bachelor of Electrical Eng.
Tokyo University of Agriculture and
Technology 1990
Specializing in Liquid Crystal
Devices

Super High Information Content Projection Display Using an NCPT Liquid Crystal

• Akihiro Mochizuki • Shigeo Kasahara • Yoshikazu Yabe

(Manuscript received February 3, 1992)

A multiplexed high luminance liquid crystal projection display with $2\,240 \times 2\,240$ (5 million) pixels for use with a conventional overhead projector has been developed. It has been clarified theoretically and by experiment that the surface effect on the cholesteric-nematic phase transition results in stable bistability. Optimizing the helical pitch of chiralnematic liquid crystal in conjunction with the surface anchoring strength has made possible super-high information content. Moreover the fact that this display requires no polarizers enables very bright screen images. These characteristics match with high resolution (typically 300 dpi) printer output. The combined result of the theoretical investigation and the materials research is a practical high performance liquid crystal display.

1. Introduction

Large projection displays are currently popular for presentations, public announcements, and showing moving pictures. Particularly for presentations, systems consisting of a liquid crystal display (LCD) pad, a personal computer and an overhead projector (OHP) are now widely used. This kind of system may be called the electronic overhead projector (E-OHP). The light weight, thin LCD pads are quite convenient to carry, and using an overhead projector keeps the cost of the system low. Currently available LCD pads use multiplexed supertwisted nematic (STN) LCDs or active matrix driven twisted nematic (AM-TN) LCDs.

However, the most popular STN LCD pad has a dim screen because the two polarizers that it uses absorb a lot of the incident light. Its information content is limited to 640×480 pixels¹⁾ because of its poor electrooptical threshold properties. Moreover, its drive voltage shifts when the pad heats up, and this reduces the screen display contrast ratio. Also, light absorption by the polarizers heats up the LCD,

which deteriorates screen image quality. This is particularly noticeable with conventional OHPs, which do not have uniform light intensity across the display field. The brighter center of the screen tends to have a lower contrast ratio than the outer part due to the temperature distribution in the LCD pad.

We report on a new type of projection display using a nematic-cholesteric phase transition (NCPT) LCD²⁾⁻⁴⁾ which overcomes these drawbacks of conventional LCD pads. The NCPT projection display needs no polarizers, thus the screen image is bright.

Also, for the same reason, light absorption does not heat up the LCD pad significantly so screen image quality does not deteriorate, even after several-hour continuous operation. Moreover, NCPT mode uses the memory effect of the liquid crystal, and the information content is theoretically unlimited. We have previously reported a $1\,120 \times 768$ pixel NCPT projection display⁵⁾. However, recent improvements in data storage systems, for example

document filing using optical disks, require higher information content and higher resolution (i.e. more legible) displays. It is especially important that such displays, with about a couple of million pixels, are free of flicker. Otherwise it is not easy to recognize what is displayed on the screen. On this point the NCPT mode, which uses the memory effect of the liquid crystal, is preferable.

Also, higher information content will extend the application field of this kind of display. Potential applications include soft copies for printer output, image reader output, and fax output. As previously stated, the information content of NCPT displays is theoretically unlimited. However, a practical high information content E-OHP display would need improvements in the drive stability of the liquid crystal electrooptical hysteresis over a wide temperature range, gray scale capability, and high density packing technology.

We aimed to develop a large screen display for E-OHP presentations with the following general specifications. First, a high information content of at least $1\,200 \times 1\,000$ pixels. Second, a bright screen using a liquid crystal light valve with no polarizers. Third, a high resolution: a fine screen image with gray shades needs both high information content and high resolution. Using a printer interface as an input source needs at least $2\,000 \times 2\,000$ pixels. Fourth, a flicker-free image is essential for good legibility. A memory-type LCD is preferable for this because once written, the image is fixed.

To develop an E-OHP which meets the above requirements we looked into the electrooptical hysteresis behavior of nematic-cholesteric liquid crystals under an applied electric field. Their hysteresis memory effect makes possible a high information content, and their non-polarizer light scattering mode enables a bright screen. Also, electrical addressing makes it possible to keep the display small and to connect displays together into a network system.

2. An NCPT liquid crystal display

An NCPT-type liquid crystal mixture with positive dielectric anisotropy changes state as

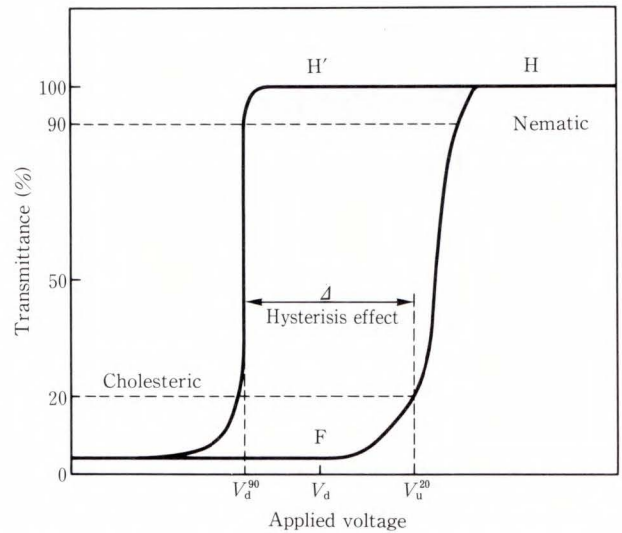


Fig. 1—Phase transition and transmittance change of the nematic-cholesteric phase transition (NCPT) liquid crystal display.

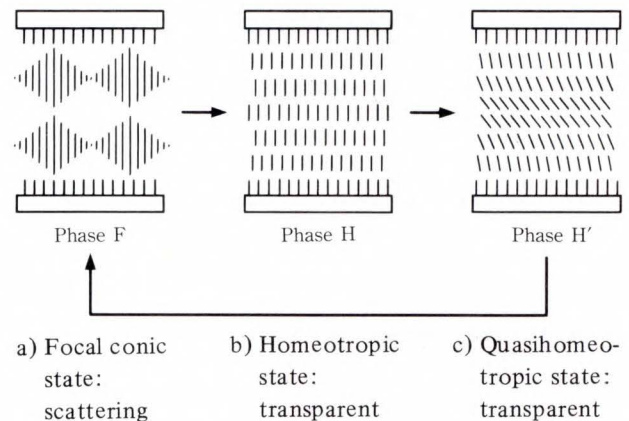


Fig. 2—Texture changes of the NCPT liquid crystal.

shown in Fig. 1. When the applied voltage is increased it changes from a cloudy state, cholesteric phase F, to a transparent state, nematic phase H. When the voltage is decreased the mixture changes from phase H to a metastable transparent state, nematic phase H', then to phase F. In phase F the liquid crystal in the panel has the helical structure shown in Fig. 2a). Because the axis of the helix is parallel to the glass substrates, incident light is scattered, making phase F cloudy. In phase H, the liquid crystal has a homeotropic structure as shown in Fig. 2b). Incident light passes through the homeotropic structure, making phase H transparent. In phase H' the structure of the liquid crystal layer is still homeotropic, but the molecules in the center are thought to be slight-

ly inclined as shown in Fig. 2c). Phase H' is a metastable, or supersaturated state. Supersaturation may make hysteresis in the nematic-cholesteric phase transition stable. The stability of the hysteresis effect is thought to be affected by the specific balance between surface anchoring and the thermal properties of the helical structure^{2),6)-9)}.

The width of the hysteresis effect is designated Δ as shown in Fig. 1. That is, Δ is the difference between the voltage, V_u^{20} , which gives 20 percent transmittance in cholesteric to nematic phase transitions and the voltage, V_d^{90} , which gives 90 percent transmittance in nematic to cholesteric phase transitions. Figure 1 also shows how the drive voltage, V_d , is set between V_u^{20} and V_d^{90} .

3. Addressing method of the NCPT mode

The NCPT panel addressing method uses electrooptical hysteresis; writing also uses electrooptical hysteresis behavior. The screen is written one line at a time. Typical writing time for each scanning line is 2.2 ms. Thus it takes 4.9 s ($2.2 \text{ ms} \times 2240 \text{ lines}$) to write the whole screen.

The first stage of the writing operation is initializing all the pixels (see Fig. 3). Sufficient voltage (usually twice the drive voltage) is applied to all the pixels to change them from cholesteric to transparent nematic phase. The second stage is writing to selected pixels. The

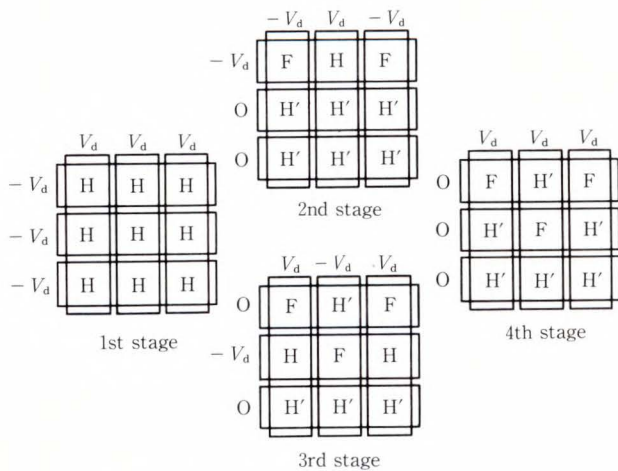


Fig. 3—Writing to the NCPT LCD.

selected pixels are changed to cloudy cholesteric phase by removing the voltage then applying drive voltage. The third stage is writing to non-selected pixels. The nonselected pixels are maintained in the transparent nematic phase by continuing to apply either drive voltage or twice drive voltage. The fourth stage is maintaining the written images. Selected pixels are maintained by continuing to apply drive voltage. Due to the bistability between nematic and cholesteric phases, once selected or nonselected, pixels do not change state. Therefore high information content is obtained for a virtually unlimited number of scanning lines.

Partial rewriting also relies on bistability as shown in Fig. 4. The selected pixels in cholesteric phase are switched to nematic phase without disturbing the other pixels by applying $2V_d$ then V_d . The selected pixels in nematic phase are switched to cholesteric phase without disturbing the other pixels by removing, then re-applying V_d .

An NCPT projector with the characteristics described in chapter 1 needs two further

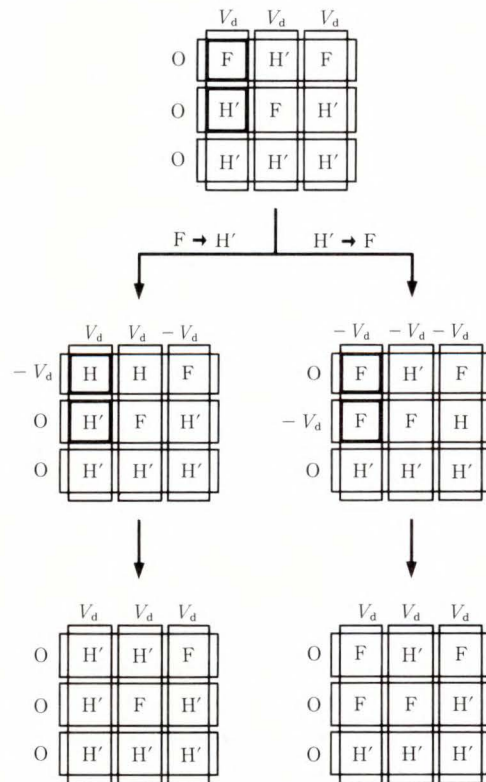


Fig. 4—Partial rewriting to the NCPT LCD.

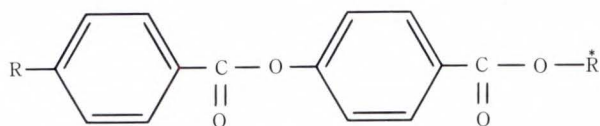


Fig. 5—Molecular structure of the chiralnematic liquid crystal.

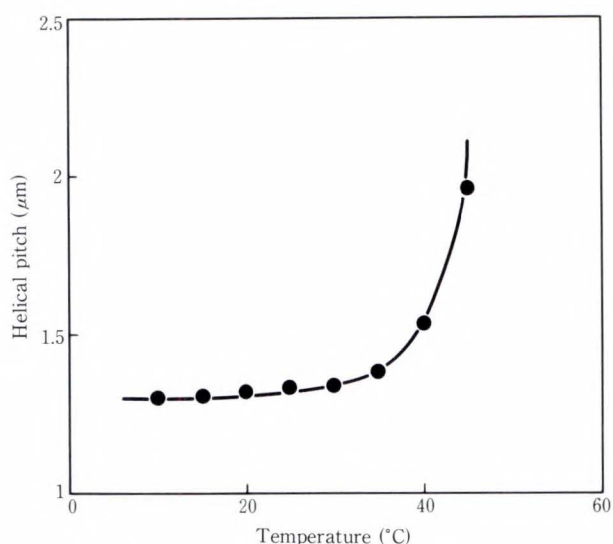


Fig. 6—Temperature dependence of helical pitch: conventional long helical pitch liquid crystal.

developments: first, practical bistability during writing; second, after writing, enough bistability to maintain the written image with a good contrast ratio over a wide temperature range.

4. An electrooptical bistability

It is assumed that the liquid crystal's elastic modulus and the surface anchoring govern the stability of the NCPT mode. The molecular alignment of the chiralnematic liquid crystal is particularly important for stable hysteresis behavior. We used a short helical pitch chiralnematic liquid crystal which contains two ester groups in its molecular structure as shown in Fig. 5. We found that the short (1 μm) helical pitch of the NCPT mixture is associated with wide electrooptical hysteresis. We also found that, for a chiralnematic liquid crystal which contains two ester groups, both hysteresis width and threshold voltage are largely independent of temperature over a wide range. We assume that this is due to the temperature independence of short helical pitch liquid crystals. Figure 6 shows the temperature dependence of helical

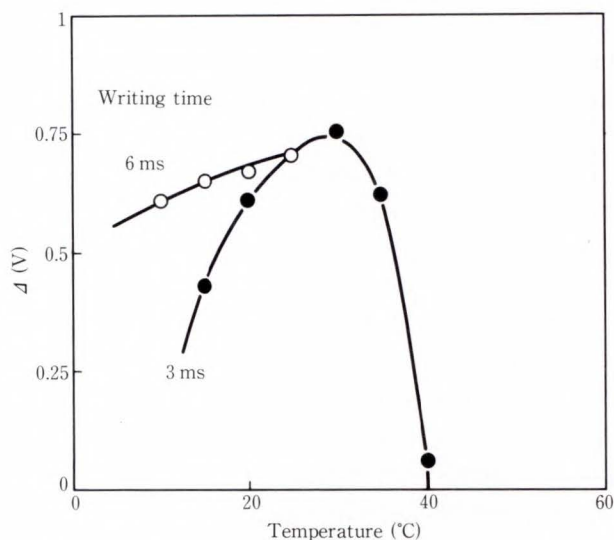


Fig. 7—Temperature dependence of electrooptical hysteresis Δ : conventional long helical pitch liquid crystal.

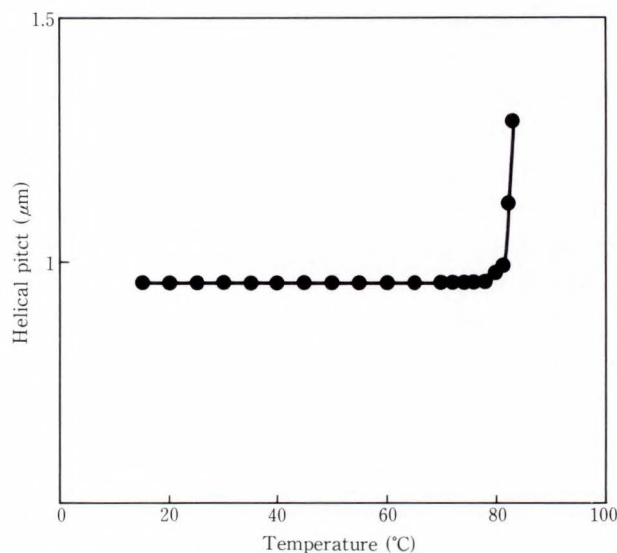


Fig. 8—Flat helical pitch. Short helical pitch liquid crystal material with the proper nematic liquid crystal realizes flat helical pitch over a wide temperature range.

pitch for an NCPT-type liquid crystal whose helical pitch at room temperature is 1.5 μm. The helical pitch of this liquid crystal mixture shows a typical temperature dependence; i.e. it becomes longer as temperature increase. This liquid crystal did not provide enough hysteresis width, as shown in Fig. 7. The chiralnematic liquid crystal which contains two ester groups, shown in Fig. 5, also has a short helical pitch. It has the flat characteristic shown in Fig. 8.

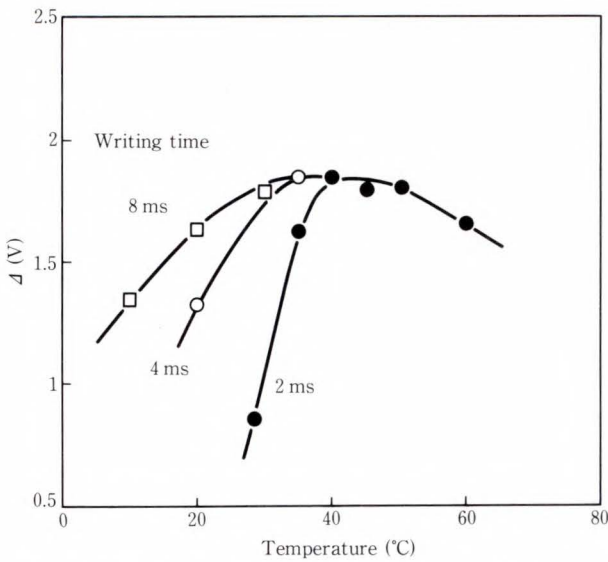


Fig. 9—Electro-optical hysteresis effect of short helical pitch and proper nematic liquid crystal mixture panel.

In addition to the behavior of the chiral-nematic liquid crystals, the elastic modulus of the nematic liquid crystals is another important factor affecting hysteresis. Our experiments indicate that a large elastic modulus of bend, K_{33} , permits a large and stable hysteresis. In particular, we assume that a specific balance between the anchoring force and the helical twisting force governs the threshold voltage for switching from the homeotropic to the focal conic state. To increase the threshold voltage for switching from cholesteric to nematic phase, it needs a strong helical force with a large K_{22} , which is the elastic modulus of twist. However, a practical NCPT display needs a low drive voltage in the drive range of conventional CMOS LSIs, typically 13 V. Thus we tried to make a specific balance between the surface treatment and the helical pitch of the liquid crystal materials. By taking the temperature dependence of the hysteresis width into account, we were able to obtain enough hysteresis width over a wide temperature range as shown in Fig. 9. A Δ of about 1.5 V is enough when driving the panel with a V_d of 13 V.

5. The surface anchoring effect on the NCPT mode

An electric field induced phase transition

from cholesteric to nematic is expressed as

$$E_1 = \frac{\pi^2}{P_0} \sqrt{\frac{K_{22}}{\epsilon_0 \Delta \epsilon}}, \dots \dots \dots (1)$$

by De Gennes¹⁰⁾, where E_1 is the threshold electric field from cholesteric to nematic, P_0 is the helical pitch in the absence of the electric field, K_{22} is the elastic constant of twist, ϵ_0 is the vacuum permittivity, and $\Delta \epsilon$ is the dielectric anisotropy of the liquid crystal. However, experimental results suggest that the threshold field, E_{CN} , should take the surface effect into account. A surface anchoring energy A_θ is assumed to assist the cholesteric to nematic phase transition when the surface treatment is homeotropic, because the nematic phase is equivalent to the whole homeotropic state. This surface effect, given by $1/d^*$, is only significant if d^* , the effective liquid crystal layer thickness, is small, i.e. if the LC layer is thin. Here d^* , equals $d - \xi$, where ξ is the thickness of the unwound layer of the helical structure. Thus the surface effect for cholesteric to nematic is assumed to be

$$\frac{2A_\theta}{\epsilon_0 \Delta \epsilon (d - \xi)} \dots \dots \dots (2)$$

Here $2A_\theta$ means the contributions from both upper and lower substrates. Therefore E_{CN} , the threshold field which takes the surface effect into account⁹⁾, is given by

$$E_{CN} = \sqrt{E_1^2 - \frac{2A_\theta}{\epsilon_0 \Delta \epsilon (d - \xi)}} \dots \dots (3)$$

For the nematic to cholesteric phase transition, Greubel has derived that for $K_{22} \geq (P_0 K_{33})/d$ the threshold E_2 is expressed as

$$E_2 = \frac{\pi}{P_0} \sqrt{\frac{4K_{22}^2 - \left(\frac{P_0 K_{33}}{d}\right)^2}{\epsilon_0 \Delta \epsilon K_{33}}}, \dots \dots (4)$$

where K_{33} is the elastic modulus of bend⁶⁾.

In this transition, the cell gap influence on the threshold field is already taken into account in the E_2 equation. However, in a usual cell

configuration, K_{22} is much larger than $(P_0 K_{33})/d$, thus E_2 is almost

$$E_2 \approx \frac{\pi}{P_0} \sqrt{\frac{4K_{22}^2}{\epsilon_0 \Delta \epsilon K_{33}}} \dots \dots \dots (5)$$

The experimental results which show the strong dependence of cell gap suggest that the

elastic constant, K_{22} , should be modulated by the surface effect. Therefore the effective twist elastic constant, K_{22}^* , is expressed as⁹⁾

$$K_{22}^* = K_{22} \left(1 - \frac{\xi}{d}\right) \dots \dots \dots (6)$$

Thus the threshold electric field strength of the nematic to cholesteric phase transition is expressed as

$$E_{NC} = \frac{\pi}{P_0} \sqrt{\frac{4K_{22}^2 \left(1 - \frac{\xi}{d}\right)^2 - \left(\frac{P_0 K_{33}}{d}\right)^2}{\xi_0 \Delta \xi K_{33}}} \dots \dots \dots (7)$$

The electrical hysteresis width, Δ , is

$$\frac{E_{CN}}{E_{NC}} = \frac{\sqrt{\frac{\pi^2}{P_0^2} \left\{ \frac{\pi^2 K_{22}}{\epsilon_0 \Delta \epsilon} - \frac{2A_\theta \cdot P_0^2}{\pi^2 \epsilon_0 \Delta \epsilon (d - \xi)} \right\}}}{\sqrt{\frac{\pi^2}{P_0^2} \cdot \frac{4K_{22}^2 \left(1 - \frac{\xi}{d}\right)^2 - \left(\frac{P_0 K_{33}}{d}\right)^2}{\epsilon_0^2 \Delta \epsilon^2 K_{33}^2}}} = \frac{\frac{1}{\epsilon_0 \Delta \epsilon} \left\{ \pi^2 K_{22} - \frac{2A_\theta \cdot P_0^2}{\pi^2 (d - \xi)} \right\}}{\frac{1}{\epsilon_0 \Delta \epsilon} \left\{ \frac{4K_{22}^2 \left(1 - \frac{\xi}{d}\right)^2 - \left(\frac{P_0 K_{33}}{d}\right)^2}{K_{33}} \right\}}$$

Here, $\xi \ll d$

$$\cong \frac{K_{33} \left\{ \pi^2 K_{22} - \frac{2A_\theta \cdot P_0^2}{\pi^2 (d - \xi)} \right\}}{4K_{22}^2 \left(1 - \frac{2\xi}{d}\right) - \left(\frac{P_0 K_{33}}{d}\right)^2} \dots \dots \dots (8)$$

This equation indicates that the hysteresis width Δ requires that

$$K_{33} \left\{ \pi^2 K_{22} - \frac{2A_\theta \cdot P_0^2}{\pi^2 (d - \xi)} \right\} > 4K_{22}^2 \left(1 - \frac{2\xi}{d}\right) - \left(\frac{P_0 K_{33}}{d}\right)^2 \dots \dots \dots (9)$$

Here, again $\xi \ll d$ leads to

$$\pi^2 K_{22} K_{33} - \frac{2A_\theta \cdot P_0^2 \cdot K_{33}}{\pi^2 d} > 4K_{22}^2 \left(1 - \frac{2\xi}{d}\right) - \left(\frac{P_0 K_{33}}{d}\right)^2 \dots \dots \dots (10)$$

This equation suggests that large ξ provides a wide hysteresis.

6. A 5 million pixel NCPT projector

We aimed to develop an LCD pad with 2240×2240 pixels to use with a conventional overhead projector; thus the effective display area of the LCD pad to be 240×240 mm. Accordingly, we fabricated a 10-line/mm pitch electrode pattern panel. The LCD and the drive circuit are connected by a chip on a flexible printed board. The controller and the drive circuit are connected with the panel on four sides as shown in Fig. 10.

The screen image data created on the personal computer are transferred to the image processor of the NCPT panel through the printer interface. To make the screen image, the processed character codes, image data and control codes are sent to the LCD panel in 24-line groups. Our improvements to the liquid crystal material and the packaging technology have enabled us to construct a stable driven 5 million pixel NCPT electronic OHP display with a screen image five times brighter than the conventional STN-LCD. Figures 11 and 12 show example screen images. The display characteristics are summarized in Table 1.

The high resolution of the developed NCPT display makes possible gray scale images like those shown in Figs. 11 and 12. Although the NCPT display uses the bistability of nematic-cholesteric phase transition type liquid crystal, the use of dithering produces a flicker-free gray scale image. Moreover, because the NCPT

projector uses no polarizers, there is no coloration. When the liquid crystal is in the homeotropic

Table 1. Characteristics of the 5 million pixel NCPT projector

Number of pixels	2 240 × 2 240
Pixel size (μm^2)	85 × 85
Display area of the panel (mm^2)	224 × 224
Screen size (in)	100
Contrast ratio	4:1
Screen luminance (cd/m^2) (1.2 kW OHP, screen gain 8)	800
Transmittance of the LC panel (%)	60
x-y color chart	x: 0.419, y: 0.38
Line addressing time (μs)	2.2
Screen addressing time (s)	4.9

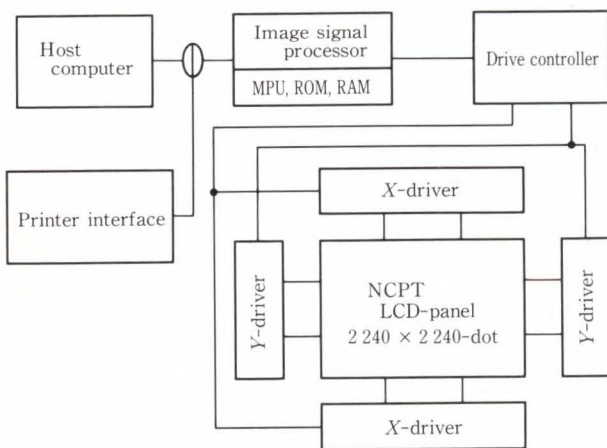


Fig. 10—Block diagram of the NCPT projector.

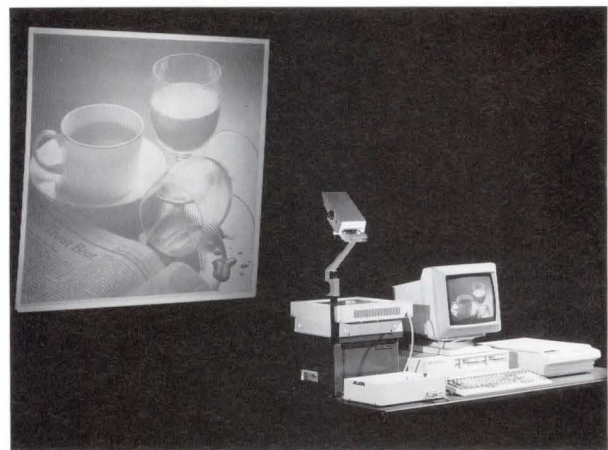


Fig. 11—Screen image of the 5 million pixel NCPT electronic OHP display (picture).

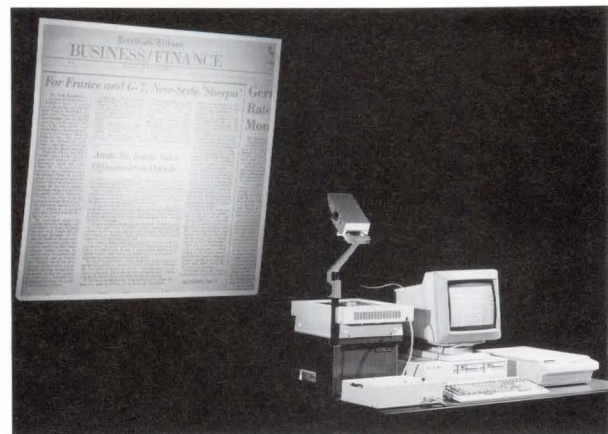


Fig. 12—Screen image of the 5 million pixel NCPT electronic OHP display (characters).

state the incident light passes straight through the panel, thus the screen is the same color as the light source.

7. Conclusion

The developed NCPT technology provides a bright, 5 million pixel, high resolution E-OHP display. Although the LCD pad uses the bistability of the nematic-cholesteric phase transition, its high resolution and high information content make it possible to create a gray scale by dithering. The LCD pad will be extremely cheap to produce compared to a laser beam-addressed liquid crystal projector with the same order of information content. The NCPT display is suitable for CAD/CAM uses.

The low cost, high resolution E-OHP display has potential for graphics and documentation displays, for example as an output device for document filing systems using optical disk memory. In addition, this type of E-OHP display is quite suitable for view-graphs in a presentation.

8. Acknowledgement

The authors would like to thank Professor S. Kobayashi of Tokyo University of Agriculture and Technology for discussions about the cholesteric-nematic phase transition.

References

- 1) Conner, R.A., and Gulick, E.P.: High-Resolution Display System Based on Stacked Mutually Com-

- pensated STN-LCD Layers. Conf. Rec. SID, 1991, pp. 755-757.
- 2) Mochizuki, A., Gondo, H., Watanuki, T., Saito, K., Ikegami, K., and Okuyama, H.: New Nematic-Cholesteric LCD Using Hysteresis Behavior. *Proc. SID*, **26**, 4, pp. 243-248 (1985).
- 3) Mochizuki, A., Iwasaki, M., Yamagishi, Y., Gondo, H., and Yamaguchi, H.: A nematic-cholesteric bistable liquid crystal display for projectors. *Proc. SPIE*, **760**, Large Screen Projection Displays, pp. 74-77 (1987).
- 4) Yamagishi, Y., Iwasaki, M., Yoshihara, T., Mochizuki, A., and Haraguchi, M.: A Multicolor Projection Display Using Nematic-Cholesteric Liquid Crystal. *Proc. SID*, **30**, 2, pp. 91-94 (1989).
- 5) Mochizuki, A., Yoshihara, T., Iwasaki, M., Yamagishi, Y., Koike, Y., Haraguchi, M., and Kaneko, Y.: A 1120 × 768 Pixel Four-Color Double-Layer Liquid-Crystal Projection Display. *Proc. SID*, **31**, 2, pp. 155-161 (1990).
- 6) Greubel, W.: Bistability behavior of texture in cholesteric liquid crystals in an electric field. *Appl. Phys. Lett.*, **25**, 1, pp. 5-7 (1974).
- 7) Lin-Hendel, C.G.: Tristability in the electric-field-induced phase transformation of liquid-crystal films. *Appl. Phys. Lett.*, **38**, 8, pp. 615-617 (1981).
- 8) Lin-Hendel, C.G.: Electric-field-induced texture and phase transformation of liquid-crystal films. *J. Appl. Phys.*, **53**, 2, pp. 916-920 (1982).
- 9) Mochizuki, A., and Kobayashi, S.: Surface effect on the threshold electric fields of cholesteric-nematic phase transition and its reverse process. Accepted for publication in *Mol. Cryst. Liq. Cryst.*
- 10) De Gennes, P.: *Physics of Liquid Crystals*. London, Oxford Press, 1974, pp. 110-113.



Akihiro Mochizuki

Imaging Materials Laboratory
FUJITSU LABORATORIES, ATSUGI
Bachelor of Natural Science
The University of Tokyo 1980
Dr. of Electronics
Tokyo University of Agriculture and
Technology 1991
Specializing in Liquid Crystal
Materials and Organic Conducting
Materials



Yoshikazu Yabe

Development Engineering Dept.
Fujitsu Kiden Limited
Bachelor of Chemical Eng.
Nihon University 1983
Master of Chemical Eng.
Nihon University 1985
Specializing in Liquid Crystal
Materials and Display Devices



Shigeo Kasahara

Imaging Materials Laboratory
FUJITSU LABORATORIES, ATSUGI
FUJITSU Technical College 1988
Specializing in Liquid Crystal Materi-
als and Organic Thin Film Materials

Polysiloxane as a Bi-Level Resist for VLSI Lithographies

• Keiji Watanabe • Takahisa Namiki • Yasuhiro Yoneda

(Manuscript received February 3, 1992)

A newly designed organosilicon resist, three-dimensional polysilphenylenesiloxane (TSPS), has been developed for use as a high-resolution negative bi-level electron-beam resist or KrF-excimer laser resist. The TSPS molecule is a rigid three-dimensional mesh consisting of a silphenylenesiloxane core surrounded by functional groups. The advantages of such a structure are low swelling, a high oxygen-reactive ion etching resistance, and a high softening temperature. A 0.075 μm line-and-space pattern is well-defined after electron beam exposure. TSPS can also be used as a deep-UV resist. A 0.25 μm pattern can be delineated using a TSPS/novolac bi-level resist systems with a KrF-excimer laser stepper (NA = 0.37).

1. Introduction

Because the minimum VLSI pattern size is now in the sub-half micron region, conventional monolayer resists can no longer satisfy all VLSI fabrication requirements. Due to the excessive absorbency and the light reflected from the patterned substrates, it is difficult to control the pattern profile and line width using a monolayer resist.

In a typical bi-level resist process¹⁾, a thick bottom layer coats the wafer providing a uniform surface. Then, a thin resist layer is spun on the bottom layer. After exposure, the upper resist pattern is developed and the bottom layer is etched by oxygen-reactive ion etching (O_2 -RIE). The bi-level resist system has many advantages over a monolayer resist system, for example, planarization of substrate topography, reduction of light reflected from the patterned substrate, and fine pattern fabrication with a high aspect ratio. To be suitable for sub-half micron fabrication, a bi-level resist must meet many requirements, for example, high sensitivity, high resolution, and resistance to O_2 -RIE.

A number of polysiloxane resists²⁾⁻⁸⁾ have been proposed as a top imaging resist layer for

bi-level resists because their high silicon content makes them resistant to O_2 -RIE. However, due to the increased proximity effect and resist swelling, it is difficult to obtain pattern spacing closer than 0.2 μm .

We developed a negative organosilicon resist, three-dimensional polysilphenylenesiloxane (TSPS). TSPS is a three-dimensional mesh consisting of a silphenylenesiloxane core surrounded by functional groups. TSPS is more rigid than conventional linear and ladder-siloxane resists because bulky aromatic rings are introduced into the three-dimensional mesh core to correct the Si-O bond angle. The advantages of this rigidity are improved resist contrast, suppressed swelling, and improved thermal stability.

2. Experiment

2.1 Synthesis

Figure 1 shows the synthesis flow of TSPS. To synthesize the TSPS core, we hydrolyzed 1, 4-bis (trialkoxysilyl) benzene, followed by dehydrated condensation polymerization using an acid catalyst. After core polymerization, residual silanol groups around the core were

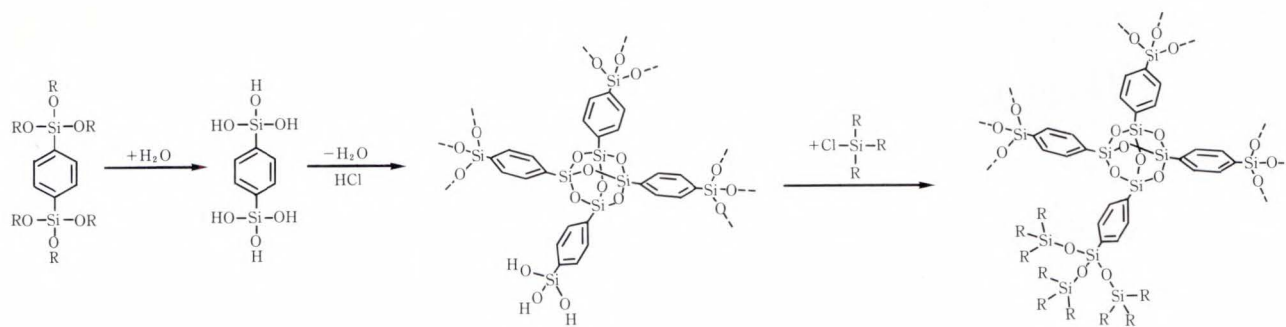


Fig. 1—Synthesis flow of TSPS.

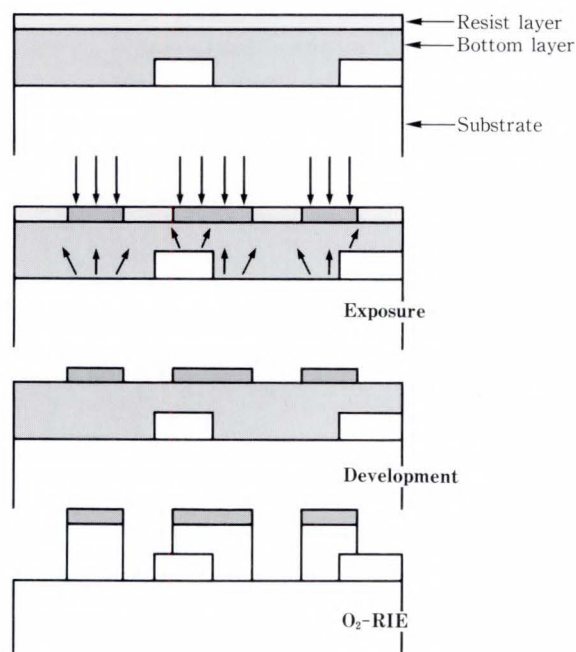


Fig. 2—Bi-level resist process.

terminated with triorganochlorosilane.

The mixture was washed several times with water, then poured into acetonitrile to isolate the solid polymer. The original TSPS polymer was fractionated to obtain a narrow molecular weight distribution.

2.2 Bi-level resist process

Figure 2 shows the bi-level resist process. We dissolved the TSPS resist in methylisobutylketone (MIBK), spin coated a 0.1-0.2 μm thick TSPS top layer on a 0.5-1 μm thick hard-baked nobolak resist (Shipley: MP-1300) bottom layer,

and then prebaked the structure at 80 $^{\circ}\text{C}$ for 20 min.

The TSPS resist was exposed using an electron beam lithography system (Elionix: ELS-3300, 30 kV) and a KrF-excimer laser stepper (248 nm, NA = 0.37). The exposed resists were spin-developed in alcohol mixture solvents.

The resist pattern was transferred to the bottom layer by O_2 -RIE (Anelva: DEM-451) at an oxygen pressure of 2.6 Pa, a gas flow of 10 sccm (standard $\text{cm}^3 \text{min}^{-1}$), and an applied power density of 0.16 W/cm^2 .

3. Results and discussion

3.1 Molecular structure

We studied the TSPS structure using ^{29}Si -NMR (Nuclear Magnetic Resonance) (Jeol: GX500) and GPC-LALLS gel-permeation chromatography equipped with a low-angle laser light scattering photometer⁹⁾ (Tosoh: HLC-8020, LS-8000). Figure 3 shows the ^{29}Si -NMR spectra of TSPS. In the intermediate state of synthesis, the spectrum showed two broad peaks centered at -60 ppm and -70 ppm. These peaks indicate the presence of residual SiOH and $\text{Si}(\text{OH})_2$ groups. As synthesis advanced, silanol groups were dehydrated. In the final state of synthesis, the peaks due to the silanol groups had almost completely been eliminated.

Figure 4 shows the GPC-LALLS chromatograms of TSPS and ladder-polysilphenylene-siloxane {SPS⁸⁾}. Elution curves were obtained using a LALLS photometer (LS) and refractometer (RI). The LS peak of TSPS appears before

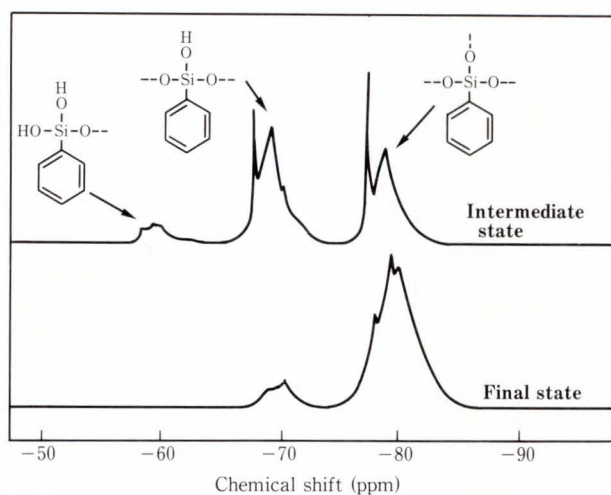


Fig. 3—²⁹Si-NMR spectra.

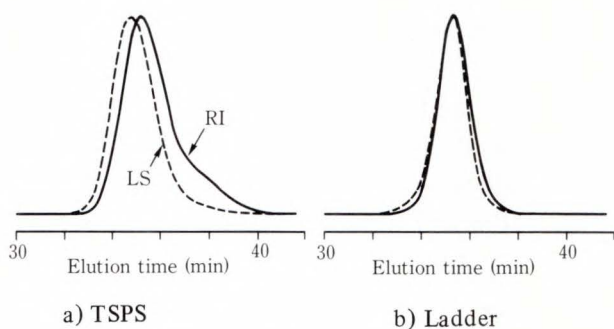


Fig. 4—GPC-LALLS chromatograms.

the RI peak. The average molecular weights (M_w) of TSPS and ladder-SPS as determined using a conventional GPC calibrated with polystyrene and GPC-LALLS are shown in Table 1. The M_w of TSPS as determined using GPC-LALLS is higher than that of ladder-SPS; whereas the M_w of TSPS as determined by conventional GPC is lower than that of ladder-SPS. This suggests that TSPS's M_w is higher than that of ladder-SPS, even though its molecular size is smaller. It may therefore be concluded that the TSPS molecule has a closely packed three-dimensional mesh structure (see Fig. 5).

3.2 Electron beam contrast and sensitivity

Figure 6 shows the sensitivity curves for TSPS and ladder-SPS with a dispersion of 1.6. The functional groups of both TSPS and ladder-SPS are methyl. The film thickness was mea-

Table 1. M_w of TSPS as determined using conventional GPC and GPC-LALLS

Material	Conventional GPC	GPC-LALLS
TSPS	4.5×10^4	1.7×10^5
Ladder	5.8×10^4	1.2×10^5

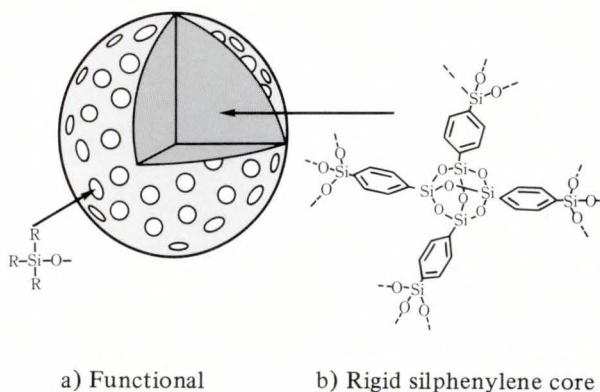


Fig. 5—Structure model of TSPS.

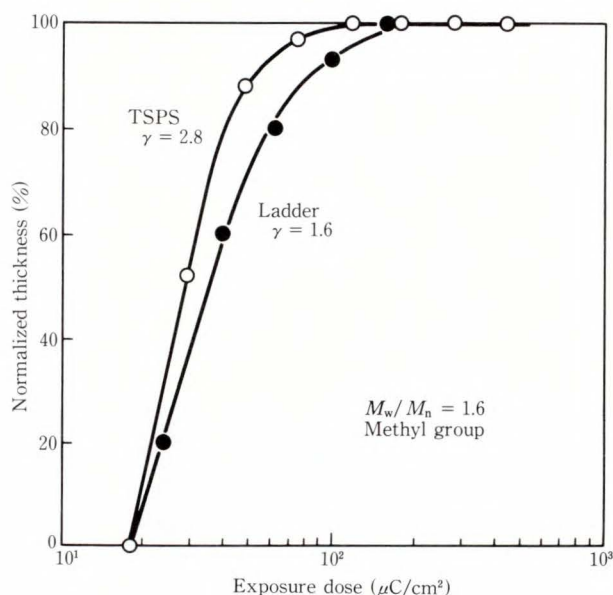


Fig. 6—Sensitivity curves for electron beam exposure

sured using the alpha-step (TENCOR). The TSPS gamma value obtained from the sensitivity curve is about 2.8. The gamma of ladder-SPS is about 1.6. The contrast of TSPS is higher than that of conventional siloxane negative resists such as linear and ladder types. The electron dose for a residual 50 percent resist thickness is $28 \mu\text{C}/\text{cm}^2$. Introducing more sensitive function-

al groups, for example, chloromethyl, produces an even higher sensitivity.

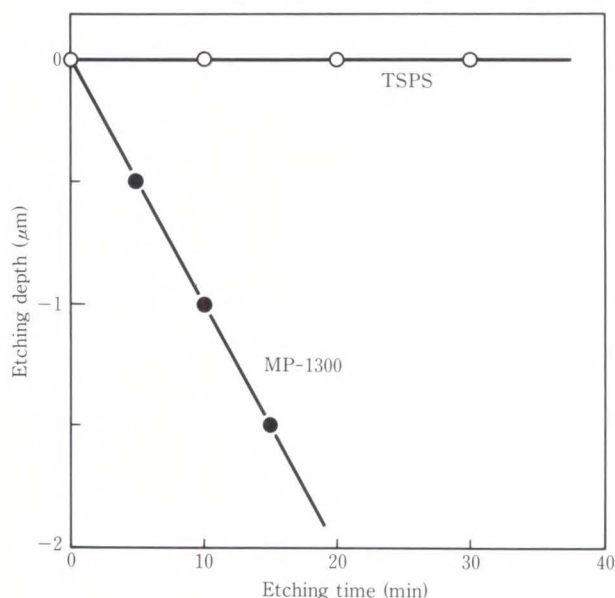


Fig. 7—O₂-RIE rates.

Table 2. Softening temperatures

Molecular weight (M_w)	Softening temperature (°C)	
	TSPS	Ladder
5 000	> 400	150
10 000	> 400	210
50 000	> 400	360

3.3 O₂-RIE resistance and thermal resistance

Figure 7 shows the oxygen plasma etching rates for TSPS films and the hard-baked MP-1300 resist bottom layer. The TSPS resist was etched at about 10 Å/min (1 nm/min) and the MP-1300 at 1 000 Å/min (100 nm/min), making the rate for the TSPS resist one one-hundredth of the rate for MP-1300.

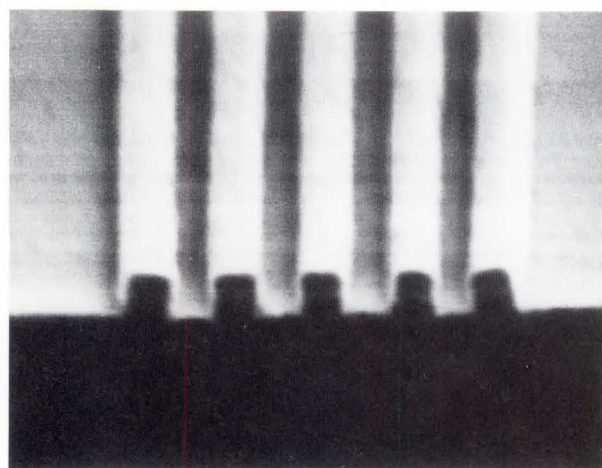
Table 2 shows the softening temperatures of TSPS and ladder-type polysiloxane { polymethylsilsesquioxane⁵⁾}. TSPS has no softening temperature under 400 °C, but the ladder-type's softening temperature at these molecular weights ranges from 150 °C to 360 °C. This suggests that TSPS exhibits high thermal stability due to its rigid structure.

3.4 Resolution

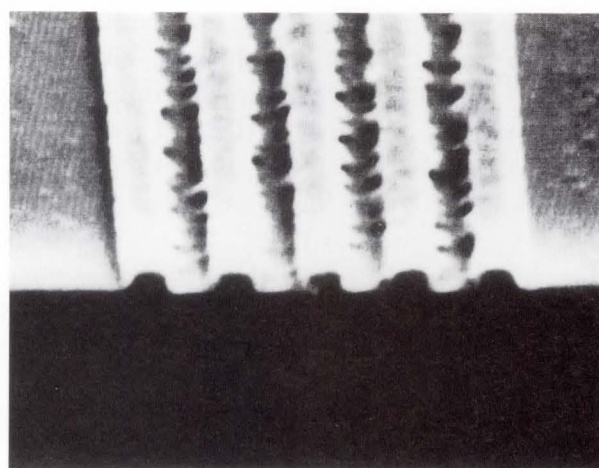
Table 3 shows the molecular particle sizes of TSPS and ladder-type polysiloxane when they are dissolved in a poor solvent, isopropylalcohol (IPA), and a good solvent, methylisobutylketone (MIBK). The particle size was determined

Table 3. Particle sizes in solvents

Solvent	Ladder (nm)	TSPS (nm)
Poor (IPA)	16.2	16.5
Good (MIBK)	54.2	17.3



a) TSPS



b) Ladder

0.5 μm

Fig. 8—Resist patterns after electron beam exposure.

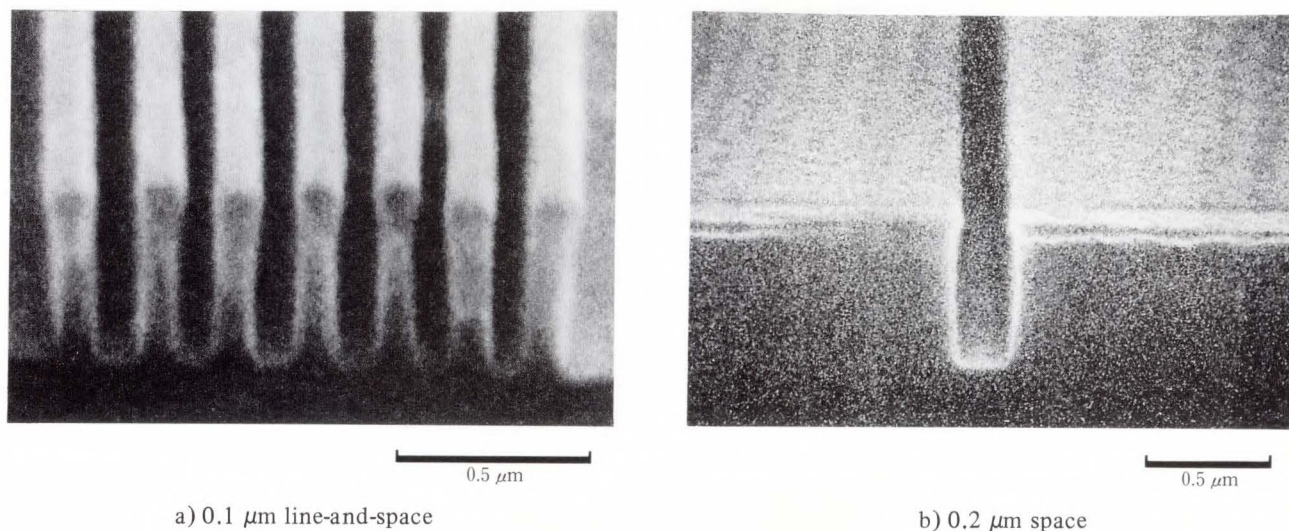


Fig. 9—Bi-level resist patterns.

using a dynamic light scattering system (Otsuka Electronics; DLS-700). Due to swelling of the ladder-polymer's random coil structure, the molecular size of ladder-siloxane is larger in the good solvent than that in the poor solvent. In contrast, TSPS shows little variation in particle size, indicating that swelling is suppressed due to its rigid structure. Figure 8 shows the imaging-layer resist patterns of TSPS and ladder-type polysiloxane after electron beam exposure. TSPS exhibits a higher resolution with its well-defined 0.2 μm line-and-space pattern. The increased resolution is a direct result of the suppressed swelling because of polymer rigidity.

Figure 9 shows bi-level resist patterns obtained using the TSPS/MP-1300 bi-level resist system. The TSPS functional groups are methyl and chloromethyl groups, and the exposure dose was 16 $\mu\text{C}/\text{cm}^2$. Using O_2 -RIE, 0.1 μm line-and-space patterns and 0.2 μm space patterns can be transferred accurately to the bottom layer without thermal deformation. Figure 10 shows 0.075 μm line-and-space patterns obtained using the TSPS/MP-1300 bi-level resist system. These patterns are possible because of the small particle size of TSPS.

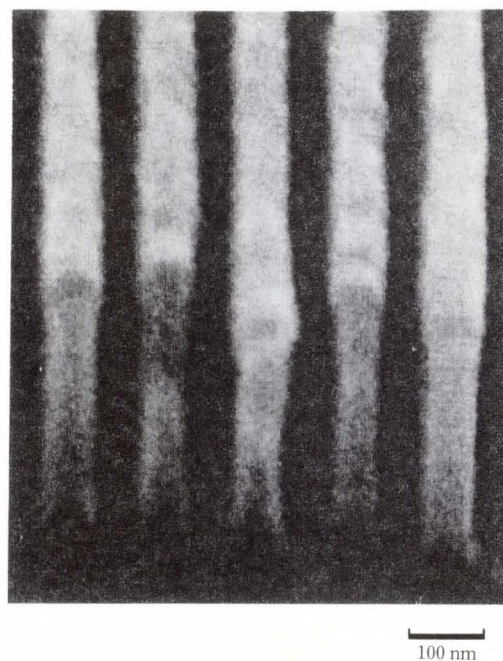


Fig. 10—0.075 μm line-and-space patterns.

3.5 Application as a KrF-excimer laser resist

TSPS can also be used as a negative bi-level deep-UV resist when suitable functional groups, for example, vinyl and phenyl, are introduced. These functional groups make the TSPS sensitive to a KrF-excimer laser. Figure 11 shows the

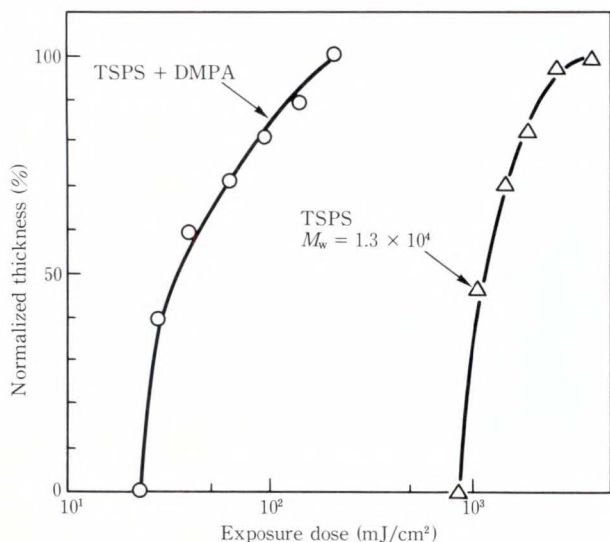


Fig. 11—Sensitivity to deep-UV light of TSPS plus DMPA.

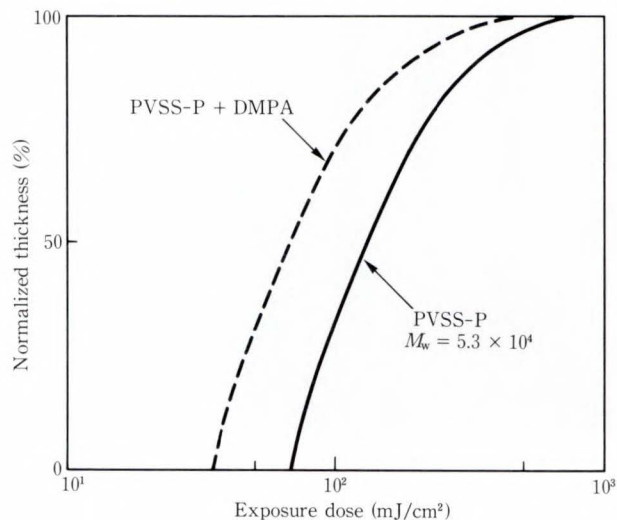


Fig. 13—Sensitivity to deep-UV light of ladder-siloxane plus DMPA.

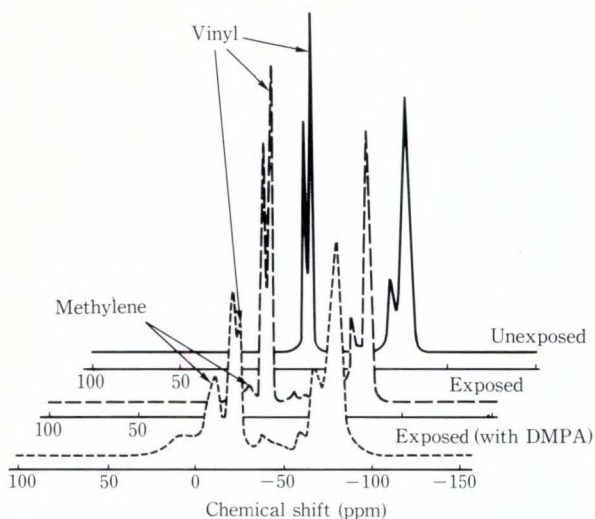


Fig. 12—²⁹Si CP-MAS NMR spectra.

KrF-excimer laser sensitivity curves for TSPS with a M_w of 1.3×10^4 . To increase TSPS sensitivity, a free radical photoinitiator was incorporated into the polymer. We selected 2, 2-dimethoxy-2-phenyl acetophenone (DMPA) as a photoinitiator because it is compatible with the polymer, and solvents containing DMPA formed a uniform film upon spinning. Adding 10 percent of DMPA increases TSPS's sensitivity by a factor of about 20.

Figure 12 shows the ²⁹Si CP-MAS NMR (Jeol: EX-270) spectrum of the exposed TSPS

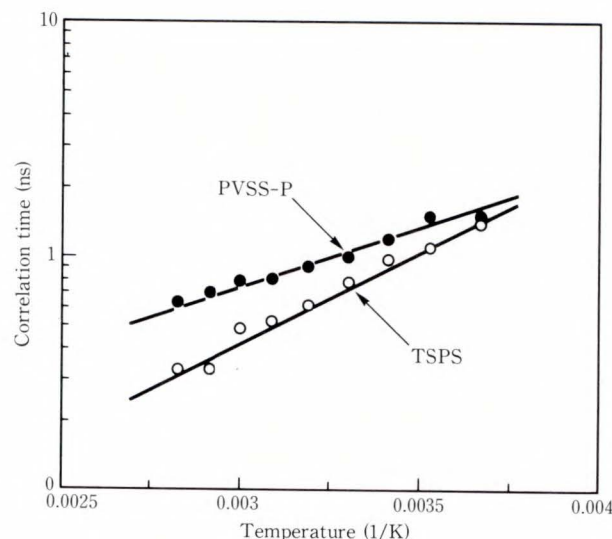


Fig. 14—Relationship between correlation time and temperature.

resist with and without DMPA and that of the unexposed resist. We found that exposure produced methylene groups and reduced the number of vinyl groups. These changes are more dramatic when DMPA is added. This suggests that DMPA acts as a catalyst for the cross-linking of vinyl groups.

DMPA efficiently generates a benzoyl and substituted benzylic radical with deep-UV irradiation¹⁰. The benzylic radical rearranges to

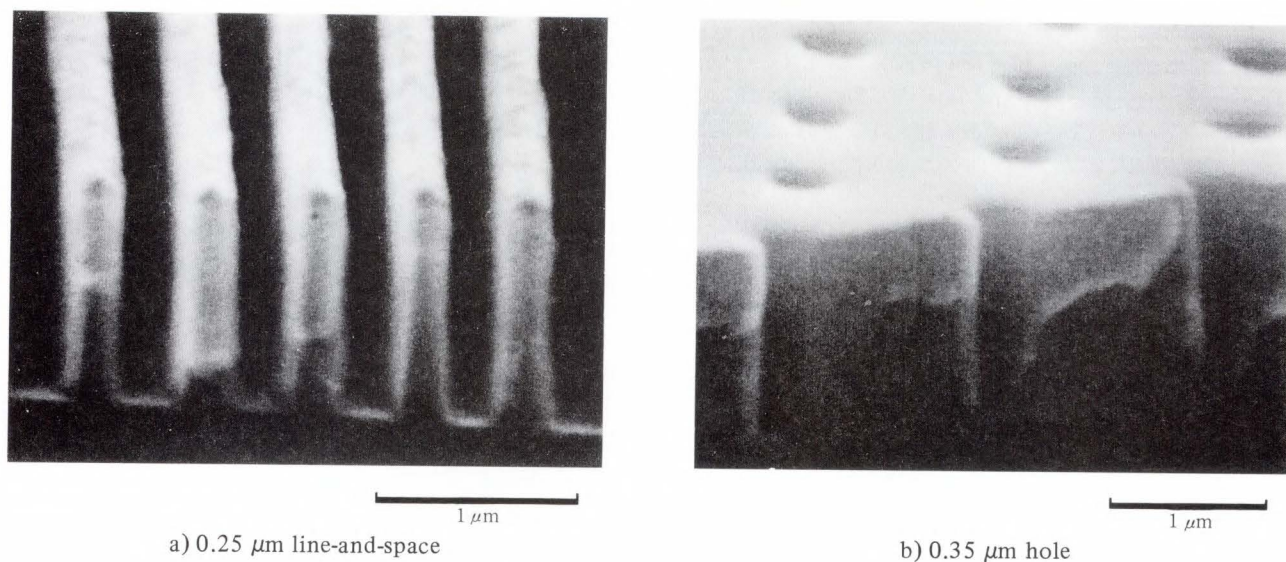


Fig. 15—Bi-level TSPS resist patterns exposed using KrF-excimer laser.

give a highly reactive methyl radical which diffuses readily and initiates crosslinking of the polymer. This means however that the crosslinkage efficiency is limited by the polymer structure. Adding DMPA to ladder-siloxane having vinyl and phenyl functional groups⁷⁾ had little effect on sensitivity (see Fig. 13). We studied the difference in crosslinkage efficiency using spin probe analysis¹¹⁾ with electron spin resonance (ESR) spectrometry (Jeol: JES-FE3XG). Figure 14 shows the relationship between the correlation times of TEMPO probes dispersed into the polymers and the temperature. The correlation time of the TSPS is shorter at 0 °C to 80 °C, indicating that the probe in the TSPS is more mobile than the probe in the ladder siloxane. This suggests that radicals generated by exposing the DMPA in TSPS can readily diffuse around the vinyl functional groups of the polymer. Thus, cross-linking can be initiated easily.

Figure 15 shows bi-level TSPS resist patterns that were exposed using a KrF-excimer laser. A 0.25 μm line-and-space pattern and a 0.35 μm hole pattern can be delineated using the TSPS/MP-1300 bi-level resist system with a KrF-excimer laser stepper.

4. Conclusion

We developed a organosilicon resist, three-dimensional polysilphenylenesiloxane (TSPS), for use as a negative bi-level electron-beam resist or KrF-excimer laser resist. The TSPS molecule is a rigid three-dimensional mesh consisting of a silphenylenesiloxane core surrounded by functional groups. The structure's advantages are high contrast, low swelling, and high thermal stability. A 0.075 μm rectangular pattern is easily delineated using a TSPS/MP-1300 bi-level resist system. TSPS can also be used as a negative bi-level deep-UV resist when suitable functional groups, for example, vinyl and phenyl, are introduced. These functional groups make TSPS sensitive to a KrF-excimer laser, enabling a 0.25 μm pattern resolution. Bi-level resist systems using TSPS show high sensitivity and high resolution. TSPS has great potential for applications in quarter micron ULSI chip production.

References

- 1) Lin, B. J.: Multilayer Resist Systems and Processing. *Solid-State Technol.*, **26**, 5, pp. 105-112 (1983).
- 2) Morita, M., Tanaka, A., Imamura, S., and Kogure, O.: High Resolution Double Layer Resist System Using New Silicon Based Negative Resist (SNR). *Jpn. J. Appl. Phys.*, **22**, pp. L659-L660 (1983).
- 3) Sakata, M., Ito, T., and Yamashita, Y.: Silicon

- Containing Deep UV Resist. *J. Photopolym. Sci. Technol.*, **3**, 2, pp. 173-178 (1990).
- 4) Sugito, S., Ishida, S., and Iida, Y.: Development of High Contrast Siloxane Electron-Beam Resist and Application. *NEC Res. Develop.*, **92**, 1, pp. 18-24 (1989).
 - 5) Fukuyama, S., Yoneda, Y., Miyagawa, M., and Nishii, K.: Fujitsu Limited. Use of polysilisesquioxane without hydroxyl group for forming mark. US Patent 4 657 843, 1987-04-14.
 - 6) Saito, K., Shiba, S., Kawasaki, Y., Watanabe, K., and Yoneda, Y.: Ladder structure silicone resist PVSS. *Proc. SPIE*, **920** (Advances in Resist Technology and Processing V), pp. 198-202 (1988).
 - 7) Watanabe, K., Shiba, S., Saito, K., and Yoneda, Y.: Polyladder-organosiloxane Bi-level Resist. *J. Photopolym. Sci. Technol.*, **2**, 1, pp. 103-108 (1989).
 - 8) Oikawa, A., Fukuyama, S., Yoneda, Y., Harada, H., and Takada, T.: Polysilphenylenesiloxane Resin as an Interlevel Dielectric for VLSI Multilevel Interconnections. *J. Electrochem. Soc.*, **137**, 12, pp. 3923-3925 (1990).
 - 9) Takagi, T.: Determination of protein molecular weight by gel permeation chromatography equipped with low-angle laser light scattering photometer. *Progress in HPLC*, **1**, Parrez, eds. VNU Sci. Press, 1985, pp. 27-41.
 - 10) Tokumaru, K., and Ohkawara, M.: "4. Polymerization Reaction". (in Japanese), Sensitizer, 1st ed., Tokyo, Kodansha, 1987, pp. 64-99.
 - 11) Kanbara, S.: "4. ESR". (in Japanese), Magnetic Resonance of Polymer, 1st ed., Kyoritsu, 1975, pp. 371-555.



Keiji Watanabe

Advanced Materials Laboratory
FUJITSU LABORATORIES, ATSUGI
Bachelor of Chemical Eng.
Tokyo University of Agriculture and
Technology 1986
Specializing in Resist Materials and
Microlithography



Yasuhiro Yoneda

Advanced Materials Laboratory
FUJITSU LABORATORIES, ATSUGI
Bachelor of Industrial Chemistry
Seikei University 1970
Specializing in Resist Materials and
Lithography



Takahisa Namiki

Advanced Materials Laboratory
FUJITSU LABORATORIES, ATSUGI
Bachelor of Chemistry
Tokyo Metropolitan University 1986
Master of Chemistry
Tokyo Metropolitan University 1988
Specializing in Resist Materials and
Microlithography

Polysiloxane as an Interlevel Dielectric for VLSI Fabrication

• Shun-ichi Fukuyama • Michiko Kobayashi • Yasuhiro Yoneda

(Manuscript received February 3, 1992)

A new silylated polymethylsilsesquioxane (PMSS) resin has been developed and evaluated for use as an interlevel dielectric in VLSI multilevel interconnections. PMSS has good heat resistance. The dielectric constant is 3, which is lower than that of conventional inorganic dielectrics. Degassing from PMSS is very low. PMSS does not crack even when it is 4 μm thick on a 1 μm thick metal topographic substrate that is heated to 450 °C in nitrogen. PMSS has excellent planarity. Trilevel interconnections using PMSS as an interlevel dielectric can be fabricated. Well-planarized metal wiring patterns can be obtained, and no cracks have been found in PMSS layers.

1. Introduction

The fabrication of multilevel interconnections requires a planarized interlevel dielectric layer. Inorganic chemical vapor deposition (CVD) dielectric materials such as silicon dioxide (SiO_2), silicon nitride (SiN), and phosphosilicate glass (PSG) have been widely used. However, these materials conform to the surface topography of the substrates, which leads to severe step-coverage problems with metalization patterns.

Spin-coating resins have been used to flatten the surface^{1),2)} because they can be easily spun on wafers and make planarization relatively easy. Spin on glass (SOG) materials are widely used for planarization, but they usually easily crack when cross-linked by heating on the substrate at temperatures of 350 °C and above.

Siloxanes are useful for interlevel dielectrics and are expected to exhibit a high crack resistance. Conventional carbon-based resists can be used as masks for subsequent dry etching because siloxanes are easily etched by fluorocarbon gases. Siloxanes adhere to inorganic materials such as SiO_2 , SiN , PSG, and wiring metals.

Siloxanes do not readily adsorb water, so

the increase in contact resistance of vias caused by outgassed moisture from polymers can be avoided. The low dielectric constants of siloxanes should also reduce the interconnection delay.

However, all current siloxane polymers undergo thermal decomposition in their organic side chains at temperatures above 400 °C. There is therefore a need for a new interlevel dielectric layer that can be heated above 400 °C without decomposing.

In this study we developed a silsesquioxane resin for use as an interlevel dielectric that does not readily crack, even when heated to 500 °C in nitrogen. We synthesized a silylated polymethylsilsesquioxane (PMSS) resin and examined its properties.

This paper describes the polymer design, preparation, and properties of PMSS and discusses its application as an interlevel dielectric. This paper also describes a trilevel interconnection that we fabricated.

2. Methods

PMSS was prepared as explained below (see Fig. 1). Methyltrichlorosilane (I) was dissolved in a solvent, to which water was slowly

excellent thermal resistance, phenyl groups make siloxanes very brittle, which decreases the spin-coatability and makes them unsuitable as an interlevel dielectric. We therefore chose a PMSS with methyl groups as side chains because of its good thermal resistance and spincoatability.

Because they have many cross-linkers (Si-OH), SOG materials crack easily when they are cross-linked by heating. The number of cross-linkers determines crack resistance in siloxanes. A PMSS with only a few cross-linkers was synthesized by silylation. Silylation of silanol groups is commonly used to make them stable. Silylation can also be used to control residual silanol groups, so PMSS can be hardened.

3.2 Polymer preparation

PMSS was synthesized from methyltrichlorosilane (I). The weight-averaged molecular weights of polymers obtained were 5×10^3 to 5×10^4 . Polymerization for longer than 3 h at 90 °C yielded polymers with a molecular weight of more than 1×10^6 that were still soluble in some solvents. When the hydrolysis was carried out at high temperature or water was introduced rapidly into the flask, insoluble compounds were formed. These insoluble compounds were probably three-dimensional

compounds that formed because of the rapid random condensation. We determined the structure of these compounds from their IR spectra (see Fig. 2). However, the exact molecular structure of PMSS is still unclear. Figure 3 shows the ^{29}Si -NMR spectrum of non-silylated PMSS. The figure shows a broad peak from -51 ppm to -60 ppm, corresponding to the presence of residual silanol groups. The ratio of silanol to silicone units of PMSS is about 0.16. The ideal molecular structure of PMSS is shown in Fig. 4. Silylation was done using trimethyl-

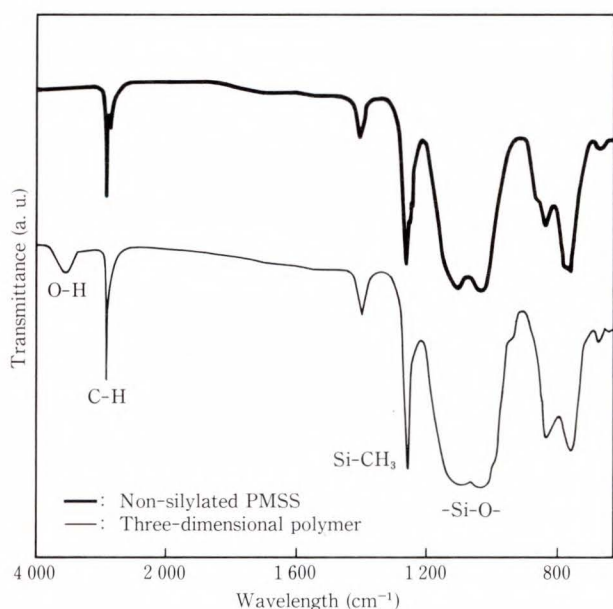


Fig. 2—IR spectra.

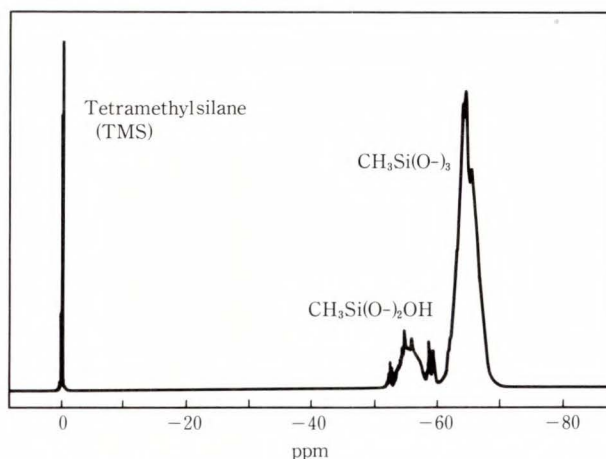


Fig. 3— ^{29}Si -NMR spectrum of non-silylated PMSS.

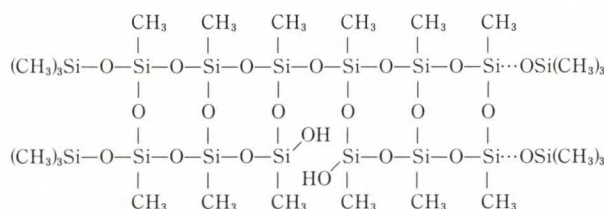


Fig. 4—Ideal molecular structure of PMSS.

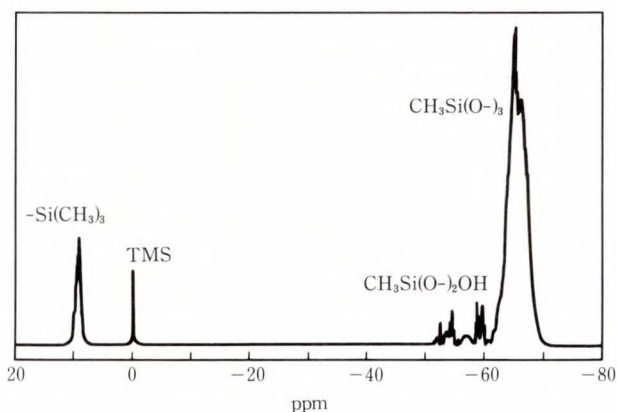


Fig. 5— ^{29}Si -NMR spectrum of PMSS.

chlorosilane as an endblocker and pyridine as catalyst. The ^{29}Si -NMR spectrum (see Fig. 5) showed that almost 80 percent of the silanol-groups had been replaced by trimethylsilyl-groups.

3.3 PMSS properties

3.3.1 Thermal resistance

We compared the thermal resistances of a PMSS and a non-silylated polymer using thermogravimetric analysis. Figure 6 shows that PMSS exhibits substantially no weight loss up to 600 °C in nitrogen. However, the non-silylated polymer begins to lose weight at 350 °C. This is because non-silylated PMSS has many silanol groups which hydrate easily on heating.

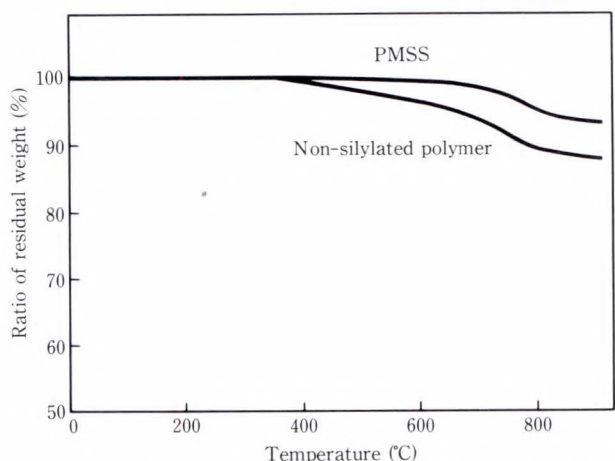


Fig. 6—Results of thermogravimetric analysis (TGA) in nitrogen flow. Heating rate was 10 °C/min.

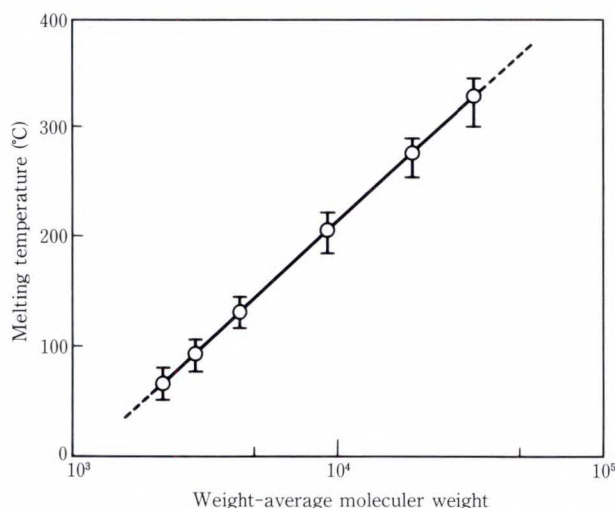


Fig. 7—Melting temperature of PMSS powder in nitrogen flow. Heating rate was 10 °C/min.

3.3.2 Melting temperature

When a PMSS polymer with a weight-averaged molecular weight of less than 3.5×10^4 is heated at 350 °C, it melts. But non-silylated PMSS polymer does not melt because of cross-linking by the dehydrated condensation of the silanol groups that do not react during polymerization and remain in polymers (see Fig. 3). Because a small number of silanol groups still remain in the silylated polymer (see Fig. 5), the PMSS is cured by heating it above its melting temperature. When a polymer powder is heated, it becomes a transparent viscous liquid before it becomes insoluble. Figure 7 shows the relationship between the melting temperature and molecular weight. Even PMSS with a molecular weight as high as $M_w = 3.5 \times 10^4$ melts below 350 °C, which makes it easy to planarize the topography using PMSS. Planarization is discussed in detail in subsection 3.3.8.

3.3.3 Stress

Table 1 shows the stresses in PMSS film and a conventional organic SOG film (OCD-TYPE7: Tokyo Ohka Kogyo Co., Ltd.). Both films are tensile and the stress in the SOG film is five times as large as that in the PMSS film. This difference in stress is probably related to the densities of cross-linking. Because SOG originally has a large quantity of silanol and alkoxy groups, it should become a highly cross-linked layer after condensation and have a high tensile stress when heated.

Silanol groups are very rare in PMSS, so the density of cross-linking is very low. Thick SOG films crack easily. SOG films are usually applied up to about 0.5 μm thick on the metal topographic substrates. High crosslinked SOG is very brittle and cracks because of the thermal expansion of the metal. PMSS films are more flexible because of their low cross-linking density and are clearly less susceptible to cracking than SOG films. Crack resistance is described in detail in subsection 3.3.7.

Table 1. Stress in PMSS and SOG films

Samples	Stress (dyne/cm ²)
PMSS	3.2×10^8 (Tensile)
SOG	1.6×10^9 (Tensile)

Table 2. Dielectric constants of PMSS and other inorganic materials after curing

Samples	Dielectric constants
PMSS	3 (350 °C in N ₂)
	3 (500 °C in N ₂)
	6.8 (450 °C in Air)
SiO ₂	4
SiN	7
PSG	4

Table 3. Heating conditions for samples used in degassing measurements

Samples	Heating conditions
PMSS	350 °C, 30 min in N ₂
SOG	450 °C, 30 min in N ₂

3.3.4 Dielectric constant

So far, interlevel dielectrics have been used only for planarization and insulation. However, to satisfy the growing demand for faster devices, dielectric constants must be reduced in order to reduce the interconnection delay. In conventional multilevel interconnections, chemical vapor deposition (CVD) of SiO₂, SiN, and PSG has been used for interlevel dielectrics. The dielectric constants of SiO₂ and PSG are about 4, and that of SiN is about 7.

Table 2 lists the dielectric constants of PMSS and other inorganic materials after curing. The dielectric constant of PMSS is 3 after heating in nitrogen at 500 °C and 6.8 after heating in air at 450 °C. This shows that PMSS can be heated in nitrogen to up to 500 °C without decomposing.

Except when heated to 450 °C in air, PMSS never decomposes. This shows that the dielectric constant of PMSS is intrinsically 3.

The dielectric constant of PMSS is very low compared to that of SiO₂, SiN, and PSG – even when heated at high temperatures. Therefore, PMSS should reduce the interconnection delay when used as an interlevel dielectric.

3.3.5 Degassing

Reducing degassing from an interlevel dielectric resin is important for good conductivity in vias⁵⁾.

Samples were cured as shown in Table 3 before being placed in the chamber. After a

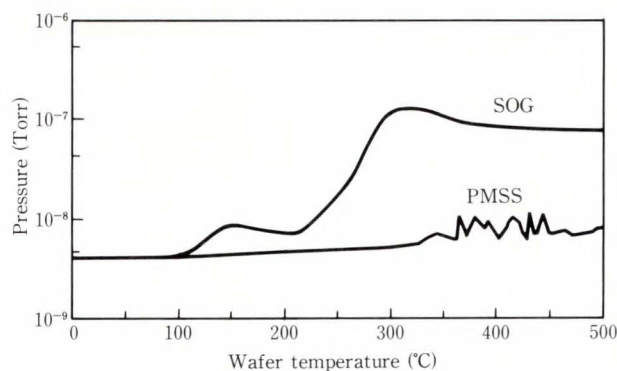
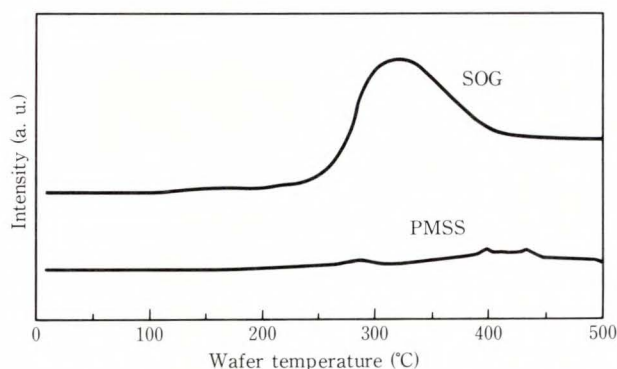


Fig. 8—Degassing from a SOG film cured at 450 °C and a PMSS film cured at 350 °C.

Fig. 9—MS intensity of H₂O from SOG and PMSS films.

sample was inserted, the chamber was evacuated for 15 min to about 5×10^{-9} Torr. The wafer temperature was then raised to 500 °C by microwave irradiation and maintained for 5 min.

The wafer temperature and the pressure of the vacuum chamber during heating were recorded. During heating, the mass spectrum (MS) intensities of MS No. 18, 28, and 44 were measured.

There is considerable degassing from a SOG film during heating (see Fig. 8). The main outgassed component is water (see Fig. 9). The pressure curve is similar to the MS intensity curve of water. Degassing from PMSS is as low as that for a bare Si wafer, indicating that PMSS provides better conductivity in vias than SOG.

There are two possible explanations for the very low degassing from PMSS. The first is that PMSS film has a hydrophobic surface, so water is not easily produced by dehydrated condensation. SOG, on the other hand, contains a large quantity of silanols and alkoxy groups and has a hydroscopic surface. Therefore, SOG readily

produces water, which causes a lot of degassing. The second explanation is that PMSS has a high film density. The film density of SOG should be low because it contains a lot of alkoxy groups before heating, and heating generates large spaces into which water molecules can easily enter.

3.3.7 Crack resistance

Figure 10 shows the maximum usable film thickness of PMSS on wafers with 1 μm high aluminum wiring patterns. We define this maximum as the thickest PMSS film that can be heated to a given temperature without cracking. Heating was done at various temperatures for 1 h in nitrogen. Since the film thickness depends on the pattern profile, the values on the y-axis are for PMSS thicknesses on bare silicon wafers which were coated with PMSS and heated under

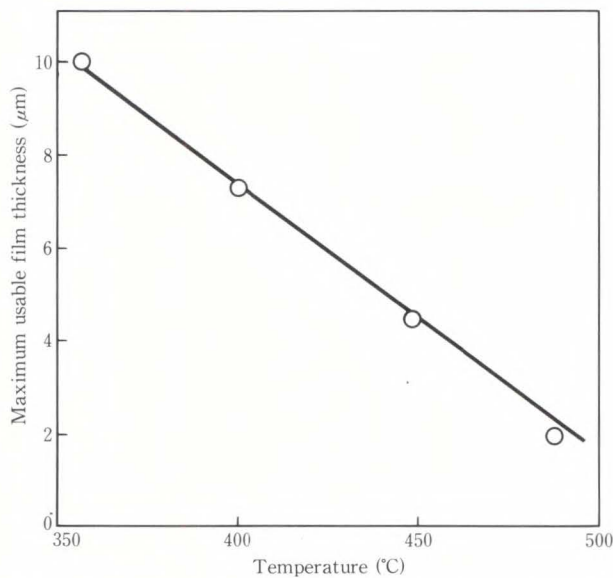


Fig. 10—Maximum usable film thickness of PMSS on wafer with 1 μm high aluminum wiring patterns as a function of heating temperature.

the same conditions as these topographic wafers.

PMSS films up to 4 μm can be heated to 450 $^{\circ}\text{C}$ without cracking. If the heating temperature is decreased to 350 $^{\circ}\text{C}$, the PMSS film can be more than 10 μm thick. PMSS therefore has considerable crack resistance.

3.3.8 Planarity

The best planarizing resins are believed to be resins whose thermal flow and hardening steps can be separated^(6),7). We therefore propose the following tentative explanation of PMSS planarization: PMSS first melts into a low viscosity liquid, flows into cavities, attains well-planarized surfaces at the earlier stages of the heat treatment, and then hardens. Figure 11 shows the dependence of the final step height on the thickness of PMSS layers coated over a substrate having a stepwise difference in height of 1 μm . One curve indicates the final step height of spin coated PMSS over the substrate before heating. The other curve indicates the final step height of

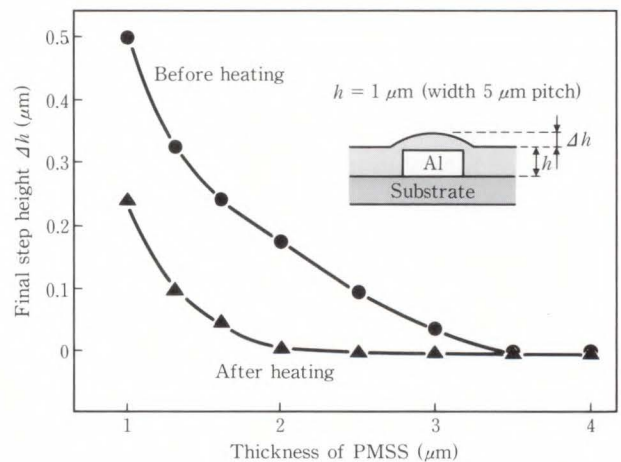


Fig. 11—Dependence of final step height on the thickness of PMSS layers coated on a 1 μm high topographic substrate

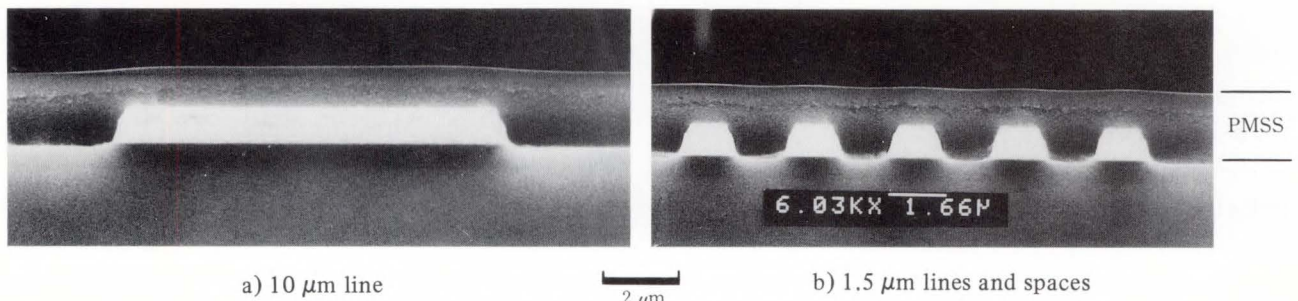


Fig. 12—Planarized profiles of PMSS.

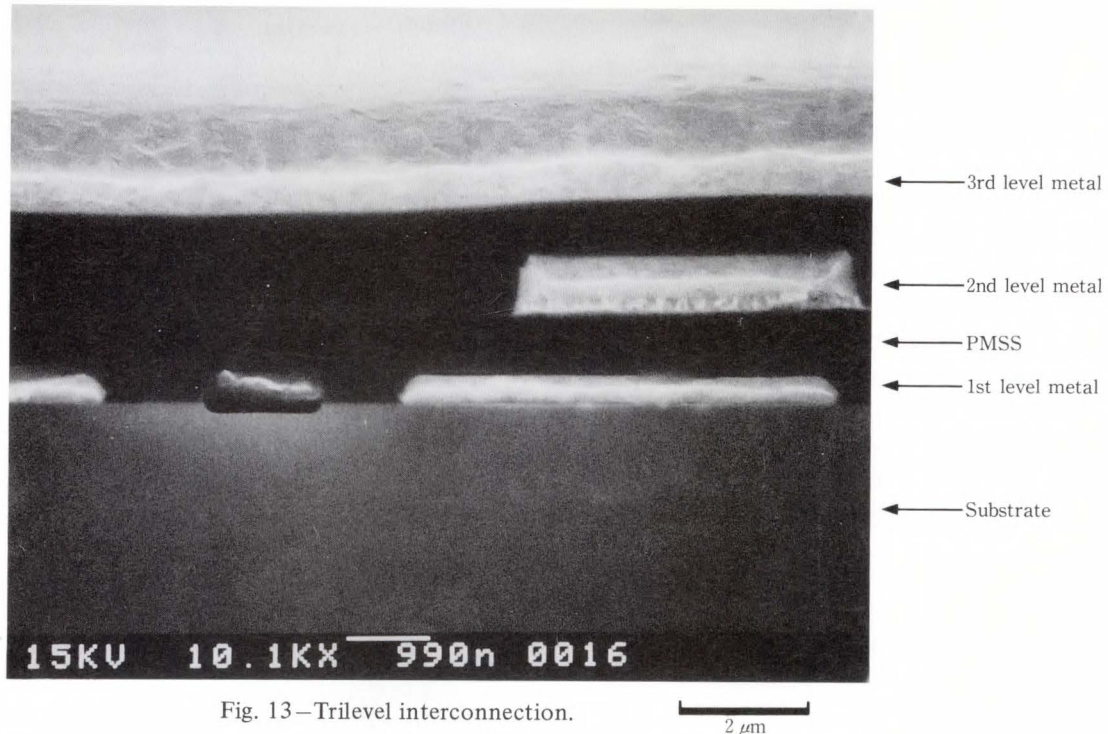


Fig. 13—Trilevel interconnection.

PMSS after heating above the melting temperature. The planarity can be improved by melting the silylated polymer. The final step height of a $1.2\ \mu\text{m}$ thick PMSS film on the substrate was less than $0.1\ \mu\text{m}$. On the other hand, the final step height of the non-silylated PMSS was more than $0.3\ \mu\text{m}$.

The SEM photographs in Fig. 12 show the planarity of PMSS on topographic substrates. The film thickness is $1.8\ \mu\text{m}$ as measured on the bare Si substrate. Heat-treatment was done at $350\ ^\circ\text{C}$ for 1 h in nitrogen. Several patterns are shown, and all patterns were almost perfectly planarized. Even on the isolated pattern (the most difficult to planarize), the planarization is almost perfect {see Fig. 12a}.

3.4 PMSS as an interlevel dielectric

The properties described in the previous sections make PMSS suitable as an interlevel dielectric. An SEM photograph of a trilevel interconnection (see Fig. 13) also shows the suitability of PMSS. It is therefore clear that this method yields excellent planarization. For example, the remaining step height of a $1.6\ \mu\text{m}$ thick second interlevel PMSS layer over $1\ \mu\text{m}$ thick metal is less than $0.1\ \mu\text{m}$. No cracks were

found in these PMSS layers even when a $3.5\ \mu\text{m}$ thick PMSS layer was used to form the metal layers.

PMSS is a promising resin for interlevel dielectrics for VLSI multilevel interconnections⁸⁾.

4. Conclusion

A new silylated polymethylsilsequioxane (PMSS) resin has been developed and evaluated for use as an interlevel dielectric in VLSI multilevel interconnections.

PMSS has good heat resistance. The stress is $10^8\ \text{dyne/cm}^2$, which is lower than that of conventional SOG materials. The dielectric constant is 3, which is lower than that of conventional inorganic dielectrics. Degassing from PMSS is very low. PMSS has good resistance to cracking. It does not crack even when it is $4\ \mu\text{m}$ thick on a $1\ \mu\text{m}$ thick metal topographic substrate that is heated to $450\ ^\circ\text{C}$ in nitrogen. Its planarity is excellent. A trilevel interconnection using PMSS as an interlevel dielectric can be fabricated. Well-planarized metal wiring patterns can be obtained, and no cracks have been found in PMSS layers.

References

- 1) Sato, K., Harada, S., Saiki, A., Kimura, T., Okubo, T., and Mukai, K.: A Novel Planar Multi-level Interconnection Technology Utilizing Polyimide. *IEEE Trans. Parts, Hybrids, Packag.*, **PHP-9**, 3, pp. 176-180 (1973).
- 2) Adams, A.C., and Capio, C.D.: Planarization of Phosphorus-Doped Silicon Dioxide. *J. Electrochem. Soc.*, **128**, 2, pp. 423-429 (1981).
- 3) Brown, J.F., Vogt, L.H., Katchman, A., Eustance, J.W., Kiser, K.M., and Krantz, K.W.: Double Chain Polymers of Phenylsilsesquioxane. *J. Am. Chem. Soc.*, **82**, pp. 6194-6200 (1960).
- 4) Brown, J.F.: Double Chain Polymers and Nonrandom Crosslinking. *J. Poly. Sci.*, **IC**, pp. 83-87 (1963).
- 5) Tompkins, H.G., and Tracy, C.: Desorption from Spin-On Glasses. *J. Electrochem. Soc.*, **136**, 8, pp. 2331-2335 (1989).
- 6) Pampalone, T.R., DiPiazza, J.J., and Kanen, D.P.: Novolac Resin Planarization Layer for Multilayer Resist Imaging Systems. *J. Electrochem. Soc.*, **133**, 11, pp. 2394-2398 (1986).
- 7) Stillwagon, L.E.: Planarization of Substrate Topography by Spin-coated Films: A Review. *Solid State Technol.*, **30**, 6, pp. 67-71 (1987).
- 8) Kosugi, M., Tanaka, A., Mimura, T., and Abe, M.: Multi-level Interconnect Technology for HEMT LSIs. (In Japanese), *IEICE*, **ED89-55**, pp. 37-42 (1989).



Shun-ichi Fukuyama

Advanced Materials Laboratory
FUJITSU LABORATORIES, ATSUGI
Bachelor of Applied Chemistry
Yokohama National University 1983
Specializing in Heat Resistant Resins
and Multi-Level Processes



Yasuhiro Yoneda

Computer Packaging Materials
Laboratory
FUJITSU LABORATORIES, ATSUGI
Bachelor of Industrial Chemistry
Seikei University 1970
Specializing in Resist Materials and
Micro-Lithography



Michiko Kobayashi

Advanced Materials Laboratory
FUJITSU LABORATORIES, ATSUGI
Bachelor of Materials Science and
Chemical Eng.
Yokohama National University 1990
Specializing in Heat Resistant Resins
and Multi-Level Processes

Micromachined Clark Oxygen Electrodes and Biosensors

• Hiroaki Suzuki • Akio Sugama • Naomi Kojima

(Manuscript received February 3, 1992)

Miniature Clark oxygen electrodes were fabricated using micromachining. The type I model has the following components: a cathode and anode formed in a V-groove made by anisotropic etching of silicon, a solid electrolyte, and a gas-permeable membrane. Improving the electrolyte and membrane materials produced excellent long-term storage stability and sterilization tolerance. The type I model was used to monitor fermentation and to make miniature biosensors. The type II model consists of a glass substrate with detecting electrodes bonded to a silicon container substrate with V-grooves. The gas-permeable membrane is thermally adhered fluorinated ethylene-propylene (FEP). Improving the membrane adhesion made the oxygen electrode tolerant to steam-sterilization.

1. Introduction

The Clark oxygen electrode is an electrochemical oxygen sensor. The original design consists of a cathode and anode, an electrolyte, a gas-permeable membrane, and a container for these components. The electrode produces current by electrochemical oxygen reduction at the cathode. The electrode does not suffer from cathode fouling and features room temperature operation, amperometric detection, and stable use in an aqueous solution. The electrode can therefore be applied in fields such as fermentation, clinical diagnosis, and biosensing¹⁾.

A miniature disposable oxygen electrode is required in the clinical and biosensing fields. Currently available oxygen electrodes are relatively large and are too expensive to be discarded after single use. A typical electrode is the size of a fountain pen and costs from several hundred to several thousand dollars. Therefore, several miniature oxygen electrodes were developed including several Clark oxygen electrodes²⁾⁻⁷⁾.

Micromachining has great potential in the development of miniature chemical sensors, and its use in the fabrication of miniature physical

sensors and actuators has increased over the last decade⁸⁾.

The basic techniques include anisotropic etching of silicon, direct and field-assisted bonding, etch-stopping, and conventional photolithography. This paper discusses the miniaturization of the Clark oxygen electrode using these techniques and the incorporation of the electrode in several biosensors.

2. Type I miniature oxygen electrode

2.1 Structure of the type I oxygen electrode

Figure 1 shows a diagram of our type I miniature Clark oxygen electrode. The electrode was fabricated on a 2 mm × 15 mm × 400 μm nondoped (100) silicon substrate. The sensitive area, which contains the essential components of the Clark-type electrode (i.e., the cathode and anode, electrolyte, and membrane), is 0.2 × 2 mm. The electrolyte is contained in two anisotropically-etched 0.2 × 0.7 mm V-grooves⁸⁾⁻¹⁰⁾. The anode was formed in the grooves and the cathode was formed on the area between the grooves. The cathode and anode consist of a 400 nm thick gold film with an intermediate 40 nm thick chromium adhesive

layer. The cathode area exposed to the electrolyte is 0.08 mm^2 . The cathode and anode are connected to pads to which a constant voltage is applied and from which the oxygen reduction current is detected. All areas other than the pads and the sensitive area are covered with negative photoresist. The sensitive areas are filled with electrolyte and then sealed with a gas-permeable membrane.

The type I oxygen electrode is polarographic; that is, it generates a current proportional to oxygen concentration under the applied voltage. The current is generated by electrochemical oxygen reduction at the cathode. The applied cathode-to-anode voltage is typically -1.2 V .

2.2 Electrolyte and gas-permeable membrane materials

Table 1 gives details on the electrolyte and gas-permeable membrane materials that have been tried up to now. The gas-permeable membrane must be hydrophobic so that it passes only gaseous materials and rejects other materials dissolved in an aqueous solution. It must also

be chemically and physically strong, have a good adhesion to the substrate, and should be easy to form into patterns. The membranes for these electrodes were made using silicone rubber and a negative photoresist to which we made slight improvements in terms of strength, adhesion, and other properties.

We chose electrolyte materials that are more compatible with the wafer process. At first, we used an electrolyte impregnated with a gel. We then developed a process that enabled us to form the electrolyte layer on the sensitive area only. We found that forming the gas-permeable membrane on a gel containing water produced a membrane that was weak and incomplete, and had poor sterilization tolerance and long-term stability.

To solve these problems, we used an electrolyte made of poly (vinyl-4-ethylpyridinium bromide) (PVEP) and a double-layered gas-permeable membrane. The oxygen electrode thus produced exhibited good tolerance to steam-sterilization and long-term stability (see Sec. 2.4). It was difficult, however, to batch-fabricate electrode chips on a wafer because the electrolyte and gas-permeable membrane layers could not be formed on certain areas of the wafer.

To solve this problem, we screen-printed a potassium chloride (KCl) electrolyte suspended in polyvinylpyrrolidone (PVP). The pattern formation problem of the gas-permeable membrane was solved using a screen-printing lift-off technique.

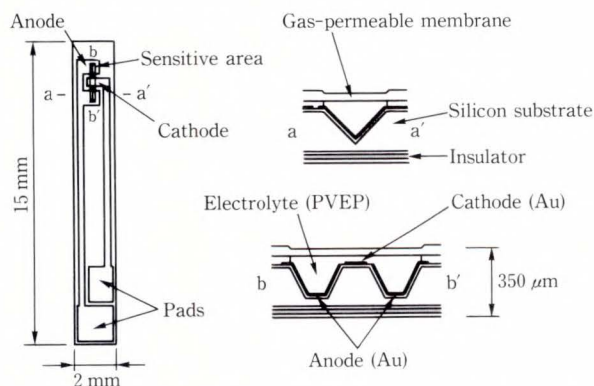


Fig. 1—Oxygen electrode. Cross-sections along the lines aa' and bb' are shown on the right.

2.3 Fabrication of the type I oxygen electrode

The body of the oxygen electrode including

Table 1. Electrolytes and gas-permeable membranes

Electrolyte	Matrix	Electrolyte pattern formation	Membrane	Sterilization
0.1 M KCl	Agarose	Not possible	Negative photoresist	Not tolerant
	Polyacrylamide	Possible	Negative photoresist	Not tolerant
	Calcium alginate	Possible	Silicone resin	Not tolerant
PVEP	—	Not possible	Silicone rubber/negative photoresist	Tolerant
KCl *	PVP paste	Possible	Silicone rubber/negative photoresist	Tolerant

*: Concentration can not determined.

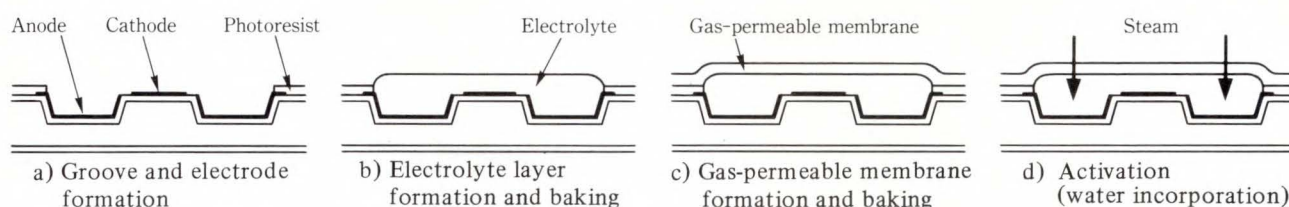


Fig. 2—Fabrication of the type I miniature oxygen electrode with a polyelectrolyte.

the silicon container and electrodes was made by ordinary photolithography. The method is described elsewhere⁷⁾. Our first oxygen electrodes with the PVEP polyelectrolyte were made as follows¹¹⁾ { see Figs. 2a)-d)}:

- 1) The body of the oxygen electrode with the sensitive area delineated by the negative photoresist was prepared.
- 2) The electrolyte layer was formed by applying an aqueous solution of the polymer to the sensitive area with a small rod. Then, the water in the electrolyte was completely removed by baking the electrode at 120 °C for 10 min.
- 3) The double-layered gas-permeable membrane was formed on the electrolyte by applying liquid resin with a small rod. The membrane was then baked to make it stronger and more durable.
- 4) Since the oxygen electrode does not produce a current if there is no water available in the electrolyte for oxygen reduction, water was incorporated into the sensitive area by sterilizing the electrode in steam at 120 °C and 2.2 atm for 15 min.

To solve the problems regarding batch-fabrication and pattern formation, steps 2) and 3) were modified as follows:

- 2') We used an electrolyte consisting of KCl and phosphate salt in the form of precipitated powders having a particle size of less than 10 μm suspended in a PVP paste. The phosphate salt was added to adjust the pH. The viscosity of the electrolyte was adjusted using PVP of various molecular weights. The electrolyte was screen-printed onto the sensitive areas of the electrodes on the wafer.
- 3') Before applying the gas-permeable membrane resins, the pad areas were protected

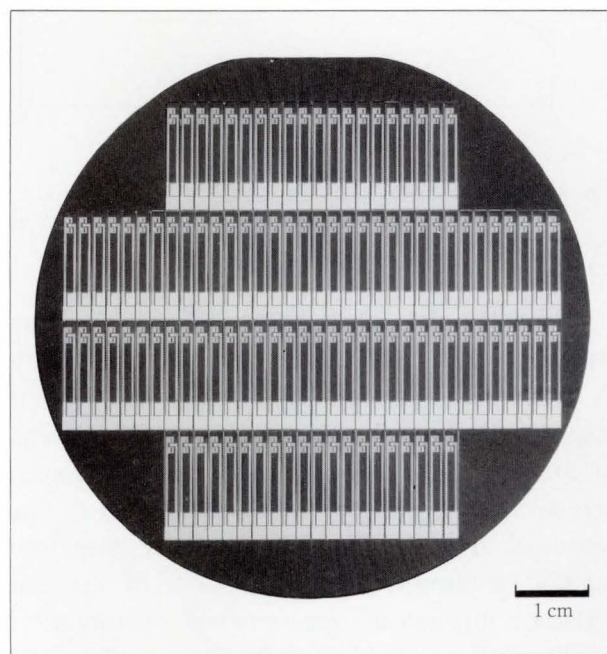


Fig. 3—Miniature oxygen electrodes on a three-inch wafer.

with a screen-printed removable paint which was baked at 150 °C for 10 min. The double-layered gas-permeable membrane was spin-coated onto the substrate. The lower layer was the negative photoresist layer and the upper layer was a silicone membrane. The membrane was baked at 70 °C for 60 min in a humid atmosphere, and then baked at 150 °C for 30 min. Finally, the paint was removed from the pad area along with the gas-permeable membrane. Figure 3 shows a completed three-inch wafer.

2.4 Characteristics of the type I oxygen electrode

This section mainly describes the characteristics of the oxygen electrode having the PVEP polyelectrolyte and double-layered gas-permeable membrane.

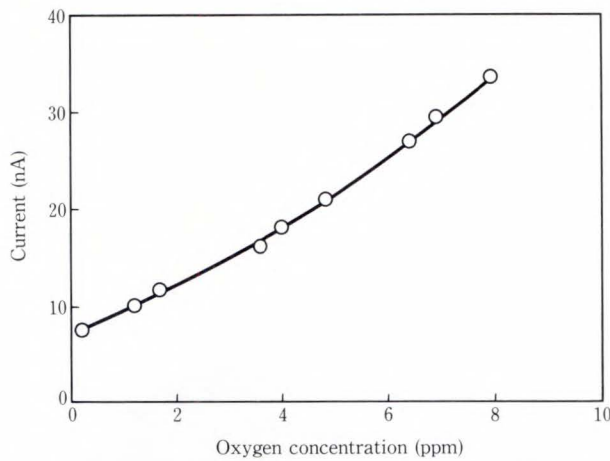


Fig. 4—Calibration curve of the type I oxygen electrode. Calibration was done in 10 mM phosphate buffer (pH 7.0, 27 °C)

Provided the substrate is well insulated the oxygen electrode has a very good response with no appreciable noise. The average 90 percent response time is 80 s. The average response time of an identical electrode made using a single-layered gas-permeable membrane is 30 s. The response time of our electrode is therefore mainly determined by the rate of oxygen diffusion through the gas-permeable membrane.

Sensor response in applications in which the dissolved oxygen concentration level is relatively low (e.g. fermentation) is largely determined by the level of residual current at zero oxygen concentration. Hence, the residual current must be as small as possible. The residual current of this electrode is ten percent of the difference between the levels at oxygen saturation and zero oxygen concentration.

Figure 4 shows a typical calibration curve of generated current versus dissolved oxygen concentration. The curve shows good linearity below 7.9 ppm, at which point the oxygen concentration is saturated at 27 °C. Electroactive materials produced from the gold anode are reduced on the cathode, which causes an increase in residual current and a deterioration in linearity. However, the curve in Fig. 4 shows only a slight non-linearity at lower oxygen concentrations. We have found in another study that electrochemical crosstalk¹²⁾ in the type I electrode is small but not negligible¹³⁾⁻¹⁴⁾.

Two of the most important requirements for

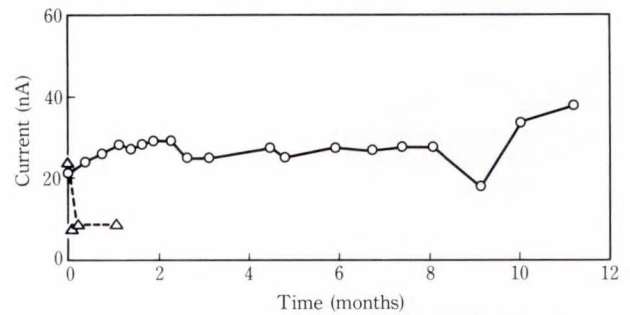


Fig. 5—Long-term stability of oxygen electrodes. Circles indicate stability of the oxygen electrode with the polyelectrolyte and double-layered membrane. Triangles indicate stability of the electrode with a 0.1 M KCl electrolyte impregnated with calcium alginate gel and a single-layered membrane. Measurements were done in 10 mM phosphate buffer (pH 7.0, 27 °C).

practical use of electrodes are long-term storage stability and sterilization tolerance. The most dominant factor affecting these properties is the strength of the gas-permeable membrane. Figure 5 shows the long-term stability of two oxygen electrodes having different electrolytes and gas-permeable membrane materials. Both electrodes were stored in deionized water at room temperature when not in use. Water was incorporated into the membrane of the polyelectrolyte electrode before the experiment was started.

The oxygen electrode with the gel electrolyte and the single-layered gas-permeable membrane frequently malfunctioned, mainly because of deterioration of the membrane and adhesion between the membrane and the substrate. The membrane was quickly deteriorated by the water in the electrolyte and the solution used for measurement⁷⁾. This deterioration occurred because the gel electrolyte was difficult to bake at a high temperature. The soft gel electrode could not be used for more than a month because its membrane broke. However, the output of the oxygen electrode with the PVEP polyelectrolyte and double-layered gas-permeable membrane was stable after nine months of storage. The fluctuation in output current after 250 days occurred not because of membrane deterioration but because the oxygen electrode cell was near the end of its life span. The elec-

trode also exhibits a normal response after at least six months of dry storage. For convenience, an oxygen electrode that is steam-sterilized and then discarded after a single use can be stored dry and activated with steam just before use.

Problems related to long-term stability are closely associated with sterilization tolerance. When we sterilized electrodes having the PVEP electrolyte and a single-layered gas-permeable membrane, the membranes easily broke. Whereas the double-layered membranes survived at least one sterilization with no breaks.

Similar results were obtained for the oxygen electrodes having the screen-printed electrolyte. (We are still refining the performance of these electrodes.) We have resolved all major problems related to the fabrication of type I oxygen electrodes.

2.5 Application to fermentation monitoring

For this application, the oxygen electrode

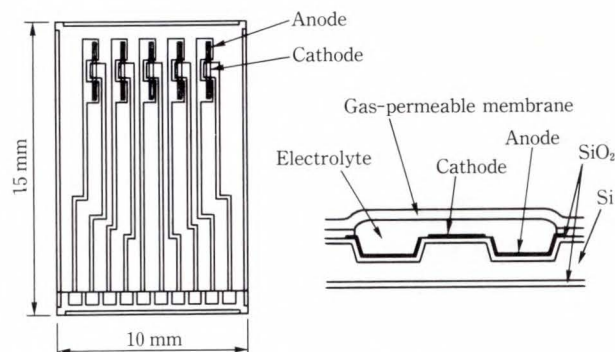


Fig. 6—Miniature oxygen electrode for fermenter. Cross section on the right is similar to the one along line bb' in Fig. 1.

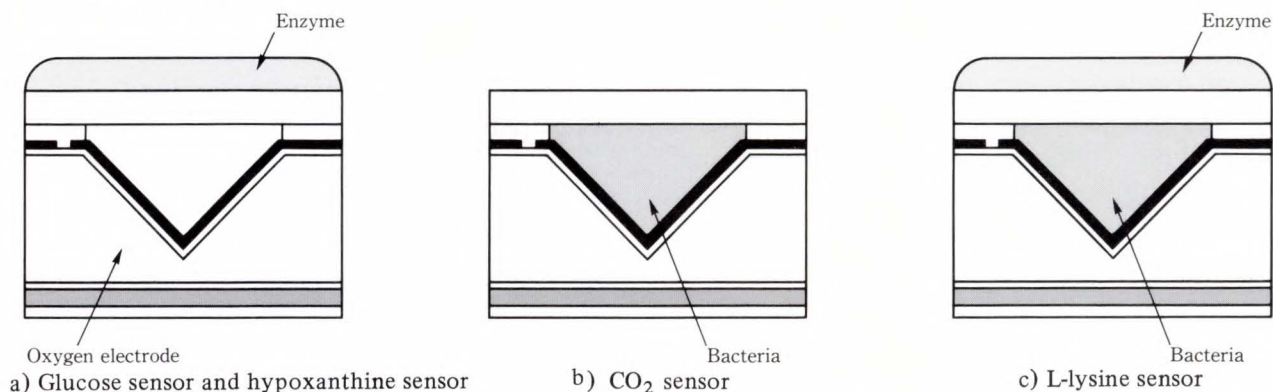


Fig. 7—Cross-sections of sensitive areas of the biosensors. The lower part of each figure is the same as that of the oxygen electrode shown in Fig. 1 with the exception that the cathode areas of b) and c) have been etched.

does not need to be small. However, an inexpensive disposable oxygen electrode will simplify maintenance and handling because gas-permeable membranes are often seriously damaged during incubation. Because our miniature oxygen electrode can be steam-sterilized we made a 5-electrode model that was specially designed for use in a fermenter (see Fig. 6). Endo et al. have used this sensor to monitor the variations in dissolved oxygen concentration in a fermenter during incubation of *Escherichia coli*, *Saccharomyces cerevisiae*, *Aspergillus niger*, and *Azotobacter vinelandii*. Their observations show a good correlation with the output of a commercially available electrode¹⁵⁾. The electrode operated for 125 h. They also monitored the variations in oxygen concentration in a similar experiment done in a test tube.

2.6 Application to biosensors

Using the type I miniature oxygen electrode shown in Fig. 1, biosensors for glucose, CO₂, L-lysine, and hypoxanthine were developed by immobilizing enzymes or microorganisms on the sensitive area. The structures of the sensitive areas of these sensors are shown in Fig. 7.

The glucose sensor was made using the oxygen electrode having the PVEP polyelectrolyte¹¹⁾. Its operation is based on the fact that the sensor detects variations in oxygen concentration following glucose oxidation by a glucose oxidase enzyme. Before forming the enzyme-immobilized membrane, 98 percent γ -aminopropyltriethoxysilane (γ -APTES) was applied to

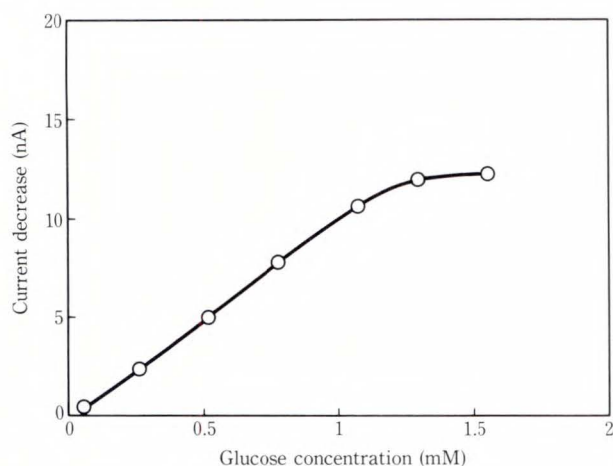


Fig. 8—Calibration curve of the glucose sensor. Calibration was done in 10 mM phosphate buffer (pH 7.0, 37 °C).

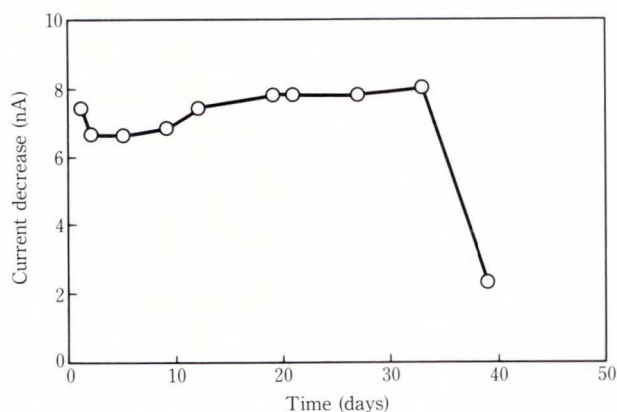


Fig. 9—Long-term stability of the glucose sensor. Measurement was done in 10 mM phosphate buffer (pH 7.0, 37 °C). Glucose concentration was 4 mM.

the gas-permeable membrane to improve the adhesion of the enzyme-immobilized matrix to the membrane. The enzyme (from *Aspergillus niger* activity: 106 unit/mg) was dissolved in a solution containing one percent bovine serum albumin (BSA) and one percent glutaraldehyde. The enzyme concentration was five percent. After mixing, the solution was immediately applied to the sensitive area of the oxygen electrode at room temperature. The electrode was then allowed to react overnight at 4 °C, after which it was rinsed in deionized water.

The response time of this sensor was from 60 s to 110 s. Figure 8 shows a typical calibration curve. The sensor has good linearity in

Table 2. Characteristics of biosensors

Sensor	Response time (min)	Linearity	Stability
Glucose	1	0.06-1.1 mM	30 days
CO ₂	1-3	0.5-3 mM	7 days
L-lysine	2-3	25-400 μM	8 days
Hypoxanthine	5	6.7-180 μM	2 days

glucose concentrations between 56 μM and 1.1 mM at 37 °C, pH 7.0. Figure 9 shows the long-term stability of the sensor. Treating the membrane surface with γ-APTES before forming the BSA matrix extended the lifetime to about one month. After one month the BSA matrix also detached from the gas-permeable membrane.

The CO₂ sensor was made by immobilizing CO₂ using autotrophic bacteria (S-17) in the groove of the miniature oxygen electrode with calcium alginate gel¹⁶⁾. The L-lysine sensor was made by immobilizing L-lysine decarboxylase on the sensitive area of the CO₂ sensor¹⁷⁾. This sensor indirectly monitors L-lysine concentration as follows: the L-lysine decarboxylase decomposes L-lysine, and the resultant CO₂ that is evolved is monitored by the bacterial CO₂ sensor. Suzuki et. al. used this oxygen electrode to make a hypoxanthine sensor to monitor the freshness of fish¹⁸⁾. This electrode has xanthine oxidase on its sensitive area. It monitors the oxygen consumption of an enzyme in a way similar to the glucose sensor described above. The characteristics of these sensors are summarized in Table 2 and are discussed in detail elsewhere¹⁶⁾⁻¹⁸⁾.

3. Type II miniature oxygen electrode

3.1 Structure of the type II oxygen electrode

Although we successfully developed the type I miniature oxygen electrode shown in Fig. 1, several problems remained. The most serious of these problems was the electrochemical crosstalk between electrodes that was mentioned in Sec. 2.4. To obtain the best response time, calibration, and long-term stability, the crosstalk must be minimized. There also remained several problems regarding fabrication.

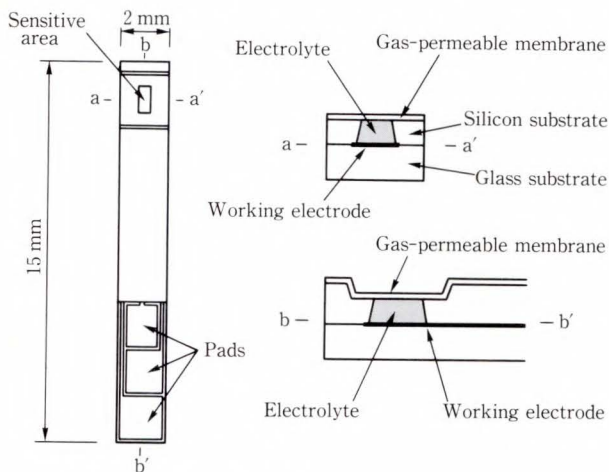


Fig. 10—Type II miniature oxygen electrode.

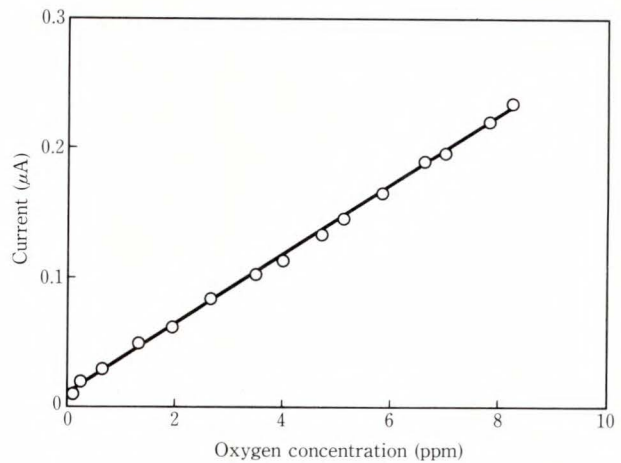


Fig. 12—Calibration curve.

Calibration was done in 10 mM phosphate buffer (pH 7.0, 25 °C).

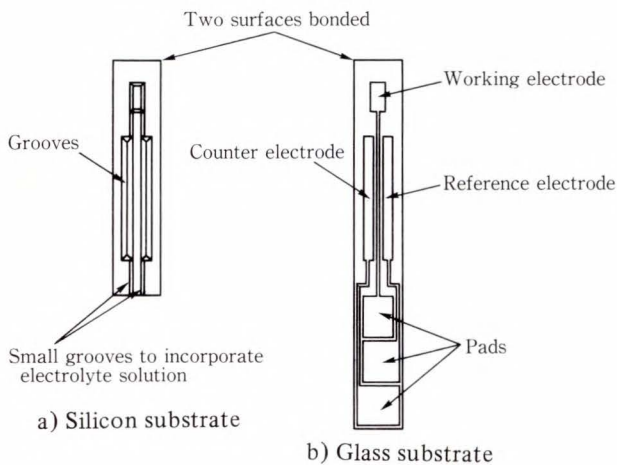


Fig. 11—Silicon substrate with grooves and glass substrate with electrodes.

Therefore, the oxygen electrode shown in Fig. 10 was developed.

This electrode consists of two bonded substrates and is 2 × 15 mm. Silver working, gold counter, and Ag/AgCl reference electrodes are formed on a 500 μm Pyrex glass substrate (see Fig. 11). The electrodes were formed at the bottoms of etched grooves 9 μm deep. Unlike the type I oxygen electrode, the bottoms of these grooves are almost flat, so electrode pattern formation is much easier and more accurate.

The container for the electrolyte solution {0.1 M KCl in 50 mM tris-(hydroxymethyl)-aminomethane/HCl buffer (pH 8.5)} was made by anisotropically etching a 400 μm silicon (100) substrate. To eliminate crosstalk between

electrodes, the grooves were formed only over the electrode areas and the electrodes were connected via long grooves. Also, the area of silicon substrate surrounding the working electrode was thinned to reduce the distance between the electrode and the gas-permeable membrane to 150 μm. Bonding was done by applying 1 200 V between the two substrates in a nitrogen atmosphere at 250 °C.

A 12-μm-thick gas-permeable membrane (fluorinated ethylenepropylene: FEP) was thermally adhered by melting it over the working electrode (see Fig. 10). The membrane is physically and chemically strong, and is therefore durable over long periods. To improve adhesion, we removed the fluorine atoms from the FEP membrane using an agent containing metallic sodium, processed the membrane with γ-APTES, and then adhered it at 280 °C in a vacuum.

The oxygen electrode chips were cut using a dicing saw before electrolyte incorporation. The electrolyte solution is easily incorporated via the long grooves into the small cavity by dipping the chip into the electrolyte solution and placing it in a chamber which is then evacuated. Typically, the voltage applied to the working electrode with respect to the reference electrode is -0.6 V.

3.2 Characteristics of the type II oxygen electrode

The 90 percent response time of the type II

electrode is 30 s, the residual current at zero oxygen concentration is negligible, and the linearity between zero oxygen concentration and saturation at 25 °C is very good (see Fig. 12). Due to the low crosstalk between electrodes the linearity over multiple tests is very stable.

We studied this electrode's tolerance to sterilization using high pressure steam. Completed oxygen electrodes were sterilized in an autoclave at 120 °C and 2.2 atm for 15 min, and then checked for damage to the gas-permeable membrane by adding 2 mM $K_3Fe(CN)_6$. If the sensitive area is not completely covered with the gas-permeable membrane, the $K_3Fe(CN)_6$ reaches the working electrode, causing an electrochemical reaction and a consequent increase in current. After sterilization, all of the membranes that were not treated with the agent had detached. Whereas all of the treated membranes remained attached, proving that the treatment improves adhesion.

4. Conclusion

Miniature Clark oxygen electrodes were fabricated. One type of oxygen electrode was made using anisotropic etching of silicon. By using a polyelectrolyte and a double-layered gas-permeable membrane the characteristics of this electrode were improved, especially the long-term stability and sterilization tolerance. The oxygen electrode was applied to fermentation monitoring and was used to fabricate biosensors. To further improve performance another miniature oxygen electrode was developed using anisotropic etching and field-assisted bonding.

The sensor structures and techniques described here can also be used to fabricate chemical sensors other than the Clark oxygen electrode.

References

- 1) Janata, J.: Principles of Chemical Sensors. Prentice Hall, New York & London, 1990, 201p.
- 2) Miyahara, Y., Matsu, F., Shiokawa, S., Moriizumi, T., Matsuoka, H., Karube, I., and Suzuki, S.: Biosensor Using Anisotropic Etching of Si. Proc. 3rd Sensor Symp., Inst. Elec. Engrs., Jpn., Tsukuba, 1983, pp. 21-26.
- 3) Karagounis, V., Lun, L., and Liu, C.C.: A Thick-film Multiple Component Cathode Three Electrode Oxygen Sensor. *IEEE Trans. Biomed. Eng.*, **BME-33**, 2, pp. 108-112 (1986).
- 4) Suzuki, H., Tamiya, E., and Karube I.: Fabrication of an Oxygen Electrode Using Semiconductor Technology. *Anal. Chem.*, **60**, 10, pp. 1078-1080 (1988).
- 5) Sansen, W., Wachter, D.D., Callewaert, L., Lambrechts, M. and Claes, A.: A Smart Sensor for the Voltammetric Measurement of Oxygen or Glucose Concentrations. *Sensors and Actuators*, **B1**, 1-6, pp. 298-302 (1990).
- 6) Koudelka, M.: Performance Characteristics of a Planar 'Clark-type' Oxygen Sensor. *Sensors and Actuators*, **9**, pp. 249-258 (1986).
- 7) Suzuki, H., Kojima, N., Sugama, A., and Takei, F.: Development of a Miniature Clark-type Oxygen Electrode Using Semiconductor Techniques and its Improvement for Practical Applications. *Sensors and Actuators*, **B2**, 3, pp. 185-191 (1990).
- 8) Petersen, K.E.: Silicon as a Mechanical Material. *Proc. IEEE*, **70**, 5, pp. 420-457 (1982).
- 9) Lee, D.B.: Anisotropic Etching of Silicon. *J. Appl. Phys.*, **40**, 11, pp. 4569-4574 (1969).
- 10) Bean, K.E.: Anisotropic Etching of Silicon. *IEEE Trans. Electron Devices*, **ED-25**, 10, pp. 1185-1193 (1978).
- 11) Suzuki, H., Sugama, A., Kojima, N., Takei, F., and Ikegami, K.: A Miniature Clark-type Oxygen Electrode Using a Polyelectrolyte and its Application as a Glucose Sensor. *Biosensors and Bioelectronics*, **6**, 5, pp. 395-400 (1991).
- 12) Cha, C.S., Shao, M.J., and Liu, C.C.: Problems Associated with the Miniaturization of a Voltammetric Oxygen Sensor: Chemical Crosstalk among Electrodes. *Sensors and Actuators*, **B2**, 4, pp. 239-242 (1990).
- 13) Suzuki, H., Sugama, A., and Kojima, N.: Effect of anode materials on the characteristics of the miniature Clark-type oxygen electrode. *Anal. Chim. Acta.*, **233**, 2, pp. 275-280 (1990).
- 14) Suzuki, H., Sugama, A., and Kojima, N.: Miniature Clark-type Oxygen Electrode with a Three-electrode Configuration. *Sensors and Actuators*, **B2**, 4, pp. 297-303 (1990).
- 15) Endo, H., Yamaguchi, T., Sode, K., Suzuki, H., Sugama, A., Uchiyama, S., Suzuki, S., Tamiya, E., and Karube, I.: On-line Bioprocess Monitoring Using a Disposable Miniature Oxygen Electrode. (in

- Japanese), *Nippon Nogekagaku Kaishi*, **64**, 3, p. 104 (1990).
- 16) Suzuki, H., Tamiya, E., and Karube, I.: Disposable Amperometric CO₂ Sensor Employing Bacteria and a Miniature Oxygen Electrode. *Electroanalysis*, **3**, 1, pp. 53-57 (1991).
- 17) Suzuki, H., Tamiya, E., and Karube, I.: Development of a Disposable Miniature L-lysine Sensor. *Anal. Chim. Acta.*, **229**, 2, pp. 197-203 (1990).
- 18) Suzuki, M., Suzuki, H., Karube, I., and Schmid, R.D.: A Disposable Hypoxanthine Sensor Based on a Micro Oxygen Electrode. *Anal. Lett.*, **22**, 15, pp. 2915-2927 (1989).



Hiroaki Suzuki

Advanced Materials Laboratory
FUJITSU LABORATORIES, ATSUGI
Bachelor of Applied Physics
The University of Tokyo 1981
Master of Applied Physics
The University of Tokyo 1983
Specializing in Micromachining,
Chemical Sensors, and Biosensors



Naomi Kojima

Advanced Materials Laboratory
FUJITSU LABORATORIES, ATSUGI
Bachelor of Science
Tokyo Metropolitan University 1985
Specializing in Biochemistry



Akio Sugama

Advanced Materials Laboratory
FUJITSU LABORATORIES, ATSUGI
Bachelor of Science
Tohoku University 1985
Specializing in Biochemistry

Development of a Molecular Orbital Package for Spectroscopy (MOS-F) and its Application to Nonlinear Optics

• Azuma Matsuura • Tomoaki Hayano

(Manuscript received July 30, 1992)

A molecular orbital package, MOS-F (semiempirical Molecular Orbital package for Spectroscopy-Fujitsu version), has been developed for high-speed computations for large organic optical molecules. MOS-F has been used to screen and design organic nonlinear optical materials. A novel electro-optic polymer which shows an optical nonlinearity almost as large as that of lithium niobate was found. Using MOS-F, optical nonlinearity of long azomethine conjugated systems was predicted. Frontier molecular orbital analysis revealed that donor/acceptor regions are induced in the main chain without a donor/acceptor substituent. It was also found that nonlinearity is improved by substituting donor groups at donor regions and acceptor groups at acceptor regions.

1. Introduction

In recent years, computational chemistry based on molecular orbital (MO) calculations have been used as a design and screening tool for organic materials such as nonlinear optical materials¹⁾⁻⁸⁾.

The MO methods are classified as being non-empirical (*ab initio*) or semiempirical⁹⁾. In the *ab initio* MO methods, the correct Hamiltonian is used and all integrals which express electron-electron repulsion, electron-nucleus attraction, orbital overlap, and so on are derived by pure calculation. However, although the results of computation are reliable, the *ab initio* methods are prohibitively time consuming. In contrast, semiempirical MO methods omit or parametrize many integrals, and are therefore much faster and better suited to the computation of large systems. The semiempirical MO methods are especially advantageous in the computation of optical properties such as molecular absorption spectra and polarizabilities. Two of the common semiempirical MO methods which give a good account of the electronic spectra for organic systems are the Pariser-Parr-Pople (PPP) method¹⁰⁾⁻¹²⁾ with singly excited configuration

interaction (SCI), and the spectroscopic version of the complete or intermediate neglect of differential overlap method with SCI {CNDO/S-CI¹³⁾⁻¹⁶⁾, INDO/S-CI¹⁷⁾}. The CNDO/S-CI and INDO/S-CI methods have several advantages over the PPP method in that they can be applied to a nonplanar molecule. However, there is no readily obtainable CNDO/S-CI package that can be applied to organic molecules having more than 30 carbon atoms. To realize high-speed, large-scale CNDO/S-CI calculation, we developed the "semiempirical MO package for Spectroscopy-Fujitsu version" (MOS-F), which can be applied to a wide range of organic optical materials.

One of the most important applications of computational chemistry is in the design of organic nonlinear optical materials. Nonlinear optical polymer, which will be used in monolithic light modulators and optical switch arrays in optical circuit boards, is a key material for the optical interconnection of future computer systems operating at high bit rates. As is well-known, the macroscopic optical nonlinearity of a material is closely related to the hyperpolarizabilities of the constituent mole-

cules¹⁾. In order to find molecular structures which improve optical nonlinearity, the frequency-dependent hyperpolarizabilities of organic molecules have been extensively calculated using the semiempirical molecular orbital methods mentioned above.

In this paper, we describe the features and performance of the MOS-F package in terms of the frequency-dependent hyperpolarizability calculation. Then, we report on the computation of frequency-dependent first hyperpolarizabilities for the electro-optic Pockels effect, $\beta(-\omega; 0, \omega)$, in azomethine systems using the MOS-F package, and clarify the donor/acceptor site-dependence of $\beta(-\omega; 0, \omega)$.

2. MOS-F package

The main function of the MOS-F package is to assist in the screening and molecular design of organic functional dyes, especially organic nonlinear optical molecules. To increase the speed of computations for large organic molecules, the MOS-F package features the following:

- 1) The introduction of the acceleration algorithms used in the *ab initio* methods, i.e. the four index transformation method¹⁸⁾ and the density matrix extrapolation procedure¹⁹⁾, into a semiempirical method.
- 2) Fujitsu's SSL2/VP scientific subroutine library.
- 3) Processing of all scratch data on the memory space, i.e. no write operation of data in the scratch file.
- 4) Maximum use of available memory space by using the INCLUDE statement of FORTRAN.

From the physical point of view, the MOS-F package features the following:

- 1) The CNDO/2²⁰⁾, CNDO/S, CNDO/S2²¹⁾, and CNDO/S3²¹⁾ semiempirical MO methods.
- 2) SCI calculation for singlet and triplet states.
- 3) Frequency-dependent first hyperpolarizabilities for electro-optic Pockels effect (EOPE), second harmonic generation (SHG), and optical rectification (OR) using the sum-over-states method^{1),2),22)}.

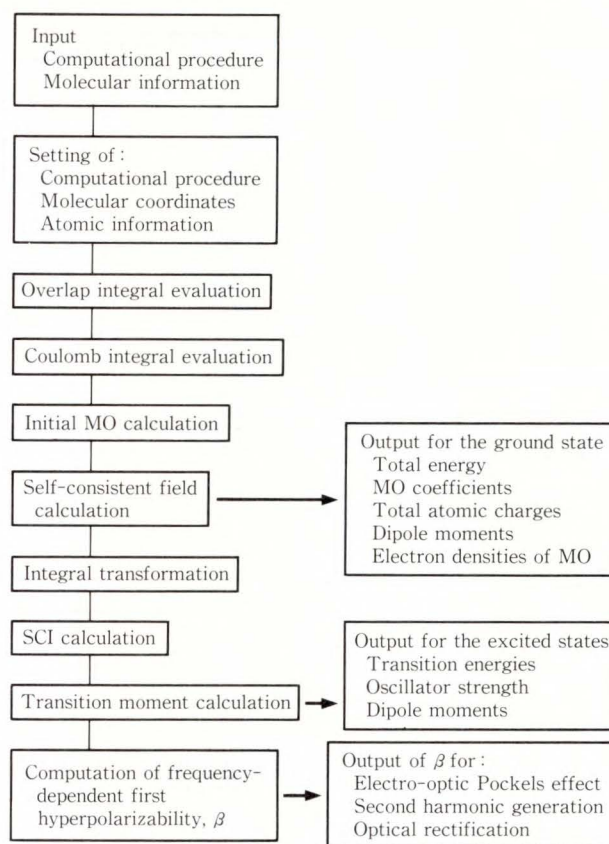


Fig. 1—MOS-F flowchart.

- 4) Analytic²²⁾, Pariser-Parr¹¹⁾, Nishimoto-Mataga²³⁾ (includes new formula), Nishimoto-Mataga-Weiss¹⁷⁾, Ohno²⁴⁾, Ohno-Klopman²⁵⁾, and DasGupta-Huzinaga²⁶⁾ formulas for evaluation of the two-center electron repulsion integrals.
- 5) Analytic computation of the one-center dipole integrals over the atomic orbitals in the evaluation of electronic transition moments¹⁴⁾.

The flowchart of the MOS-F computation is shown in Fig. 1. MOS-F contains FORTRAN codes, quoted from or copied from Quantum Chemistry Program Exchange (QCPE) programs^{19),27)-32)}.

3. Performance of MOS-F

Table 1 shows the memory size required by MOS-F in the Fujitsu FORT77/VP V10L30 FORTRAN compiler. Using a main memory resource of 256 Mbytes, the MOS-F package can theoretically be applied to a molecule of 1 250

Table 1. MOS-F program size

Atoms	Maximum number of		Program size (Mbytes)
	Atomic orbitals	Excited states	
100	250	225	2.7
100	250	400	4.5
150	300	400	4.6
300	600	400	12.6
600	1 200	400	48.3
1 000	2 000	400	133.1
1 250	2 500	400	207.4
1 250	2 500	2 500	207.5

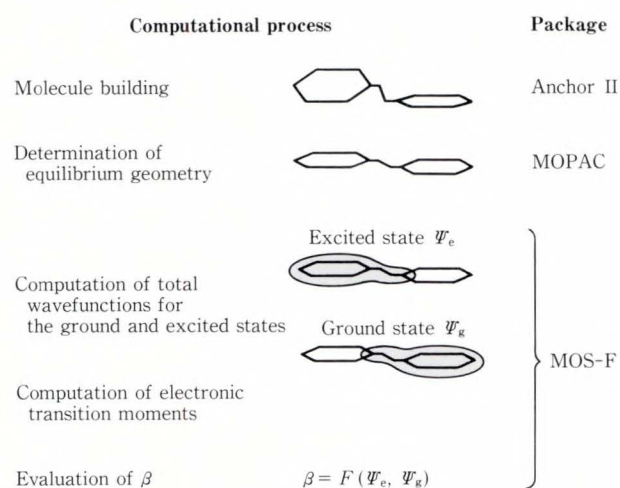


Fig. 2—Outline of hyperpolarizability calculation.

atoms and 2 500 atomic orbitals, which corresponds to $C_{416}H_{834}$ (1 250 atoms, 2 498 atomic orbitals, molecular weight: 5 837.26). This means that MOS-F can be applied to molecules that are as much as about six times the size of common molecules having molecular weights less than 1 000. In the case of the paraffin hydrocarbon with 50 carbon atoms, i.e. $C_{50}H_{102}$ (152 atoms, 302 atomic orbitals), the required memory size is about 6 Mbytes. An engineering work station (EWS) such as the S-4/2 can be used for MOS-F calculations for these large molecules.

The computation of the frequency-dependent first hyperpolarizability for EOPE, $\beta(-\omega; 0, \omega)$, was performed for various kinds of organic nonlinear optical molecules. The hyperpolarizability calculation is outlined in Fig. 2. The

molecules were built using Fujitsu's Anchor II package. The Austin model 1 (AM1)³³⁾ and parametric method 3 (PM3)³⁴⁾ MO calculations for the geometry optimization of the molecules listed in Table 2 were done using MOPAC Version 5.0³²⁾. In the SCI calculation, all of the possible singly excited configuration state functions (CSFs) formed from the ten highest occupied orbitals and the ten lowest unoccupied orbitals were employed; therefore, the number of singly excited CSFs was 100. The computation of $\beta(-\omega; 0, \omega)$ was done in 0.05 eV steps over the range of $\hbar\omega = 0$ to the vicinity of the transition energy of the lowest excited state. Details on the computation of $\beta(-\omega; 0, \omega)$ using the CNDO/S-CI sum-over-states method are given in the appendix.

$\beta(-\omega; 0, \omega)$ calculations for 50 organic molecules were carried out using the VP-200 supercomputer system. The average number of atoms and atomic orbitals of these molecules is 37 and 108, respectively. In the CNDO/S-CI calculation, the main factor affecting CPU time is the number of atomic orbitals and excited states. One hundred and eight orbitals corresponds to the paraffin hydrocarbon with 18 carbon atoms, i.e. $C_{18}H_{38}$. Table 2 shows the CPU times for MOS-F computations of $\beta(-\omega; 0, \omega)$ for the 50 molecules. The total and average CPU times are 344.7 s and 6.90 s, respectively, i.e. the $\beta(-\omega; 0, \omega)$ calculations for the 50 molecules is completed within six minutes. MOS-F is therefore fast enough for the screening of candidate molecules.

Tables 1 and 2 show that MOS-F is an excellent tool for the design and screening of large organic molecules with optical functions.

4. Application to nonlinear optics

In this chapter, we report on an application of MOS-F to nonlinear optical materials development to demonstrate the power of computational chemistry for material research. All MO calculations were performed using Fujitsu's VP-200 system, M-380 system, and S-4/2 EWS.

4.1 Pendant-attached poled polymer

Poled electro-optic (EO) polymers with

Table 2. CPU times for MOS-F computations of $\beta(-\omega; 0, \omega)$ using Fujitsu's VP-200 supercomputer system with FORT77/VP V10L30 FORTRAN compiler

Molecular information			CPU time (s)	Molecular information			CPU time (s)
Stoichiometry	Number of			Stoichiometry	Number of		
	Atoms	Atomic orbitals			Atoms	Atomic orbitals	
C ₁₆ H ₁₀ O ₂ N ₂	30	90	5.53	C ₁₅ H ₁₃ O ₃ N ₃	34	97	6.25
C ₁₁ H ₉ ON ₃	24	69	4.31	C ₁₄ H ₁₀ O ₂ N ₂	28	82	5.42
C ₁₂ H ₁₀ O ₂ N ₄	28	82	4.40	C ₁₅ H ₉ O ₄ N	29	89	5.85
C ₁₂ H ₁₀ O ₃ N ₄	29	86	4.39	C ₁₄ H ₁₁ O ₂ N ₃	30	87	5.74
C ₁₁ H ₁₀ N ₅ Cl	27	78	4.03	C ₁₄ H ₁₁ O ₂ N ₃	30	87	5.66
C ₁₁ H ₉ O ₂ N ₅	27	81	4.10	C ₁₄ H ₁₂ ON ₂ S ₃	32	92	6.22
C ₁₂ H ₁₁ O ₂ N ₅	30	87	4.54	C ₁₄ H ₁₂ ON ₂ S ₃	32	92	6.03
C ₁₃ H ₁₀ O ₄ N ₄	31	94	4.80	C ₁₃ H ₁₀ O ₂ N ₂	27	78	4.85
C ₃₆ H ₃₈ O ₄ N ₄	82	214	17.66	C ₁₃ H ₁₁ N	25	67	5.14
C ₁₄ H ₁₀ O ₂ N ₂	28	82	4.67	C ₁₅ H ₁₃ N ₃	31	85	5.28
C ₁₆ H ₁₀ O ₂ N ₂	30	90	6.66	C ₁₅ H ₁₂ O ₂ N ₄	33	96	5.26
C ₁₂ H ₁₀ ON ₂	25	70	4.14	C ₁₅ H ₁₂ O ₂ N ₄	33	96	6.10
C ₁₃ H ₁₁ ON	26	71	4.36	C ₁₅ H ₁₂ O ₂ N ₄	33	96	4.94
C ₁₉ H ₁₆ ON ₂	38	104	6.03	C ₁₅ H ₁₂ O ₂ N ₄	33	96	5.93
C ₁₈ H ₁₄ ON ₄	37	106	5.56	C ₁₅ H ₁₂ O ₂ N ₄	33	96	5.83
C ₁₇ H ₁₃ O ₂ N ₅	37	109	6.06	C ₁₅ H ₁₂ O ₂ N ₄	33	96	5.83
C ₁₄ H ₁₂ O ₂ N ₄	32	92	5.54	C ₂₉ H ₂₃ N ₅	57	159	9.16
C ₁₃ H ₉ ON	24	69	4.57	C ₂₇ H ₂₁ O ₈ N ₁₁	67	205	13.35
C ₁₅ H ₉ ON	26	77	4.90	C ₂₉ H ₂₃ O ₈ N ₁₃	73	223	15.97
C ₁₃ H ₉ ON	24	69	4.72	C ₂₉ H ₂₃ O ₈ N ₁₃	73	223	15.56
C ₁₃ H ₁₁ ON	26	71	4.83	C ₂₉ H ₂₃ O ₄ N ₉	65	191	11.95
C ₁₈ H ₁₆ O ₂ N ₂	38	104	6.33	C ₂₉ H ₂₃ O ₈ N ₁₃	73	223	14.87
C ₁₅ H ₁₄ ON ₂ S ₂	34	94	5.55	C ₂₉ H ₂₃ O ₈ N ₁₃	73	223	15.35
C ₁₂ H ₆ O ₂ N ₄	24	78	5.70	C ₂₉ H ₂₃ O ₄ N ₉	65	191	11.80
C ₁₄ H ₁₂ O ₂ N ₂	30	84	5.48	Total	1 861	5 419	344.76
C ₁₈ H ₁₀ O ₂ N ₂	32	98	7.56	Average	37	108	6.90

The number of CSFs in CNDO/S-CI calculation is fixed to 100. $\beta(-\omega; 0, \omega)$ is calculated in 0.05 eV steps over the range of $\hbar\omega = 0$ eV to the vicinity of the lowest excited state transition energy.

organic nonlinear optical side-chains, i.e. pendant-attached poled polymers, have been investigated³⁵⁾ because of their high performance and good processability. In this system, one of the dominant factors affecting the EOPE, which is a second-order nonlinear optical effect, is the magnitude of the hyperpolarizability for side-chain molecules. Therefore, it is important to screen candidate side-chain molecules when attempting to improve EO materials by calculating the molecular hyperpolarizability using theoretical computation. In theoretical prediction using semiempirical MO methods, however, we need to verify the reliability of the hyperpolarizability.

In this section, we first examine the EO

coefficients, which are macroscopic quantities corresponding to the molecular hyperpolarizabilities for EOPE, of a pendant-attached poled polymer with a screened side-chain molecule. Then we verify the reliability of the calculated $\beta(-\omega; 0, \omega)$ using two different types of side-chain molecules.

4.1.1 Screening of side-chain molecules

$\beta(-\omega; 0, \omega)$ at $\hbar\omega = 1.96$ eV, which corresponds to the photon energy of the He-Ne laser, was calculated for the 50 molecules listed in Table 2. All the computational procedures were the same as those described in Chap. 3. It should be noted that some of these molecules cannot be synthesized. We found that diacetylene deriva-

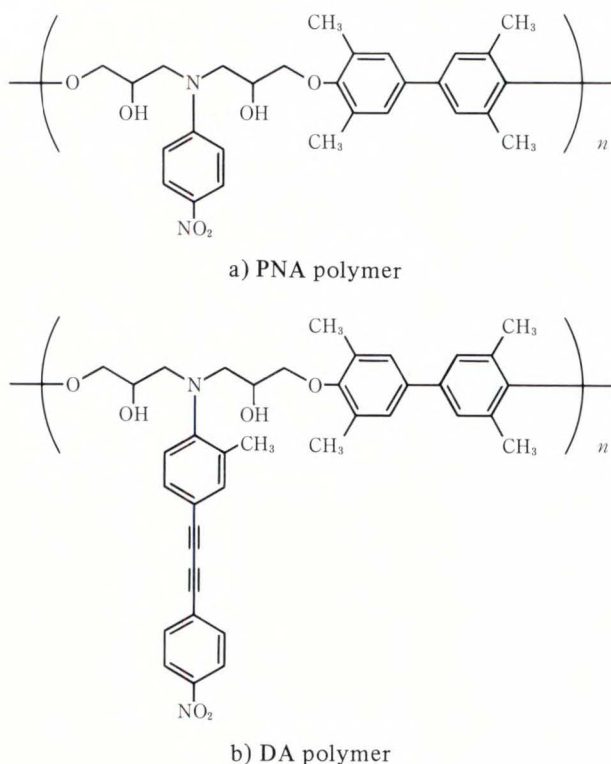


Fig. 3—Two types of EO polymers.

tive 1-(4-aminophenyl)-4-(4-nitrophenyl)-1, 3-butadiyne (DA) has the largest $\beta(-\omega; 0, \omega)$ of all the synthesizable molecules.

Then we measured the EO coefficients for DA-bonded epoxy polymer (DA polymer) film using a conventional simple reflection technique³⁶⁾ after the poling procedure. We found that the EO coefficient of DA polymer is 25 pm/V and is about as large as that of lithium niobate, which is the commonest commercial inorganic nonlinear optical material. This demonstrates that the screening of organic nonlinear optical molecules using the MOS-F package is very useful in the development of nonlinear optical materials.

4.1.2 Reliability of calculated hyperpolarizability

To verify the reliability of the calculated hyperpolarizability, we compared the calculated $\beta(-\omega; 0, \omega)$ of side-chain molecules with experimental EO coefficients of poled polymers for two different types of side chain molecules.

Table 3. Calculated $\beta(-\omega; 0, \omega)$ for DA and experimental EO coefficients for DA polymer at $\hbar\omega = 1.96$ eV

	β	EO coefficients
DA	8.82	4.17
<i>p</i> -nitroaniline	1	1

The values listed here are values relative to *p*-nitroaniline or PNA polymer.

Figure 3 shows the structures of pendant-attached EO polymers. One is DA polymer and the other is *p*-nitroaniline-bonded epoxy polymer (PNA polymer). In the computational procedure, $\beta(-\omega; 0, \omega)$ for two side-chain molecules, i.e. *p*-nitroaniline and DA were calculated after determining their stable structures under the constraint of C_{2v} symmetry using the AM1 method.

Table 3 shows the calculated relative value of $\beta(-\omega; 0, \omega)$ for DA and the experimental EO coefficient for the poled DA polymer. The calculated and experimental values indicate that DA has a larger optical nonlinearity than *p*-nitroaniline. Therefore, the calculated optical nonlinearity is in qualitative agreement with the experimental values. It should be noted that statistical treatments are required for a quantitative prediction since an EO coefficient also depends on the orientation and density of the nonlinear optical molecules in the material.

4.2 π -conjugated polymer

Recently, it was reported that terephthalaldehyde and *p*-phenylenediamine are connected by an azomethine bond (RCH = NR') through -CHO and -NH₂ groups to form polymer films via chemical vapor deposition (CVD) and molecular layer deposition (MLD)³⁷⁾ (see Fig. 4). These methods of deposition enable monomolecular-order control of a one-dimensional polymer structure. Therefore, the design of constituent molecules and the resultant polymer structures by theoretical computation play an important role in the enhancement of the nonlinear properties of polymer materials.

In this section, we report on an application of the MOS-F package to π -conjugated systems containing azomethine bonds and clarify the

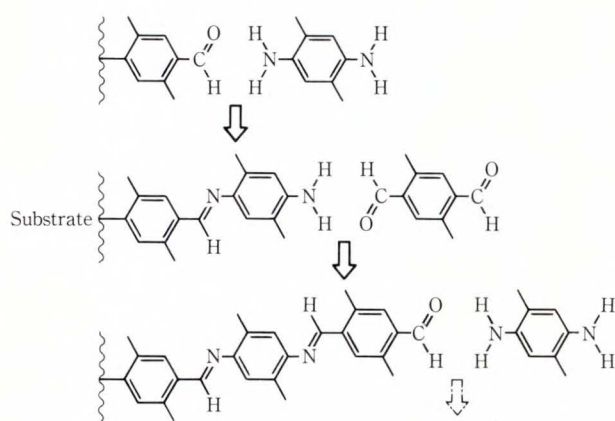


Fig. 4—Layer by layer growth of azomethine polymer film using MLD.

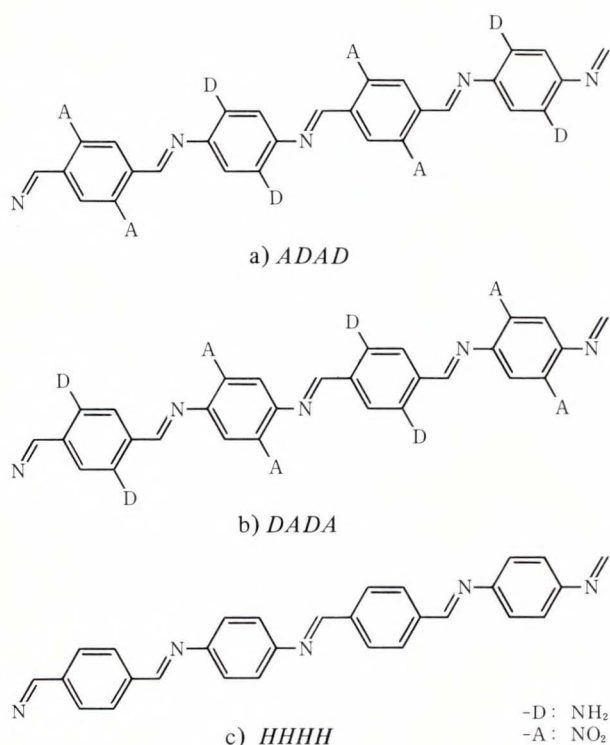


Fig. 5—Structural formulas of the model molecules containing azomethine bonds.

donor/acceptor site-dependence of hyperpolarizabilities.

4.2.1 Model molecules

Figure 5 shows the structural formulas of the model molecules. These molecules differ in their substitution sites of donors and acceptors. *D* is the donor ($-\text{NH}_2$), *A* the acceptor

Table 4. Bond lengths of donor ($-\text{NH}_2$) and acceptor ($-\text{NO}_2$) in Å units

<i>p</i> -dinitrobenzene		<i>p</i> -phenylenediamine	
R_{NO}	R_{CN}	R_{NH}	R_{CN}
1.200	1.492	0.983	1.383

The values are taken from AM1 optimized geometries for planar *p*-dinitrobenzene and *p*-phenylenediamine, both of which belong to the D_{2h} point group.

($-\text{NO}_2$), and *H* the hydrogen atom. Molecule *HHHH* has neither a donor nor acceptor.

Our purpose was to investigate the relationship between the magnitude of β and the donor/acceptor substitution sites. Full geometry optimization for all the model molecules complicates the above relationship due to geometrical differences such as conformational dependence of β and the geometrical change versus the type of donor and acceptor. Therefore, optimized geometry of *HHHH* was used throughout when calculating β for all the model molecules so that we could focus on the site dependence. The semiempirical AM1 method was used to optimize the geometry of molecule *HHHH*. All the benzene rings were fixed to a planar structure. The bond lengths of $-\text{NH}_2$ and $-\text{NO}_2$ were taken from AM1 optimized geometry for planar *p*-phenylenediamine and *p*-dinitrobenzene, respectively. (Both of these molecules have D_{2h} symmetry during the optimization procedure.) The bond angles were fixed to 120 degrees. The bond lengths are shown in Table 4. In the SCI calculation, all of the possible singly excited CSFs formed from the 20 highest occupied orbitals and the 20 lowest unoccupied orbitals were employed; therefore, the number of singly excited CSFs was 400.

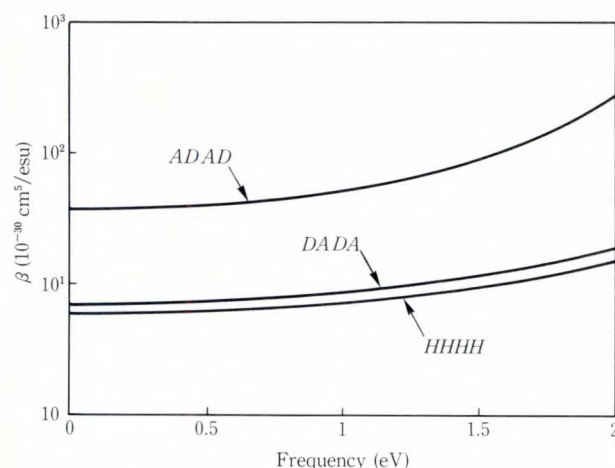
4.2.2 Effect of donor/acceptor substitution sites on the calculated hyperpolarizabilities

We will now discuss the relationship between the magnitude of β and the donor/acceptor substitution site. Table 5 shows the calculated $\beta(-\omega; 0, \omega)$ for the model molecules and *p*-nitroaniline (*p*-NA), a common nonlinear optical molecule, at $\hbar\omega = 1.96$ eV, which

Table 5. Calculated $\beta(-\omega; 0, \omega)$ at $\hbar\omega = 1.96$ eV

Molecule	β	
	Absolute value (10^{-30} cm ⁵ /esu)	Relative value*
<i>ADAD</i>	242.6	38.6
<i>DADA</i>	18.34	2.92
<i>HHHH</i>	14.52	2.31
<i>p</i> -nitroaniline	6.291	1

*: Value of molecule with respect to *p*-nitroaniline.

Fig. 6— $\beta(-\omega; 0, \omega)$ for the model molecules.

corresponds to the photon energy of the He-Ne laser. The donor/acceptor substitution sites have a big influence on the magnitude of $\beta(-\omega; 0, \omega)$. The magnitude of $\beta(-\omega; 0, \omega)$ for *ADAD* is the largest of the four and is about 40 times the magnitude for *p*-nitroaniline. In contrast, despite its many donor/acceptor substituents, the magnitude for *DADA* is small. We also found that the magnitude of $\beta(-\omega; 0, \omega)$ for *HHHH*, which has neither a donor nor acceptor, is more than double the magnitude for *p*-nitroaniline.

Figure 6 shows $\beta(-\omega; 0, \omega)$ over the range of $\hbar\omega = 0$ eV to 2 eV for the three model molecules. The $\beta(-\omega; 0, \omega)$ values are consistent over this $\hbar\omega$ region, i.e. at any $\hbar\omega$, $\beta(-\omega; 0, \omega)$ for *ADAD* is greater than that for *DADA*, which is in turn greater than that for *HHHH*.

4.2.3 Frontier MO analysis

In this subsection, we discuss in detail the site-dependence of $\beta(-\omega; 0, \omega)$ using Frontier

Table 6. Frontier orbital energies and their energy gaps, $\Delta\epsilon$, in eV units

Molecule	ϵ_{HOMO}	ϵ_{LUMO}	$\Delta\epsilon$
<i>ADAD</i>	-8.17	-3.57	4.60
<i>DADA</i>	-8.82	-3.04	5.78
<i>HHHH</i>	-8.36	-2.29	6.07

MO analysis³⁸). Table 6 shows the energies for the highest occupied MO (HOMO), the energies for the lowest unoccupied MO (LUMO), and the energy gaps between these two orbitals. *ADAD* has the highest HOMO energy, the lowest LUMO energy, and the smallest energy gap. In general, a donor raises the energy level of the HOMO and an acceptor lowers the energy level of the LUMO. Thus, in *ADAD*, donors and acceptors are substituted at sites which make the donor/acceptor properties large. Conversely, in *DADA*, the HOMO energy, despite the many donor/acceptor substituents, is lower than that in *HHHH*. Moreover, from Table 5 and 6 and from Fig. 6, we find that molecules with a smaller energy gap between the HOMO and LUMO tend to have a large $\beta(-\omega; 0, \omega)$. This suggests the importance of investigating the energy gap when enhancing molecular optical nonlinearity.

Figure 7 shows the Frontier electron densities (FEDs) for the constituent heavy atoms of *HHHH*. The FED of atom A for the *i*th Frontier MO, f_A^i , is expressed as follows:

$$f_A^i = \sum_{\mu \in A} (C_{\mu i})^2,$$

where $C_{\mu i}$ is the MO coefficient, and μ runs over the atomic orbitals belonging to atom A. In this paper, the summation of FEDs over all constituent atoms is normalized to unity. From Fig. 7, we find the following FED characteristics:

- 1) FEDs for the HOMO are localized in benzene ring 2.
- 2) FEDs for the LUMO are localized in benzene ring 3 and in the two azomethine regions bonded to benzene ring 3.

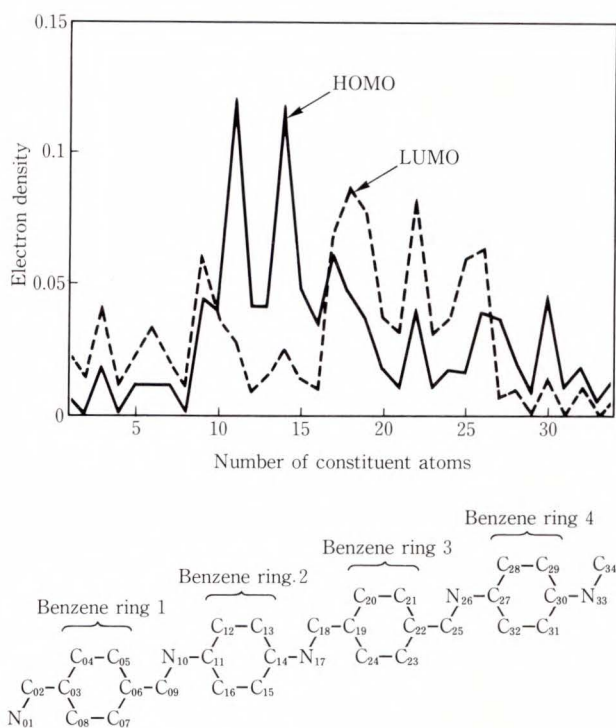


Fig. 7—Frontier electron densities of heavy atoms, f_A^i , of model molecule *HHHH*. The summation of f_A^i over the constituent atoms (i) is normalized to unity.

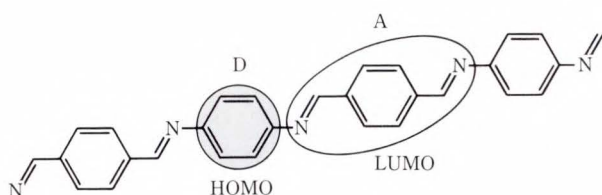


Fig. 8—Donor/acceptor regions of model molecule *HHHH* as predicted by Frontier MO analysis.

As is well known, the regions in which the LUMO are localized have an acceptor property and the regions in which the HOMO are localized have a donor property. Thus, we find that *HHHH*, a molecule with no donor/acceptor substituent, can be divided into donor and acceptor regions as shown in Fig. 8. This is the origin of the donor/acceptor site-dependence of $\beta(-\omega; 0, \omega)$, and is consistent with the discussion on the relationship between the

magnitude of $\beta(-\omega; 0, \omega)$ and the HOMO/LUMO energies. Actually, the computational results mentioned above show that the substitution of donor/acceptors for hydrogen atoms without cancellation of the main chain donor/acceptor properties increases the value of $\beta(-\omega; 0, \omega)$. $\beta(-\omega; 0, \omega)$ for *ADAD*, which locates donors in the main chain donor regions and acceptors in the acceptor regions without canceling the main chain donor/acceptor properties, is much larger than $\beta(-\omega; 0, \omega)$ for *DADA*, which locates donors in the main chain acceptor regions and acceptors in the donor regions, thus canceling the donor/acceptor properties.

From the above discussion on site dependence, it is clear that the investigation of donor/acceptor regions in a molecule using Frontier MO analysis is a powerful method of locating the donor/acceptor substitution sites which enhance the optical nonlinearity of molecular systems.

5. Conclusion

A spectroscopic version of the semiempirical MO package, MOS-F, has been developed for the design and screening of organic optical materials. When used with a main memory resource of 256 Mbytes, MOS-F can be applied to extremely large molecules, i.e. molecules corresponding in size to a paraffin hydrocarbon containing more than 400 carbon atoms. Using MOS-F, it takes 344.76 s in the CPU time to calculate the frequency-dependent first hyperpolarizabilities for electro-optic Pockels effect on a Fujitsu VP-200 supercomputer system for 50 organic molecules whose average size corresponds to that of the paraffin hydrocarbon with 18 carbon atoms. We used MOS-F to screen the side-chain molecules of EO polymers for nonlinear optical properties. We found a novel polymer with the large EO coefficient of 25 pm/V, which is about as large as that of lithium niobate. We also used MOS-F to predict optical nonlinearity in π -conjugated systems containing azomethine bonds. Frontier MO analysis indicated that a molecule with no donor/acceptor substituent can be divided into donor and acceptor regions. Study of the

relationship between optical nonlinearity and the substitution sites of donors and acceptors revealed that the investigation of donor and acceptor regions in a molecule using Frontier MO analysis is a powerful method of locating the substituents that enhance the optical nonlinearity of a molecule. MOS-F is an excellent

tool for the design and screening of large organic molecules with optical functions.

Appendix CNDO/S-CI sum-over-states method

$\beta(-\omega; 0, \omega)$ was evaluated using the sum-over-states method. In this method, the expression for $\beta(-\omega; 0, \omega)$ is written as follows:

$$\begin{aligned} \beta(-\omega; 0, \omega) &= \sqrt{\beta_x^2 + \beta_y^2 + \beta_z^2}, \\ \beta_i(-\omega; 0, \omega) &= \frac{1}{3} \sum_k (\beta_{ikk} + \beta_{kik} + \beta_{kki}), \\ \beta_{i,j,k}(-\omega; 0, \omega) &= \frac{1}{8} \sum_{e,e' \neq g} [(\langle ijk \rangle + \langle kji \rangle) \left\{ \frac{1}{(E_e - \hbar\omega)(E_{e'} - \hbar\omega)} + \frac{1}{(E_e + \hbar\omega)(E_{e'} + \hbar\omega)} \right\} \\ &\quad + (\langle jik \rangle + \langle jki \rangle) \left\{ \frac{1}{E_e(E_{e'} - \hbar\omega)} + \frac{1}{E_e(E_{e'} + \hbar\omega)} \right\} \\ &\quad + (\langle ikj \rangle + \langle kij \rangle) \left\{ \frac{1}{(E_e - \hbar\omega)E_{e'}} + \frac{1}{(E_e + \hbar\omega)E_{e'}} \right\}], \quad \dots \text{(A-1)} \end{aligned}$$

where,

$$\langle ijk \rangle = \langle \Psi_g | \tilde{\mu}_i | \Psi_e \rangle \langle \Psi_e | \tilde{\mu}_j | \Psi_{e'} \rangle \langle \Psi_{e'} | \tilde{\mu}_k | \Psi_g \rangle,$$

$$\tilde{\mu}_i = \hat{\mu}_i - \langle \Psi_g | \hat{\mu}_i | \Psi_g \rangle.$$

$$\hat{\mu}_i = -e \sum_{s=1}^N i_s,$$

where ω is the angular frequency of the incident light; E_e and $E_{e'}$ are the electroic transition energies; $\hbar = h/2\pi$ is Dirac's h ; Ψ_g is the total wavefunction of the ground state; Ψ_e and $\Psi_{e'}$, are the total wavefunctions of the excited states; subscripts i, j , and k are the Cartesian components; $\hat{\mu}_i$ is the dipole operator for the i th component; i_s is the i th component of the position vector of the s th electron; and N is the number of electrons in the molecule. Unlike Ward's expression²²⁾, Equation (A-1) is multiplied by a factor of $-1/4$ to equalize $\beta(-\omega; 0, \omega)$ with the frequency-dependent hyperpolarizability for second harmonic generation over the limit $\omega \rightarrow 0$. The basic quantities in Equation (A-1), i.e. E_e , Ψ_g , Ψ_e , and $\langle ijk \rangle$, can be evaluated using MO calculation. The CNDO/S-CI method was employed using Chang's atomic parameters¹⁵⁾. The two-center Coulomb integrals, γ_{AB} , are evaluated using the NM formula, which is expressed as follows:

$$\gamma_{AB} = \frac{14.399}{R_{AB} + 28.797/(\gamma_{AA} + \gamma_{BB})},$$

where R_{AB} is the distance between atom A and atom B, and γ_{AA} is the one-center Coulomb integral. The units for energy and bond length are eV and Å, respectively.

In the transition moment calculation, the one-center dipole integrals over atomic orbitals are evaluated analytically.

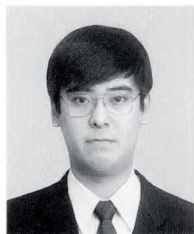
References

- 1) Chemla, D.S., and Zyss, J., ed.: Nonlinear Optical Properties of Organic Molecules and Crystals. New York, Academic, 1987.
- 2) Morrell, J.A., and Albrecht, A.C.: Second-order Hyperpolarizability of *p*-Nitroaniline Calculated from Perturbation Theory Based Expression using CNDO/S Generated Electronic States. *Chem. Phys. Lett.*, **64**, pp. 46-50 (1979).
- 3) Lalama, S.J., and Garito, A.F.: Origin of the Nonlinear Second-Order Optical Susceptibilities of Organic

- Systems. *Phys. Rev.*, **A20**, pp. 1179-1194 (1979).
- 4) Docherty, V.J., Pugh, D., Morley, J.O.: Calculation of the Second-Order Electronic Polarizabilities of some Organic Molecules. *J. Chem. Soc., Faraday Trans.*, **2**, 81, pp. 1179-1192 (1985).
 - 5) Dirk, C.W., Twieg, R.J., and Wagnière, G.: The Contribution of π Second Electrons to Harmonic Generation in Organic Molecules. *J. Am. Chem. Soc.*, **108**, pp. 5387-5395 (1986).
 - 6) Li, D., Ratner, M.A., and Marks, T.J.: Molecular and Macromolecular Non-linear Optical Materials. Probing Architecture/Electronic Structure/Frequency Doubling Relationships via an SCF-LCAO MECI π Electron Formalism. *J. Am. Chem. Soc.*, **110**, pp. 1707-1715 (1988).
 - 7) Yoshimura, T.: Enhancing Second-order Nonlinear Optical Properties by Controlling the Wave Function in One-Dimensional Conjugated Molecules. *Phys. Rev.*, **B40**, pp. 6292-6298 (1989).
 - 8) Tsunekawa, T., Gotoh, T., and Iwamoto, M.: New Organic Non-Linear Optical Crystals of Benzylidene-Aniline Derivative. *Chem. Phys. Lett.*, **166**, pp. 353-357 (1990).
 - 9) Levine, I.N.: Quantum Chemistry. 4th ed., N.J., Prentice-Hall, 1991.
 - 10) Pariser, R., and Parr, R.G.: *J. Chem. Phys.*, **21**, p. 466 (1953).
 - 11) Pariser, R., and Parr, R.G.: A Semi-Empirical Theory of the Electronic Spectra and Electronic Structure of Complex Unsaturated Molecules. II. *J. Chem. Phys.*, **21**, pp. 767-776 (1953).
 - 12) Pople, J.A.: *Trans. Faraday Soc.*, **49**, p. 1385 (1953).
 - 13) Del Bene, J., and Jaffé, H.H.: Use of the CNDO Method in Spectroscopy. I. Benzene, Pyridine, and the Diazines. *J. Chem. Phys.*, **48**, pp. 1907-1913 (1968); Del Bene, J., and Jaffé, H.H.: Use of the CNDO Method in Spectroscopy. II. Five-Membered Rings. *J. Chem. Phys.*, **48**, pp. 4050-4055 (1968).
 - 14) Ellis, R.L., Kuehnlenz, G., and Jaffé, H.H.: The Use of the CNDO Method in Spectroscopy VI. Further $n - \pi^*$ Transitions. *Theor. Chim. Acta*, **26**, pp. 131-140 (1972).
 - 15) Chang, H.M., Jaffé, H.H., and Masmanidis, C.A.: Use of the CNDO Method in Spectroscopy. XIV. Electronic Spectra of Free Radicals and Free Radical Ions. *J. Phys. Chem.*, **79**, pp. 1118-1129 (1975).
 - 16) Lipari, N.O., and Duke, C.B.: The Electronic Structure of Dialkylbenzenes. *J. Chem. Phys.*, **63**, pp. 1748-1757 (1975).
 - 17) Ridley, J., and Zerner, M.: An Intermediate Neglect of Differential Overlap Technique for Spectroscopy: Pyrrole and the Azines. *Theor. Chim. Acta (Berl.)*, **32**, pp. 111-134 (1973).
 - 18) Schaefer, H.F., ed.: Methods of Electronic Structure Theory. Plenum, 1977, (Modern Theoretical Chemistry, 3).
 - 19) Foley, C.K., and Chesnut, D.B.: Gaussian 80. Quantum Chemistry Program Exchange, #500. (This program is the modified version of QCPE #406 written by Binkley, J.S., Whiteside, R.A., Krishnan, R., Seeger, R., Schlegel, H.B., Defrees, D.J., and Pople, J.A.)
 - 20) Pople, J.A., and Segal, G.A.: *J. Chem. Phys.*, **44**, p. 3289 (1966).
 - 21) Ward, J.F.: Calculation of Nonlinear Optical Susceptibilities Using Diagrammatic Perturbation Theory. *Rev. Mod. Phys.*, **37**, pp. 1-18 (1965).
 - 22) Roothaan, C.J.J.: *J. Chem. Phys.*, **19**, p. 1445 (1951).
 - 23) Nishimoto, K., and Mataga, N.: *Z. Phys. Chem.*, **13**, p. 140 (1957).
 - 24) Ohno, K.: *Theor. Chim. Acta (Berl.)*, **2**, p. 219 (1964).
 - 25) Klopman, G.: *J. Am. Chem. Soc.*, **87**, p. 3300 (1965).
 - 26) DasGupta, A. and Huzinaga, S.: New Developments in CNDO Molecular Orbital Theory. *Theor. Chim. Acta (Berl.)*, **35**, pp. 329-340 (1974).
 - 27) Hase, H.L., and Schweig, A.: CNDO 2/3R. Quantum Chemistry Program Exchange, #261.
 - 28) Jaffé H.H.: CNDO/M. Quantum Chemistry Program Exchange, #315.
 - 29) Baumann, H.: CNDOUV99. Quantum Chemistry Program Exchange, #333.
 - 30) Rajzmann, M., and Francois, P.: CINDO/SHIFT/UV. Quantum Chemistry Program Exchange, #382.
 - 31) Davidson, E.R.: MELDF. Quantum Chemistry Program Exchange, #580.
 - 32) Stewart, J.J.P.: MOPAC, Version 5. Quantum Chemistry Program Exchange, #581.
 - 33) Dewar, M.J.S., Zoebisch, E.G., Healy, E.F., and Stewart, J.J.P.: A New General Purpose Quantum Mechanical Molecular Model. *J. Am. Chem. Soc.*, **107**, pp. 3902-3909 (1985).
 - 34) Stewart, J.J.P.: Optimization of Parameters for Semiempirical Method I. Method. *J. Comput. Chem.*, **10**, pp. 209-220 (1989).
 - 35) For example, Jungbauer, D., Teraoka, I., Yoon, D.Y., Reck, B., Swalen, J.D., Twieg, R., and Wilson, C.G.: Second-Order Nonlinear Optical

- Properties and Relaxation Characteristics of Poled Linear Epoxy Polymers with Tolane Chromophores. *J. Appl. Phys.*, **69**, pp. 8011-8017 (1991).
- 36) Teng, C.C., and Man, H.T.: Simple Reflection Technique for Measuring the Electro-Optic Coefficient of Poled Polymer. *Appl. Phys. Lett.*, **56**, pp. 1734-1736 (1990).
- 37) Yohimura, T., Tatsuura, S., and Sotoyama, W.: Polymer Films Formed with Monolayer Growth

- Steps by Molecular Layer Deposition. *Appl. Phys. Lett.*, **59**, pp. 482-484 (1991).
- 38) Fukui, K., Yonezawa, T., and Shingu, H.: *J. Chem. Phys.*, **20**, p. 722 (1952); Fukui, K., Yonezawa, T., Nagata, C., and Shingu, H.: Molecular Orbital Theory of Orientation in Aromatic, Hetero-aromatic, and Other Conjugated Molecules. *J. Chem. Phys.*, **22**, pp. 1433-1442 (1954).



Azuma Matsuura

Imaging Materials Laboratory
FUJITSU LABORATORIES, ATSUGI
Bachelor of Applied Chemical Eng.
Waseda University 1981
Master of Applied Chemical Eng.
Waseda University 1984
Specializing in Computational
Chemistry



Tomoaki Hayano

Imaging Materials Laboratory
FUJITSU LABORATORIES, ATSUGI
Bachelor of Applied Chemical Eng.
Waseda University 1983
Master of Applied Chemical Eng.
Waseda University 1986
Specializing in Computational
Chemistry

Interactive Extraction of Rules Concerning Variations in Speech

• Shinta Kimura

(Manuscript received February 28, 1992)

This paper describes the interactive extraction of rules that estimate acoustic-segment sequences from an orthography of Japanese language. The rules are in the format of context-sensitive rewriting rules and are arranged into four layers. Initial rules are given by traditional Japanese phonology. In the interactive rule extraction, top-down segmentation is used to automatically detect speech data that contains variations that are not described by the existing rules. In the extraction experiments, 163 rules were extracted from 1 000 Japanese phrases spoken by one male and 255 rules were extracted from 10 000 Japanese phrases spoken by ten males. The rules account for 21 kinds of variation phenomena.

1. Introduction

To realize a continuous speech recognizer, we must develop a highly accurate phoneme recognizer. The major problem in achieving this is how to treat variations of phonemes in continuous speech. When the phonemes in continuous speech vary, they are not recognized using the registered phoneme templates; therefore, the input speech cannot be correctly recognized. The variation of a phoneme depends on its phonemic context.

Using a large speech database, we investigated which kinds of phonemic contexts cause the phonemic variations. We extracted computer-readable rules that represent the phonemic variations. To efficiently extract the rules from the speech database, we constructed a support system using top-down segmentation. This paper focuses on the extraction process of the rules concerning the phonemic variations in continuous speech and the extracted rules.

The rules hypothesize the phonemic variations in top-down manner. That is, the rules convert a Japanese orthography to phonemes, then the phonemes to allophones, and finally the allophones to acoustic segments. The acoustic segment (a new speech unit which we have

defined) represents physical phenomenon in speech. In speech recognition, the acoustic segment can be easily recognized by machine. In our method of using the acoustic segments, the boundaries of phonemes are not always consistent with those of the acoustic segments. This is because a glide between phonemes is represented as an acoustic segment.

The top-down segmentation system used to detect the variations that are not represented by rules are described in chapter 2. The basic concept of rule extraction is described in chapter 3. The support system for rule extraction is introduced in chapter 4. The rule-extraction experiments are described in chapters 5 and 6. Early reports on the work described in this paper can be found in references 1) and 2). See also references 3), 4), 5), and 6) for our related work.

2. Top-down segmentation

2.1 Outline

The idea of top-down segmentation was first introduced by Aikawa, Sugiyama, and Shikano⁷⁾. Their system segments speech into phonemes. Phoneme segmentation, however, is very difficult because phoneme boundaries are not

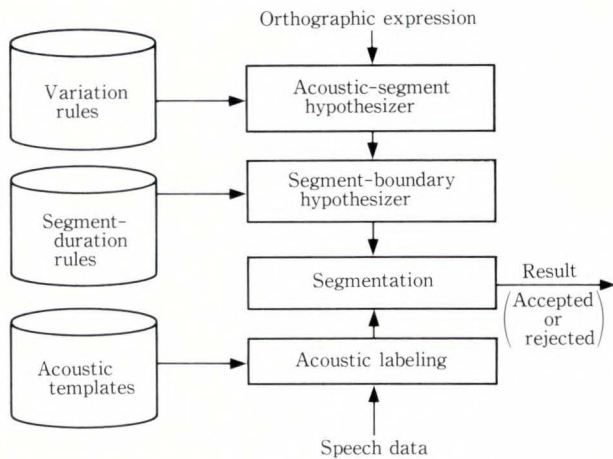


Fig. 1—Top-down segmentation.

Table 1. Structure of variation rules

Layer	From	To	Variation
0	Orthographic	Phoneme	—
1	Phoneme	Phone	Obligatory allophone
2	Phoneme	Phone	Optional allophone
3	Phone	Acoustic-segment	Glide

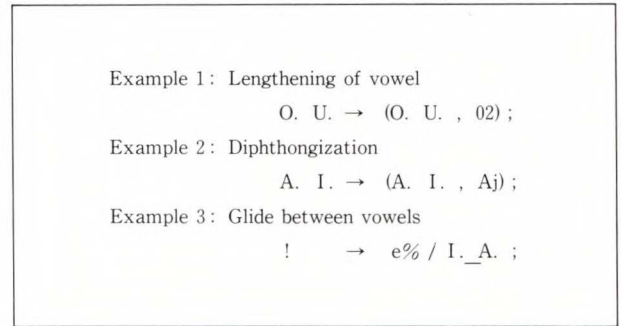
always consistent with the positions of acoustic events. This is especially true when speech includes phonemic variations.

Our top-down segmentation system segments speech into acoustic segments by matching the speech data and hypotheses of acoustic segments. The hypotheses of acoustic segments are automatically generated from the orthographic expression of the speech data using rules that account for the variations in the speech data. The flow diagram of the top-down segmentation system is shown in Fig. 1. The function of each part is described below.

2.2 Variation rules

The rules are described using the format of the context sensitive rewriting rules, and are arranged into four layers as shown in Table 1. Some examples of the variation rules are shown in Fig. 2. The rules in layer 0 translate an orthographic expression of the speech data into a phonemic expression.

The rules in layer 0 are well formulated by traditional Japanese phonology^{8),9)}. The rules in layers 1 and 2 translate a phonemic expression



A., I., U., E., and O. :
Japanese short vowels
02 : Japanese long vowel of O.
Aj : A diphthong like the English closing diphthong /ai/
! : A null symbol
e% : An acoustic segment in a transition that has the spectrum of vowel E.

Fig. 2—Examples of variation rules.

into phonetic (allophonic) hypotheses. The rules in layer 1 translate a phoneme into an obligatory allophone. The rules in layer 2 translate a phoneme into two or more optional allophones. Most rules for obligatory allophones and some rules for optional allophones are also formulated by traditional Japanese phonology. The rules in layer 3 translate a phonetic hypothesis into acoustic-segment hypotheses. If a rule in layer 2 or 3 is applied once, two or more hypotheses are generated. All of these hypotheses except one have variations. The 111 acoustic-segment symbols are used to represent the speech that contains Japanese-language phonemes and their variants.

2.3 Acoustic-segment hypothesizer

One or more lists of acoustic-segment hypotheses are generated by applying the variation rules to the orthographic expression of the speech data. The method of generating the acoustic-segment hypotheses is shown in Fig. 3.

2.4 Segment-duration rules

The segment-duration rules are based on isochronism of Japanese-language syllables. Some rules account for variations of segment duration in particular phoneme contexts and in allophonic variations. Some examples of the segment-duration rules are shown in Fig. 4.

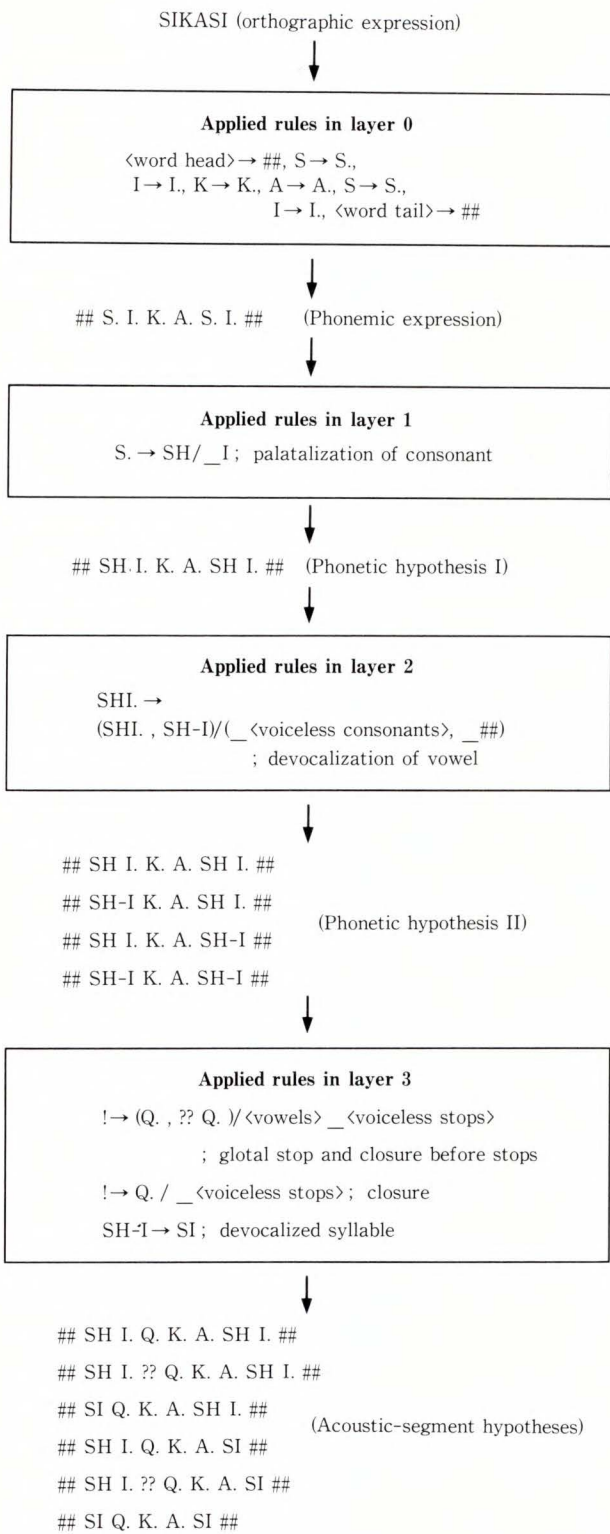


Fig. 3—Generation of acoustic-segment hypotheses.

2.5 Segment-boundary hypothesizer

Segment-boundary hypotheses are generated by applying the segment-duration rules to

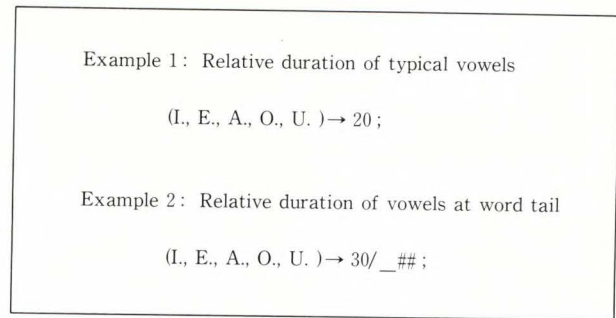


Fig. 4—Examples of segment-duration rules.

acoustic-segment hypotheses. A segment-boundary hypothesis represents the end positions of individual hypothesized acoustic segments. An end position of a segment is described using a relative frame number.

2.6 Acoustic templates

The acoustic templates mainly represent the place of articulation. Twenty one categories are defined in the acoustic templates. Each category consists of multiple templates to represent the minor spectrum variation of the category. Each acoustic template consists of a 16-channel FFT (Fast Fourier Transform) power spectrum (see section 2.7). Speaker-dependent acoustic templates are generated from 100-word training data³). To generate the templates, each training token is segmented by a rough top-down segmentation method that uses the speech power data and rules on the power shape around the phoneme boundaries. The result of the segmentation is checked by segment-evaluation rules. The segment evaluation rules reject 5 percent to 15 percent of the segmentation results of the training data. If the segmentation result is accepted, the acoustic templates are sampled at the plural frames in the individual segments. Template-extraction rules define the places of the sampling frames in the segment. For example, the rule for vowels is that their acoustic templates are sampled at 25 percent, 50 percent, and 75 percent positions in the vowel segment.

2.7 Acoustic labeling

Speech data is sampled at 16 kHz and



Fig. 5—Example of acoustic labeling and segmentation result.

quantized to 16 bits. The power spectrum of each frame is calculated by a 512-point FFT. The frame length is 32 ms, and the interval is 5 ms. The 257 components of the FFT power spectrum are compressed to 16 channels equally spaced on the mel scale.

The distances between each frame of input speech and the acoustic templates of individual categories are calculated using the K -nearest neighborhood method ($K = 3$). An acoustic-label lattice that contains the distance of each label is constructed as shown in Fig. 5. The labels in the lattice of Fig. 5 are aligned in order of distance. In Fig. 5, if the distance of the label is greater than a threshold, the label is not indicated.

The acoustic segment-boundary hypotheses are aligned with the acoustic-label lattice using dynamic programming. In this process, an island-driven method is employed to avoid propagating errors in segment-boundary hypotheses. That is, silence portions before voiceless stops and voiceless fricative portions in speech data and in segment-boundary hypotheses are time-aligned to make them anchor points. The speech data and the segment-boundary hypotheses are divided into islands by the anchor points, and segment-boundary hypotheses are aligned island by island using dynamic programming. If the distance between the acoustic label lattice and the hypotheses in the island, which is calculated in time alignment using DP (dynamic programming), is greater than a threshold, the alignment fails. If the alignment of every island succeeds, the segment boundaries are output as a result of segmentation. In other cases, the segment-boundary hypothesis is rejected. If all the

segment-boundary hypotheses are rejected, the top-down segmentation fails.

3. Basic concept and procedure of rule extraction

The rule extraction is based on the facts that top-down segmentation fails if the speech contains variations that are not represented in the existing rules, and that new rules can be appended until the top-down segmentation succeeds. Rules concerning variations whose production mechanisms cannot be explained, however, are not appended. This is because our current target is not to find new variation phenomena but to translate our knowledge about the variations into machine readable rules in order to use them for speech recognition. To perform this interactive rule-extraction, we use various resources, for example, the experience of speech researchers and papers on phonology⁸⁾⁻¹⁰⁾. We detect a variation phenomena in the segment labeling or in the spectrogram of speech data whose top-down segmentation fails, and translate each phenomenon into a rule. At this stage, the rule is called a "rule candidate".

The system generates acoustic-segment hypotheses using the existing rules and the rule candidate. To check whether each variation hypothesized by the rule candidate generally occurs in speech data, the hypotheses are matched with several utterances that contain the contexts in which the variation may occur. From the result of the check, we can determine the generality of the rule candidate. If the rule candidate is a general one, it is regarded as a meaningful rule and is registered in the system.

4. Support system for rule extraction

4.1 Overview

We have developed a support system to efficiently extract the rules from a large speech database. The support system is implemented on a Fujitsu M-780 large scale computer connected to a workstation for A/D and D/A conversions. The system consists of a speech database management subsystem, a rule database management subsystem, and an automatic rule evaluation subsystem.

4.2 Speech database management subsystem

This subsystem quickly selects speech data that contains phonemes in the specific contexts we want to investigate, and displays the waveforms and the spectrogram of the speech data on a 960 × 672 bit-map display terminal. Currently, the speech database contains 96 000 utterances of 6 females and 40 males (two sets of 1 000 Japanese phrases per speaker), and 20 000 utterances of 5 females and 5 males (two sets of 1 000 city names per speaker). All the speech data were recorded in a sound-proof room and automatically segmented into phrases or words using an ordinary speech boundary detection algorithm. After the segmentation results are checked by human operators using the display and the D/A conversion system, the segmented data are stored with a label.

4.3 Rule database management subsystem

This subsystem consists of the rule tracer, the rule counter, and the rule editor. The tracer displays how the rules are used in the top-down segmentation process, and displays the rules used to generate the accepted hypotheses. The counter measures the frequency of use of each rule in the accepted hypotheses.

4.4 Automatic rule evaluation subsystem

This subsystem automatically evaluates the existing rules. Using the top-down segmentation with the existing rules, this subsystem segments the speech data selected from the speech database, and offers the speech data whose segmentations fail. Then, new rules can be extracted from the offered speech data.

5. Rule extraction from a male speaker

The numbers of variation rules that were extracted from 1 000 phrases of Japanese spoken by a male speaker are shown in Table 2. This male speaker is referred to as speaker #0. In layers 1 and 2, rules concerning well-known variation phenomena, for example, the devocalization of vowels, are extracted. In layer 3, many rules concerning semivowels, on-glides (vowel to consonant transition), and off-glides (consonant to vowel transition) are extracted. Since each vowel-consonant-vowel syllable or vowel-semivowel-vowel syllable has a different glide pattern, the number of rules is large. All the speech data from which these rules are extracted are correctly segmented into acoustic segments using these rules. It is not necessary to extract the rules concerning unknown variation phenomena.

By examining the frequency of use of each rule that generates a hypothesis whose segmentation succeeds, we can estimate the occurrence

Table 2. Numbers of variation rules

Layer	Variation phenomena	For one male	For ten males
1	Allophone of syllabic nasal	2	2
	Palatalization of consonant	1	1
2	Devocalization of vowel	21	23
	Neutralization of vowel	20	20
	Falling of closure	7	19
	Rounding of vowel	3	3
	Lengthening of vowel	3	3
	Buzz bar	1	8
	Nasalization of /g/	1	3
	Assimilation of vowel	—	22
	Nasalization of vowel	—	18
	Assimilation of consonant	—	13
	Addition of aspiration	—	5
	Diphthongization	—	3
	Insertion of closure	—	2
Vocalization of /h/	—	1	
3	On-glide and off-glide	44	46
	Glide of semivowel	31	31
	Glide between vowels	10	10
	Glide of /y/ compound sound	15	22
Total		159	255

Table 3. Estimated occurrence probabilities of variation phenomena of speaker #0

Variation phenomena	Number of phonemes	Occurrence probability (%)
Addition of buzz bar at word-initial voiced stops	148	24.3
Vowel lengthening /OU/	226	96.9
Vowel lengthening /EI/	41	0
Devocalization of vowel	259	20.8
On-glide /a/ → /m/	31	51.6
Off-glide /m/ → /a/	61	11.5
Off-glide /d/ → /a/	59	88.1
Glide between vowels /a/ → /i/	119	95.8
Glide between vowels /i/ → /a/	5	100
Nasalization of word-medial /g/	110	85.5

probability of each variation. Table 3 shows examples of the variations detected in 1 000 phrases of speech data, the numbers of the phonemes in which the variation is hypothesized, and the estimated occurrence probability of each variation.

6. Rule extraction for multiple speakers

6.1 Questions and experiments

After the rules for speaker #0 were formulated, the following questions were raised:

- Q1. Are the rules for speaker #0 enough to represent the variations in the speech of other speakers?
- Q2. Does the number of rules converge to a reasonable number when extracting the new rules for multiple speakers?
- Q3. On average, how many of the rules for multiple speakers are used for an individual speaker?

To answer these questions, the following experiments were conducted:

- E1. Evaluation of the rules for speaker #0 using 46 000 phrases spoken by 46 speakers
- E2. Extraction of new rules by investigating the variations in 10 000 phrases spoken by ten males
- E3. Extraction of a new-rule subset for each speaker

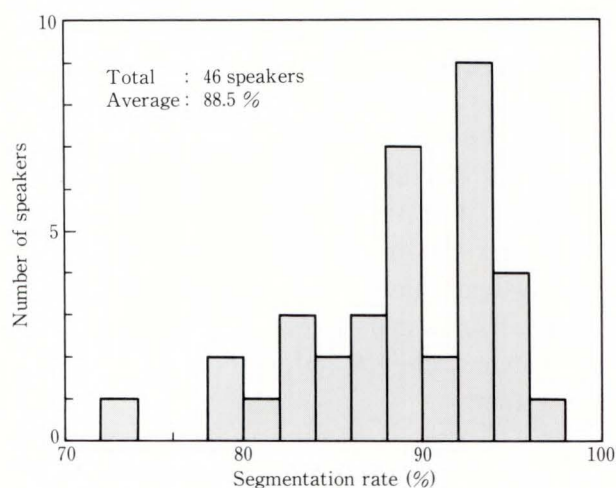


Fig. 6—Distribution of correct segmentation rates (rules for speaker #0).

6.2 Evaluation of the rules for speaker #0

The rules extracted for speaker #0 were automatically evaluated by the top-down segmentation of 46 000 Japanese phrases spoken by 46 speakers (1 000 phrases per speaker). As shown in Fig. 6, 11.5 percent of the 46 000 phrases could not be segmented with the rules for speaker #0. This indicates that the rules for speaker #0 are not capable of segmenting the speech of other speakers.

6.3 Extraction of new rules for ten males

First, we randomly selected ten males from the 46 speakers and extracted new rules for multiple speakers. Then, 1 112 phrases which could not be segmented using the rules for speaker #0 were automatically selected from the 10 000 phrases spoken by those ten speakers. Finally, we investigated the variations in the 1 112 phrases and extracted new rules.

Figure 7 shows the extraction process for new rules. The new rules were extracted sequentially for speakers #1 to #10. Before we extracted new rules for speaker #*n*, all rejected data of speakers #*n* were segmented again using the rules extracted for speakers #0 to #*n*-1. Then, we investigated the data that were rejected again. In this way, the number of phrases to be investigated was reduced from 1 112 to 334. The continuous line in Fig. 7 represents the investigation rate. The investigation rate is the

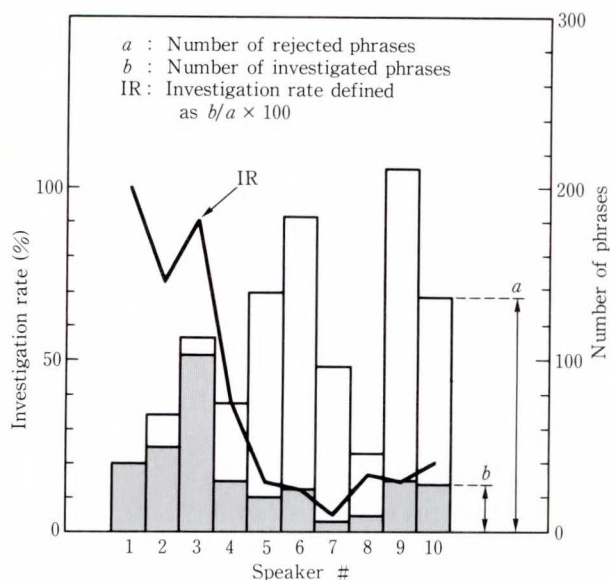


Fig. 7—Extraction process for new rules.

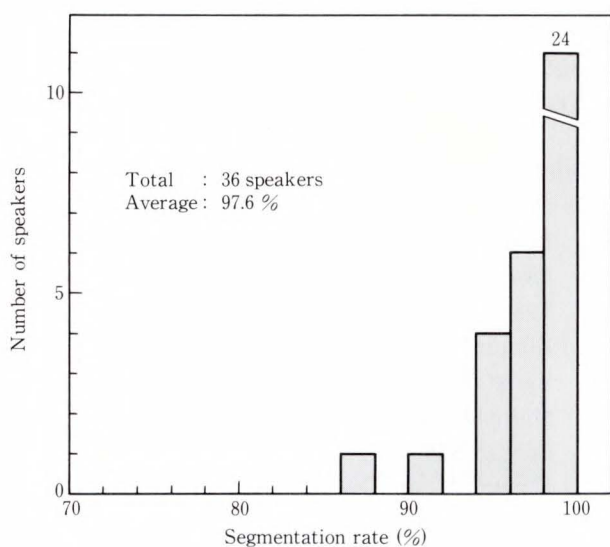


Fig. 8—Distribution of correct segmentation rates (rules for ten males).

ratio of the number of investigated phrases, b , to the number of phrases rejected by the rules for speaker #0, a . This rate decreases drastically at speaker #5. After speaker #5, the number of error phrases for a new speaker (represented by the dark portions of the bar graph) is about 30, which is three percent of 1000 phrases. From this trend in the investigation rate, we can assume that the number of rules does not increase drastically when new rules are extracted

Table 4. Segmentation rates for males and females

	Number of speakers	Average segmentation rate (%)
Males	30	97.04
Females	6	98.71

for multiple speakers.

Using the above-mentioned extraction procedure, we obtained a total of 255 rules in layers 1 to 3. These rules concern 21 kinds of variation phenomena. The numbers of rules that were extracted from the ten male speakers are shown in Table 2.

Several variation phenomena were appended to these rules, for example, diphthogizations, vocalization of glottal fricatives, nasalization of vowels, assimilation of consonants, addition of aspirations, and insertion of silences. (These variation phenomena were not appended to the rules for speaker #0.) Layer 3 has the greatest number of rules.

We evaluated the new rules using 36 000 phrases spoken by 36 test speakers (6 females and 30 males). Figure 8 shows the distribution of the correct segmentation rates. Of the 36 000 phrases, 97.6 percent were correctly segmented by our top-down segmentation system using the rules extracted from the ten speakers.

Table 4 shows the correct segmentation rates obtained using the new rules for females and males. As the table shows, there is no significant difference between the rates for males and females.

6.4 Extraction of new-rule subset for each speaker

Using the support system, we can automatically obtain a subset of the rules for each speaker. While the speech data for each speaker is being processed, the support system counts the frequency of use of each rule in layers 2 and 3. The system then rejects the rules whose frequencies are zero to obtain a subset of the rules for the speaker. Each subset contains all the rules in layers 0 and 1. Figure 9 shows the distribution of the rule utilization rate for each speaker. The rule utilization rate is defined as

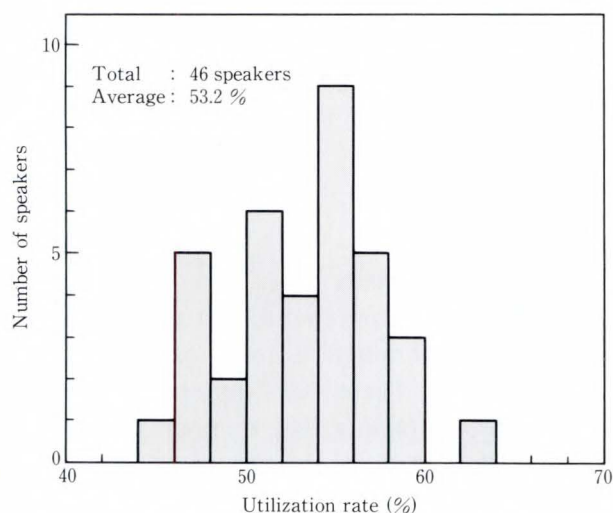


Fig. 9—Distribution of rule utilization rates.

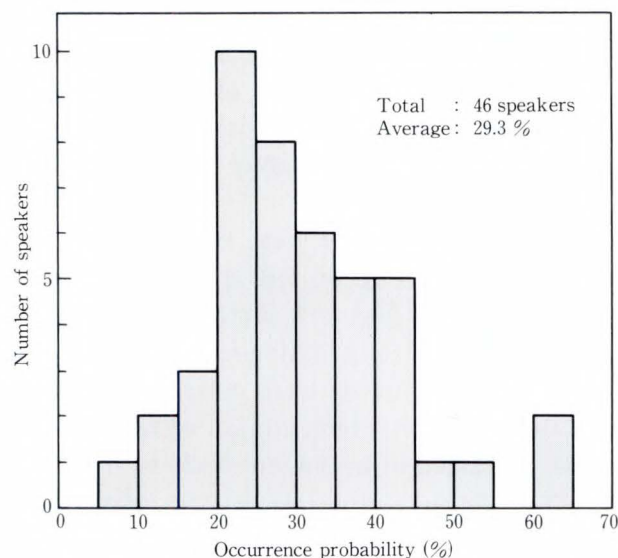


Fig. 10—Distribution of occurrence probabilities of vowel devocalizations.

the ratio of the number of rules in the subset to the total number of rules for multiple speakers. On average, each subset contains 53.2 percent of the rules for multiple speakers.

Using the method described in chapter 5 (see Table 3), we can estimate the occurrence probability of each variation for multiple speakers. Figure 10 shows the distribution of the estimated occurrence probabilities of vowel devocalizations for the 46 speakers.

7. Conclusion

The interactive extraction of the rules for estimating the variations in speech was described.

We proposed an interactive method for extracting the rules that account for the variations in speech data, and developed a support system for rule extraction. We experimentally determined that the rules for individual speakers cannot be applied to other speakers, but the rules for ten male speakers can be applied to multiple male and female speakers. Furthermore, we found that the number of rules does not increase drastically when rules are extracted for multiple speakers, and the rule subset for each speaker contains about half of the total rules for the ten male speakers.

We have presented our evaluations of the use of the extracted rules in large vocabulary speech recognition in recent papers⁵⁻⁶). These evaluations indicate that the rules are very promising for use in speech recognition.

In the future, we will use our support system to study speech data that contains phonemic contexts that are not included in the 1 000 phrases used in this work.

References

- 1) Kimura, S., and Nara, Y.: Interactive Extraction of Phonemic Variation Rules in Continuous Speech. Proc. IEEE Int. Conf. Acoust. Speech Signal Process., 1986, pp. 2279-2282.
- 2) Kimura, S., and Nara, Y.: Extraction of Phonemic Variation Rules in Continuous Speech Spoken by Multiple Speakers. Proc. IEEE ICASSP, 1987, pp. 825-828.
- 3) Kimura, S., and Nara, Y.: Automatic generation of phoneme dictionary using top-down phoneme segmentation method. (in Japanese), Proc. Spring Meet., Acoust. Soc., Jpn., 2-4-1, 1985, pp. 45-46.
- 4) Kimura, S., Iwamida, H., and Sawada, T.: Extraction and Evaluation of Phonetic-Acoustic Rules for Continuous Speech Recognition. Proc. IEEE ICASSP, 1989, pp. 338-341.
- 5) Kimura, S.: 100,000-Word Recognition Using Acoustic-Segment Networks. Proc. IEEE ICASSP, 1990, pp. 61-64.
- 6) Kimura, S., and Yamazaki, Y.: Boosting the Accuracy of a 100,000-Word Japanese Speech Recognition System. Proc. IEEE ICASSP, 1991, pp. 717-720.
- 7) Aikawa, K., Sugiyama, M., and Shikano, K.: Spoken Word Recognition Based on Top-Down Phoneme Segmentation. Proc. IEEE ICASSP, 1985, pp. 33-36.

- 8) Hattori, S.: Phonetics. (in Japanese), 1st ed., Tokyo, Iwanami, 1984, 215p.
9) Amanuma, Y., Ootsudo, K., and Mizutani, O.: Japanese Phonetics. (in Japanese), 1st ed., Tokyo,

- Kuroshio Shuppan, 1978, 191 p.
10) Zue, V.W., and Cole, R.A.: Experiments on Spectrogram Reading. Proc. IEEE ICASSP, 1979, pp. 116-119.



Shinta Kimura

Multimedia Systems Laboratory
FUJITSU LABORATORIES,
KAWASAKI
Bachelor of Electronics
Kobe University 1978
Master of Electronics
Kobe University 1980
Specializing in Speech Recognition
and Synthesis

Automated MDF System for Switching System

• Shun-ichi Tominaga • Sadao Fujii • Akira Fukuoka

(Manuscript received February 28, 1992)

This paper describes an automated main distributing frame (MDF) system designed to provide the MDF system of a switching system with remote control and automatic jumpering. The MDF system crossconnects between subscriber cables and office equipment cables by jumpering. Until now, jumpering has been done manually and automating this operation for telephone services has been an objective for a long time. In this system, a high-precision robot jumpers telephone lines by inserting miniature contact pins into cross-point holes in matrix boards. A single automated MDF system can handle up to 2 100 office-equipment cable terminals, and a larger automated MDF system can be realized by operating multiple systems in parallel.

1. Introduction

To process a service order for a new subscriber, the MDF must connect the subscriber's cable to the switching system.

The switching systems have evolved from the crossbar system to the analog electronic switching system, then to the digital switching system. This has improved the operability and maintainability of switching systems.

The connection terminal boards in the MDF have been partially revised but are still dependent on manual labor. This has prevented the connection of new subscribers from being completely automated and controlled remotely. Therefore, there have been various problems, such as reduced efficiency, increased annual MDF operation costs and delays in connecting new subscribers for telephone services.

Matrix switches are needed for connecting any subscriber to a switching system. Relays are generally used to compose the matrix switch. But, because the number of relays increases substantially as the number of connection terminals increases, matrix switches using relays are not practical.

The automated MDF system is realized by

utilizing the following three kinds of components¹⁾⁻³⁾.

- 1) A matrix board consisting of a printed wiring board with cross-point holes used as matrix switches
- 2) Miniature contact pins
- 3) A high-precision robot to insert and extract the contact pins

These components are highly reliable, cost effective, and able to be mass produced. They were developed by Fujitsu together with the Nippon Telegraph and Telephone Corporation (NTT) and Oki Electric Industry Co., Ltd. based on fundamental technology held by the NTT. The automated MDF is small enough to perform automatic remote-control jumpering.

This automated MDF system has been developed for public switching systems, but it can also be applied to PBX use.

The main technologies used in the automated MDF system are described in chapters 3 and 4. Chapter 3 describes the contact pins and the matrix boards. Chapter 4 describes the high-precision robot.

2. System overview

2.1 System configuration

Figure 1 shows a block diagram of the automated MDF system^{4),5)}. The automated MDF system consists of a modem, a system controller, a robot mechanism, and a connection mechanism. The modem is an interface between the automated MDF system and the operation terminals through the telephone network. The system controller manages and controls the whole system. The robot inserts and extracts the contact pins into and from the cross-point holes of the matrix board.

The connection mechanism has a three-stage link configuration^{1),2)} for two reasons:

- 1) To reduce the number of cross-points to make the automated MDF system smaller.
- 2) To reduce the jumpering time.

The three-stage link configuration has about one-ninth the number of cross points of the non-link configuration, where the inlets and outlets are connected by a one-stage matrix switch.

A remote operator can connect an operation terminal, such as a personal computer, to the automated MDF system through a modem and the telephone network. When an operation terminal is connected to the automated MDF system, an identification (ID) check is executed to ensure safe transmission through the telephone network.

2.2 System specifications

Table 1 lists the automated MDF system specifications^{2),4)}. The specifications in Table 1 ensure that the system will be used in the same way as a switching system. The external dimensions, weight, and power supply are designed to comply with the switching system installed on the same floor. The switches form a three-stage link configuration so that the inlets and outlets can be connected arbitrarily⁶⁾. The matrix boards are split and located on both sides of the robot to halve the robot's movement. The jumpering time is designed according to human interfaces. The mean time between failures

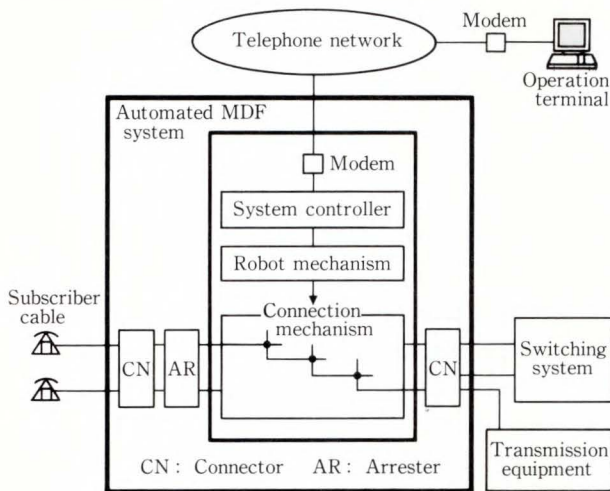


Fig. 1—System block diagram.

Table 1. System specifications

Type		I	II	III
Number of terminals accommodated	Subscriber cable	1 000	1 800	3 600
	Office-equipment cable	540	1 000	2 100
External dimensions (mm)	Length	1 500	1 800	2 800
	Breadth	600		
	Height	1 800		
Weight (kg)		About 480	About 530	About 780
Switch configuration	Three-stage link (non-blocking)			
Number of matrix boards used		58	108	216
Matrix board mounting	Double-sided (front and back)			
Number of pin-supply matrix boards		2		
Jumpering time		3 min or less		
Power supply		48 V DC 600 W or less		
MTBF		2 000 h		

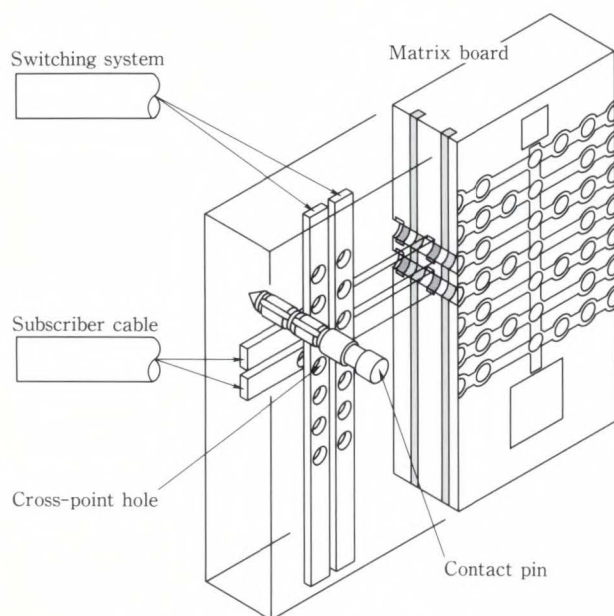


Fig. 2—Principle of jumpering.

(MTBF) is calculated by the robot's mechanical operations.

2.3 Jumpering function

Figure 2 shows the principle of jumpering¹⁾⁻⁴⁾. The matrix board has many closely spaced cross-point holes configured as matrix switches. The subscriber cables are connected to the switching system by inserting contact pins into the cross-point holes.

The robot of the automated MDF system inserts one contact pin per stage. Therefore three contact pins are subsequently inserted into each cross-point hole per jumpering operation.

2.4 Hardware configuration

Figure 3 shows the automated MDF system^{2),4)}. The system consists of a system controller, a robot mechanism, a connection mechanism, and a modem. The system controller consists of a robot mechanism control unit, an alarm panel, an amplifier unit, a control unit, and a power unit. The control unit accommodates a microprocessor unit (MPU), one megabyte of main memory, a forty megabyte hard disk, and a floppy disk drive. The alarm panel indicates the alarm status.

The robot mechanism consists of a transport

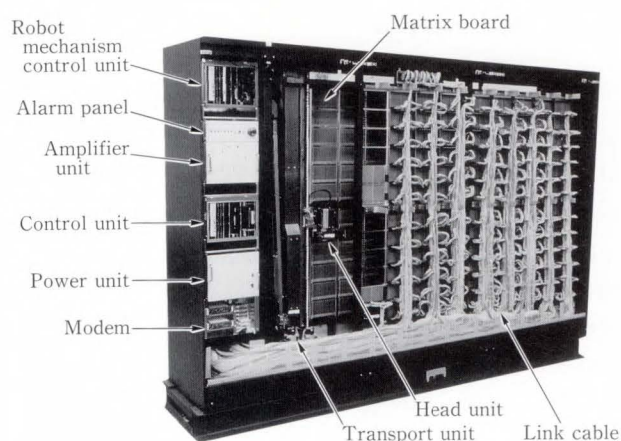


Fig. 3—Automated MDF system.

unit and a head unit.

The connection mechanism connects the matrix boards between the first and second stages, and between the second and third stages, installed at the front and back, with link cables. The link cables are routed through the lower part of the system controller to connect the front and back matrix boards.

3. Contact pins and matrix boards

The requirements of the MDF system are as follows: To connect any subscriber cable terminal to any office-equipment cable terminal, to be able to handle a pair of wires because a telephone signal is a balanced transmission signal, and to be small. Therefore, MDF needs a high-density matrix switch in which pairs of wires are handled by each unit switch. Contact pins and matrix boards were developed for use in the high-density matrix switch in the automated MDF system (see Fig. 4).

A pair of switches can be closed by inserting a contact pin with two contact springs into a hole in the matrix board. These holes have divided through-hole contacts, which are contacts on the inner layer edges of an unplated drilled hole in a multilayer printed wiring board⁷⁾⁻⁹⁾ (see Fig. 5).

The automated MDF system uses laser tracking to find the target hole and then inserts a contact pin into the hole. Laser tracking requires a special optical pattern on the matrix board^{10),11)}.

Table 2 lists the functions of the matrix board and contact pin.

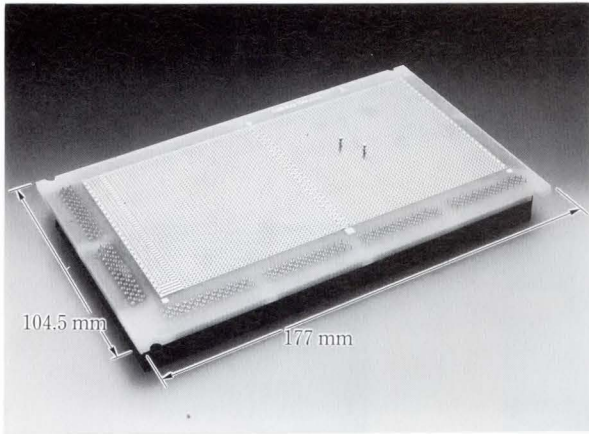


Fig. 4—Matrix board.

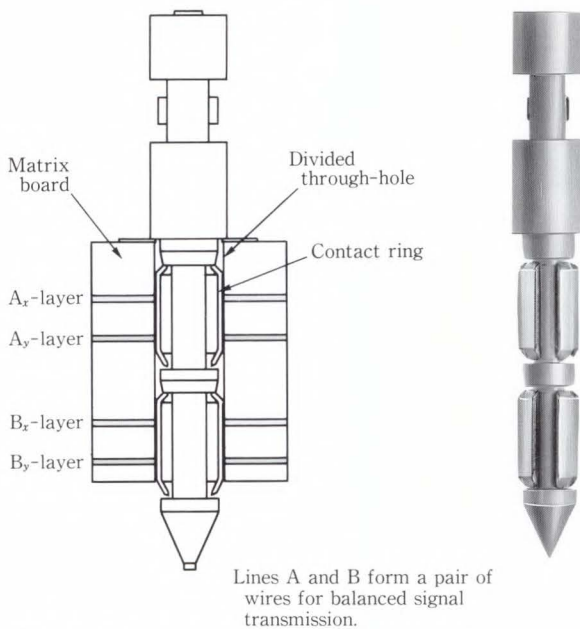


Fig. 5—Insertion of contact pin into divided through-hole on matrix board.

Table 2. Functions of matrix board and contact pin

Device name	Function	New technology	
Matrix board	Contact	Technology to make a divided through-hole contact Contact technology with a contact pin	
	Speech path	Technology to reduce cross-talk loss in a speech path	
	Optical device	Tracking pattern	Normal reflection
Technology to make a miniature contact pin with micro springs			
Contact pin	Contact		

3.1 Miniature contact pin⁷⁾⁻⁹⁾

Figure 6 shows the structure and dimensions of the miniature contact pin. The technology to make the contact pin core requires precision plastic molding with engineering plastics. The contact pin has a pair of springs. The spring has a ring shape to give it enough contact force and to produce a stable contact resistance with the opposed ring-type contact in the matrix board. Additional reasons for using the ring-shaped springs are to simplify presswork in mass production and to provide a close match with the core design. Both sides of the ring-shaped spring are narrow for assembly with the core, as shown in Fig. 6. The dimensions of the core and the spring were determined as shown in Fig. 6. This design ensures there is enough contact force and stable contact resistance by compensating for variations in mass production. The spring specifications are given in Table 3.

The communication system requires highly reliable contacts. The main considerations in designing the contacts are: i) cross-rod type contact, ii) twin contacts, iii) sliding contact,

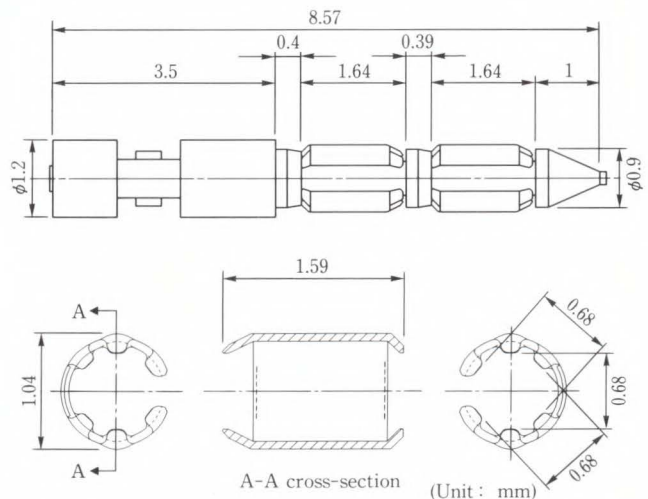


Fig. 6—Structure and dimensions of contact pin.

Table 3. Spring specifications

Item	Specifications
Plate thickness	70 μ m
Spring width	1.18 mm
Stiffness	3 000 gf/mm
Limit of spring	160 kgf/mm ²

iv) the contact force, and v) the contact material.

The spring has two projections that make two cross-rod type contacts with the opposed ring-shaped contact on the matrix board. Furthermore, this cross-rod contact provides a sliding contact during insertion and extraction of the contact pin, which removes the contami-

nation film that is naturally formed. The contact is gold-plated to ensure reliability and to make the conductivity of the electric contact stable.

3.2 Matrix board

1) Process technology to make divided through-hole contacts⁷⁾⁻⁹⁾

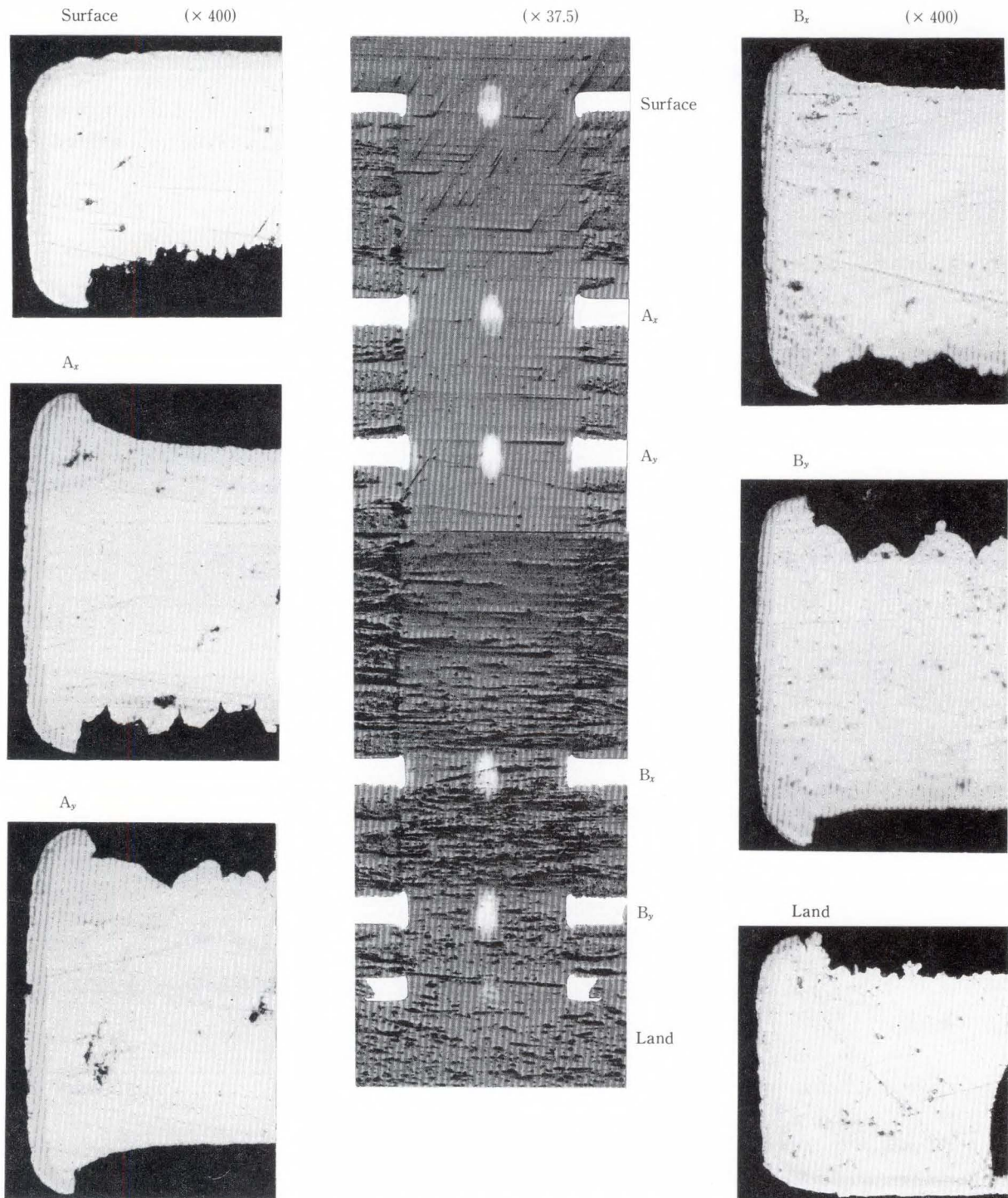


Fig. 7—Cross-section of ring-shaped contact of divided through-hole.

The major problems are the formation of a cross-rod type contact with the spring of the contact pin and the connection of these contacts to make a matrix.

Making a matrix involves making *X*- and *Y*-axis contacts. Furthermore, the method should be suitable for mass production. To solve these problems, multilayer printed wiring board technology is employed. Process technology was developed to make contacts on the edges of layers in a drilled hole. This involves a Cu, Ni, and Au plating process. Figure 7 shows the cross section of the ring-shaped contacts that make cross-rod contact with projection contacts of the spring of the contact pin. The Au plating process was also developed so that the contact edges and surface patterns are formed in one process. The surface patterns have good reflectivity for the optical tracking pattern.

The through-hole diameter and pitch was minimized to reduce the MDF size. However, they must ensure contact with a reasonable contact force. A small contact force makes the contact conductivity unstable, and a large contact force will crush the contact pin. It is necessary that these design conditions are realized, even if the dimensions of the ring-shaped spring and matrix board contact vary during production. To solve these problems, the through-hole diameter was set to 0.96 mm and the pitch to 1.5 mm.

2) Contact technology using the matrix board and contact pin⁹⁾

The divided through-hole of the matrix board and the contact spring of the contact pin form an electrical contact. Inserting the contact pin into the divided through-hole closes the contact, and extracting the contact pin from the divided through-hole opens the contact. Figure 8 shows the contact force as well as the insertion and extraction force for mass production giving the experimentally estimated data as a reference. The contact force is over 100 gf, which is sufficient for telecommunications equipment. The insertion and extraction force is less than 500 gf, which is small enough to ensure that the contact pin is not broken.

When the contact pin is inserted in the divided through-hole, the contact spring is fixed only in the radial direction by the ring-shaped

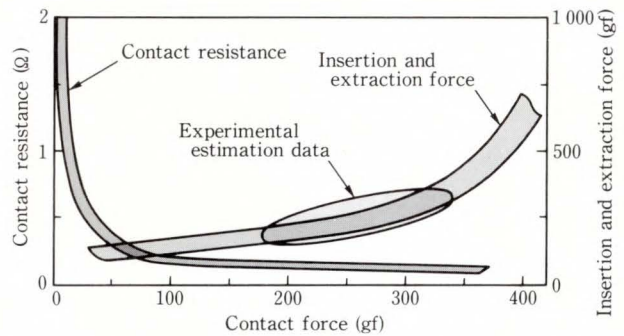


Fig. 8—Contact force, and insertion and extraction force.

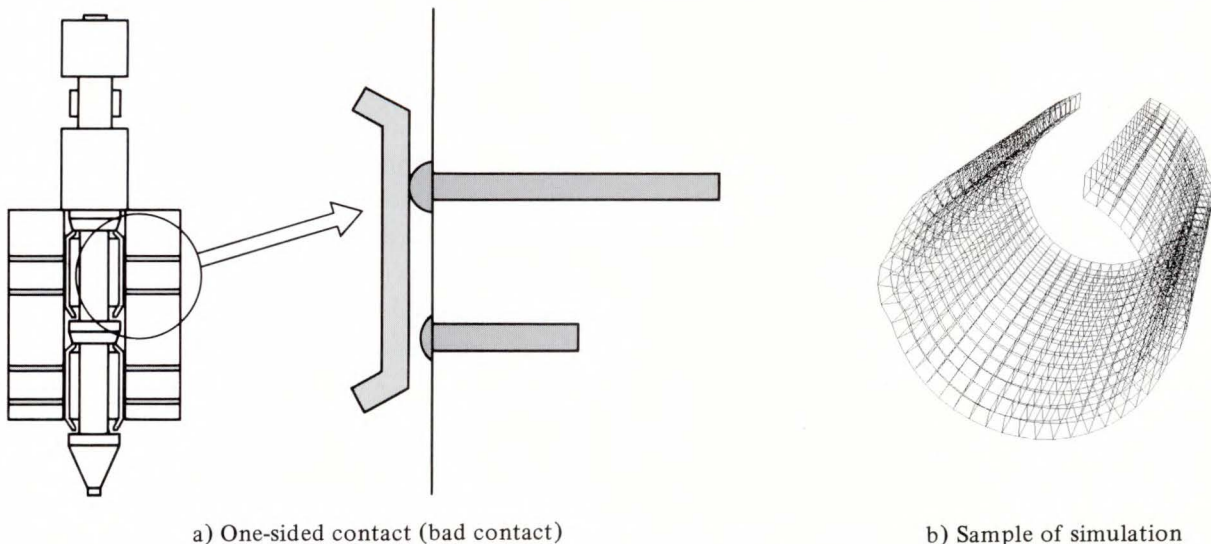


Fig. 9—Contact force when diameters of two ring-shaped contacts are different.

Table 4. Qualification test of matrix board and contact pin (contact pin inserted into divided through-hole)

Test item	Test condition
Temperature-humidity cycle test	-10 °C to +65 °C 90-98%*, 30 cycles
Galvanic corrosion test	40 °C 90% 1 000 h
Sulfur dioxide test	25 °C 75% 25 ppm SO ₂ 500 h
Mixed accelerated deterioration test	10 cycles of -10 °C to +65 °C 90-98%*, and after 200 ppm H ₂ S 500 h
High temperature creep test	85 °C 1 000 h

*: MIL STD 202 METHOD106

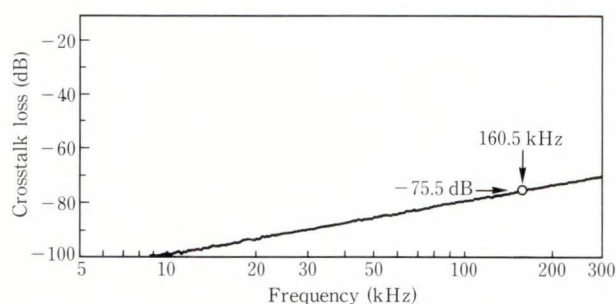


Fig. 10—Crosstalk loss of matrix board.

contact of the matrix board. Therefore, if a pair of ring-shaped contacts have different diameters, one of the contacts might not have enough contact force as shown in Fig. 9a). To get a balanced contact force, the authors determined the contact force by computer simulation as shown in Fig. 9b). This simulation calculated the allowable variation in the diameter of the ring-shaped contact.

The reliability of the matrix board and contact pin was evaluated by the acceleration tests listed in Table 4.

3) Technology to reduce crosstalk loss in the speech path^{12),13)}

Since integrated service digital network (ISDN) subscriber circuits may be connected, the MDF crosstalk loss should be under 70 dB in a band of up to 160 kHz. To secure the crosstalk characteristics, the pattern width and line pitch of the internal layers in the matrix board were optimized. Figure 10 shows the actual measure-

ments of the matrix board. The pattern width, line pitch, and matrix board thickness were determined to minimize the size of the matrix board under these conditions.

4) Surface finish technology

The laser tracking pattern should have both normal and diffused optical reflection characteristics. The normal optical reflection characteristic is used for the robot sensor to track the route and find the center of the target hole. The diffused optical reflection characteristic is used to measure the distance between the robot hand and the surface of the matrix board.

The normal optical reflection characteristic depends on the luster and thickness of the Ni under the plating and the material characteristics of the surface Au plating¹⁴⁾. The authors developed the optimum Ni and Au plating for the matrix board surface finish by optimizing these factors. The Au plating has a sufficient normal optical reflection rate. To ensure uniformity in the normal optical reflection over the entire surface of the matrix board, a process was developed that limits the damaged areas to less than 100 μm .

There are two methods to make a surface with a diffused optical reflection:

- i) using optical refraction, reflection, and scattering of a laser beam through a transparent thin film, and
- ii) making a rough surface.

Both methods produce a sufficiently diffused optical reflection surface. To simplify mass production and to ensure long-term reliability, the rough surface method was employed. A process was also developed to control the surface roughness of the matrix board. Using these techniques ensured satisfactory uniformity of the diffused optical reflection characteristics of the matrix board. Figure 11 shows data on mass-produced matrix boards.

5) Long-term reliability of optical characteristics

The authors verified the long-term optical reliability of the matrix boards using accelerated aging tests, which were equivalent to leaving the matrix boards in a machine room atmosphere for ten years.

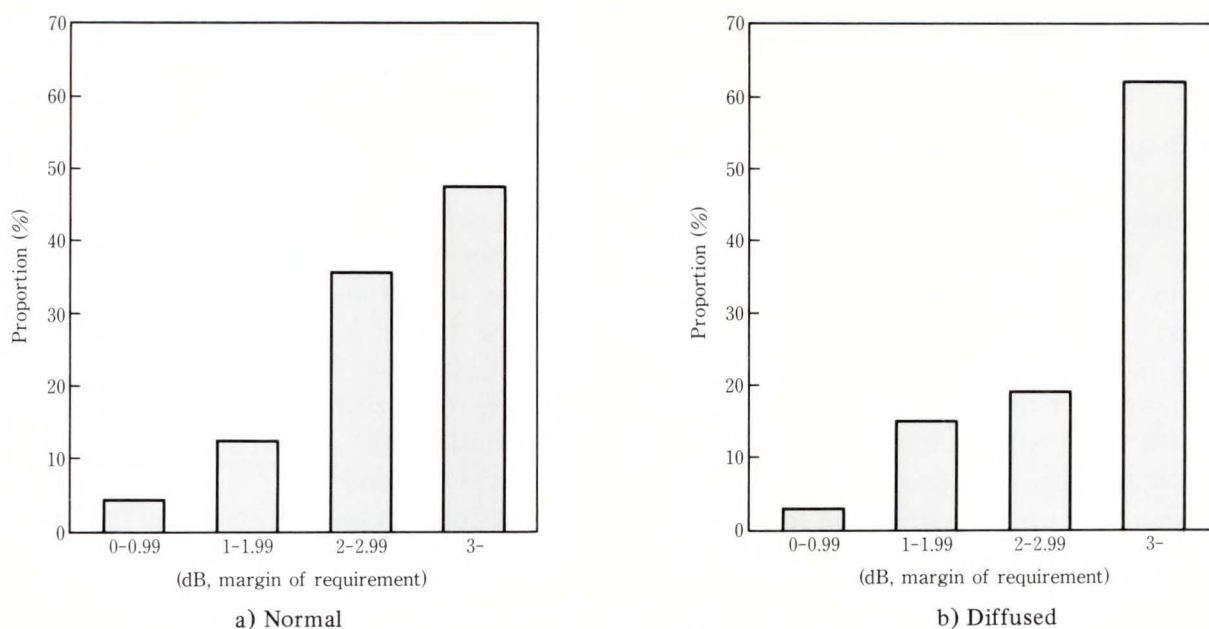


Fig. 11—Optical reflection characteristics of the surface of matrix board.

4. High-precision robot

4.1 Outline of the robot

The robot's function is to insert and extract contact pins in a matrix board. Because of the three-stage link configuration, three contact pins are inserted to form a connection circuit for each subscriber. For quick service, the three contact pins must be inserted within three minutes.

The robot has vertical and horizontal transport units, and can move 1 400 mm vertically and 2 000 mm horizontally. To reduce the work space and to increase the installation capacity, up to 216 matrix boards can be installed on each side of the transport unit. The head unit, another component of the robot, consists of a handling subunit, a precision positioning subunit and a laser sensor. To enable access to both sides, the handling subunit can turn through 180° while holding a contact pin.

4.2 Technical requirements

The automated MDF robot must meet the following performance requirements:

1) High-speed precision positioning

The robot must move over a work area holding up to 216 matrix boards and insert or extract three contact pins within three minutes. Each matrix board has about 5 000 cross-point

holes. The cross-point hole pitch is 1.5 mm and the contact pin diameter is 1.04 mm. To correctly locate a target hole and to insert or extract a contact pin positively, the positioning error must be ± 0.35 mm or less over in the whole work area. Therefore, the robot must cover a large work area at high speed and locate a target hole in the specified matrix board accurately.

2) Contact pin insertion and extraction

Considering of the contact force, a contact pin must be inserted with a force of 500 gf to ensure a stable contact. Since the pin diameter is 0.58 mm at its thinnest part, a radial force of 110 gf breaks the contact pin. It is necessary to ensure that the radial force does not exceed 110 gf at the maximum misalignment of the contact pin with the center of the hole (0.35 mm) when the contact pin is inserted with the maximum force.

3) High reliability

In the automated MDF system, extracting the wrong contact pin breaks a necessary channel, and inserting a contact pin into the wrong hole cannot make a channel. Since the system is installed in a remote location, troubleshooting and recovering from errors will take many hours and a lot of expense to go there. Therefore, the system must be able to insert and extract the

contact pins with high reliability and to recover automatically from minor errors.

4.3 High-speed precision positioning

Since the robot must move about 2 000 mm horizontally, a high-speed transport unit and a precision positioning subunit are installed and driven by separate servomotors. The high-speed transport unit (X -axis, Y -axis) enables the robot to move to the target matrix board at 500 mm/s. The precision positioning subunit (ΔX -axis) moves the robot within the same matrix board. The laser tracking mechanism reads the reflection from the plated pattern on the matrix board to position the robot at the target cross-point hole. High-speed precision positioning is achieved by two positioning mechanisms^{10),11)} (see Fig. 12).

1) High-speed movement

The system is too large to determine the mounted positions of the matrix boards with high precision. The robot learns and stores all the matrix board positions when the system is installed. When inserting or extracting a contact pin, the head unit of the robot is moved to the target matrix board according to learned data at high speed for rough positioning. The motor encoder is used for the positioning and the row

and column marks are counted to double check the position.

2) Tracking^{10),11)}

The robot must access the specified cross-points on the matrix board correctly. A path pattern is printed on each matrix board to help the robot to locate the target cross-point by scanning it with the laser sensor. The reflection from the pattern is detected and compared with the expected data. The laser tracking mechanism enhances the reliability of positioning at the target cross-point.

3) Precision positioning^{10),11)}

The robot measures where the origin mark of the matrix board is on the robot coordinate system by cross scanning vertically and horizon-

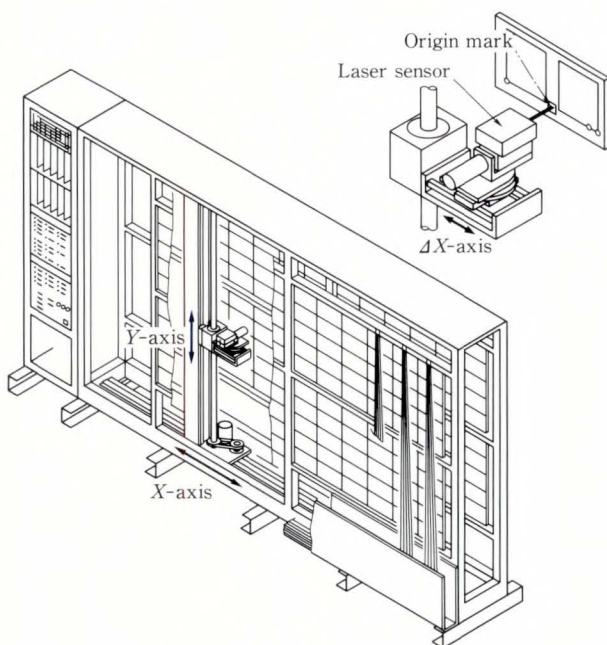


Fig. 12— X -axis and ΔX -axis.

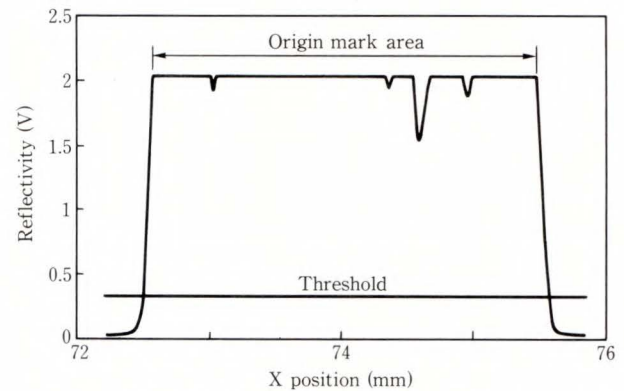


Fig. 13—Reflectivity of origin mark.

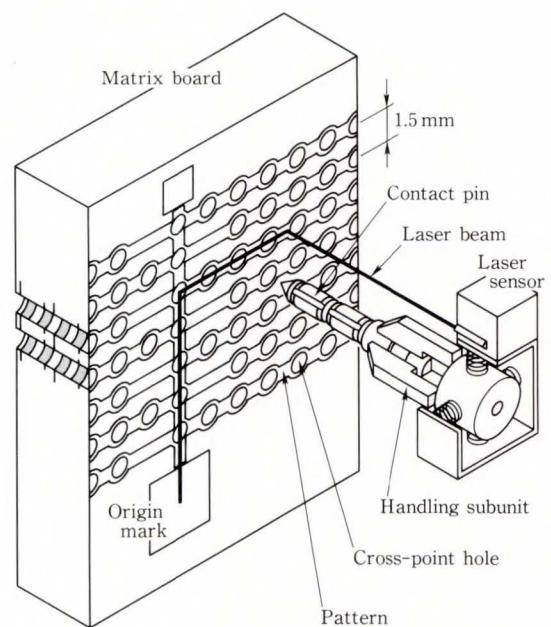


Fig. 14—Positioning at cross-point hole.

tally with the laser sensor. This obtains correction data for the matrix board coordinate system. Figure 13 shows an example of the data output from the laser sensor when the origin mark is scanned.

The robot is positioned precisely at the target cross-point hole. While monitoring the matrix board surface pattern with the laser sensor, the robot moves to the target cross-point calculated from the correction data. For example, to position at target cross-point P (coordinate X_p, Y_p), the robot moves a distance of Y_p vertically along the ID pattern, then a distance of X_p horizontally as shown in Fig. 14. During the movement, deviations from the pattern and the number of holes passed are checked by tracking. This enhances the positioning precision. Figure 15 shows the sensor output data when the robot moves horizontally. Similar data is also output when the robot moves vertically.

Finally, the target cross-point hole is located by cross scan measurement and the hand is positioned over the center of the hole with high

precision. The hand is positioned with an error of 0.35 mm or less so that the contact pins can be inserted or extracted smoothly. Figure 16 shows the laser scanning for cross scan measurement, and Fig. 17 shows an example of laser sensor output.

4) Laser sensor for positioning¹⁴⁾⁻¹⁶⁾

The robot calculates the displacement from the encoder data. It also checks the matrix board mounting status, measures the cross-point hole positions, and confirms the contact pin statuses before and after insertion and extraction. To do this, the robot needs an eye to recognize the target position. Therefore, the authors developed the laser sensor shown in Fig. 18.

A laser beam is emitted from the laser diode toward the surface of matrix board. Its normal reflected light is measured by the photodiode where the intensity is converted into an electric signal. The diffused reflected light is converged to the position sensitive device. The distance from the matrix board is measured by using the principles of trigonometry.

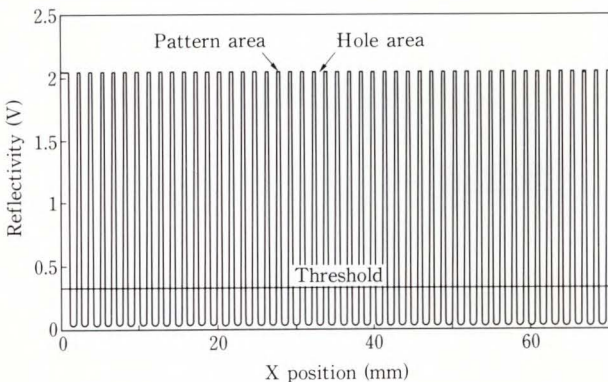


Fig. 15—Reflectivity during X-scan.

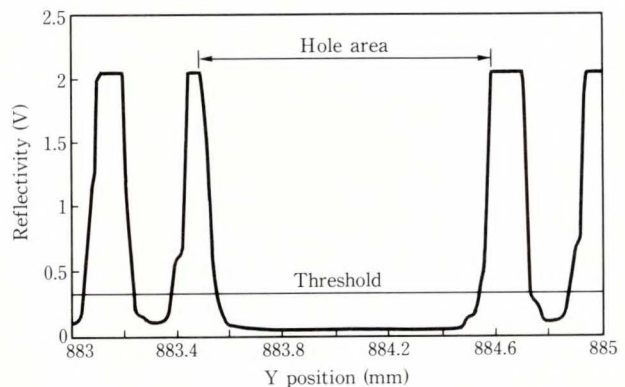


Fig. 17—Reflectivity at cross-scan measuring.

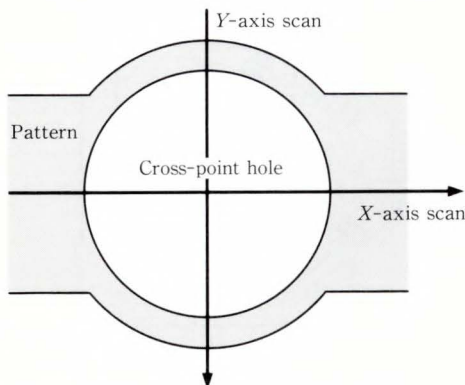


Fig. 16—Cross-scan measurement.

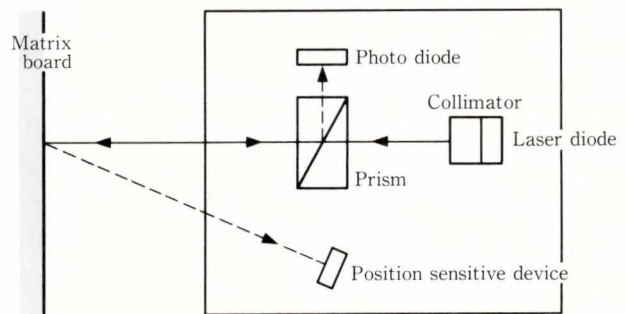


Fig. 18—Block diagram of laser sensor.

This sensor is attached to the robot to locate the mounted position of the matrix board, to measure the distance from the matrix board, to detect patterns, to locate the cross-point hole position, and to detect the contact pins.

4.4 Contact pin insertion and extraction

Even after the robot is positioned at the target cross-point with the laser sensor, the center of the contact pin may not match the center of the cross-point hole. If the contact pin is then forcibly inserted, it will be damaged. To prevent this problem, a handling subunit was developed, equipped with a compliance assembly, to move the contact pin to the center of the cross-point hole^{17),18)}.

1) Compliance assembly

The handling subunit consists of a grasping assembly, a compliance assembly, and a pivot. The grasping assembly holds a contact pin with four fingers. The compliance assembly flexibly supports the grasping assembly, and aligns the contact pin with the hole. The pivot precisely positions the grasping assembly.

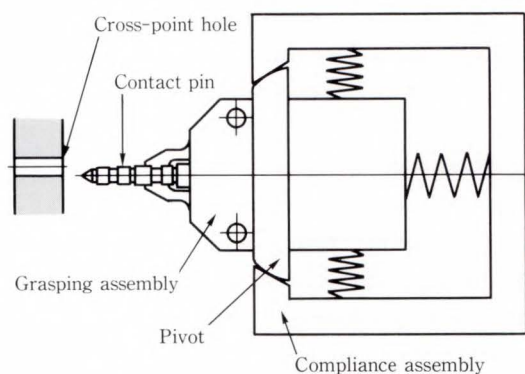
Since a contact pin has two contact rings slightly larger than the cross-point hole in the matrix board, they must be inserted with 500 gf. In Fig. 19a), the grasping assembly is pressed against the pivot by the rear spring of the compliance assembly until immediately before the contact pin is inserted.

In Fig. 19b), if the robot begins to insert the contact pin in the cross-point hole off-center, the grasping assembly and contact pin follow and rotate towards the cross-point hole.

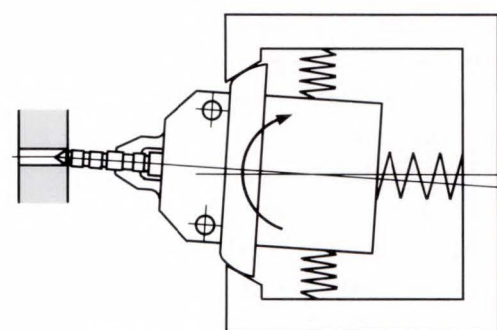
In Fig. 19c), if the robot keeps inserting the contact pin, the rear spring contracts due to the insertion force of the contact spring. This causes the grasping assembly to come away from the pivot. The grasping assembly and contact pin then move in the direction of the center.

In Fig. 19d), even if the contact pin is inserted as in Fig. 19c), the contact pin is loaded with the pressure difference between the upper and lower springs, the grasping assembly opens in the middle of insertion and the contact pin is only inserted by the pin pusher.

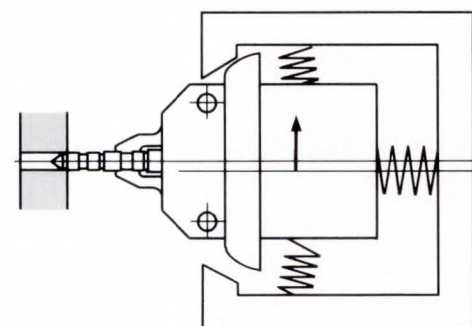
2) Efficiency of compliance



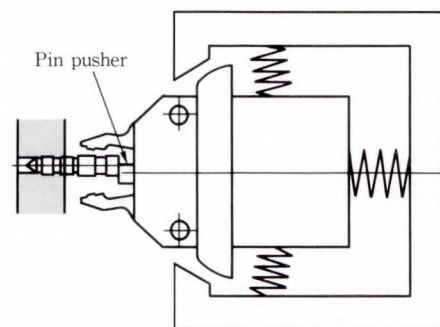
a) Holding a contact pin



b) Insertion with misalignment



c) Correcting misalignment



d) End of insertion

Fig. 19—Compliance assembly.

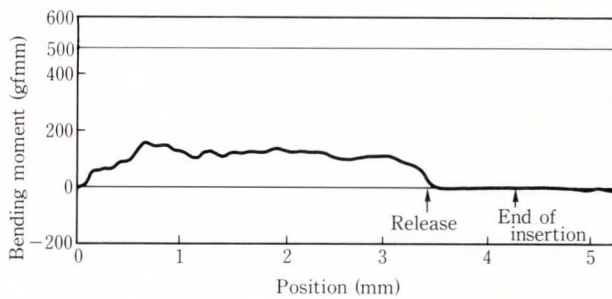


Fig. 20—Bending moment.

As mentioned before, the breaking strength of a contact pin is 110 gf. The narrow part (4.67 mm from the tip) of the contact pin receives a bending moment of about 500 gfmm. If the handling subunit does not give a greater bending moment, the contact pin will not be damaged.

Figure 20 shows the measured bending moment when a contact pin is inserted. The deviation of the contact pin from the center of the cross-point hole is 0.35 mm. The horizontal axis indicates the insertion distance and the vertical axis indicates the bending moment. Figure 20 also shows the release position and the end position of insertion. The graph indicates that the maximum bending moment of the contact pin is about 160 gfmm, well below the upper limit of about 500 gfmm. The compliance assembly keeps the bending moment stable during insertion. The bending moment is almost zero when the grasping assembly is opened. This indicates that opening the grasping assembly to insert a contact pin is very effective.

4.5 High reliability

The automated MDF system does not permit erroneous insertions or extractions. However, since it is not possible to reduce the number of errors to zero, the erroneous insertion and extraction rate was set to 4×10^{-7} . This is almost the same value as the line fault rate of 200 FIT. As matrix board patterns are tracked by laser, however, no erroneous insertions and extractions can occur unless a pattern or a nonpattern is erroneously recognized. Therefore, the erroneous pattern recognition rate (P_0) per line should be lower than the erroneous insertion and extraction rate.

$$P_0 = a \times N \times (P_P + P_H) < 4 \times 10^{-7},$$

a : Contact pin insertion and extraction count per line,

N : Cross-point pass count per contact pin insertion or extraction,

P_P : Erroneous pattern recognition rate per pitch,

P_H : Erroneous cross-point hole recognition rate per pitch.

During tracking, patterns and cross-point holes appear alternatively. Each area is sampled and patterns and holes are recognized to identify the correct path. The off-track status is judged if more than half the sampled areas are erroneously recognized. So the relationship between the erroneous pattern recognition rate per pitch and that per sampling becomes as follows:

$$P_P = \sum_{s=n/2}^n {}_n C_s p_P^s (1 - p_P)^{n-s},$$

$$P_H = \sum_{s=m/2}^m {}_m C_s p_H^s (1 - p_H)^{m-s},$$

n : Effective sampling count per pattern area,

m : Effective sampling count per cross-point hole area,

p_P : Erroneous pattern recognition rate per sampling,

p_H : Erroneous cross-point hole recognition rate per sampling.

The erroneous pattern recognition rate is dependent on the pattern reflection rate. According to the above expressions, the erroneous insertion and extraction rates are reduced to 4×10^{-7} or less by improving the pattern reflection rate.

In addition, the rows and columns are also counted to confirm that the robot has stopped at the specified matrix board. On the matrix board, the cross-point holes are counted and the parity holes are checked to enhance the reliability of locating holes.

5. Mounting technology

The automated MDF system is a precision machine consisting of electronic and mechanical

Table 5. Main mounting technologies

Technology	Description
Miniaturization	Developing the miniature contact pin and matrix board Optimizing the matrix board layout The matrix boards are allocated at both sides of the robot to reduce the distance the robot covers and the space occupied by the system. Sharing cable accommodation space Accommodating the link and external interface cables at the front of the matrix board. Sharing a link cable space connecting the front and back at the lower part of the system controller.
Earthquake protection	Earthquake protection control Retract the head unit when an earthquake begins. Restart and continue the operation after it ceases. Earthquake resistant structure to prevent destruction Reinforcing the framework and the robot structure. Optimizing the distance between the robot and matrix boards.

Table 6. Earthquake protection specifications and solutions

Earthquake protection specifications	Robot operating state	Problems caused by earthquake	Solution
No operational problem at 80-250 gal (cm/s ²) ground surface acceleration	Standby, moving, or inserting or extracting contact pin	Collision between robot, contact pin, and matrix board	Earthquake protection control ²⁾ (Retracting the robot in case of an earthquake)
No communication failures at 250-400 gal (cm/s ²) ground surface acceleration (Quality deterioration is acceptable)		Destruction of framework or robot itself	Reinforcing the framework and the robot Optimizing the distance between the robot and the matrix board

technologies in one frame. The system must accommodate many matrix boards with link cables and must also accommodate interface cables from outside.

To develop this system, the matrix board size must be reduced and the matrix boards and cables must be installed compactly. This reduces the space required to install the system and minimizes jumpering time.

Since Japan is subject to earthquakes, the system must be protected against them. Therefore, the framework needs to be able to withstand the force of an earthquake, and the robot must not strike the matrix boards if an earthquake occurs during operation.

The major mounting technologies unique to the automated MDF system are miniaturization and earthquake protection technologies. Table 5 outlines the technologies. The mounting technologies related to the contact pin and matrix board were explained in chapter 3. This chapter gives details of the earthquake protection technologies.

5.1 Details of earthquake protection technology

Table 6 gives an outline of the earthquake protection specifications and solutions. The solutions are detailed below.

1) Earthquake protection control²⁾

If an earthquake occurs while the robot is inserting or extracting a contact pin, the robot must not collide with the matrix board.

There are two solutions to this problem:

- i) Make the framework and robot strong enough to withstand the force of an earthquake.
- ii) Retract the robot and the contact pin in its hand to a safe place.

The latter solution is called "earthquake protection control". If an earthquake occurs, the jumpering is temporarily suspended and the head unit is retracted a safe distance. Once the earthquake ceases, the operation can continue normally. Table 7 gives an outline of the earthquake protection control.

2) Reinforcing the framework and robot

To protect the framework and robot from

Table 7. Outline of earthquake protection control

Earthquake condition	Earthquake protection control	
	Stage	
Just after start	1	Detects the earthquake with internal sensor
In progress	2	Suspends jumpering. Locks the operating robot (Y-axis) Retracts the head unit to a safe distance
End	3	Restarts and continues jumpering automatically

Table 8. Automated MDF FEM analysis results

Analysis items		Analysis results	
		Y-axis	Framework
Maximum displacement	X direction	0.196 mm	1.219 mm
	Y direction	0.014 mm	0.306 mm
	Z direction	0.207 mm	1.797 mm
Maximum stress	X direction	9.81 kgf/mm ²	9.86 kgf/mm ²
	Y direction	0.37 kgf/mm ²	2.13 kgf/mm ²
	Z direction	3.08 kgf/mm ²	8.74 kgf/mm ²
Natural frequency	Primary	43.45 Hz	11.96 Hz
	Secondary	58.17 Hz	16.74 Hz
	Tertiary	118.41 Hz	25.79 Hz

Note: The acceleration was set to 1 G considering the response magnification of the floor on which the equipment is installed.

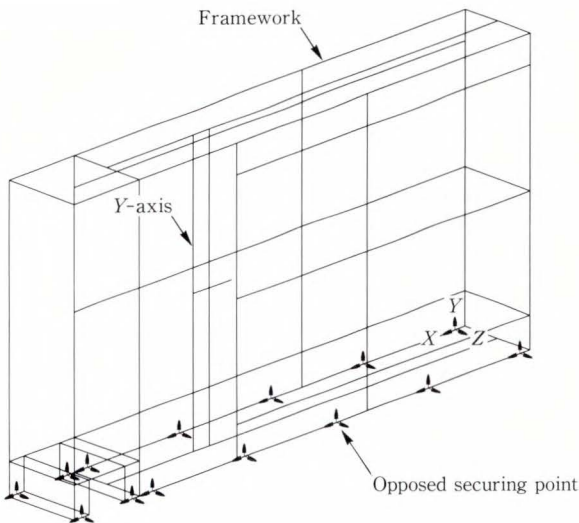


Fig. 21—Automated MDF finite element method (FEM) analysis model.

being destroyed by an earthquake, they should be reinforced to increase the natural frequency of the equipment. Resonance between the vibrations in the floor and equipment can then be avoided during an earthquake. The authors created the structural model shown in Fig. 21 and analyzed the displacement, stress, and natural frequency of each section by the finite element method (FEM). Table 8 lists the results of analysis. The displacement and stress confirmed that the framework withstands an earthquake sufficiently. The primary natural frequency of the framework became 11.96 Hz, higher than the natural frequency of the floor (about 5 Hz) where the equipment is installed.

3) Optimizing the distance between the robot and the matrix board

Even when the framework and robot are reinforced, they move differently when an earthquake occurs. If the robot and the matrix

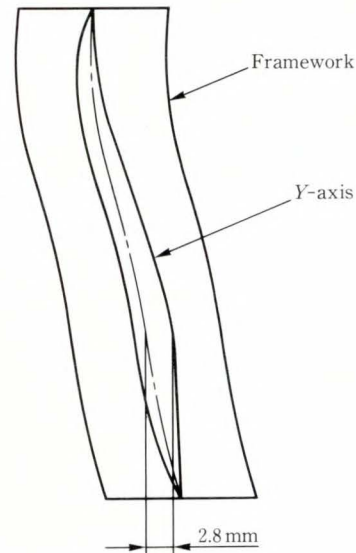


Fig. 22—Results of analyzing the distance between Y-axis and framework.

board are close to each other, they may collide with each other and be damaged.

To prevent such a collision, there must be sufficient clearance for the robot and the matrix board to move independently without colliding. Therefore, the displacements of the robot and the framework were analyzed by FEM, using the structural model.

The analysis data indicates that the distance between the Y-axis and the framework decreased by up to 2.8 mm as shown in Fig. 22. The distance between the tip of the contact pin in the robot's hand and the matrix board was therefore set to 10 mm or greater for safety.

Table 9. Earthquake test results

Test items	Robot operating state	Waveform	Maximum acceleration (3 dimensions at once)	Test results
Function measurement	Not operating	Sine wave	0.1 G	Maximum response magnification Framework: 10.2 Y-axis: 9.2 Head unit: 10.7 Primary natural frequency of the equipment: 8.9 Hz
Connected path	Not operating	White noise Sine wave	0.1 G	No bit error No DC resistance change at connected path
	Not operating	Earthquake wave	1 G*	
	Operating	Earthquake wave	1 G*	
Earthquake protection performance	Not operating	Earthquake wave	1 G*	No physical damage
Earthquake protection control	Operating	Earthquake wave	1 G*	Earthquake protection control stage 1, 2, and 3 was normal (see Table 7)

* : The acceleration was set to 1 G considering the response magnification of the floor on which the equipment is installed.

5.2 Earthquake protection tests

The tests were performed on the actual system to verify the earthquake protection. The earthquake protection specifications were all satisfied, as follows:

- 1) The primary natural frequency of the equipment was 8.9 Hz,
- 2) No momentary line disconnection due to earthquake vibration,
- 3) No damage to the construction due to earthquake vibration, and
- 4) The earthquake protection control was normal.

Table 9 lists the test items and their results.

6. Software

6.1 Function outline

The automated MDF system supports three dedicated software programs, one each for the operation terminal, the system controller, and the robot mechanism.

1) Operation terminal software functions

The operation terminal displays instructions issued to or responses received from the automated MDF system. It is designed to be easy-to-understand. The database in the system controller is also backed up.

2) System controller software functions

The system controller software is the

nucleus for controlling the automated MDF system. The software has a database to manage free and blocked cross points in a network consisting of three-stage links. It also has an algorithm to select a cross-point to connect a subscriber cable terminal with an office-equipment cable terminal while checking whether the cross-point is being used.

3) Robot mechanism software functions

This software responds to instructions from the system controller. It provides fine control to move the robot at high speed, track the matrix board to the target cross-point, and precisely position the robot.

6.2 Operation outline

This section outlines the operations of the automated MDF system by using path connections as an example.

First, the operator must access the automated MDF system at the remote location by inputting a message at the operation terminal and then transmitting it through the telephone network. Then the operator specifies the subscriber cable number and office equipment terminals number and requests a path connection.

The system controller selects the free cross-points in the three-stage link to create a connec-

tion path from the specified subscriber cable terminal to the specified office-equipment cable terminal. To connect terminals at a selected cross-point, the controller instructs the robot to extract a contact pin from the pin-supply matrix board. The system controller then orders the robot to insert a contact pin into the target cross-point.

The robot extracts a contact pin from the pin-supply matrix board and moves to the target cross-point by tracking the matrix board. It then inserts the contact pin into the cross-point.

6.3 Error recovery functions

If a fault occurs while the robot is tracking the matrix board or handling a contact pin, the software programs work together for hierarchical error recovery. By using path connection as an example, this section explains how each type of software performs error recovery when the cross-point is faulty.

1) Error recovery by robot mechanism software

The software positions the robot at the matrix board cross-point specified by the system controller. If the robot fails to insert a contact pin, the software returns the robot to the origin mark. It then moves the robot to the same cross-point again to insert the contact pin (failure retry). If the contact pin cannot be inserted the second time, the matrix board inclination is measured and the robot is self-diagnosed. The fault is then attributed to the contact pin, matrix board, or robot, and reported to the system controller.

2) Error recovery by system controller software

The software instructs the system controller to abandon the contact pin and try with a new contact pin (failure retry). If the error recurs, the software determines that the cross-point hole is faulty and closes it. If the contact pin is already inserted, it is extracted. The result of operation is then reported to the operation terminal.

3) Error recovery by operation terminal software

The software checks the error report from the system controller. If the error is located in the third step, the software selects a new office-

equipment cable terminal and issues the instruction again.

7. Conclusion

An automated MDF system has been developed by integrating switching technology, robot technology, and printed wiring board technology.

The automated MDF system is now operating without any problems. We believe the automated MDF system is making a major contribution to providing a quick and efficient service¹⁹⁾.

This automated MDF system was developed for small unattended offices handling 540, 1 000, or 2 100 office-equipment cable terminals. The authors are now developing a larger-scale automated MDF system. An automated MDF system for a small office can be installed in parallel to increase the capacity. Presently, the authors will start developing a multiple-robot control system which integrates control functions for medium-sized and large offices.

8. Acknowledgement

The authors would like to thank the staff of the Nippon Telegraph and Telephone Corporation for their guidance and fruitful discussions during the development and application of the automated MDF system.

References

- 1) Hosokawa, S., Kanai, T., Kimura, H., and Nagayama, A.: Robot Automation of MDF-Jumping Operation. (in Japanese), *Trans. IEICE*, B-I, **J73-B-1**, 12, pp. 922-931 (1990).
- 2) Yoshida, K., Hirono, T., Hosokawa, S., and Nagayama, A.: A New Automated Main Distributing Frame System Using Robot. 1991 IEEE Int. Conf. Commun., 2, 1991, pp. 977-982.
- 3) Hosokawa, S.: Robot Automation of MDF Jumping Operations. (in Japanese), *NTT Tech. J.*, **1**, 4, pp. 50-53 (1989).
- 4) Hirono, T., Takahashi, M., Nagahama, M., and Seino, T.: Remote Automated MDF Work. (in Japanese), *NTT Tech. J.*, **2**, 9, pp. 32-35 (1990).
- 5) Kase, I., and Yoshida, K.: Current Statuses and Future Outlook of MDF Enhancements. (in Japanese), *NTT Tech. J.*, **1**, 2, pp. 76-79 (1989).

- 6) Clos, C.: A Study of Non-Blocking Switching Networks. *Bell. Syst. Tech. J.*, **32**, 2, pp. 406-424 (1953).
- 7) Umemura, S., Kanai, T., Inagaki, S., and Kumakura, Y.: High-Density Pin-Board-Matrix Switches for Automated Main Distributing Frame Systems. (in Japanese), 1991 Spring Nat. Conv. Rec., IEICE, Part 5, 1991, pp. 5-271-5-272.
- 8) Umemura, S., Kanai, T., Inagaki, S., and Kumakura, Y.: High-Density Pin-Board-Matrix Switches for Automated Main Distributing Frame Systems. (in Japanese), IEICE Tech. Rep., **91**, 7, EMC91-2, pp. 7-11 (1991).
- 9) Umemura, S., Kanai, T., Inagaki, S., and Kumakura, Y.: Design of High Density Pin Board Matrix Switches for Automated Main Distributing Frame Systems. *IEEE Trans. Comp., Hybrids, Manuf. Technol.*, **15**, 2, pp. 266-277 (1992).
- 10) Sakai, M., Nagayama, A., and Sasakura, K.: High Precision Crosspoint Positioning Control on the Automated Reconnection System. (in Japanese), 1988 Autumn Conv. Rec., Inst. Precis. Eng., 1988, pp. 149-150.
- 11) Sakai, M., Nagayama, A., and Sasakura, K.: Positioning Method Using Polarization-Detecting Optical Sensor for Precision Robot Systems. *SPIE, Optics, Illumination, and Image Sensing for Machine Vision V*, **1385**, pp. 8-14 (1990).
- 12) Inagaki, S., Kanai, T., and Hosokawa, S.: Crosstalk Analysis on Matrix-Switch Link System. (in Japanese), 1990 Spring Nat. Conv. Rec., IEICE, Part 3, 1990, p. 3-116.
- 13) Inagaki, S., and Kanai, T.: Crosstalk Characteristics on High-Density Matrix-Board. (in Japanese), 1991 Spring Nat. Conv. Rec., IEICE, Part 5, 1991, p. 5-5.
- 14) Sasakura, K., Nagayama, A., and Sakai, M.: New Polarization-detecting Optical Sensor for Positioning to Matrix Cross-connection Hole on a Printed Board. (in Japanese), *J. Jpn. Soc. Precis. Eng.*, **57**, 7, pp. 51-56 (1991).
- 15) Sasakura, K., Nagayama, A., and Sakai, M.: Optical Sensor with Polarization Characteristics for Detecting Matrix-Board Crosspoint Center. (in Japanese), 1988 Autumn Conv. Rec., Inst. Precis. Eng., 1988, pp. 337-338.
- 16) Sasakura, K., Nagayama, A., and Sakai, M.: New Polarization-Detecting Optical Sensor for Precision Robot Systems. Tech. Digest Conf. Lasers and Electro-Optics, **7**, Paper CFS2 (1990).
- 17) Kimura, H.: Pin Handling and Insertion Process by 4-Finger Compliant Mechanism. (in Japanese), 1988 Autumn Conv. Rec., Inst. Precis. Eng., 1988, pp. 627-628.
- 18) Kimura, H., Ifukube, T., Ino, S., and Izumi, T.: Role of Tactile Sense of Fingers in Pin Insertion/Extraction and Design of Force Vector Sensor Modeled after the Tactile Sense. (in Japanese), *J. Robotics Soc. Jpn.*, **8**, 6, pp. 32-39 (1990).
- 19) Ono, M., Yamazaki, T., Kase, I., and Hinohara, T.: Reducing Costs at Small-Scale Offices. (in Japanese), *NTT Tech. J.*, **2**, 3, pp. 81-83 (1990).



Shun-ichi Tominaga
 Hardware Development Dept.
 Switching Systems Group
 FUJITSU LIMITED
 Bachelor of Electronics
 Kagoshima University 1970
 Specializing in Switching System



Akira Fukuoka
 Micro-Component & Module
 Technology Dept.
 Communication Systems Group
 FUJITSU LIMITED
 Bachelor of Electronics
 Shizuoka University 1971
 Master of Electronics
 Shizuoka University 1973
 Specializing in Development of
 Components and Inter-Con-
 nection Technology



Sadao Fujii
 Corporate Manufacturing System
 Development Div.
 FUJITSU LIMITED
 Bachelor of Precision Eng.
 Hokkaido University 1968
 Specializing in Computer Aided
 Design and Robotics

International Network

Offices

Abu Dhabi Office

P.O. Box 47047 Suite 802.
Al Masadood Tower,
Sheikh Hamdan Street,
Abu Dhabi, U.A.E.
Telephone : (971-2)-333440
FAX : (971-2)-333436

Algiers Office

9 Rue Louis Rougie Chateau Neuf.
El Biar, Alger 16030. Algeria
Telephone : (213)-2-78-5542
Telex : 408-67522

Amman Project Office

P.O. Box 5420, Ammán, Jordan
Telephone : (962)-6-662417
FAX : (962)-6-673275

Bangkok Office

3rd Floor, Dusit
Thani Bldg., 1-3, Rama IV,
Bangkok 10500, Thailand
Telephone : (66-2)-236-7930
FAX : (66-2)-238-3666

Beijing Office

Room 2101, Fortune Building,
5 Dong San Huan Bei-lu,
Chao Yang District, Beijing,
People's Republic of China
Telephone : (86-1)-501-3261
FAX : (86-1)-501-3260

Brussels Office

Avenue Louise 176, Bte 2
1050 Brussels, Belgium
Telephone : (32-2)-648-7622
FAX : (32-2)-648-6876

Harare Office

CABS House, Corner Central Avenue,
4th Street, Harare, Republic of Zimbabwe
Telephone : (263-4)732-627
FAX : (263-4)732-628

Hawaii Office

6660 Hawaii Kai Drive, Honolulu,
Hawaii 96825, U.S.A.
Telephone : (1-808)-395-2314
FAX : (1-808)-396-7111

Jakarta Representative Office

16th Floor, Skyline Bldg.,
Jalan M.H. Thamrin No.9,
Jakarta, Indonesia
Telephone : (62-21)-333245
FAX : (62-21)-327904

Kuala Lumpur Office

Letter Box No.47, 22nd Floor,
UBN Tower No.10, Jalan P.
Ramlee, 50250, Kuala Lumpur, Malaysia
Telephone:(60-3)-238-4870
FAX : (60-3)-238-4869

Munich Office

c/o Siemens Nixdorf Informationsysteme
AG, D8 SC,
Otto-Hahn Ring 6, D-8000,
München 83, F.R. Germany
Telephone:(49-89)-636-3244
FAX : (49-89)-636-45345

Nairobi Office

Flat No.10, Fairview Flats, Bishop Road,
P.O. Box 21290, Nairobi, Kenya
Telephone : (254-2)727934
FAX : (254-2)723201

New Delhi Liaison Office

Mercantile Home
1st Floor, 15 Katsurba, Gandhi Marg
New Delhi-110001, India
Telephone : (91-11)-331-1311
FAX : (91-11)-332-1321

New York Office

680 Fifth Avenue, New York,
N.Y. 10019, U.S.A.
Telephone : (1-212)-265-5360
FAX : (1-212)-541-9071

Shanghai Office

Shanghai Centre,
1376 Nanjing Road West,
Shanghai, People's Republic of China
Telephone : (86-21)-279-8410
FAX : (86-21)-279-8411

Sucursal de Colombia

Cra. 9a. A No. 99-02 ofc. 811
Edificio Seguros Del Comercio
Santa Fe De Bogotá, Colombia
Telephone : (57-1)-618-3147
FAX : (57-1)-618-3134

Taipei Office

Sunglow Bldg., 66, Sung Chiang
Road, Taipei, Taiwan
Telephone : (886-2)-551-0233
FAX : (886-2)-536-7454

Washington, D.C. Office

1776 Eye Street, N.W.,
Suite 880, Washington, D.C.,
20006, U.S.A.
Telephone : (1-202)-331-8750
FAX : (1-202)-331-8797

Subsidiaries

ASIA AND OCEANIA

Fujitsu Australia Ltd.
Fujitsu Australia Software Technology. Pty. Ltd.
Fujitsu Component(Malaysia)Sdn. Bhd.
Fujitsu Electronics(Singapore)Pte. Ltd.
Fujitsu Hong Kong Ltd.
Fujitsu Korea Ltd.
Fujitsu Microelectronics Asia Pte. Ltd.
Fujitsu Microelectronics(Malaysia)Sdn. Bhd.
Fujitsu Microelectronics Pacific Asia Ltd.
Fujitsu New Zealand Ltd.
Fujitsu(Singapore)Pte. Ltd.
Fujitsu(Thailand)Co., Ltd.
Fujitsu Trading Ltd.

NORTH AMERICA

Fujitsu America, Inc.
Fujitsu Business Communication Systems, Inc.
Fujitsu Canada, Inc.
Fujitsu Computer Packaging Technologies, Inc.
Fujitsu Computer Products of America, Inc.
Fujitsu Microelectronics, Inc.
Fujitsu Network Switching of America, Inc.
Fujitsu Network Transmission Systems, Inc.
Fujitsu Systems Business of America, Inc.

Fujitsu Systems Business of Canada, Inc.
Open Systems Solutions, Inc.
Fujitsu Personal Systems, Inc.

EUROPE

Fujitsu Deutschland GmbH
Fujitsu España, S.A.
Fujitsu Europe Ltd.
Fujitsu Europe Telecom R&D Centre Ltd.
Fujitsu Finance(U.K.)PLC
Fujitsu France S.A.
Fujitsu International Finance(Netherlands)B.V.
Fujitsu Italia S.p.A.
Fujitsu Microelectronics Ireland Ltd.
Fujitsu Microelectronics Italia S.r.l.
Fujitsu Microelectronics Ltd.
Fujitsu Mikroelektronik GmbH
Fujitsu Nordic AB
Fujitsu Systems Business of Europe Ltd.
Fulcrum Communications Ltd.

LATIN AMERICA

Fujitsu do Brasil Ltda.
Fujitsu Vitória Computadores e Serviços Ltda.

FUJITSU LIMITED

6-1, Marunouchi 1-chome, Chiyoda-ku, Tokyo 100, Japan

Phone: National (03) 3216-3211 International (Int'l Prefix) 81-3-3216-3211 Telex: J22833 Cable: "FUJITSULIMITED TOKYO"

Fax: National (03) 3213-7174 International (Int'l Prefix) 81-3-3213-7174